FIBRE-REINFORCED MATERIALS

FABRICATED BY POWDER EXTRUSION

by

HENRY MCSHANE, B,SC,(ENG,)

A thesis submitted for the
Degree of Doctor of Philosophy of the
University of London

John Percy Research Group,
Department of Metallurgy and
    Materials Science,
Imperial College of Science
    and Technology,
London SW7 2BP

March 1978

ABSTRACT

The powder extrusion process as a consolidation technique
for pre-alloyed aluminium and aluminium alloy powders has been
thoroughly investigated. Analyses have been proffered to pre-
dict. extrusion load, strain rate and "steady state" temperature
during the extrusion process. Classical hot working theory has
been applied to powder compacts during extrusion and to the re-
sulting extrudes relating flow stress, strain rate and tempera-
ture. The controlling effect of the extrusion parameters on
the product structure and mechanical properties has been clearly
demonstrated. Al-Mg-Si powder extrudes have been subjected to
various heat treatments and the resulting mechanical properties
investigated.

Glass fibre reinforced rods have been produced, by this
powder extrusion route, from mechanically mixed quantities of
aluminium alloy powder and glass powder. The extrusion process
has served three purposes:-

(1) Fibre formation (in situ in the deformation zone and
die neck)

(2) Fibre alignment

(3) Matrix consolidation

The structure and mechanical properties of the resulting rein-
forced extrudes have been observed in some detail. A knowledge
of the   glass content, extrusion temperature and ram speed
required to give optimum properties has been obtained.

In all, the results of several hundred extrusions, the cor-
responding mechanical tests and microscopical examinations are
reported in this thesis.

ACKNOWLEDGEMENTS

The author wishes to express his sincere appreciation

CONTENTS

LIST OF FIGURES

LIST OF PLATES

LIST OF TABLES

CHAPTER 1

INTRODUCTION

1.1.1 Powder Metallurgy

In the early fifties considerable interest
was shown in S.A.P. products manufactured by A.I.A.G.
These possessed high strength at elevated temperatures
due to the high oxide content, (6-15%), but low ductility
due to the brittle nature of the oxide. Various alloy-
ing additions were used in an attempt to improve the
ductility but little success was achieved. Atomised
Al alloy powders have a lower oxide content (0.2-5%)
depending on the process used. However, due to the
high cooling rate from the liquid state, atomized powders
possess a very fine, homogeneous, (though non-equilibrium)
structure which improves the ductility considerably.
Alloys which are very difficult to manufacture by
normal casting procedures, due to poor solid solubility
of a particular phase in the bulk metal e.g. Al-Fe, can
be produced by atomization. The resulting powder may be
consolidated by a number of mechanical working processes
including forging, rolling, and extrusion. To ensure
complete consolidation in the extrusion process a mini-
mum extrusion ratio (5:1 to 10:1) must be exceeded.
However, evidence [19] exists that lower extrusion loads
and faster extrusion speeds (compared to cast billet
extrusion) are possible. These advantages compensate
for the restricted minimum extrusion ratio.

1.1.2 Precipitation Hardening

Many of the Aluminium alloys are very responsive
to heat treatments. The Al-Cu and Al-Mg-Si (which
behaves as an $Al-Mg_2Si$ binary alloy) systems are classic

examples of precipitation hardening alloys. The usual
form of the heat treatment consists of the three stages:-

1) heat soaking
2) quenching
3) ageing

Such a treatment is fairly costly when applied to a
fabricated component and in the extrusion industry a
compromise treatment is used. This much more convenient
process involves:-

1) heating the billet to the soaking temperature

2) press quenching the extrude

3) ageing the extrude

Part of this project involved finding out if extruded
Al-Mg-Si alloy powders would prove responsive to a
suitable heat treatment resulting in an increase in
the strength of the product.

1.2.1 Fibre Reinforcement

Approximately ten years ago a series of papers
concerning fibre reinforcement was published when certain
firms, including Rolls-Royce, were interested in carbon-
fibre products. The possibility of including strong,
high elastic modulus fibres in a ductile metal matrix
was and indeed still is very interesting. The main
advantage of such a system is that the rigidity as well
as the strength of fairly light metals, such as aluminium,
may be significantly improved. However, the large draw-
back of the high production cost of the composite has
greatly hindered general development. Such composites
have been manufactured on a limited scale for special
purposes, especially in the aerospace industry, where
production costs are often outweighed by performance
requirements.

1.3.1 Composite Production by Powder Route - Present Work

The method of composite production employed in this investigation overcomes many of the usual difficulties and enables the strengthening mechanisms of dispersion strengthening, precipitation hardening and fibre reinforcement to be used on a major architectural alloy, HE9. The method is simple and fast so that production costs are kept to a minimum.

CHAPTER 2

LITERATURE REVIEW

2.1.1 Introduction

To achieve optimum composite properties a thorough
knowledge of the factors which dictate these properties is
required. The method of production and the type of system
employed in the composite are obviously important. A
knowledge of the press capacity required, estimated from
various load prediction models, is also advantageous.
Process conditions,defined by temperature and strain rate,
together with material properties determine the product structure
which in turn determines its properties. Methods of estimating
these conditions obtaining during extrusion must therefore be
examined in considerable detail. Possible strengthening
mechanisms for improving the composite properties, e.g. heat
treatment, are also of considerable importance.

2.2.1 Cold compaction of metal powders

Metal powders are frequently cold compacted to
facilitate handling and pre-heating operations prior to the
application of consolidation processes such as hot forging
and/or extrusion. The powder compaction process has been
extensively studied. These studies have usually involved
the formulation of a relationship between the applied pressure
and the resulting compact density. For most metal powders it
is generally agreed that the compaction process consists of
three distinct stages [1] (Fig. 1). Kunin and Yurchenko [2]
suggested that the following mechanisms operate during the
various stages:-

Stage 1 Packing of the undeformed particles into a
smaller volume.

Stage 2   Elastic and plastic deformation of the
particles.   During deformation the particles slide over
each other.   In metals having oxide surface layers e.g.
aluminium, this sliding movement causes rupturing of the
oxide layers.   This leads to metal-metal interparticle
point contact which results in cold welding.   With increasing
pressure these areas of contact increase in size.   Easterling [3.]
showed that the presence of these oxide layers greatly reduced
compact strength as well as lowering the response of the compacts
to induction heating prior to further hot working.   It will
be shown in the present investigation that mains frequency
induction heaters are incapable of preheating aluminium alloy
powder billets compacted to > 90% theoretical density. Strömgren [9]
measured the strength of aluminium powder compacts pressed
to 100% theoretical density.   He suggested that the low strength
was due to the oxide particles causing stress concentrations
at interparticle boundaries.

Stage 3   Bulk compression i.e. cold working of the
compact as a whole.   It should be noted that the processes
mentioned in stages 1 and 2 sometimes occur concurrently.

One of the most popular relationships between pressure
and compact density was first suggested by Shapiro and Kolthoff [4]
and by Konopicky [5] :

$$\ln \left(\frac{1}{1 - D}\right) = K'P + constant \qquad (1)$$

D = relative density
P = compaction pressure
K' = acompaction constant.

Equation (1) is also plotted in Fig. 1.   Good agreement between
theory and experimental results exists over the linear region of
the experimental curve (Stage 2).   The overestimation of the
density given by equation (1) at low pressures is due to the
equation not taking into consideration particle packing prior
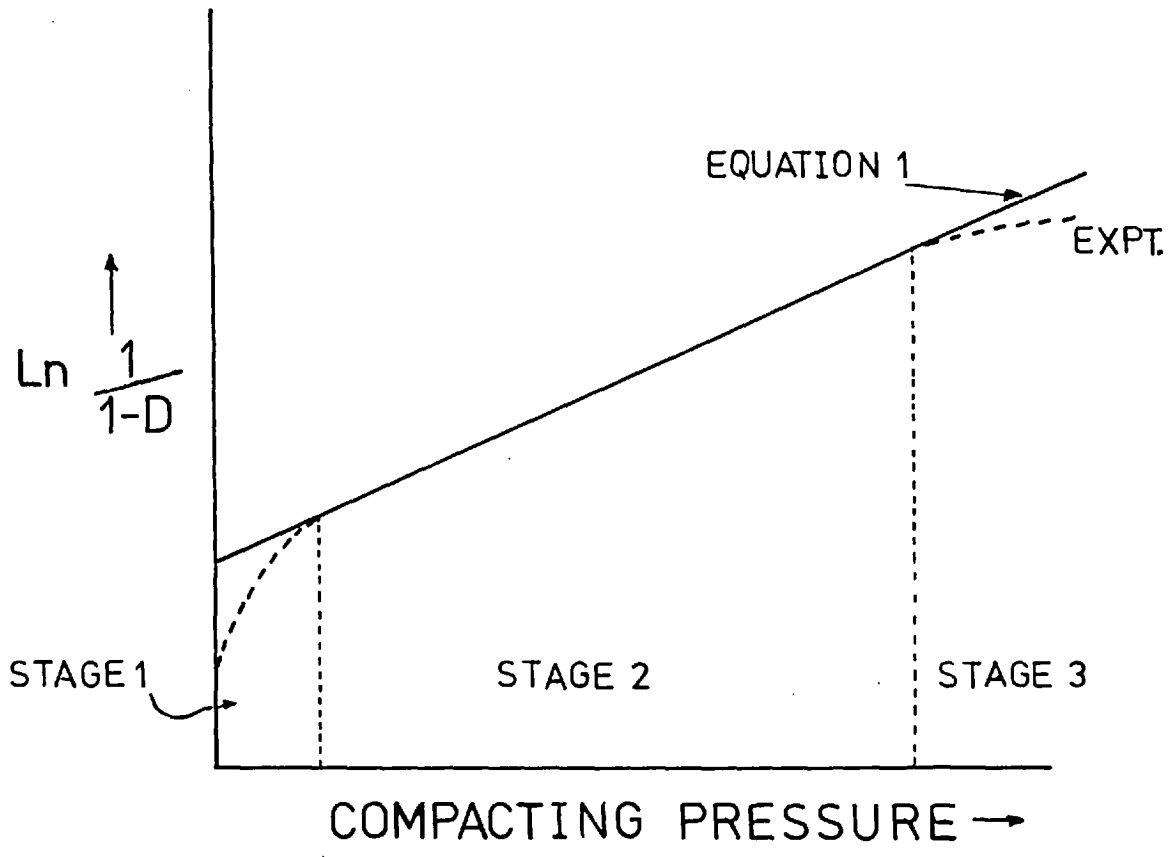
FIG. 1   Relationship between compacting pressure and relative density

FIG. 2   Extrusion pressure as a function of ram displacement (Idealised)
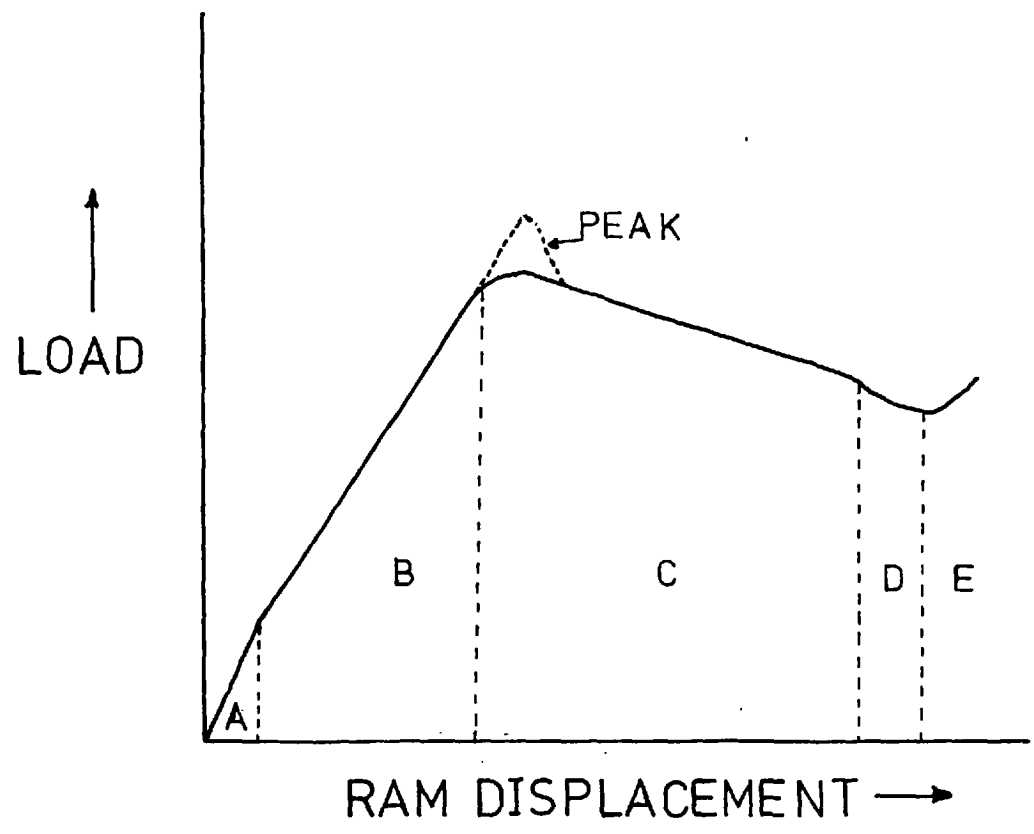
to deformation. Hewitt[6] attempted to incorporate the effects of strain hardening during compaction. His experiments with iron powder showed that the compaction behaviour during stage 2 could be predicted very accurately. However he found that the deviation from linearity during stage 3 could not be attributed to strain hardening. Hewitt suggested that stage 3 involved the closure of pores and defects and therefore could not be explained by a macroscopic model.

Heckel[7] agreed with the operating mechanisms suggested by Kunin and Yurchenko[2] and proposed a theoretically derived pressure-density relationship similar to equation (1). He considered powder compaction to be analogous to a first order chemical reaction. The pores were assumed to be the reactant so that :-

$$\frac{\text{change in density}}{\text{change in pressure}} \quad \alpha \text{ pore fraction}$$

Kawakita[8] recently proposed another empirical relationship based on volume and pressure measurements. He derived the equation :-

$$C^* = \frac{V_o - V}{V_o} = \frac{a\,b\,p}{1 + bP} \qquad (2)$$

C^* = degree of volume reduction
V_o = initial apparent volume
V = actual volume under pressure
a,b= constants

None of the relationships discussed in this section explain the behaviour of compacts under high pressure, although Hewitt attempted to explain this behaviour in terms of work hardening. All the relationships deal with the effect of compaction

pressure on theoretical density. A more useful relationship would relate the compaction pressure to compact strength as past experience has shown that 100% theoretical density does not always correspond to 100% theoretical strength (i.e. the strength of a cast and wrought material).

2.3.1. Extrusion Process

The process of extrusion seems, initially, to be a simple method of fabricating components. Basically it involves a metal billet being pushed through a hole or orifice of a particular shape and size to give a desired product. Most metals are extruded at elevated temperatures for two main reasons:

(1) To prevent work hardening increasing the required load and thus the energy used.

(2) An extrude with a "cold work" structure (i.e. a high dislocation density) is very brittle. Fig.2[10] depicts an idealised extrusion curve. During the linear region, (A), the billet is upset to fill the container. The billet is then compressed until metal begins to flow through the die,(B). After this breakthrough a "steady state" is established during which extrusion continues,(C). The load actually decreases slightly during this pseudo "steady state" region because the friction forces between billet and container wall decrease as the billet length decreases. Eventually a piping[11] defect tends to occur,(D). This happens when the rear-centre of the billet "caves" in and material from the sides of the billet flows laterally to occupy the newly created void. This often leads to a central core of undesirable, oxidised material running through the latter stages of the extrude. Finally the billet becomes so short that flow is inhibited,(E). The pressure increases

rapidly as the material tries to flow almost perpend-
icularly to the direction of extrusion.

A number of variations in Fig.(2) are commonly
observed. Steel and nimonic[12] alloys exhibit a "steady
state" region in which the load increases with ram
displacement. This is due to the billet cooling during
the extrusion process, (typical temperatures 1100-1200°C).
As the temperature decreases the flow stress increases
due to reduced dynamic softening. Very often, as in
the case of Aluminium alloys[13], a peak in the load-
displacement curve is present, (dotted line, Fig.(2)).
This peak is probably due to a thermally activated
process involving a build-up of dislocations followed
by their annihilation.

In the extrusion of light metal alloys graphite
is sometimes put on the die face and die-land to act
as a kind of "lubricant".This is not full-film
lubrication.The extrusion of steel and nimonic alloys
involves the use[14] of fibre glass as a lubricant.
This prevents the billet from being welded to the
container (thus protecting the container liner)
and also lowers the working load. Interest in the cold
extrusion of steel using a zinc phostate-sodium
stearate lubricant has grown recently[16].

A process which greatly reduces the effects of
friction is indirect extrusion[15]. In this process the
ram is used to seal the container end. The ram
and container are then moved simultaneously at the
same speed and in the same direction. This technique
prevents any relative motion between the container
walls and the billet. This action pushes the billet
through the die. Thus the only frictional forces
which must be overcome are those due to the billet/

die face contact and the extrude/die land contact.
On an industrial scale, these friction effects are
considerable and by reducing them large energy savings
become possible.

The process of extrusion does have several dis-
advantages. One of the biggest is that variations in
strain, strain rate and temperature throughout the
deforming metal produce an extrude of varying structure.
Thus the mechanical properties of the extrude vary with
position. The press capacity is dictated by the peak
load (Fig. 2). Therefore the press capacity is only
fully utilized for a fraction of the duration of each
extrusion.

Recent developements in the extrusion field
include the semi-continuous hydrostatic process,
suggested by Alexander and Lengyel[17], and the
continuous ("conform") extrusion process[18] of Green.
In the past the billet length has always been limited
to minimize the amount of power wasted in overcoming
billet-container wall friction. Both of these new
processes actually make use of this friction force
to "drag" the feedstock to the die. The "conform"
process basically involves[124] the feeding of a
rod into a peripheral square groove in a rotating
wheel, the groove side being slightly smaller than
the feedstock. A stationary shoe placed around part
of the wheel periphery completes the fourth side
of an "extrusion container". The friction between
rod and groove continuously drags the feedstock
into this "extrusion container". An abutment held
by the shoe intrudes fully into the groove to act
as a container end. The rotating wheel feeds the rod
to this point and the force generated at the abutment
upsets the feedstock to fill the container. The
increasing frictional force generated between the

groove and the upset material generates a pressure
which is sufficient to cause extrusion through
a hole in the abutment. This process appears to have
an important part to play in the future developments
of the extrusion industry.

2.3.2. Extrusion of Powders

The most widely used method for fabricating a
component from metal powder is hot forging. On an
industrial scale the extrusion of powders is in its
infancy. In experimental powder investigations
several methods have been used and these are listed
below :-

(i) loose powder extruded.
(ii) powder cold compacted, then
extruded.
(iii) powder cold compacted, sintered
then extruded.
(iv) loose powder placed in can,
evacuated, sealed, then extruded.
(v) powder isotatically compacted,
then extruded.
(vi) powder isostatically compacted,
canned, evacuated, sealed, then
extruded.

The only industrial powder extrusion processes
in operation at present involve nimonic, stainless
steel and tool steel powders. Method (iv)   is usually
employed.[20] The evacuation of the can prevents
oxidation of the powder. The can, usually made of mild
steel, acts as a lubricant although fibre-glass
is normally also used. The main disadvantage of this
method is that after extrusion the can material
must either be machined from the surface or else
removed by soaking in a pickling bath. Recent experiments

have shown that method (V) may be successfully used in the extrusion of sponge iron powder[21] and high speed steels.[22] Method (ii) is usually used by investigators working[23]with low melting point alloys. This facilitates the easy handling and preheating of the powder prior to extrusion.

Sheppard and Chare[23] showed that much lower loads were required for the extrusion of aluminium alloy powder compacts than for cast billets of the same composition. They suggested that this load reduction was due to the powder compact not achieving complete consolidation until late in the deformation cycle. Sheppard also showed that the strain-rate sensitivity of a powder compact was much less than that of the corresponding cast billet. These two, important findings are thought to hold for other high stacking fault energy metals in which dynamic recrystallisation does not occur. This strain-rate sensitivity effect indicates that extrusion speeds could be increased if powder compacts were used instead of cast billets. Another advantage of the powder route is that oxide particles,resulting from the oxide layer disintegration,cause an increase in strength due to dispersion strenghthening effects. As the oxide particles are very stable this streng thening effect is present even at elevated temperatures. The inherently fine structure of the atomized powders also prevents macrosegregation, a danger when using cast ingots.

However one important limitation to powder extrusion is that a minimum extrusion ratio must be exceeded to ensure complete densification. Gurney et al[24] found this ratio to be approximately 6:1 for 7075 aluminium alloy powder.

2.4.1. Prediction of Load.Slip-Line Field Theory.

At present several methods are used in attempts
to relate the extrusion pressure to the flow
stress of the material. The two most widely used
are based on :

      1. Slip-line field theory.

      2. Load bounding (upper bound) theory.

The slip-line field technique enables fairly
complex plastic flow equations to be solved
accurately by establishing the maximum shear
line field. Solutions for the extrusion process
have been developed for a variety of friction
conditions ranging from perfectly rough billet/die
contact surfaces to perfectly smooth ones. Various
die shapes have also been considered[26,27,28]
(square, wedged-shaped and concave). These solutions
have usually consisted of graphs of extrusion
pressure versus extrusion ratio. This theory is
mathematically correct but its use is rather tedious.
Johnson and Kudo[25] suggested the following method
for employing slip-line field theory:-

(1) Construct the slip-line field which satisfies
    given boundary conditions in terms of stresses,
    starting from certain boundary surfaces
    of the material and assumed rigid plastic
    slip-lines.

(2) Obtain the velocity distribution by means
    of the slip-line field and from some
    of the given velocity boundary conditions.
    Then find if the remaining boundary conditions
    are fulfilled.

(3) Check for a positive rate of plastic work
    everywhere in the deformation zone.

(4) Check that the yield criterion in the assumed
    non-deforming region is obeyed. If the
    boundary conditions are not satisfied
    the field must be redrawn.

Over a limited range of extrusion ratios
Johnson showed that the theoretical solutions
could be approximated by:-

$$\frac{P}{2K} = A + B \ln R$$

A and B are friction dependent constants. The
shear yield stress, K, is a constant for an ideal,
rigid, perfectly plastic material. In real materials,
especially powder compacts, K varies throughout the
deformation zone. To allow for work hardening
Dodeja and Johnson[29] suggested the use of a mean
shear flow stress, found from plane strain compression
tests. More recently Farmer and Oxley[30] produced
a modified solution for work hardening materials.
However this modification permitted maximum
reductions of only 50% to be considered.

The two biggest disadvantages[25] of the slip-line
field technique are :-

(1) It may only be rigorously applied when
    conditions of plane strain are present.

(2) Strictly it only applies to rigid, perfectly
    plastic materials.

It is therefore almost impossible to use in the
case of powder extrusion as this is not a plane
strain process and metal powder is not a rigid
perfectly plastic material.

Due to the tedious nature of the application
of this technique and the limitations involved,
Johnson developed the upper bound method of analysis.

2.4.2.   Plane Strain Upper Bound Solution

The upper bound solution, developed by Johnson[31],
produces loads which are in excess of the true
values and in excess of those predicted by the
slip-line field technique. By increasing the
complexity of the upper bound solution (i.e. the number
of velocity discontinuities in the field) the solution
is brought nearer and nearer to that given by the
slip-line field method. (It should be noted that
as the upper bound solution gives an overestimate
on the load, it must be minimized to give the solution).
In view of the approximations of plane strain,
mean yield stress and frictional boundary conditions,
common to both techniques, the great saving in effort
afforded by the upper bound technique makes the
less accurate answer acceptable in the majority
of cases.

This technique is based on strain rather than
stress equilibrium conditions. Elements of material
are assumed to offer maximum resistance to deformation
i.e. they deform in such a way as to require the
maximum amount of work to produce a given strain.
Matter is assumed to be incompressible   and only
velocity discontinuities and boundary conditions

are considered. The material is assumed to deform
as rigid plastic blocks.

The most difficult part of the procedure is the
determination of the original field. Kudo and Johnson[25]
suggested the following method:-

(1) Assume a velocity field for the body
of material which is restricted only by the need
to conform to the velocity boundary conditions
and the law of constant density.

(2) Calculate the rate of work due to the plastic
deformation and due to the slip of the material
over the tool surfaces, using the assumed velocity
field.

(3) Hence find the extrusion load from this
rate of working.

Step (1) may be simplified by basing the field
on a known slip-line field or on a knowledge
of the flow pattern gained experimentally. Sheppard
and Raybould[32] showed that a velocity field could
be established by considering the sub-grain size
at different positions in the deformation zone
of a partial extrusion. Using a minimized plane
strain upper bound solution Johnson obtained
solutions for extrusion through wedge-shaped and
square dies for conditions of zero and sticking
friction.

Although simpler to use than slip-line field theory,
plane strain upper bound solutions suffer from
serious drawbacks:-

(1) Strictly, they may be applied to plane
strain conditions only. (Extrusion is an
axisymmetric process).

(2) They must be minimized by the application
of mathematical techniques.

(3) Intermediate friction conditions prove
very difficult to consider.

(4) The load predicted is always an overestimate.

2.4.3. Axisymmetric Upper Bound Solution

As stated in the previous section extrusion
is rarely, if ever, carried out under plane strain
conditions. Therefore an axisymmetric upper bound
solution is required. Thomsen[33] made the following
experimental observations :-

(1) Material flow is similar for geometrically
similar shapes in axisymmetric and plane
strain extrusion.

(2) The velocity during axisymmetric extrusion
is the square of the velocity during plane
strain extrusion.

Using this information Sheppard and Raybould[34]
derived a simple axisymmetric upper bound solution
by first finding a minimized plane strain solution.
The areas of the discontinuity surfaces were then
obtained by revolving the plane strain field
around the centre axis and the magnitude of the
velocity discontinuities by squaring those given
by the plane strain hodograph.

The first rigorous axisymmetric solution based
on a kinematically admissable axisymmetric velocity
field was suggested by Kobayashi[35] and by Halling
and Mitchell[36] for extrusion through conical
dies. The pattern chosen by Halling and Mitchell
involved a double triangle arrangement of velocity
discontinuities. Basically, they allowed the material
inside the triangles to accelerate along the flow
lines, producing circumferential straining, and
modified the plane strain hodograph accordingly.
Suggestions were also made for the incorporation
of work hardening and friction effects. The
optimization process was carried out on a computer.
Adie and Alexander[37] extended this work by producing
three triangle arrangements of velocity discontinuities
for greater accuracy. Kinematically admissable
velocity fields were drawn for rod-can, can-can
and tube-can combined extrusions.

This investigation will show that the axisymmetric
upper bound technique may be applied to powder
extrusion if allowances are made for the effects
of strain rate and strain on the powder compact
flow stress.

Recent advances in computer technology have
enabled steady state plastic deformation processes
to be treated by numerical techniques. Zienkiewcz[121]
applied a finite element method to extrusion
and produced results which agree well with slip-line
field solutions. He improved the accuracy of the
solution by increasing the number of elements
used in the mesh and noted that any frictional
conditions could be accommodated.

With the availability of modern computers
which possess large storage capacities the finite
element method of analysing   metal working processes
such as extrusion, will probably become predominant.

2.5.1. Strain Rate Determination

The strain rate during extrusion is a very
difficult parameter to define. It is obviously
a function of extrusion ratio and ram speed.
However, the strain rate varies throughout the
deformation zone. Sheppard and Raybould[34] applied
the upper bound analysis to the problem of strain
rate determination. The strain rate was calculated
along a series of streamlines by means of the
following method :

$$\varepsilon = \frac{u}{v}$$

ε = strain

v = velocity of material perpendicular to discontinuity

u = magnitude of discontinuity

The time to extrude a unit volume of material
of unit area past the discontinuity = $\frac{1}{v}$

Therefore the strain rate,

$$\dot{\varepsilon} = \left(\frac{u}{v} \right) / \left(\frac{1}{v} \right) = u$$

An average strain rate along each stream
line is found by considering the number of velocity
discontinuities intersected. This method does give
an indication of the strain variation across
the section.

However it possesses two main disadvantages:

(1) The deformation is assumed to occur
    instantaneously at a number of
    discontinuities.

(2) A mean overall strain rate has to be
    calculated from a knowledge of the
    strain rate along each stream line.

Feltham [38] proposed a mean strain rate
calculated by assuming that the deformation
occurred within a cone of 45° semi-angle. He
also assumed the total strain = ln(Extrusion ratio).
By dividing the volume of material extruded
per unit time into the volume of the cone he
obtained a mean strain rate,

$$\bar{\varepsilon} = \frac{6V \ln R}{D_B}$$

(12)

D_B = Billet diameter.

V = Ram speed.

Alexander [39] suggested that

$$\varepsilon = a + b \ln R$$

$$\text{giving} : \bar{\varepsilon} = \frac{6V (a + b \ln R)}{D_B}$$

(4)

(a,b = constants in the load equation).

However, the deformation zone is rarely
a cone of semi-angle 45° . Wilcox and Whitton [40]
pointed out that equation (4) should contain a

term to allow for a variation in semi-angle.
Chandra and Jonas[41 - 43] produced the following
equation :-

$$\dot{\varepsilon}_x = \frac{4V \, D_B^2 \, \tan \omega}{D^3}$$

D = Deformation zone diameter at any point
    in zone.

ω = Deformation zone semi-angle.

Unfortunately, all these expressions assume
a conical deformation zone whereas, in practice,
the deformation zone / dead metal zone interface
is usually curved. However they do have the
advantage of simplicity.

2.6.1. Temperature Variation During Extrusion

It is generally agreed that during the
extrusion process 90 - 95 % of the work done
is converted to heat energy, the remaining
5 - 10 % being stored in the new structure of
the extrude. The temperature change in the material
during extrusion depends on many parameters
including :-

(1) The temperatures of the billet and tools.

(2) The conductivities of the billet and
tools.

(3) The heat capacity of the billet and
tools.

(4) The ram speed.

(5) The extrusion ratio.

(6) The flow stress of the billet material.

Clearly temperature prediction during such a process
is very difficult.

Tanner and Johnson[44] used a plane strain upper
bound analysis and assumed the following:-

(1) Plane strain extrusion

(2) Temperature of billet = Temperature of tools

(3) No conduction.

This model considered the temperature of the billet
material to remain constant until a velocity discontinuity
was encountered. The resulting shear produced a strain.
This str in was then expressed in terms of a quantity of
work done. Hence a temperature rise, proportional to this
work, was obtained. By considering the number of discontinuities
encountered by each stream line the final temperature distri-
bution in the die-throat was obtained.

Johnson and Kudo[45] extended this work for axisymmetric
extrusion through square and conical dies. The three fields
used by Johnson and Kudo are shown in Fig. 3. Terms were
introduced to allow for the work done inside regions 1 and 2
in addition to that done at the discontinuities.

Sheppard and Raybould[34] also employed an upper-
bound analysis. The validity cf this theory was confirmed
by performing several extrusions with thermocouples
inserted in the dead metal zones. The measured temperatures
agreed reasonably well with those predicted by the analysis
Sheppard and Raybould also developed an integral profile
model (see theory section) which predicted

SQUARE DIES
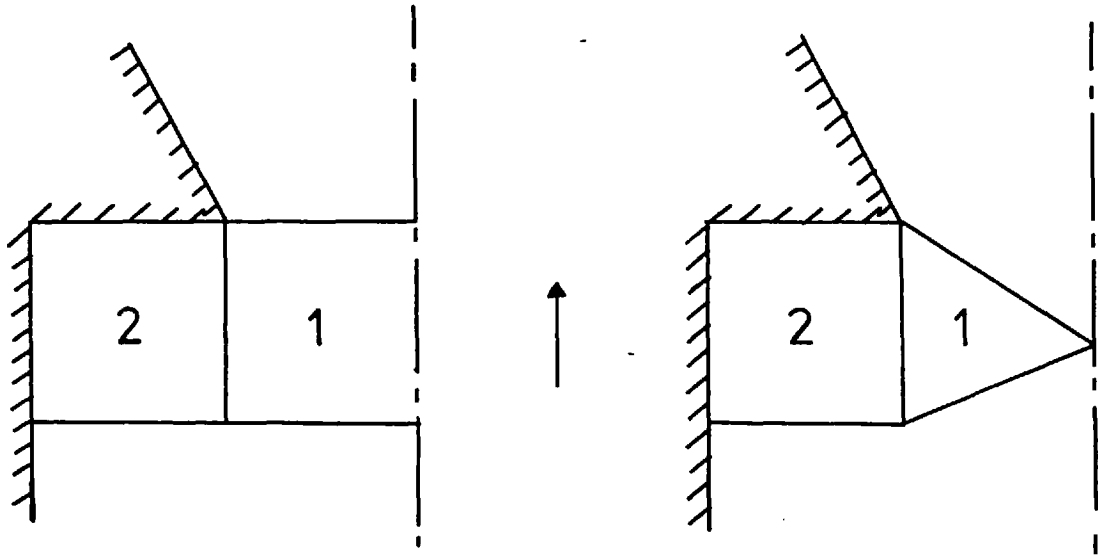
HOMOGENEOUS-HOMOGENEOUS   HOMOGENEOUS-TRIANGULAR

FIG. 3   Velocity fields for different types of extrusion

CONICAL DIE
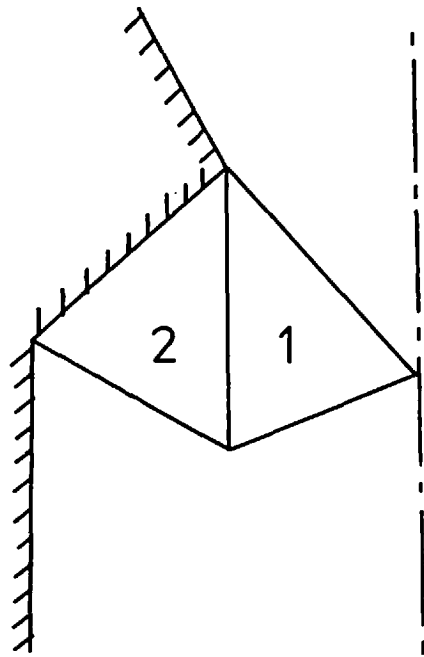
TRIANGULAR-TRIANGULAR

values close to those measured experimentally.

The method of Singer and Al-Samarrai[46] involved correcting the mean adiabatic temperature rise to give the mean temperature rise for the existing conditions. They used an empirical load formula and allowed for heat conduction to the die and container. All of the deformation was assumed to occur in the plane of the die. The results obtained were reasonably close to emergent extrude temperatures measured with a two pronged thermocouple.

Akeret[47] used a numerical analysis. He divided the billet into a series of blocks (Fig (4)) and treated extrusion as a " stepwise " process. Heat conduction from the heat source block to the billet and to the container was also taken into account. Once again the results agree reasonably well with experimentally measured values.

The analyses discussed in this section all make one of two assumptions :

    (1) Deformation occurs in one localized zone.
or (2) Deformation occurs in steps at velocity
       discontinuities.

Neither of these assumptions is entirely valid (especially not the former). Great difficulty is experienced in dealing with initial temperature differences between billet and tools. This is significant as in industry the billet and tools are rarely at the same temperature. Once again, with the aid of modern computers, finite element numerical analysis will probably prove to yield the best results.
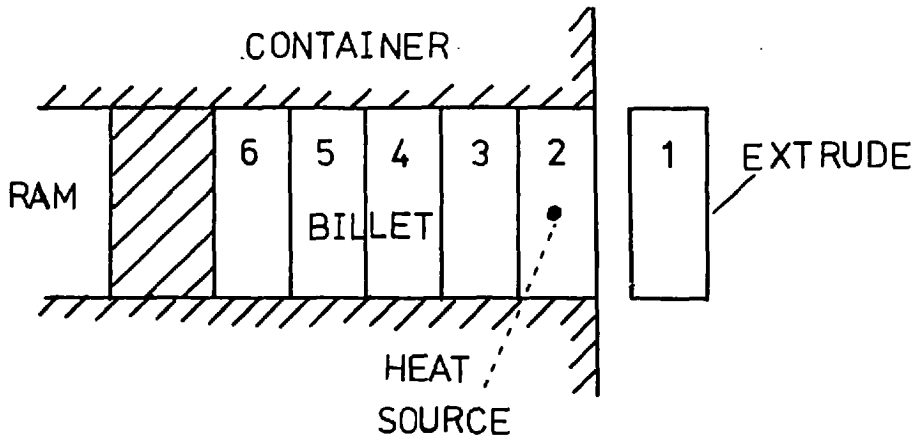
FIG. 4   Temperature rise model involving stepwise movement
of the billet

FIG. 5   Phase diagram for ideal precipitation hardening system
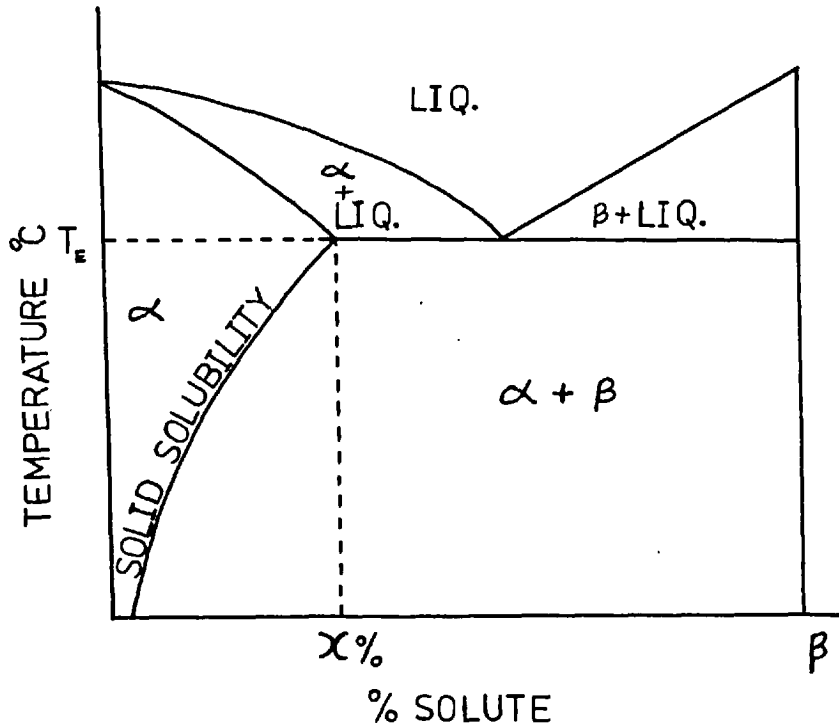
On an industrial scale, Reynolds[48] measured
the emerging extrude temperature with a lead
sulphide - cell radiation pyrometer. This proved
to be a quick and convenient method. However
although the results were within $\pm$ 4° C of those
obtained using a contact thermocouple for pure
aluminium extrusion at 450 - 500° C, the error
increased to $\pm$ 9° C at 380 - 450° C. Unfortunately
results for aluminium - magnesium silicide alloys
produced much larger errors. Thus the accuracy
of this method seems to depend on the emissivity
of the material. It is therefore unsatisfactory.

2.7.1. Extrude Structure

The structure produced by extruding aluminium,
aluminium alloys or most high stacking
fault energy metals at elevated temperatures
may be wholly recrystallised, partly recrystallised
or unrecrystallised depending on the extrusion
conditions, especially the temperature. The
tendency is for the recrystallised percentage
to increase with extrusion temperature and with
the amount of deformation. A variation in structure
across the section usually exists. Frequently
recrystallisation only occurs near the surface
due to the greater deformation occuring there.
Sometimes an unrecrystallised structure may result
from an extrusion carried out at a temperature
above the nominal recrystallisation temperature.
Such a structure usually resembles a " fibrous "
cold worked structure under the optical microscope.
However a substructure consisting of subgrains
of low misorientation produced by dynamic recovery
is revealed by the electron microscope.[48]

Jonas[49] demonstrated that annealing a dynamically
recovered aluminium structure failed to cause any recry-
stallation and merely increased the subgrain size slightly.
This indicated that dynamic recovery during hot working
was more effective than static recovery produced by con-
ventional annealing of a cold worked structure. He dis-
covered that the subgrain size and the perfection of the
wall increased with extrusion temperature.

This tendency for high stacking fault energy metals
to recover instead of recrystallise, is due to their lack
of extended dislocations and can be explained in terms of
dislocation theory. During deformation glide and forest
dislocations intersect forming tangles and increasing the
dislocation density. However at typical hot extrusion
temperatures and under the action of the deforming stress
and stress fields of other dislocations the ability of the
dislocations to climb and cross slip is enhanced[50]. The
process enables[51]:-

 (1) Dislocations to escape from the specimen surface.

 (2) Dislocations of opposite sign to annihilate each
   other.

 (3) Dislocations to arrange themselves in sub-boundaries.
   Thus cells form and become subgrains as dislocations
   migrate from within the cells to the walls. The sub-
   grain size tends to increase by subgrain coalescence
   in order to lower the free energy even further.

Recrystallised structures may be classified in three
categories depending on the stage at which recrystallisation
occurs[51]. These are:-

 (1) After deformation, during cooling to room temperature
   i.e. static recrystallisation

 (2) During deformation by recovery processes (in situ
   recrystallisation)

 (3) During deformation i.e. dynamic recrystallisation.

The difference between the processes in 2 and 3 is that
in the former the crystallographic orientation of each element

of volume is basically unchanged whereas in the latter the orientation is completely changed. This change is due to large angle boundaries sweeping through the material.

The recrystallisation process involves the nucleation and growth of new grains in a deformed structure. These new grains are relatively free from strain and dislocations. The nucleation process probably involves the growth of sub-grains both in size and misorientation by subgrain coalescence.

The type of recrystallisation occuring during aluminium and aluminium alloy extrusion remains uncertain. Castle[52] found an "elongated recrystallised" structure in some Al-Cu-Mg-Mn extrudes which indicated that dynamic recrystallisation had occurred. However, he correctly stated that this was not conclusive proof of dynamic recrystallisation. He questioned the effectiveness of the extrude quench and suggested that the structure was really produced by static recrystallisation with a preferred orientation in the extrusion direction. Li[53] and Hu[54] proposed in situ recrystallisation as the mechanism which operated during aluminium extrusion whereas Jonas[55,49] argued in favour of dynamic recrystallisation. Again these investigators failed to provide conclusive proof of the validity of their theories.

Thus we may conclude that in the extrusion of cast aluminium and its alloys the extrude structure may be wholly or partly recovered or recrystallised depending on the extrusion conditions and the alloy composition. The type of recrystallisation which occurs is uncertain. This lack of knowledge is serious in that a recrystallised structure is undesirable, being weak in comparison to a "fibrous" cold worked structure. For this reason many alloys contain recrystallisation inhibitors to prevent recrystallisation occurring.

eq. Zr is added to Al-Zn-Cu-Mg alloys.

Extrudes fabricated by Sheppard and Chare[23] from aluminium alloy powders exhibited no recrystallisation. He suggested that this was caused by oxide particles obstructing grain boundary migration. Nobili[56, 57] studied the behaviour of aluminium / alumina (S A P)alloys and reached a similar conclusion. Plumtree and Deep[58] recently extruded cast aluminium billets of different purity. By means of a Kikuchi line analysis they showed that an impurity content of 0.3 % was enough to prevent recrystallisation under certain extrusion conditions.

It therefore seems that recrystallisation is not a problem in the extrusion of aluminium powders. This is another advantage the powder route possesses over the traditional cast billet extrusion process.

2.8.1   Deformation Mode

In the previous section the processes occurring during hot working, namely recovery and recrystallisation, were discussed. Various theories have been put forward to explain the mechanisms by which these processes occur. Most of these theories have been proposed for creep deformation. Three basic models have been suggested to explain the operating mechanism during dynamic recovery. The three models are based on, respectively :-

(1) The motion of jogged screw dislocations.

(2) The climb of edge dislocations.

(3) The existence of a network of dislocations
inside the subgrains.

All three models assume that the activation
enthalpy is the same as that for self-diffusion.
The differences arise in the terms comprising
the structure factor and activation volume.

Barret and Nix[59] proposed the first model for
steady state creep. A jog is part of a screw
dislocation which does not lie in the slip plane.
Under the influence of a shear stress the screw
dislocation glides and the jog is "pulled" with
it leaving a trail of vacancies. The stress
required to move the dislocation depends on the
vacancy concentration and its effect on the jog.
This model unfortunately does not permit the
effect of alloying to be considered. Jonas[49]
showed, qualitatively, the applicability of this
theory to high strain rate deformation.

Weertman[60],[61] proposed the second model,
based on the climb of edge dislocations. Dislocation
sources are assumed to be distributed throughout
the material. Under the effects of the applied
shear stress they emit loops. These loops expand
until they are blocked by the stress fields of
loops on parallel planes. The climb of piled up
dislocations out of the slip plane then becomes
the rate controlling process. Once again, this model
was proposed for steady state creep. It does not
allow for alloying additions to be considered.
Objections to this model have been raised[66]
because the predicted substructure is not usually
found in specimens deformed in creep tests.

The third model, based on a three dimensional dislocation network within the grains, was suggested by McLean[62]. Moving dislocations intersect this network and, under the influence of the applied shear stress, the unpinned parts of the dislocations bow out decreasing the size of the network. Jogs migrate along the dislocations causing edge dislocations to climb. As a result, the network grows. The rate of recovery depends on the diffusion coefficient. McLean[63] considered the effects of alloying additions and concluded that the dispersed phase particles anchored the network.

Unfortunately, to date, the validity of all three models remains in some doubt. As all were proposed for creep deformation their applicability to high strain rate hot working processes must also be doubtful.

Stüwe and Ortner[64] proposed a model for the mechanism by which dynamic recrystallisation occurs. They based the model on the nucleation of recrystallised grains followed by deformation within the grains. However, experimental verification of this model has not yet been produced.

2.9.1 The Z Parameter

Garofalo[66] investigated creep deformation and proposed the following stress-strain rate relationships:-

$$\dot{\varepsilon} = A_2 \sigma^{n2} \quad \text{at low stresses}$$

$$\dot{\varepsilon} = A_3 \exp{(\beta \sigma)} \quad \text{at high stresses}$$

A_2 and A_3 are temperature dependent constants

β and n_2 are temperature independent constants

Zener and Holloman[65] also investigated creep deformation and found the activation energy for plastic deformation to be the same as that for self-diffusion. They introduced a temperature compensating factor into the strain rate term in an attempt to combine stress-strain rate information at different temperatures. The temperature compensated strain rate,

$$Z = \dot{\varepsilon} \; \exp \frac{\Delta H}{RT}$$

ΔH = activation energy.

Sellars and Mc G. Tegart[67] combined the work of Garofalo with that of Zener and Holloman and produced an empirical relationship for torsion:-

$$\dot{\varepsilon} = A_1 (\sinh \alpha \sigma)^n \; \exp(-\frac{\Delta H}{RT}) \qquad (6)$$

i.e. $\qquad Z = A_1 (\sinh \alpha \sigma)^n$

where A_1, α, n are temperature independent constants.

Jonas[68] showed that this equation could be applied to the hot working of aluminium over a range of strain rates and temperatures. Chare[19] showed this equation to be valid for the extrusion of aluminium alloy powders.

2.10.1 Precipitation Hardening

The phase diagram in Fig. (5) shows the essential requirement for precipitation hardening in an alloy system. The decrease in solid solubility with temperature is the aforementioned requirement. (N.B. This is a necessary condition but it may not be sufficient.) The usual heat treatment consists of three stages:-

1) Heat soaking
2) Quenching
3) Ageing

For the maximum response the alloy must contain just less than x% solute. (See Fig. 5). Examples of systems which respond are Al-Cu and Al-Mg$_2$Si.[69]

Stage 1 in the treatment involves heating the alloy to a temperature in the single phase, α, region. Maintaining this temperature enables the second phase, β, to dissolve. The temperature should not exceed T_E (Fig. 5) in order to prevent incipient melting occurring if a cored, non-homogeneous structure is present. Usually the β phase is brittle and optimum properties are obtained with 5-10% by volume of precipitate. Ideally the time of solution is that required to produce a homogeneous α structure. In practice such a structure may be unattainable if large grains are present as this automatically means large diffusion distances.

In stage 2 the specimen is quenched, usually in water. This prevents precipitation and maintains a high vacancy concentration. Quenching in water does not produce cracking because the α phase is usually very ductile. The importance of the quenched-in vacancies must be stressed[70] and it has been estimated that they increase the diffusion rate by a factor of 10^6 times. The importance[76] of vacancies as heterogeneous nucleation sites is also demonstrated by precipitate free zones which sometimes occur adjacent to grain boundaries because the vacancies in these zones have been absorbed by the grain boundaries.

Stage 3 involves an ageing treatment. The specimen is heated for several hours at a temperature just below the solid solubility curve in Fig. 5 (usually $0.4-0.5T_m$). Precipitate particles form and start to grow. The optimum particle size is 10^2-10^3 A. The effect of the ageing temperature on mechanical properties is schematically represented in Fig (6). High temperatures cause rapid rates of precipitation and precipitate
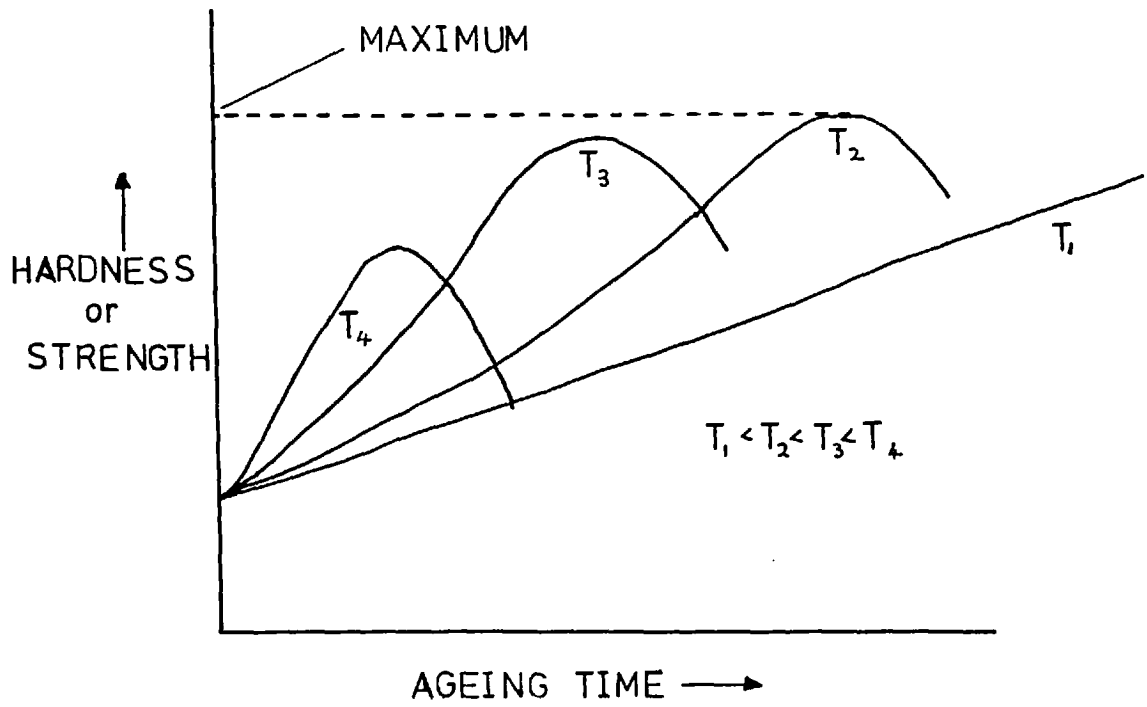
FIG. 6   Effect of temperature on age hardening curve

FIG. 7   (a) Al-Mg-Si phase diagram

(b) Al-Mg$_2$Si pseudo "binary" phase diagram

(a)

(b)
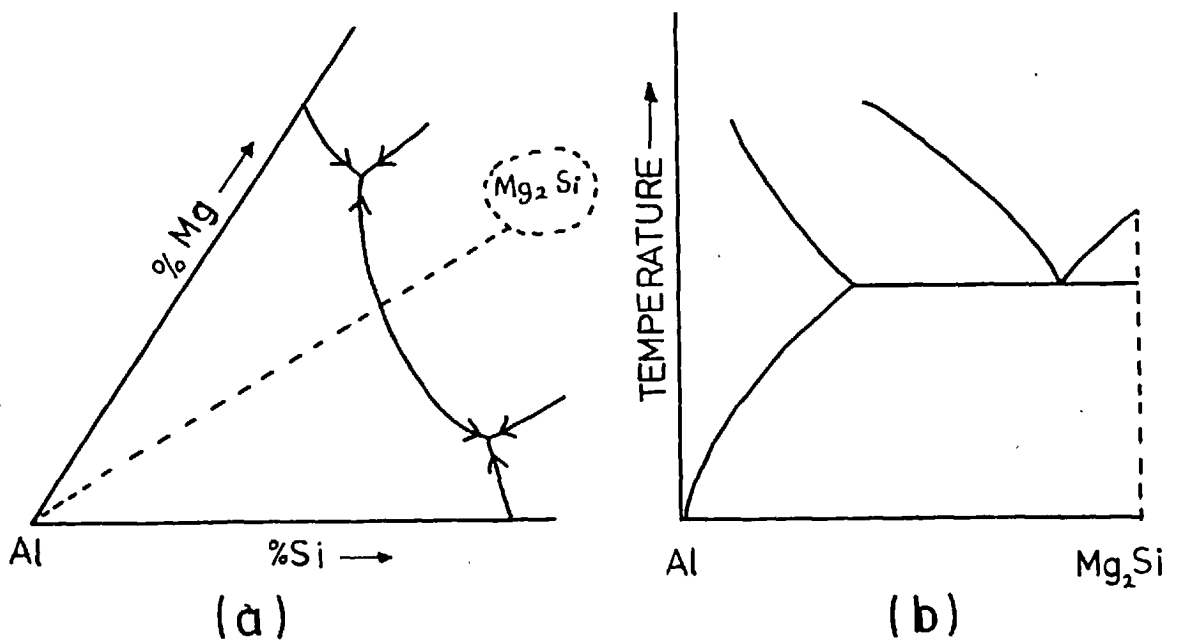
particle growth. Lower temperatures produce a greater
quantity of precipitate and finer particles due to
the greater supersaturation. If the
specimen is "overaged" the particles grow larger than
the optimum size, the interparticle spacing increases
and the mechanical properties deteriorate. It should
be noted that if an age hardened alloy is employed at
elevated temperatures overaging may occur during service
causing a rapid deterioration in properties.

The precipitation process was first investigated
in 1938 by Guinier and Preston. They used x-ray techniques
on Al-Cu alloys and discovered that solute concentration
occurred in the matrix prior to precipitation. These
concentrations were named G.P. zones after their dis-
coverers. The Al-Cu alloys were found to exhibit G.P.
zones in the form of discs 1 or 2 atoms thick and up to
100A in diameter. The discs were found to grow preferen-
tially along {100} planes. These discs caused coherency
straining due to the difference in atomic diameter
between aluminium and copper. In 1942 the formation
of a fully coherent (θ'') metastable precipitate, after
the G.P. zones, was discovered. Further research showed
that the next step in the precipitation process involved
the formation of a partially coherent, metastable preci-
pitate (θ') followed by the equilibrium, non-coherent
precipitate (θ). The optimum mechanical properties
were found to correspond to the presence of one of the
intermediate precipitates.

The Al-Mg-Si system is equivalent to a binary
system for compositions lying close to the $Al-Mg_2Si$
section.(Fig 7a and b.) Guinier and Lambot[71] investigated
this system and showed that G.P. zones occurred in the form
of <100> needles. Thomas[72] also investigated this
system by means of thin foil electron microscopy and
discovered the full precipitation sequence to be:-

            needles   ⟶ rods   ⟶ Plates (Mg_2Si)
            (G.P. zones)   (θ')   (equilibrium θ)

Jacob[77] agreed with this precipitation sequence but, in addition, suggested that the rods (hexagonal unit cell: a = 0.705nm, c = 0.405nm) were coherent until they grew to about 1μm in length whence they began to lose coherency along their major axis. Pashley[73] showed that some alloys in the Al-Mg$_2$Si system underwent room temperature ageing while awaiting (for several days) the "official" ageing treatment.

On a laboratory scale a three stage heat treatment process is, or course, acceptable but on an industrial scale it is expensive. In the large scale extrusion of cast Al-Mg-Si alloys the heat treatment schedule consists[74] of:-

(1) Preheating the billet to a temperature just below the solid *solubility line* so that the temperature rise during extrusion dissolves the Mg$_2$Si.

(2) Quenching the extrude on emergence from the die.

(3) Ageing the extrude.

This is a much more economical process than subjecting the extrude to a traditional three stage heat treatment.

In conclusion, the precipitation hardening process in aluminium alloys has been thoroughly investigated and is fairly well understood.

2.11.1 Dispersion strengthening

Since sintered aluminium products, possessing high strength at elevated temperatures, were first produced eg. by A.I.A.G. in 1948, the interest in dispersion strengthening has grown tremendously. In 1952 Lyle[78]

demonstrated the high tensile strength, at elevated
temperatures, of extruded aluminium powder. He
discovered that the strength increased with oxide .
content over the range examined (0-16 wt.% oxide).
Towner[79] found that Al-Fe and Al-Cr (up to 8%)
powder extrudes also possessed excellent high temp-
erature mechanical properties. He reasoned that this
was due to three main factors:-

(1) The very fine oxide dispersion caused
by the initial particle size.

(2) The insolubility of the oxide in the
matrix, even at high temperatures.

(3) The retardation of recrystallisation
at elevated temperatures by the oxide
dispersion.

Several models have been proposed to explain
the dispersion strengthening mechanism. The dispersed
particles may be classified according to their strength
as below:-

(1) undeformable particles

(2) deformable particles

Orowan[80] considered undeformable particles and
proposed that the yield strength was governed by the
stress required to "bow out" dislocations between
particles (Fig. 8). The dislocations eventually "short
circuit" around the particles leaving behind Orowan
loops. He presented the following equation for the
flow stress:-

$$\tau = \tau_s + \frac{2T'}{b\lambda} \qquad (7)$$

where T' = line tension in the dislocation
        τ_s = yield strength of matrix
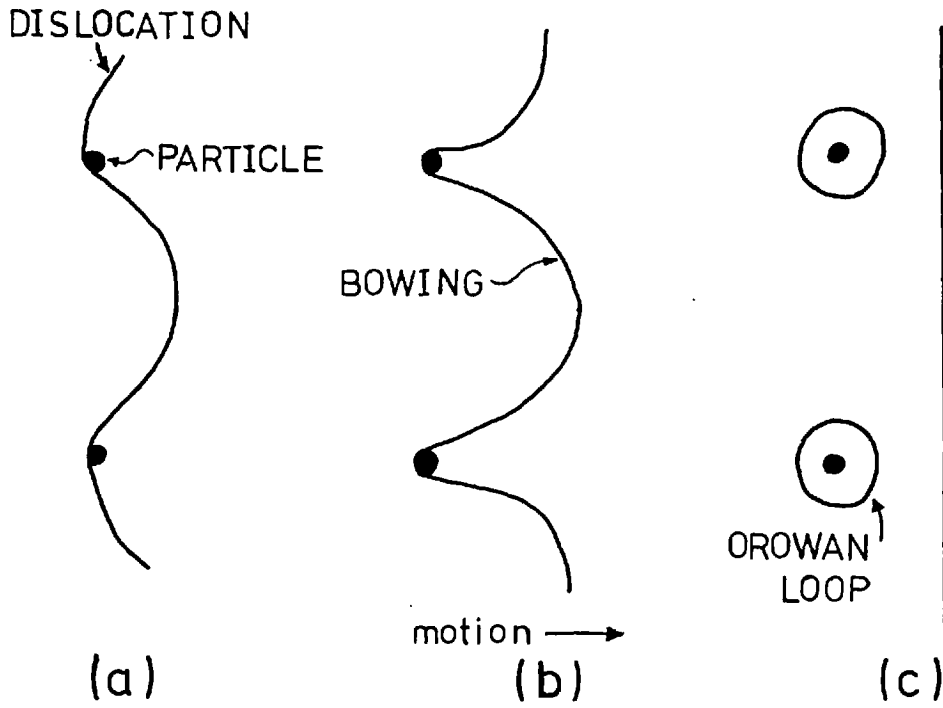
FIG. 8   Effect of second phase particles on dislocation motion
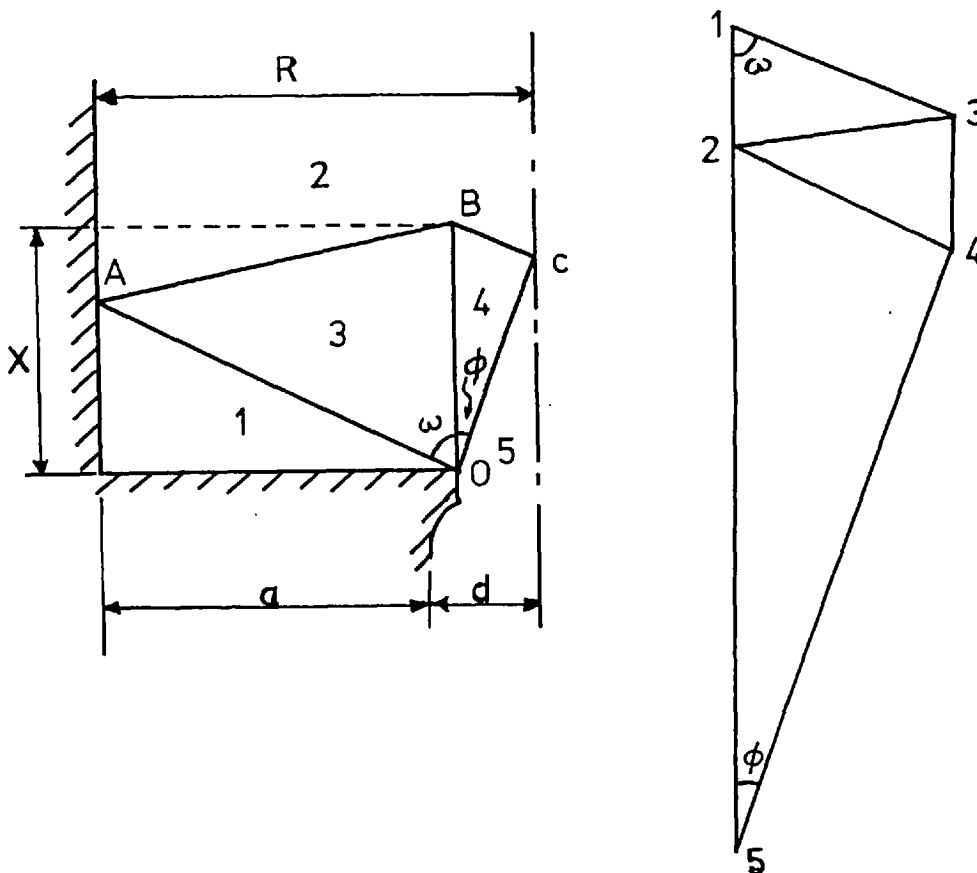
FIG. 9   Plane strain upper bound double triangle velocity field and
          hodograph

b = Burgers vector of matrix

λ = interparticle spacing

Kelly and Nicholson[81] produced the following equation for the line tension (when the dislocation forms a semi-circular loop):-

$$T' = \frac{Gb^2}{4} \theta^* \ln \frac{\lambda}{2b} \qquad (8)$$

where θ^* = averaging term (for screw and edge dislocations)

G = shear modulus

Ansell and Lenel[82] studied deformable particles and proposed that yielding occurred when the shear stress due to dislocation pile ups at the particles was sufficient to plastically deform or fracture the particles. They suggested the following equation:-

$$\tau = \tau_s + const. \quad \lambda^{-\frac{1}{2}} \qquad (9)$$

Conclusive proof of particle shearing on yielding has yet to be found.

Fisher et al[83] found that dispersed particles enhanced the effect of normal work hardening. An important shortcoming of the two models discussed is that both assume non-coherent, spherical, uniformly distributed particles, an ideal situation.

Of direct relevance to the present investigation is the work carried out by Hansen[84] on the strengthening of aluminium by Al_2O_3 particles. His fabrication procedure involved the extrusion of aluminium powder. He found that Al_2O_3 particles behaved as a three-dimensional network and he proposed a flow stress equation similar to that of Ansell.

2.12.1 <u>Extrusion Defects</u>

<u>Surface finish</u>

Johnson and Mamalis[11] classified extrusion defects
under three headings:-

    (1) cracking defects
    (2) contraction defects
    (3) skin-inclusion defects

Peripheral cracking is an example of the first type.
Caused by hot or cold shortness accompanied by secondary
tensile stresses generated in the region of the die, it
leads to the so-called "fir-tree" defect. Central bursts
or chevrons are also occassionally encountered. Piping
at the back end of the billet is an example of a contrac-
tion defect. During the final stages of extrusion, when
the billet length is very small, the centre sometimes
"caves in". This produces a central core of material
containing voids at the rear of the extrude. Consequently,
in industry, the final length of extrude is discarded.
A common example of a skin-inclusion defect involves
foreign matter or lubricant on the side of the billet,
being dragged between the flowing metal and the dead
metal zone. This produces blisters on the extrude. The
familiar 'extrusion defect' is a combined contraction-
skin-inclusion defect. In the final stages of extrusion,
after the billet centre has caved in, oxidised material
from the surfaces of the billet flows laterally to occupy
this vacant space. This produces a final length of extrude
with a core of oxide and inclusions.

In the particular case of aluminium extrusion another
problem is caused by the tendency of the aluminium to stick
to the die land surface. This accumulation can lead to
heavy scoring of the extrude surface. Williams[75] reported
that this could be prevented by two methods:-

(1) Starting and stopping the press which, unfortunately, leaves stop marks on the extrude.

(2) Using a die with a conical lead-in.

It is difficult to imagine how the first method prevents scoring. One point worth bearing in mind is that although the surface finish of the extrude may appear satisfactory on emerging from the die it may not do so following subsequent heat treatment or anodizing.

An adequate surface finish is even more difficult to obtain in powder extrusion. Chare[19] found that a pad of cast material, placed in front of the aluminium powder billet, produced a fairly smooth extrude surface. El Wakil and El Sabbagh[122] extruded Al powder billets using graphite spray, fat free lubricant with limited success. Very little research has been carried out on verification of the theories put forward to explain extrusion defects. In industry the achievement of a good surface finish is an art rather than a science. Much work remains to be done on the correlation of extrusion conditions with extrude surface finish.

2.13.1 Fibre reinforcement of Metals

In a recent review[86] Morley discussed the present state of development of the science and technology of fibre reinforced metals. He suggested that metal matrix composites should be classified according to the type of fibre employed. The four main types of fibre are listed below:-

(1) whisker crystals e.g. Al_2O_3 or SiC

(2) continuous ceramic or glass fibres e.g. SiO_2

(3) metal wire e.g. steel or W

(4) fibres produced 'in situ' in lamellar eutectics e.g. chromium fibres in Cu-Cr

These four types of fibre give rise to the four types of composite discussed in the following sections.

2.13.2 Whisker Crystal Composites

Whiskers are defined as unbranched, needle-like, single crystals produced by the filamentary growth of a solid. Examples of typical whisker crystals employed in fibre reinforcement are Al_2O_3, Si, C, and SiN. When pure and undamaged, whiskers of such materials have high values of tensile strength, melting point and elastic modulus together with high strength to weight ratios[87]. Unfortunately the slightest damage greatly reduces their strength from the theoretical value of 0.1 elastic modulus, for a single crystal.

Interest in whiskers as reinforcing fibres grew when it was demonstrated that their use enabled metals to bear considerable loads at elevated temperatures (i.e. near the melting point of the metals). This was shown[88] using Al_2O_3 reinforced silver. The percentage theoretical strength* attained for a 16% Al_2O_3 composite, varied from 90% at room temperature to 54% at 870°C. Whisker reinforced silver was also found to be much stronger than dispersion strengthened silver over a temperature range of $20{-}900^{\circ}$C. However, when the Al_2O_3 whisker content was raised to 30% the elongation of the composite dropped to only 1.5% of the whisker fracture strain. The $Al_2O_3{-}Ni$ system was also investigated for possible uses in the aerospace industry. It was found that 60-70% of the theoretical strength was attainable.

Whiskers were first produced using a batch process. In the case of Al_2O_3 an oxidizing atmosphere was passed

---

* The theoretical strength calculated from the rule of mixtures equation:

$$\sigma_c = \sigma_m \, v_m + \sigma_w \, v_w$$

σ_c = composite tensile strength

σ_m, σ_w = tensile strengths of matrix and whiskers

v_m, v_w = volume fraction of matrix and whiskers

over a boat of molten aluminium held in a furnace at
1500°C. The resulting whiskers were collected on the
side of the boat. Unfortunately slight variations in
flow rate, temperature etc. caused a considerable vari-
ation in whisker quality from batch to batch. A continuous
process using a molybdenum-base collecting surface moving
relative to a vapour source produced better results.

Several methods have been used to produce the
composites. The first method involved the three stages
mentioned below:

(1) chemical cleaning of the whiskers.
(2) the formation of bundles of whiskers.
(3) vacuum infiltration of molten metal into
the bundles.

Another method used a powder metallurgical route.
The whiskers were mixed with a metal powder e.g. Ni and
a wetting agent, dispersed in water and filtered. The
filtrate was then mixed with a binder and more water and
extruded to align the whiskers. Finally the extrude was
dried, sintered and cold rolled.

Further development of whisker composites looks
unlikely for several reasons. The production of whiskers
and their composites is slow and expensive. The whiskers
are very easily damaged which greatly reduces their strength.
Even during the growth of the whiskers surface steps some-
times occur causing considerable weakening. Adequate wetting
of the whiskers by the matrix is necessary to ensure good
bonding. Interface degradation by matrix-whisker inter-
action[89] often reduces the composite strength e.g. delayed
failure[90] in Al_2O_3 reinforced composites above 630°C.
Some doubt even remains about the effect of whisker size
on strength. Larger whiskers are easier to handle but
they tend to have poorer surfaces and consequently are
weaker. Further laboratory investigation of this last
effect would be useful.

2.13.3 Continuous Ceramic or Glass Fibre Composites

Most of the research carried out on glass fibre
reinforcement has concerned the various silicate based
glasses in various light metal matrices, the most
common combination being "E" glass in aluminium. (Silicate
glasses are viscous over a large temperature range, a
necessity for successful hot drawing). An excellent
review by Kelly and Davies[87] gives details of the pro-
duction techniques and the results obtained by various
investigators. The best method involved conventionally
drawn glass fibres being coated with aluminium. Zinc
or cadmium was added to improve the coating process.
The composite was then formed by hot pressing or vacuum
infiltrating bundles of coated fibres. The fracture
surfaces of specimens showed no indication of fibre
delamination, evidence of good bond strength. Composites
containing 20-50% glass were considerably stronger, at
temperatures above $300^{\circ}C$, than conventional aluminium
alloys. However, the fibre strength, calculated from the
measured composite strength, was much less than the theo-
retical values. This was probably caused by glass-metal
chemical interaction.

The usefulness of silicate glasses as reinforcing
materials is limited by two main factors.

(i) The elastic modulus of these glasses is
similar to that of aluminium. This dictates
that no reinforcement is possible until the
metal yields.

(ii) At temperatures in excess of $300^{\circ}C$ the
strength of silicate glasses drops markedly.

Silica fibres, produced by a hot drawing process,
have been widely used in investigations of ceramic fibre
reinforcement. A review by Cratchley[91] discusses the
production techniques and the results of several workers.

One successful method of production involved the passing
of the fibres through a molten bead of the matrix metal,
usually aluminium. This protected the fibre from hand-
ling damage and also served to form the matrix. The
coated fibres were then hot pressed, at 400-550°C, to form
the composite. The applied pressure was found to be very
important in that it was required to produce bonds between
adjacent fibre coatings while not causing damage to the
fibres. An exothermic reaction between silica and
aluminium at 643°C[86] was found to weaken the fibres con-
siderably. However, below about 400°C no such weakening
effect occurred. Cratchley and Baker[85,92,93,94] studied
the mechanical properties of silica-aluminium composites
in detail. They discovered that composites containing
50% silica were much stronger than RR58 alloy or a 10%
S.A.P. alloy between room temperature and 400°C. The
strengths of all three decreased dramatically above 300°C.
(This would seem to contradict the findings, mentioned
above, concerning the exothermic reaction between silica and
aluminium at temperatures below 400°C). Cratchley and
Baker found that the mode of failure depended on the
fabrication pressure. Specimens fabricated at low
pressures exhibited fibre "full out" on fracture whereas
those produced at high pressures did not. The fatigue
properties were found to be fairly good although the
fibre ends did generate some cracks in the matrix. These
cracks were unable to pass directly into undamaged fibres.
They travelled parallel to the fibres, causing delamination,
until reaching cracks in the fibres. This delamination
process at the interfaces also produced high notch ductility
values for these composites.

Two other materials are worth considering as possible
fibre reinforcing materials. Carbon fibres have a high
modulus of elasticity and are very strong, even at
temperatures of the order of 2000°C. Once again aluminium
is a good matrix material as carbon reacts unfavourably
with titanium and cobalt at modest temperatures and with

Nickel[96] at temperatures of the order of $900^{\circ}C$.
Baker[97] produced composites by hot vacuum pressing
aligned fibre-aluminium sheets previously produced
by electrodeposition and chemical vapour deposition
techniques. Some carbon fibre-aluminium wires were
also produced by molten infiltration. Jackson[98] et al
found the strength of composites produced by the former
method to be lower than expected although the
composites were fairly stable at temperatures up to
$500^{\circ}C$. The wires produced by molten infiltration
were found to have a uniaxial tensile strength
close to the theoretical value. The big drawback
to the widespread use of carbon fibres in metal
is the slow and costly method of fibre production
from polymer textile precursor fibres[95].

High strength boron fibres, produced by chemical
vapour deposition onto a heated $(1200^{\circ}C)$ tungsten
wire substrate from boron trichloride in the presence
of hydrogen, have also been examined[86]. No really
suitable matrix metal has been found due to the high
reactivity of boron with most metals such as aluminium;
the fibre surfaces becoming oxidised. To avoid this
the fibres require coating with silicon carbide.
Thus the production process becomes expensive and
tedious.

2.13.4 Metal Wire Composites

Metal wires are generally produced by drawing
or extrusion. Generally, they are ductile and therefore
do not experience weakening effects due to crack
propagation caused by surface damage during handling
operations. As most metal wires exhibit some plasticity
at room temperature they usually fail by partial
necking. At higher temperatures they lose strength

fairly rapidly due to enhanced dislocation movement
and, in some cases, suffer additional strength
losses due to surface alloying.

One of the first systems to be examined was
tungsten wire reinforced copper. This served as a good
model system because it was found that although
the copper wet the tungsten, ensuring a good matrix-
fibre bond, no reaction occurred. McDaniels[99] et al
prepared composites by infiltrating bundles of
tungsten wires (within ceramic tubes) with molten
copper at 1200°C. They found that the rule of mixing
predicted the composite tensile strength fairly
well for both continuous and discontinuities wires.
They calculated a critical aspect ratio of 16:1.
Observation of the fracture surfaces of tensile
specimens showed that fibre "pull out" did not
occur, emphasising the strength of the copper-tungsten
bond. Metallographic examination showed that continuous
fibres fractured at weak points during loading and
then behaved as discontinuous fibres. On further
loading random breaks continued and finally localization
of breaks in a particular region resulted in failure.
Cratchley[100] and Baker[101] investigated aluminium
reinforced with steel wires. They prepared composites
by placing steel wires in a mould with aluminium
powder and then pressing at an elevated temperature
to achieve consolidation. Care was taken to ensure
that the temperature was not sufficiently high to
cause excessive reaction between the two metals.
The tensile strength of the composite was found
to be linearly dependent on the volume fraction
of fibres. Cratchley[100] also showed that misalignment
of fibres increased with decreasing aspect ratio
producing a decrease in strength. Other examples

of systems investigated[91] include:

    1) Titanium reinforced by molybdenum wires.
    2) Nickel reinforced by tungsten wires.
    3) Cobalt reinforced by tungsten wires.

In these three systems composites were produced by mixing
pieces of wire with the matrix metal powers,cold pressing
and/or sintering and then extruding and rolling to align
the fibres and fabricate the final product.

Metal wire reinforced composites seem quite promising.
The fabrication process is fairly simple and quick and the
wires are much more robust than any glass or ceramic
fibres. The only drawback is that the elastic modulus
of such composites is much less than that attainable in
some glass/ceramic-metal systems.

2.13.5 Lamellar Eutectics

The advantages of composites produced by "in situ"
growth of fibres are considerable. The problem of pro-
ducing a uniform distribution of aligned fibres no longer
exists. Fibres do not suffer damage during handling
operations. Concern about matrix-fibre chemical inter-
action weakening the fibres is unnecessary and, finally,
wetting problems governing the bond strength are avoided.
The necessary condition for an eutectic alloy to be
lamellar in nature is that the eutectic phases must have
low entropies of melting. Unidirectional controlled
solidification of a suitable alloy is used[102] to fabricate
such composites. Several methods may be employed to
achieve the controlled, unidirectional growth of a solid
phase into a liquid phase, with a plane interface.
The mould, containing the molten metal, may be withdrawn
from a furnace held at a steady temperature or the mould
may be left to cool slowly in a furnace with a temperature
gradient. The most commonly used method involves the

the downward withdrawal of the molten alloy from a vertical furnace held at a steady temperature. The rate of solidification upwards depends on the rate of withdrawal and on the heat flow conditions. The inter-fibre distance, λ, is related to the freezing rate, R, by an equation of the form:-

$$\lambda = \text{const. } R^{-\frac{1}{2}} \qquad (10)$$

The systems on which most work has been carried out are[103]:-

1) Chromium fibres grown from the copper-chromium eutectic (2 wt.% fibres)

2) Al_3 Ni fibres grown from the $Al-Al_3Ni$ eutectic (10 wt.%).

To increase the volume fraction of fibres more complex[103] systems must be used. A minimum surface energy criterion predicts lamellae formation instead of fibre formation for volume fractions in excess of ~ 32 wt.%. Thompson and Lemkey[103] suggested that the relative advantages and disadvantages did not leave much to choose from between lamellae and fibres. They showed that the interfibre spacing had an important effect on composite tensile strength and proposed a relationship of the form:-

$$\sigma = \sigma^* + \text{const. } \lambda^{-\frac{1}{2}} \qquad (11)$$

σ^* is a frictional stress.

Some directionally solidified, complex eutectic superalloys have been produced with unidirectional pro-perties superior to those of conventional nickel and cobalt superalloys. A eutectic consisting of Ni_3Al fibres in a Ni_3-Ta matrix was found[86] to be stronger, above $1010^{\circ}C$,

than two cast nickel-based superalloys (MAR-M200$\overline{5}$D and TRW-NAS AVIA). A lamellar $Ni_3Al-Ni_3N_b$ composite exhibited greater strength than either of these conventional alloys, its superiority increasing with temperature.

In common with most other systems, the fracture toughness of these composites increased with interfibre spacing. Good fatigue properties were exhibited with endurance limits of ~60% of the tensile strengths.

Potentially, the largest scope for these eutectic composites is in the gas turbine industry. However, in this field resistance to oxidation and corrosion is important and protective, diffusion coatings are required to provide adequate protection. Advanced air-cooling technology which allows conventional alloys to be employed at ever higher operating temperatures probably also prevents a breakthrough in the use of "in situ" composites.

CHAPTER 3

THEORY

3.1.1 Introduction

In the following chapter the various analyses
used in the present work are presented in detail.
The equations predicting extrusion load, flow stress,
temperature and strain rate are derived together with
the various relationships describing the behaviour of
fibre reinforced composites under load. A general hot
working theory is also presented. This enables flow
stress to be correlated with both strain rate and
temperature in a single equation which holds for
widely varying conditions of temperature and strain
rate.

3.2.1 Plane Strain Upper Bound Solution – Prediction of P/K

The formulae most widely used to predict extrusion
loads are those developed by Johnson[25] and are of the
form:-

$$\frac{P}{\sigma} = a + b \ln R \qquad (12)$$

It has been shown that this form of equation may
also be applied to powder extrusion but the magnitude of
the flow stress, σ, is difficult to assess and the con-
stants a and b are dissimilar to those observed for as-
cast billet extrusion. Extrusion pressure is assumed
to depend only on reduction ratio and not on flow pattern
or die shape.

An alternative approach based on the flow of
metal through the die is possible using load bounding
or slip-line field techniques which are only strictly

applicable when plane strain conditions exist. Of
these two, the upper-bound approach is more flexible
because there is not the requirement of stress equili-
brium. The major consideration involves strain incre-
ments and the conditions they have to fulfil in a fully
plastic body [125]. The solution must commence with a
proposed deformation field obtained experimentally by
the examination of partial extrusions, or by conside-
ration of a slip-line field solution. The problem then
becomes one of finding a rigid triangle hodograph which
satisfies both the velocity boundary conditions and the
condition for incompressibility of the material. Thus
the load produced by an upper bound solution is always
higher than the experimental value and hence the load
expression must be minimized by some mathematical technique.

Figure 9 shows a simple deformation field defined
by the angles ω and ϕ and by the deformation zone
depth x. The hodograph which is obliged to satisfy the
deformation conditions is also shown. Let us assume that
the ram velocity is unity. The material to the rear of
ABC has been compacted to 100% density but has undergone
no shear deformation and therefore has effectively zero
shear strength. On encountering the velocity discontinuity
AB which, from the hodograph, is of magnitude $\overline{23}$, the
powder material undergoes a substantial shear deformation
and is forced to flow parallel to AO with velocity $\overline{13}$.
Thus all metal in triangle ABO is assumed to attain this
velocity and direction. This shear deformation is theo-
retically assumed to occur instantaneously over zero
distance which clearly is impossible in practice. The
material next encounters discontinuity BO, of magnitude
$\overline{34}$, giving it a velocity in direction $\overline{14}$ and finally
velocity discontinuity OC ensures that metal leaves the
die such that $\overline{15}$ is equal in magnitude to the plane-strain
extrusion ratio.

The rate of energy dissipation at each discontinuity is given by the product of the area of the discontinuity, the magnitude of the discontinuity and the shear yield strength of the metal. Thus for linear discontinuities we may write:-

$$\frac{dw}{dt} = \sum k . v .. s \qquad (13)$$

The plane strain solution may then be written (considering unit depth):-

pressure x area x velocity = $\sum k . v . s$

p x (a + d) (1) x 1 = $\sum k . v . s$

$$p(a + d) = [k_{AB} \; AB \; \overline{23} + k_{BC} \; BC \; \overline{24} + k_{BO} \; BO \; \overline{34}$$

$$+ k_{OC} \; OC \; \overline{45} + k_{AO} \; AO \; \overline{13}] \qquad (14)$$

The lengths and velocities may be defined in terms of ω, x and ϕ:-

$$AO = \frac{a}{\sin \omega} \; , \qquad \overline{13} = \frac{a}{x \sin \omega}$$

$$OC = \frac{d}{\sin \phi} \; , \qquad \overline{45} = \frac{a}{x \sin \phi}$$

$$BO = x, \qquad \overline{34} = [1 + \frac{a}{d} - \frac{a}{x} \cot \omega - \frac{a}{x} \cot \phi]$$

$$AB = [\frac{a^2}{\sin^2 \omega} + x^2 - 2ax \cot \omega]^{\frac{1}{2}} \; ,$$

$$\overline{23} = \frac{1}{x} [\frac{a^2}{\sin^2 \omega} + x^2 - 2ax \cot \omega]^{\frac{1}{2}}$$

$$BC = [\frac{d^2}{\sin^2 \phi} + x^2 - 2dx \cot \phi]^{\frac{1}{2}} \; ,$$

$$\overline{24} = \frac{a}{xd} [\frac{d^2}{\sin^2 \phi} + x^2 - 2dx \cot \phi]^{\frac{1}{2}}$$

Differentiation of equation (14) is complicated, for powder materials, by the inclusion of shear stress values varying at each discontinuity. It may be assumed, however, that the values of ω, ϕ and x giving minimum pressure for constant shear stress conditions will also yield the minimum pressure for powder compact extrusion. Thus equation (14) may be written:-

$$\text{LOAD} = \text{AK} \left[2x + \frac{2ax}{d} + \frac{2a^2}{x\sin^2\omega} + \frac{2ad}{x\sin^2\phi} \right.$$

$$\left. - 3a\cot\omega - 3a\cot\phi \right] \qquad (15)$$

Differentiation with respect to x and equating to zero gives:-

$$x^2 = \frac{a^2}{(1 + a/d)\,\sin^2\omega} + \frac{ad}{(1 + a/d)\,\sin^2\phi}$$

Differentiation with respect to ω yields:-

$$\cot\omega = 3x/4a$$

and with respect to ϕ yields:-

$$\cot\phi = 3x/4d$$

As ω and ϕ are not independent of x the function must be minimised by iteration. The program given in appendix 1 does this. By assuming a single, mean, shear flow stress in equation (14) values of P/K can thus be obtained by means of this program. .

3.2.2 Use of Plane Strain Upper Bound Solutions for
Axisymmetric Extrusion

Analyses such as that presented in the previous section may be applied to axisymmetric extrusion (as an approximation) because Thomsen [33] has shown that:

a) the material flow is similar for identical
   geometrical configurations

and

b) the magnitude of the velocity during
   axisymmetric extrusion is approximately
   the square of the velocity during plane
   strain extrusion.

There is much experimental evidence to support this
second conclusion and it quite clearly satisfies the
velocity boundary conditions.

Therefore, for axisymmetric extrusion the surface
area of the discontinuities must be considered, and the
magnitude of the velocities must be squared. Hence
equation (14) may be rewritten as:-

$$p \times \pi(a+d)^2 \times 1 = \left[k_{AB}\, A_{AB}(\overline{23})^2 + k_{BC}\, A_{BC}(\overline{24})^2\right.$$

$$\left. + k_{BO}\, A_{BO}(\overline{34})^2 + k_{OC}\, A_{OC}(\overline{45})^2 + k_{AO}\, A_{AO}(\overline{13})^2\right] \quad (16)$$

The velocities $\overline{13}$, $\overline{23}$ etc. are identical to the plane-
strain analysis and the surface areas by simple geometry
become:-

$$OC = \frac{\pi d^2}{\sin\phi} \quad , \quad AO = \frac{\pi a(a + 2d)}{\sin\omega} \quad , \quad BO = 2\pi xd,$$

$$AB = \pi(a + 2d)\, [\frac{a^2}{\sin^2\omega} + x^2 - 2dx\cot\omega\,]^{\frac{1}{2}},$$

$$BC = \pi d\, [\frac{d^2}{\sin^2\phi} + x^2 - 2dx\cot\phi\,]^{\frac{1}{2}}$$

Since metal flow patterns for plane-strain and axisymmetric
extrusions of similar geometry i..e. cross-section are
similar, the minimized values of the geometric variables
will also be identical. Hence the values of x, ϕ and ω
obtained for a plane strain extrusion ratio of R may be

used in conjunction with an axisymmetric extrusion
ratio of R^2.

3.2.3 Prediction of Load Using Plane Strain Upper Bound Solution

Equations (14) and (16) may be used to predict
the extrusion pressure if values for the shear flow
stress at each discontinuity are supplied. The results
of tensile tests, performed during this investigation
indicated a stress/strain relationship for magnesium
silicide powder compacts of the form:-

$$\sigma = \sigma_o \, \varepsilon^m \qquad \text{(see 5.9.3)}$$

where σ_o is a strain rate sensitive constant. A com-
bination of tensile and torsion tests suggested a
relationship between STRESS and strain rate given below:-

$$\sigma_o = A \, \dot{\varepsilon}^n \qquad \text{(see 5.5.1)}$$

Using the Von Mises yield criterion, the shear yield
stress at a discontinuity may be written:-

$$K_{ij} = \frac{A}{\sqrt{3}} \, \dot{\varepsilon}^n \, \varepsilon^m \qquad (17)$$

As the strain rate at a discontinuity is ∞ , an
average $\dot{\varepsilon}$ may be found from Feltham's equation(see
3.5.1.). Thus to calculate the shear flow stress at
each discontinuity the strain at each discontinuity
must be estimated. The relative shear deformation
at each 'jump' is given by the magnitude of the
velocity 'jump' divided by the velocity perpendicular
to that 'jump'. The material is also elongated in
the direction of its deflected flow and in the three
dimensional case there will be deformations of small
magnitude perpendicular to this. Figure (10) depicts
the relevant parameters. For example the shear
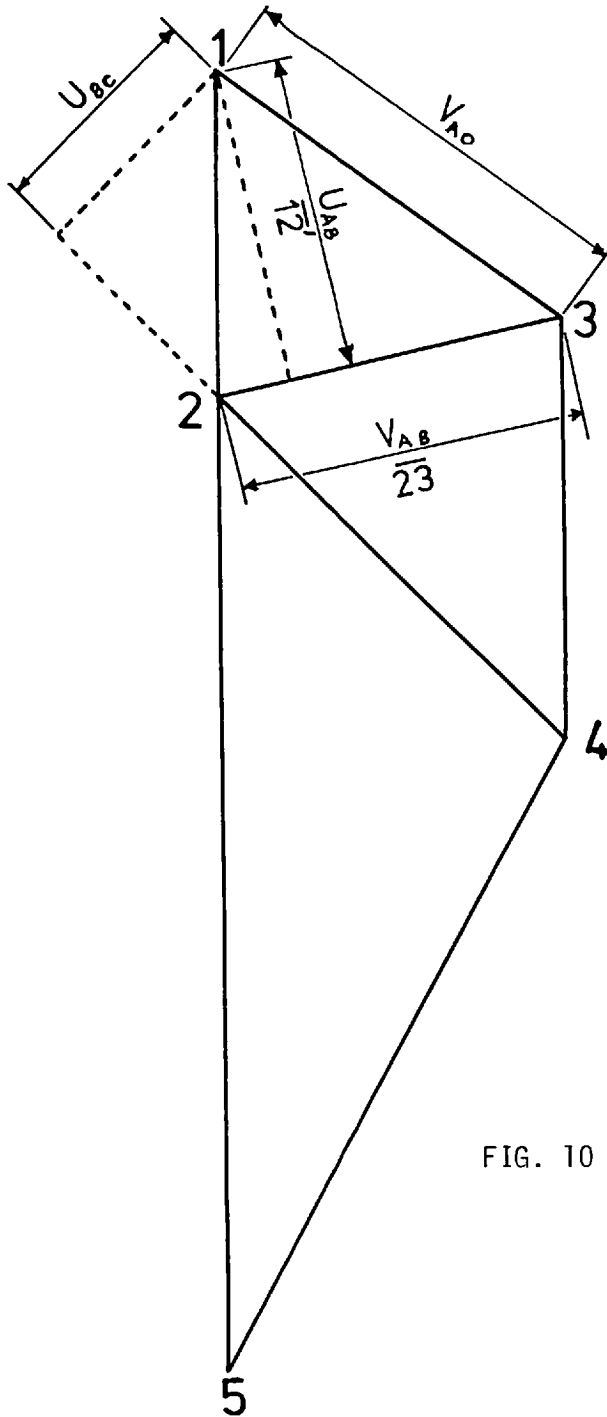
FIG. 10 Extrusion hodograph showing
incident velocity components

deformation at AB is of magnitude:

$$\ln (V_{AB}/U_{AB})^2 = \ln (\overline{23}/\overline{12'})^2 = \gamma_{AB}.$$

The deformation in the flow direction $= \ln (\overline{13})^2 = \varepsilon_{AB}$. The strains in directions perpendicular to these are an order of magnitude less so that the total equivalent strain may be written:-

$$\overline{\varepsilon}_{AB} = \sqrt{\tfrac{2}{3}} (|\varepsilon_{AB}|^2 + \tfrac{1}{2}|\gamma_{AB}|^2)^{\tfrac{1}{2}} \quad \text{etc.}$$

It should be noted that the use of the velocity squared relationship is also necessary to determine the shear yield stress to be used in the plane strain analogue; otherwise the total strain will not correlate with that actually obtaining in the extrusion process. In fact as shear deformations do not occur instantaneously i.e. a gradual deformation actually occurs, we must assume that the material properties at each discontinuity are related to those on either side of the discontinuity. This value may best be estimated by taking the mean equivalent strain such that the deformation at each discontinuity is given by:-

$$\tfrac{1}{2}\,\overline{\varepsilon}_{AB} \quad \text{at} \quad AB$$

$$\tfrac{1}{2}\,\overline{\varepsilon}_{BC} \quad \text{at} \quad BC$$

$$\overline{\varepsilon}_{AB} \quad \text{at} \quad AO$$

$$\overline{\varepsilon}_{AB} + \tfrac{1}{2}\,\overline{\varepsilon}_{BO} \quad \text{at} \quad BO$$

$$\overline{\varepsilon}_{AB} + \overline{\varepsilon}_{BO} + \tfrac{1}{2}\,\overline{\varepsilon}_{OC} \quad \text{at} \quad OC$$

These strains can then be substituted into equation (17) and an estimate of the shear flow stress found at each discontinuity. Hence the extrusion load may be predicted.

3.3.1 Axisymmetric Upper-Bound Solution

A kinematically admissable velocity field for
axisymmetric extrusion, satisfying incompressibility,
continuity and velocity boundary conditions was
produced graphically by Halling and Mitchell [36].
They assumed a mode of deformation and determined
the velocity components needed to produce the required
hodograph by considering stream-line geometry. The
solution they produced was for axisymmetric extrusion
through conical dies. This can be applied to unlubricated
extrusion through square dies, as in this case the dead
metal zone/deformation zone boundary, effectively forms
a conical lead in. A simple deformation field and hodo-
graph for a single triangle arrangement of velocity
discontinuities is shown in Figure 11. Assuming that
all metal flow within region 2 is parallel to AB i.e.
the dead metal zone boundary, then points on radial
lines through O_2 have the same velocity vector. The rate
of energy dissipation may be expressed:-

$$\dot{E} = \sum_{i,j=1}^{n} \left(\iiint_V \bar{\sigma}\, \bar{\dot{\varepsilon}}_i \; dV + \iint_S \tau_{ij}\, V_{ij} \; dS \right) \quad (18)$$

(n = number of regions into which the problem is divided)

This expression requires minimizing to give the best
solution. The various terms in (18) must now be calculated.
The rate of energy input on the left hand side can be
expressed:-

$$\dot{E} = p \times V \times A_B \qquad (19)$$

where P = extrusion pressure,   V = ram velocity and
    A_B= cross-sectional area of ram
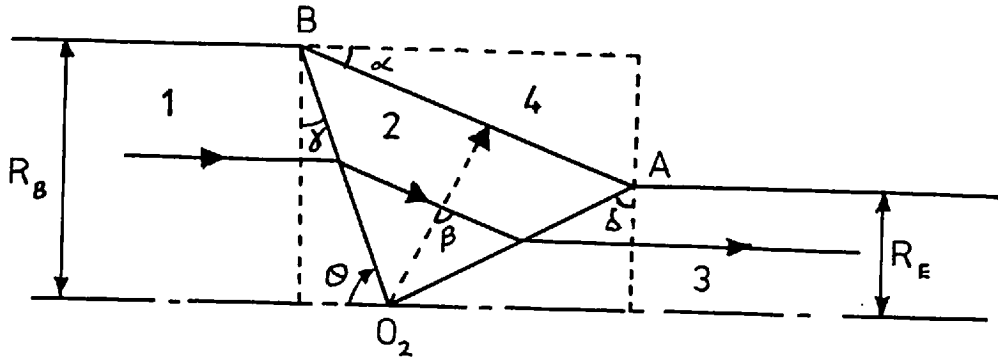
FIG. 11   Axisymmetric upper bound velocity field and hodograph
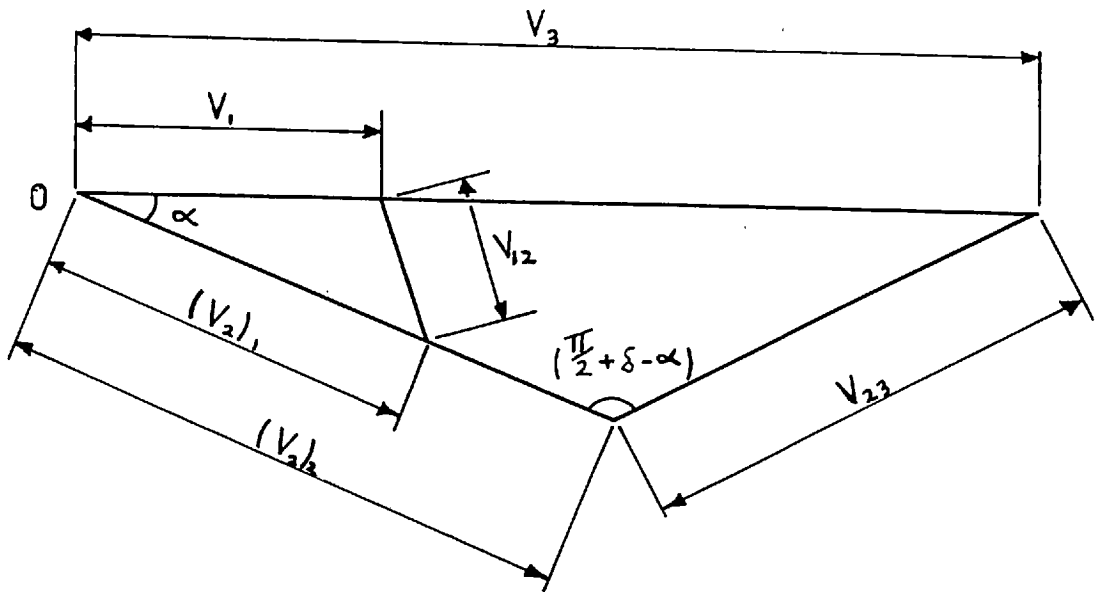
The first term on the right hand side represents the rate of energy dissipation within region 2. Alexander [37] demonstrated that the effective strain rate may be written:-

$$\overline{\dot{\varepsilon}}_1 = \sqrt{[\tfrac{2}{3}(\dot{e}_{\theta\theta}^2 + \dot{e}_{\phi\phi}^2 + \tfrac{1}{2}\dot{e}_{r\theta}^2)]} \tag{20}$$

where

$$
\left.
\begin{aligned}
\dot{e}_{\theta\theta} &= \tfrac{1}{r}[v\cos\beta\,(1+\tfrac{\partial\beta}{\partial\theta}) + \sin\beta\,\tfrac{\partial v}{\partial\theta}]\\[8pt]
\dot{e}_{\phi\phi} &= \tfrac{v}{r}[\cos\beta + \cot\theta\,\sin\beta]\\[8pt]
\dot{e}_{r\theta} &= \tfrac{1}{r}[-v\sin\beta\,(1+\tfrac{\partial\beta}{\partial\theta}) + \cos\beta\,\tfrac{\partial v}{\partial\theta}]
\end{aligned}
\right\} \tag{21}
$$

where $\beta = \theta - \alpha$, $\quad$ v = velocity in region 2

N.B. $\partial v/\partial r = \partial\beta/\partial r = 0$

In this case, the distance from O_2 to any point on AB may be expressed in terms of θ thus:-

$$r = \frac{R_B \cos(\alpha + \gamma)}{\cos\gamma \sin(\theta - \alpha)} \tag{22}$$

Using a mass balance v is given by:-

$$v = \frac{(v_2)_1 R_B}{r \sin\theta} \tag{23}$$

Using (20) and (21) we may write:-

$$\overline{\dot{\varepsilon}} = \sqrt{(\tfrac{2}{3})}\,\tfrac{1}{r}\,\varepsilon_i(\theta) \tag{24}$$

where $\varepsilon_i(\theta)$ is a function of θ only. The first term on the right hand side of (18) thus becomes:-

$$\dot{E}_2 = \pi\,\overline{\sigma}_2\,\sqrt{(\tfrac{2}{3})}\int_{\theta_1}^{\theta_2}[r^2]_{r_1(\theta)}^{r_2(\theta)}\,\varepsilon_i(\theta)\,\sin\theta\,d\theta \tag{25}$$

The limits $r_1(\Theta)$, $r_2(\Theta)$, Θ_1 and Θ_2 define the boundaries of region 2, the deformation zone. Equation (25) may be evaluated by use of Simpson's rule. In the present work the range was divided into twelve steps.

The second term on the right hand side of (18) must now be evaluated. The material deforming in region 2 is assumed to obey the Von Mises yield criterion. Therefore at all the discontinuities within the material $K_{ij} = \overline{\sigma} \, yield/\sqrt{3}$. This also applies along boundary AB as the dead metal zone, region 4, also consists of the extruding material. All the velocity discontinuities are either constants or functions of r. Therefore

$$\dot{E}_{ij} = \int \int_S \tau_{ij} \, v_{ij} \, ds \qquad (26)$$

can be evaluated exactly.

The velocity discontinuities are given below:-

$$(v_2)_1 = \frac{v_1 \cos \gamma}{\cos(\gamma+\alpha)}$$

$$(v_2)_2 = \frac{v_1 \, R_B^{\,2} \cos \delta}{R_E^{\,2} \cos(\alpha-\delta)}$$

$$v\overline{12} = \frac{v_1 \sin\alpha}{\cos(\gamma+\alpha)} \qquad\qquad (27)$$

$$v\overline{23} = \frac{v_1 \, R_B^{\,2} \sin\alpha}{R_E^{\,2} \cos(\alpha-\delta)}$$

$$v\overline{24} = \frac{v_1 \cos \gamma R_B}{r \sin\Theta \cos(\gamma+\alpha)}$$

Substituting (27) into (26) we obtain:-

$$\dot{E}_{12} = \frac{\pi R_B^2 \sigma_{12} v_1 \sin\alpha}{\sqrt{3} \cos\gamma \cos(\gamma+\alpha)}$$

$$\dot{E}_{23} = \frac{\pi R_B^2 \sigma_{23} v_1 \sin\alpha}{\sqrt{3} \cos\delta \cos(\alpha-\delta)} \qquad (28)$$

$$\dot{E}_{24} = \frac{2\pi \sigma_{24}}{\sqrt{3}} \int_{\Theta_1}^{\Theta_2} \frac{v_1 \cos\gamma R_B r \, d\Theta}{\cos(\gamma+\alpha) \cos\alpha}$$

If we assume that the values of α and δ giving the minimum value of P/K for a rigid perfectly plastic material also give the minimum for a powder material we can write:-

$$\frac{\sigma_{24}}{\sqrt{3}} = \frac{\sigma_{23}}{\sqrt{3}} = \frac{\sigma_{12}}{\sqrt{3}} = \frac{\sigma_2}{\sqrt{3}} = K \qquad (29)$$

Equation (18) can now be rewritten with P/K on the left hand side.

A computer program has been written to perform the numerical calculations and to minimize the P/K value on a CDC 6400 computer. The variables which are optimized are the angles α and δ. The only restrictions imposed are that α and δ cannot $\geq 90°$. The optimization procedure used, a standard library routine, is an adaption of the quasi-Newton method of Davidson [126] and eliminates the requirement for derivations. The program is listed in appendix 2.

3.4.1 Prediction of Load Using Axisymmetric Upper Bound Solution

In the previous section it was shown that, for a rigid perfectly plastic material, continuous functions describing the deformations along a stream-line could be written and the integral (18) evaluated exactly. However, for a material having a wide variation in rheology throughout the deforming zone the integral must be evaluated numerically. To do this the deformation zone must be divided into elements. In this investigation the region was divided into trapezoidal toroidal elements as shown in Figure 12. The strain and strain rate at each grid point must be found.

Elements at a discontinuity boundary such as $[r_n, \theta]$ in Figure 12 are the most general case and evaluation of the energy dissipated at this element must include the internal energy dissipation, the work done at the velocity discontinuity $\overline{12}$ and the work done at $\overline{24}$, due to sticking friction.

The plastic energy dissipation due to the velocity discontinuity O_2 B in element M may be written:-

$$\dot{E}_{12} = k_{12} \, (\delta S)_{12} \, v_{\overline{12}}$$

$$= 2\pi \, k_{12} \, (\delta r)_{n\xi} \, (r)_{n\xi} \, v_{\overline{12}} \qquad (29a)$$

In this expression k_{12} is a function of both strain and strain rate (as discussed in 3.2.3) and theoretically $\overline{\dot{\varepsilon}} = \infty$ at a discontinuity. Hence the strain rate must be assumed to be that obtaining in the first element after the boundary in region 2. k_{12} may then be ascertained by calculating the strain at the discontinuity as shown below.

FIG. 12 Nomenclature and
element details of
elemental upper
bound solution

Energy is also dissipated at the dead metal zone boundary due to sticking friction. Hence:-

$$\dot{E}_{24} = K_{r\theta} \; (\delta S)_2 \; V_{2(1)}$$

$$= 4\pi r_{\theta} \; K_{r\theta} \; V_{2(1)} R_B \; \frac{\sin \frac{d\theta}{2}}{\sin \beta \; \sin(\beta - \frac{d\theta}{2})} \qquad (29b)$$

A similar method may again be used to determine $K_{r\theta}$; calculating $\dot{\bar{\varepsilon}}_{r\theta}$ at the boundary element (r, θ) and evaluating as shown below.

The internal energy dissipation due to circumferential straining is written:-

$$\dot{E}_3 = \sigma_{r\theta} \bar{\varepsilon}_{r\theta} (dV)_{r\theta}$$

$$= \frac{\sigma_{r\theta} \bar{\varepsilon}_{r\theta} \; 4\pi r_{n\theta}^2 \; (\delta r)_{n\theta} \; \sin \frac{d\theta}{2}}{\sin(\beta - \frac{d\theta}{2})} \qquad (29c)$$

Therefore the total energy input is given by:

$$\sum (\dot{E}_{12} + \dot{E}_{24} + \dot{E}_3) \qquad (29d)$$

(The $\dot{E}_{12}$ and $\dot{E}_{24}$ terms applying to the boundary regions only). The external energy input is given by:-

$$\dot{E} = p \times A_B \times V$$

and hence the forming pressure p may be determined.

Calculation of the flow stress

The flow stress is both strain and strain rate sensitive and hence the strain in each element must be considered. The mean equivalent strain at a velocity discontinuity may be calculated by finding the amount of plastic work done per unit volume at the discontinuity. Thus, for the element considered, the total plastic work done per unit time is given by

$$\dot{E}_{12} = 2\pi \, K_{12} \, (\delta r)_{n\xi} \, (r)_{n\xi} \, V_{\overline{12}} \tag{29a}$$

The volume flow past this discontinuity is:

$$dV = 2\pi(\delta r)_{n\xi} \, (r)_{n\xi} \, \sin\xi \, V_1 \tag{29e}$$

$$(W_p)_{r,\xi} = \frac{K_{12} \, V_{\overline{12}}}{V_1 \, \sin\xi} \tag{29f}$$

The plastic work done per unit volume may be written (see Fig. 13)

$$\int_{\varepsilon_1}^{\varepsilon_2} \overline{\sigma} \, d\varepsilon = \overline{\sigma}_m \, (\varepsilon_2 - \varepsilon_1) \tag{29g}$$

Hence across the increment of velocity discontinuity under consideration

$$\overline{\varepsilon}_2 - \overline{\varepsilon}_1 = \frac{V_{\overline{12}}}{\sqrt{3} \, V_1 \, \sin\xi} \tag{29h}$$

and from (17) in (3.2.3)

$$K_{12} = \frac{A \, \overline{\dot{\varepsilon}}^n}{\sqrt{3} \, (m+1)} \left[\frac{\overline{\varepsilon}_2^{\,m+1} - \overline{\varepsilon}_1^{\,m+1}}{\overline{\varepsilon}_2 - \overline{\varepsilon}_1} \right] \tag{29i}$$

The material is then further strained as it traverses the element. The strain imparted may be calculated because

$$\text{work/unit volume} = \bar{\sigma}_m(\mathcal{E}_2 - \mathcal{E}_1)$$
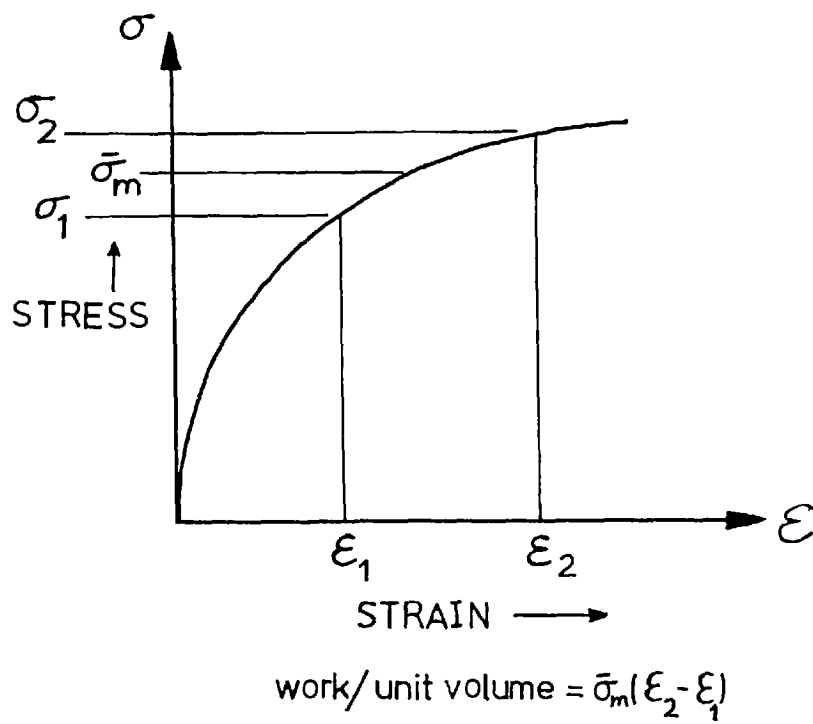
FIG. 13 Definition of mean flow stress

$$d\bar{\varepsilon} = \bar{\dot{\varepsilon}} \ dt = \bar{\varepsilon}_3 - \bar{\varepsilon}_2 \tag{29j}$$

where $\bar{\dot{\varepsilon}}$ is calculated using equation (20) in (3.3.1) and

$$dt = \frac{2 \ \bar{r}_{n\theta} \ \sin(\frac{d\theta}{2})}{V_{n\ \theta} \sin(\beta - \frac{d\theta}{2})} \tag{29k}$$

thus,

$$\sigma_{r,\theta} = \frac{A \ \bar{\dot{\varepsilon}}^n}{m+1} \left[\frac{\bar{\varepsilon}_3^{m+1} - \bar{\varepsilon}_2^{m+1}}{\bar{\varepsilon}_3 - \bar{\varepsilon}_2} \right] \tag{29l}$$

The program in appendix (3) performs the numerical calculations summing the energies and strains and calculating the pressure. The variables optimized are angles α and δ and the flow stress equation constants A, m and n. The optimization procedure adopted was written to solve the constrained problem to minimize a general objective function of many independent variables subject to bounds on the variables. A sequential penalty function technique developed by Lootsma[127] is utilised. A routine to calculate the value of the function, in this case the extrusion pressure, is included. The method involves iteration and therefore requires an initial estimate of the least possible value of extrusion pressure. The optimization routine solves the constrained problem by transforming the problem into a sequence of unconstrained problems whose solutions tend to the solution of the original problem.

3.4.2 Calculation of mean flow stress during extrusion

The flow stress may be calculated using the upper bound solutions mentioned in the previous sections. The minimum pressure at the end of extrusion divided by the load constant c (which = p/σ_{yield}) gives the mean flow

stress. In the present work the actual c values used were produced by the simple axisymmetric field discussed in section 3.3.1 and listed in appendix (2). The use of the minimum pressure in the calculation eliminates the need to consider frictional effects between the billet surface and the container wall.

3.5.1 Strain rate

It is quite obvious that material flowing along different streamlines through the deformation zone is subjected to different strain rates. Therefore it is very difficult to define a mean strain rate for a particular extrusion ratio and ram speed. Feltham[38] originally proposed the following definition for mean strain rate:

$$\bar{\dot{\epsilon}} = \frac{\text{total strain}}{\text{time for strain to occur}} \qquad (30)$$

The time in which the strain occurs may be calculated by assuming that the deformation occurs effectively in a cone of semi-angle ω (Fig. 9) and base diameter D_B. The volume of this cone is given by:-

$$V = \frac{\pi (D_B^3 - D_E^3)}{24 \tan \omega}$$

Therefore the time

$$t = \frac{V}{\text{volume extrusion rate}}$$

Now the volume extrusion rate $= \dfrac{\pi D_B^2 v}{4}$

$$\therefore t = \frac{D_B^3 - D_E^3}{6 D_B^2 \tan \omega \, v}$$

Thus the time mentioned in equation (30) is obtained.

Now the work done by the ram in moving a distance L

$$= p \times \pi \frac{D_B^2}{4} \times L.$$

∴ The work done per unit volume = p

The work per unit volume may also be expressed:-
stress x strain.

Now $p = \sigma_{yield} \, c$ (where $c = \frac{p}{\sigma}$, from theory).

∴ c may be equated to the mean strain

∴ equation (30) becomes:-

$$\bar{\varepsilon} = \frac{6 \, c \, \tan \omega \, D_B^2 \, v}{(D_B^3 - D_E^3)} \tag{31}$$

Equation (31) permits the calculation of the strain rate
during extrusion.

The axisymmetric upper bound solution, given in
3.4.1., calculates the strain rate at the centroid of
each element in the deformation zone grid. Thus an
average strain rate during extrusion may also be obtained
this way. The values produced by this latter method are
compared with those obtained from Feltham's equation (31)
in the discussion in Chapter 5.

3.6.1 General hot working equation

A relationship between strain rate, flow stress and
temperature during the hot deformation (i.e. creep testing)
of metals was first proposed by Garofalo [66]. It was later
applied to conventional hot working processes (i.e. extrusion)
by Sellars and McG. Tegart [67]. The relationship proposed
involves a sinh term and the governing equation is given
below:-

$$\dot{\varepsilon} = A_1 \left[\sinh (\alpha \sigma) \right]^n \exp \left(-\frac{\Delta H}{RT} \right) \tag{32}$$

Here A_1, α and n are temperature and stress independent constants and ΔH is the activation energy which is also assumed to be independent of temperature and stress. To make use of equation (32) and find ΔH, α must first be determined.

3.6.2 Determination of constants in hot working equation

At high stress levels the relationship between strain rate and stress may be written:-

$$\dot{\varepsilon} = A_3 \exp(\beta\sigma) \qquad (33)$$

where β is a temperature independent function. Also at high stresses $(\alpha\sigma > 1.2)$ and constant temperatures equation (32) can be rewritten:

$$\dot{\varepsilon} = A_1 \sinh(\alpha\sigma)^n \qquad (34)$$

On expanding the sinh term this approximates to:-

$$\dot{\varepsilon} = \frac{A_1}{2^n} \exp(n\,\alpha\sigma) \qquad (35)$$

At low stress levels:-

$$\dot{\varepsilon} = A_2\,\sigma^{n_2} \qquad \text{i.e.} \quad (\alpha\sigma < 0.8) \qquad (36)$$

where n_2 is also assumed temperature independent.

Comparing (33) and (35) gives:-

$$\beta = n\,\alpha \qquad (37)$$

Now $\quad n \simeq n_2$

Therefore $\quad \alpha = \dfrac{\beta}{n_2}$. β is found by plotting $\ln\dot{\varepsilon}\ v\ \sigma$

n_2 is found by plotting $\ln\dot{\varepsilon}\ v\ \ln\sigma$

hence α is evaluated.

3.6.3 The activation energy

To find the activation energy we must reconsider equation (32). Taking natural logarithms we obtain:-

$$\ln \dot{\varepsilon} = n \ln \left[A_1 \sinh (\alpha\sigma) \right] - \left(\frac{\Delta H}{RT} \right) \qquad (38)$$

Now at constant flow stress:-

$$- R \frac{\partial \ln \dot{\varepsilon}}{\partial \frac{1}{T}} = \Delta H \qquad (39)$$

Equation (39) may be expanded[107] to give:-

$$- R \left(\frac{\partial \ln \dot{\varepsilon}}{\partial \ln \sinh(\alpha\sigma)} \right)_T \left(\frac{\partial \ln \sinh(\alpha\sigma)}{\partial \frac{1}{T}} \right)_{\dot{\varepsilon}} = - \Delta H \qquad (40)$$

Hence from plots of $\ln \dot{\varepsilon}$ vs $\ln \sinh(\alpha\sigma)$ and . $\ln \sinh(\alpha\sigma)$ vs. $\ln \frac{1}{T}$ the activation energy may be obtained.

3.7.1 Introduction to fibre-reinforcement theory

There are several conventional methods which may be used to strengthen metals. The metal can be work hardened to increase both the dislocation density and the strength. This method is useless if the metal is to be employed at elevated temperatures as recovery and/or recrystallisation will occur causing softening and loss of strength.

Other obstacles to dislocation motion such as solute atom atmospheres and second phase particles may be used to improve the strength. Such strengthening mechanisms can be quite effective, even at elevated temperatures.

Yet another way of increasing the strength of a metal is to introduce fibres of high ultimate tensile strength and, preferably, of high elastic modulus. Basically three

types of fibre are available (neglecting special eutectic alloys):-

(1) Glassy type fibres which have a high U.T.S but unfortunately an elastic modulus similar to that of most light metals. Such fibres do not deform plastically. This is the type used in the present series of investigations.

(2) Ceramic materials such as alumina, graphite, boron, silicon nitride and silicon carbide all of which can be prepared as long, thin fibres with diameters of about 10^{-4} to 10^{-3} cms. These materials have smooth surfaces free from deep notches and steps. They are light, have high melting points and high elastic moduli.

(3) Metallic wires such as steel or nickel wires. These have higher values of U.T.S. and elastic modulus than most matrix metals such as aluminium.

Materials in groups (1) and (2) are inherently strong with those in group (2) having high Pierls-Nabarro forces presenting great difficulties to the motion of dislocations. However, although these materials have high "shear" strength they are brittle and have low resistance to crack initiation and propagation. Thus the theoretical high strength of materials in groups (1) and (2) can only be made use of if they are produced relatively defect free. Their surfaces must also be protected against damage which might lead to crack initiation, propagation and "premature" failure. This protection can be provided by embedding these fibres in a ductile metal matrix of relatively low flow stress. Plastic flow of the matrix occurs early in the loading cycle and the load is transferred to the fibres. The product is called a fibre reinforced composite. This matrix must serve two other important purposes:-

(1) It must prevent direct fibre-fibre contact.
If the fibres contact one another a crack in
one fibre may spread catastrophically to
another fibre and so on. However, the ductile
matrix can terminate crack propagation by
"blunting" the crack tip thus giving the
overall composite quite a high fracture
toughness.

(2) It must prevent the application of the load
from causing any damage to the fibres which
might lead to crack initiation.

3.7.2 Stress/strain behaviour of continuous fibre composites

In the following sections on fibre reinforcement
two assumptions are made concerning composite structure
and behaviour. They are:-

(1) The fibres are uniaxially aligned.
(2) The matrix-fibre bond is sufficiently strong,
to ensure efficient load transference.

During loading, the $Al-B_2O_3$ system under investigation
exhibits three distinct modes of deformation in succession:-

(1) Both fibres and matrix deform elastically
(2) The fibres deform elastically and the matrix
plastically. The transition from (1) and (2)
occurs at strains slightly greater than the
yield strain of the bulk, unreinforced matrix
metal.

(3) Fracture of the fibres followed by composite
failure. It should be noted that composite
failure occurs immediately upon fibre fracture
only when the fibre volume fraction exceeds a
minimum value. This minimum volume fraction
will be discussed later in section 3.7.3.

The three modes of composite deformation are discussed below.

(a) Elastically deforming matrix and fibres

The elastic moduli of aluminium and B_2O_3 glass are similar. Thus when a load is applied to the composite transference occurs, due to the interfacial bond, and the stresses and strains in the metal and fibres are equal. As the load increases the strain in the matrix and fibres continues to increase linearly until the yield strain of the matrix is reached (Fig. 14).

If the elastic modulus of the fibre is greater than that of the matrix i.e. Fig. 15, it has been shown experimentally that:-

$$E_{composite} = E_{fibre} \, V_{fibre} + E_{matrix} \, V_{matrix} \qquad (41)$$

Hill[130] has shown that (41) is the theoretical lower bound to the modulus when the Poisson's ratios of the components are equal. Thus $E_{composite}$ will never be less than the value given by (41) no matter what the poisson's ratios of the components are.

(b) Elastically deforming fibres - plastically deforming matrix

During this stage in the deformation the strain in the matrix is greater than the strain in the fibre for a given stress and so a shear force exists at the interface and contributes to load transference.

The stress/strain behaviour of the composite may be described as quasi-elastic. If at any stage the load is removed the specimen returns almost to its original length. At first this recovery is fully elastic but the final stage of recovery sees the matrix being deformed plastically in compression. When the load has been completely removed the specimen retains a small
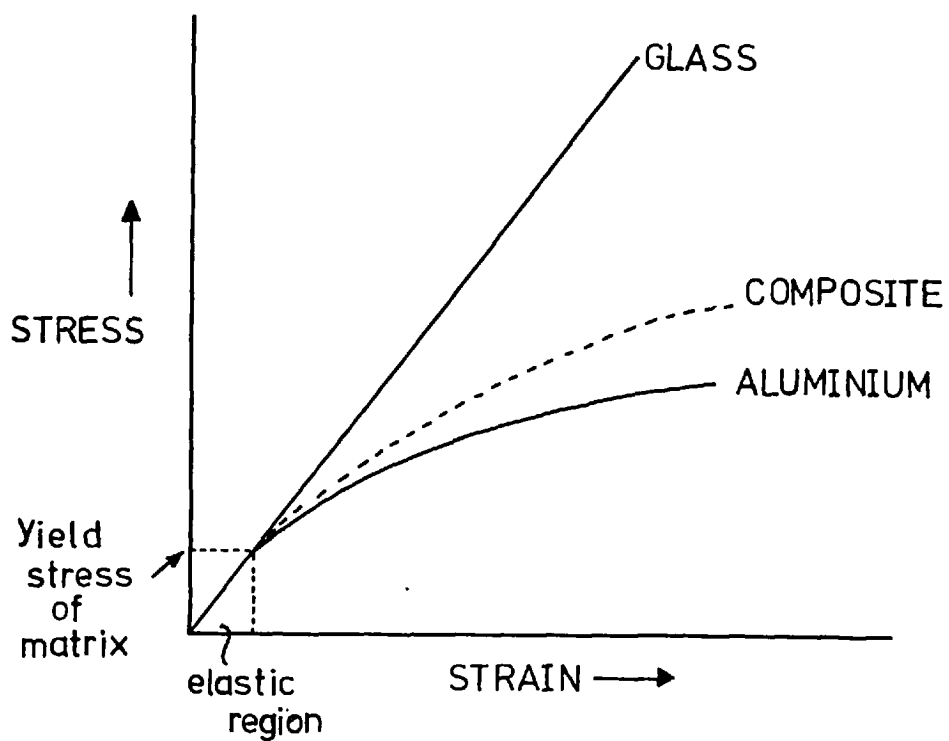
FIG. 14 Stress-strain behaviour of Al-glass composite

FIG. 15 Stress strain behaviour of composite in which $E_F > E_M$
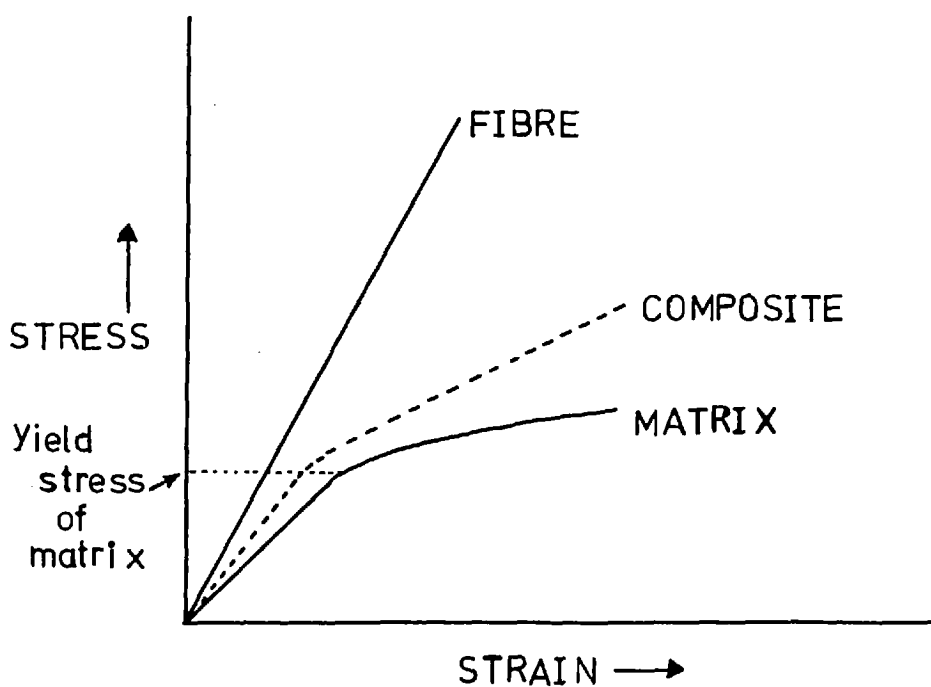
permanent set (Fig. 16) with the fibres in tension and the matrix under compression. Fig. (16) also shows the result of repeating [85] the stress cycle. On loading again the initial elastic region is extended because the matrix was initially in compression and hence, on completing the cycle, the permanent set is removed.

This is the most important part of the stress/strain curve when the load bearing capacity of the fibres is being utilised. In this region:-

$$E_{composite} = E_{fibre} \, V_{fibre} + (\frac{d\sigma_m}{d\epsilon_m})_\epsilon \, V_m \qquad (42)$$

where $d\sigma_m/d\epsilon_m$ = slope of stress/strain curve of the matrix at a strain, ϵ, to which the composite has been subjected. Effectively as:

$$\frac{d\sigma_m}{d\epsilon} \lesssim \frac{E_m}{100} \, , \qquad E_c = E_F \, V_F \qquad (43)$$

    (c) Fracture of the composite occurs when the stress in the fibres reaches their U.T.S.

3.7.3 Strength of continuous fibre composites

The general expression for the strength of the composite may be written:-

$$\sigma_C = \sigma_F \, V_F + \sigma'_m \, (1 - V_F) \qquad (44)$$

when V_F exceeds a value denoted by V_{min}. Failure of all the fibres results in immediate failure of the composite only if σ_C, given by (44), is greater than $\sigma_u(1 - V_F)$. (σ_u = U.T.S. of matrix). This defines

$$V_{min} = \frac{\sigma_u - \sigma'_m}{\sigma_F + \sigma_u - \sigma'_m} \qquad (45)$$

Another important limiting value must be noted and considered. No fibre reinforcement at all occurs unless
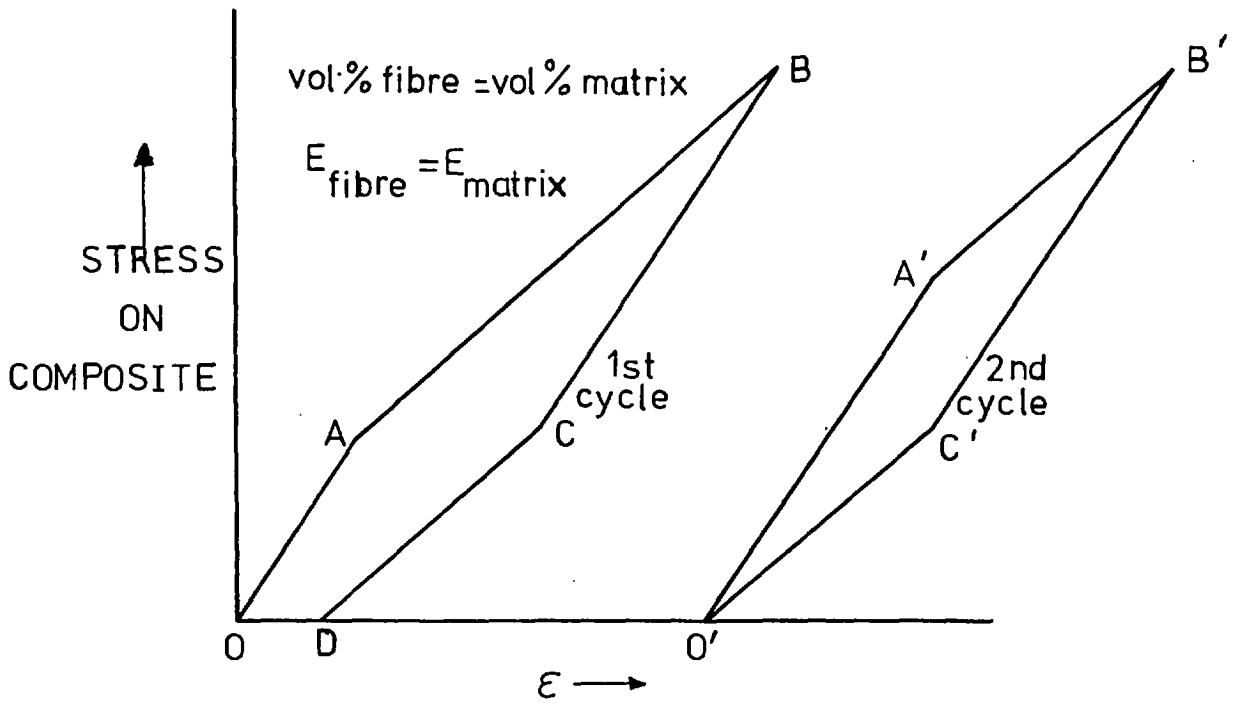
FIG. 16 Stress-strain behaviour of composite subjected to
repeated loading
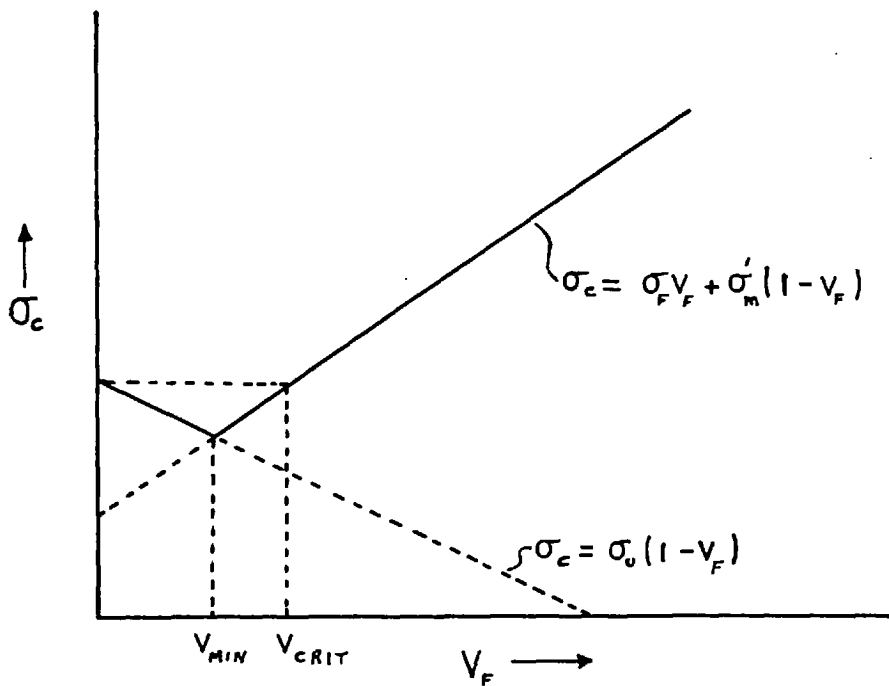
FIG. 17 Relationship between composite strength and fibre content

the volume fraction of fibres exceeds a value denoted
by V_{crit}. This may be defined as:-

$$V_{crit} = \frac{\sigma_u - \sigma_m'}{\sigma_F - \sigma_m'} \qquad (46)$$

(see Fig. 17). This expression is obtained by equating
the right hand side of (44) with σ_u, the ultimate
tensile strength of the bulk matrix. It should be noted
that equation (44) assumes that all the fibres break in
a given cross-section and that the presence of the con-
tinuous fibres does not interfere with the work hardening
characteristics of the matrix material.

3.7.4 Stress/strain behaviour of discontinuous fibre composites

In most practical cases, including the case of
composites produced by extrusion, the fibres involved
are not continuous. Therefore the previous two theory
sections must be modified to allow for:-

(1) Possible composite fracture by the "pulling out"
of fibres from the matrix if the fibre aspect
ratio is less than a critical value (3.7.5).

(2) The stress concentrating effects of the fibre
ends.

One additional assumption required for this modified
analysis is that the fibre content, in any cross section,
is constant. Stages (1), (2) and (3), mentioned previously
in section 3.7.2, are once again present. For fibres with
aspect ratios greatly exceeding the critical value of (σ_F/τ_m)
equation (42) applies.

3.7.5 Stresses present in discontinuous fibre composites

We must once again consider the first two stages
in the behaviour of the composite under load:

    (a) Elastic matrix - elastic fibre
    (b) Plastic matrix - elastic fibre

(a) Elastic matrix - Elastic fibre

As the elastic moduli are similar in the
aluminium - B_2O_3 glass system the stresses and strains
in the matrix and fibres are the same in this elastic
region.

(b) Plastic matrix - Elastic fibre

When the load has been increased to such an
extent that the stress in the matrix exceeds its flow
stress σ_m, we can assume that the matrix everywhere
starts to flow plastically. As the load continues to
increase the "effective" modulus, $d\sigma_m/d\varepsilon$, of the matrix
becomes very much smaller than E_F. This means that
different displacements now occur in the bulk matrix and
in the interfacial matrix. The flow of the bulk matrix
along the interfacial matrix produces shear stresses causing
the stress in the fibres to build up from the ends.
(Fig. 18 and Fig. 20). This build up of tensile stress
can be expressed thus:-

$$\frac{dp}{dZ} = 2\pi r \, \tau_m \qquad (47)$$

where p is the tensile load in the fibre, r = fibre radius,
τ_m is the shear flow stress of the bulk matrix or of
the interface, whichever is the least and Z is the distance
along from the fibre end. (See Fig. 18)

If we assume that the work hardening in the matrix
is very small we may integrate (47) and obtain:-

$$p = 2\pi \, rZ \, \tau_m \qquad (48)$$
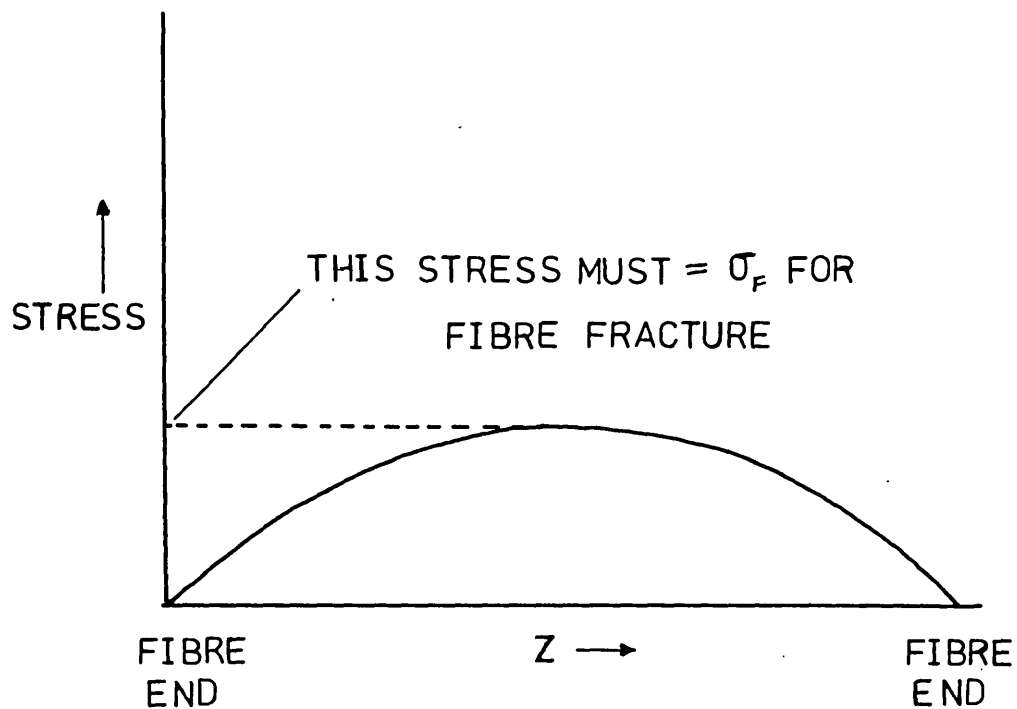
FIG. 18   Stress build up in fibre

FIG. 19   Strain distribution across matrix-fibre interface
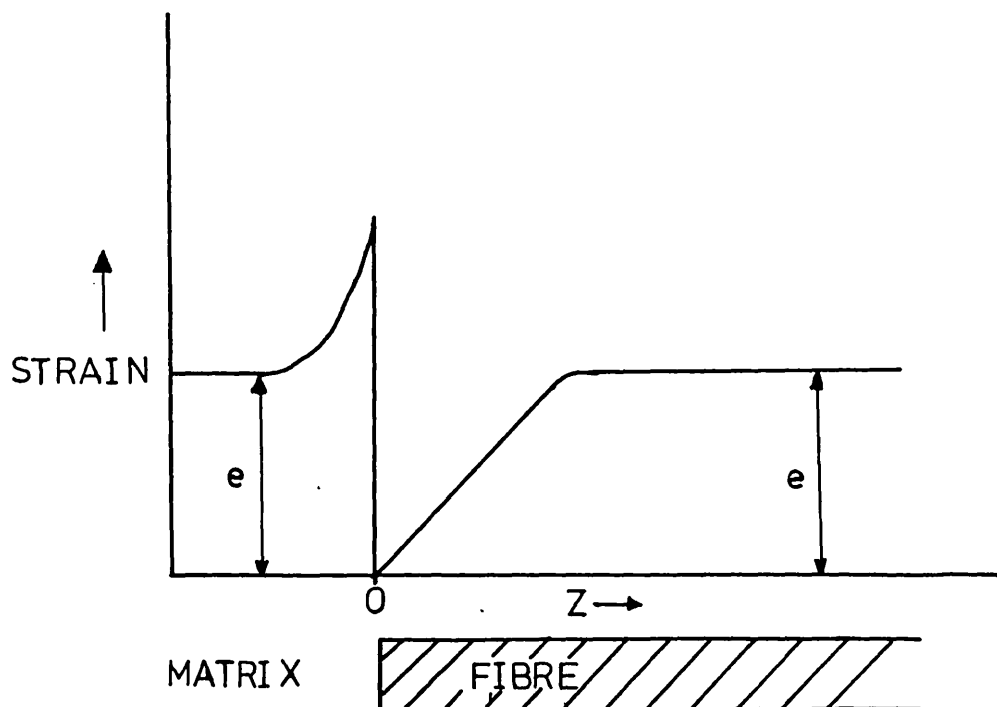
This predicts a linear build up of tensile stress in the fibre from the ends. Now p can also be expressed as:-

$$p = \pi r^2 \, \sigma_{ZZ} \tag{49}$$

where σ_{ZZ} is the stress in the fibre at a distance Z from the end.

$$\therefore \quad \sigma_{ZZ} = \frac{2\tau_m Z}{r} \tag{50}$$

To make full use of the strength of the fibre i.e. to make sure that composite failure occurs by the breaking of the fibres, σ_{ZZ} in (50) must reach σ_F, the U.T.S. of the fibre. For this to occur we can see that the fibre length must be greater than a certain value i.e. Z must exceed L_{crit} for a given fibre radius r. Since the fibre is loaded from both ends L_{crit} may be expressed as:-

$$L_{crit} = \frac{r \, \sigma_F}{\tau_m} \tag{51}$$

Equation (51) may be rewritten:

$$\frac{L_{crit}}{r} = \frac{\sigma_F}{\tau_m} \tag{52}$$

The left hand side is the limiting fibre aspect ratio which must be exceeded for efficient reinforcement to occur. When the fibre length is greater than L_{crit} the strain distribution around a fibre end is as shown in Fig. 19.

For composites formed by extrusion, clearly a minimum extrusion ratio exists for the formation of fibres having this limiting aspect ratio. This minimum extrusion ratio can be estimated approximately as shown

below.[†]

If the fibre length is less than L_{crit}, for a given fibre radius, fracture of the composite occurs by the failure of the matrix - fibre interface. If such a failure occurs the τ_m value is equal to the frictional force per unit area which the matrix exerts on the fibre while sliding over it. It should be noted that if V_{min} is not exceeded failure of the interfaces will not cause instant composite fracture .

If composite failure occurs by the breaking of fibres we can see from (Fig. 18) that the average stress in the fibre is less than σ_F and may be expressed as

$$\sigma = \frac{1}{1} \int_0^1 \sigma_{zz} \, dZ \qquad (53)$$

[†] Assuming that the glass particles are spherical with radius r_1 and that after extrusion their shape is cylindrical with radius r_2 and length 1.

The ratio $r_1^2/r_2^2 \simeq R$, the extrusion ratio. Constant volume requirements of the glass reinforcement yields:-

$$\frac{4}{3} R^{3/2} r_2 = 1$$

The critical fibre length $1_c = \dfrac{r_2 \, \sigma_F}{\tau}$

where σ_F is the stress in the fibre and τ the fibre shear strength.

Hence for satisfactory reinforcement:-

$$\frac{4}{3} R^{3/2} r_2 > \frac{r_2 \, \sigma_F}{\tau}$$

Now for this system σ_F = 2412 MN/m^2 (assuming ideal fibres) τ = 100/$\sqrt{3}$ MN/m^2 and $\therefore$ R = 9.94.

3.7.6 Strength of discontinutious fibre composites

The ultimate tensile strength of a composite containing discontinuous, uniaxially aligned, randomly distributed fibres can be expressed as:-

$$\sigma_c = \sigma_F \ V_F \ [1 - \alpha] + \sigma_m' \ (1 - V_F) \qquad (54)$$

if V_F > V_{min}. The term α allows for the fact that the average stress in the fibres at fracture is less than σ_F.

3.7.7 Effect of fibre orientation

Fig. 21 shows a schematic representation [87] of a fibre reinforced composite in which the fibres are inclined at an angle ϕ to the tensile axis. Even assuming that the fibre aspect ratio/fraction of fibres exceed the
and the volume

critical values failure may occur by one of the following modes:-

1) The fibres break due to the stress transfer by flow of the matrix parallel to fibres. The failure stress is then given by:-

$$\sigma_c = \sigma \cos^2\phi \qquad (55)$$

2) The matrix fails due to shear stresses on planes parallel to the fibres. The failure stress becomes:-

$$\tau_s = \sigma \sin\phi \cos\phi \qquad (56)$$

3) The matrix fails by flow transverse to the fibres. The failure stress is given by:-

$$\sigma_p = \sigma \sin^2\phi \qquad (57)$$

STRESS DISTRIBUTION
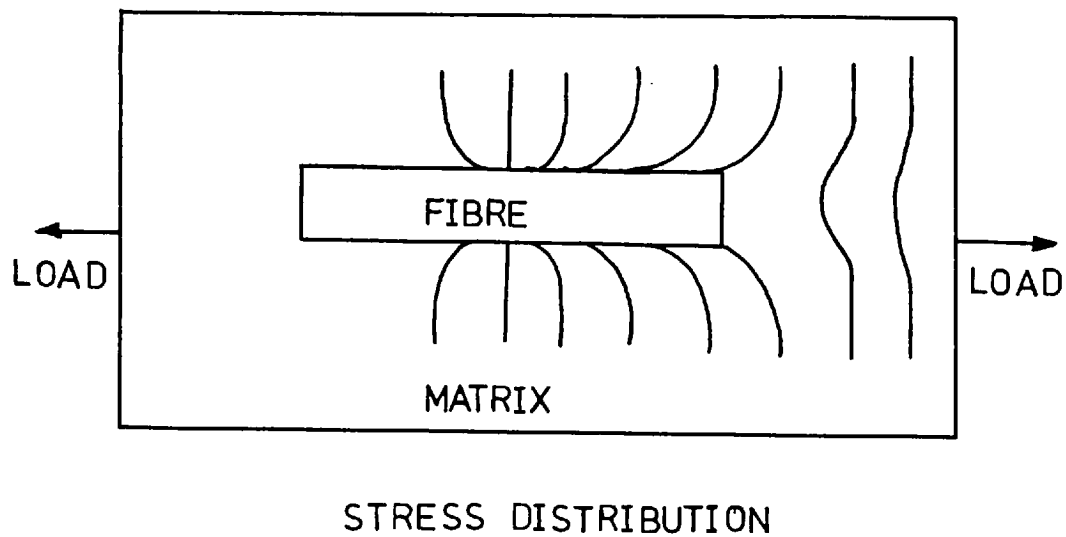
FIG. 20   Stress distribution in matrix
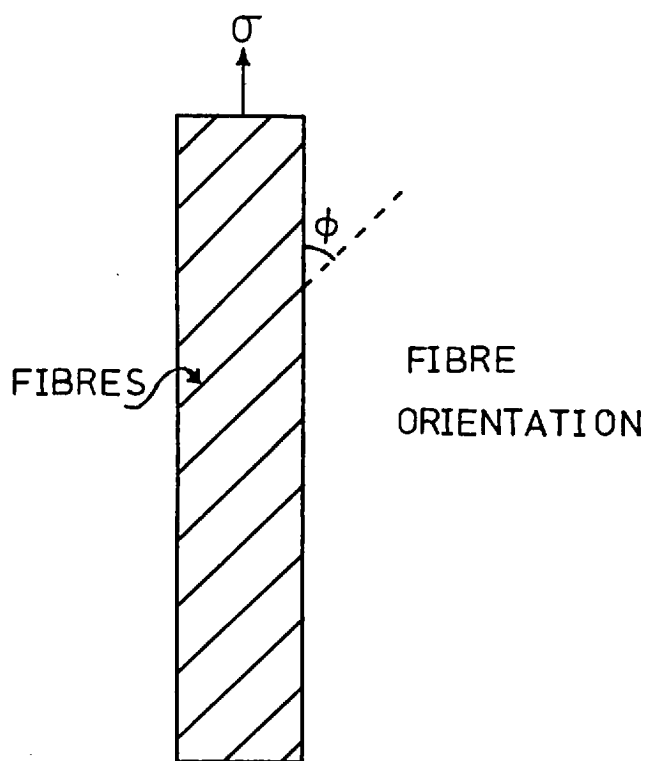
FIG. 21   Composite with fibres inclined to stress axis

The flow stress in shear for a constrained matrix
e.g. when it contains fibres fairly close together, is
increased by a factor of 1.5[87]. Also the value of
σ_p in (57) is the U.T.S. of the matrix in plane strain
and is therefore ~ 1.15 times the value measured in a
tensile test. Obviously the composite fails by the
mechanism requiring the lowest value of σ. Fig. 22
gives the minimum value of σ predicted by the three
equations as a function of ϕ. It can be seen that
when the fibres are inclined to the tensile axis at
angles greater than 6° the strength of the composite
falls drastically. The effect of random alignment of
fibres was investigated by Cox[104]. His theory predicts
that the tensile strength of a random, three-dimensional
array of fibres equals one sixth of the theoretical value
for the same composite containing uniaxially aligned
fibres, provided that a sufficient volume fraction of
fibres is present.

3.7.8 Fracture toughness of composites

Fig. 23 depicts fracture toughness as a function
of notch depth for two types of materials:

    a) notch insensitive
    b) notch sensitive.

The straight line (a) shows that the fracture strength
of an insensitive material is directly proportional to
the cross sectional area of the specimen. Curve (b) can
be represented by the equation:-

$$\sigma_y = \sigma_A (1 + 2 \sqrt{a/\rho}) \tag{58}$$

where σ_A = bulk applied stress (in y direction)
       a = depth of notch
       ρ = radius of curvature of notch
       σ_y = local tensile stress perpendicular to the notch
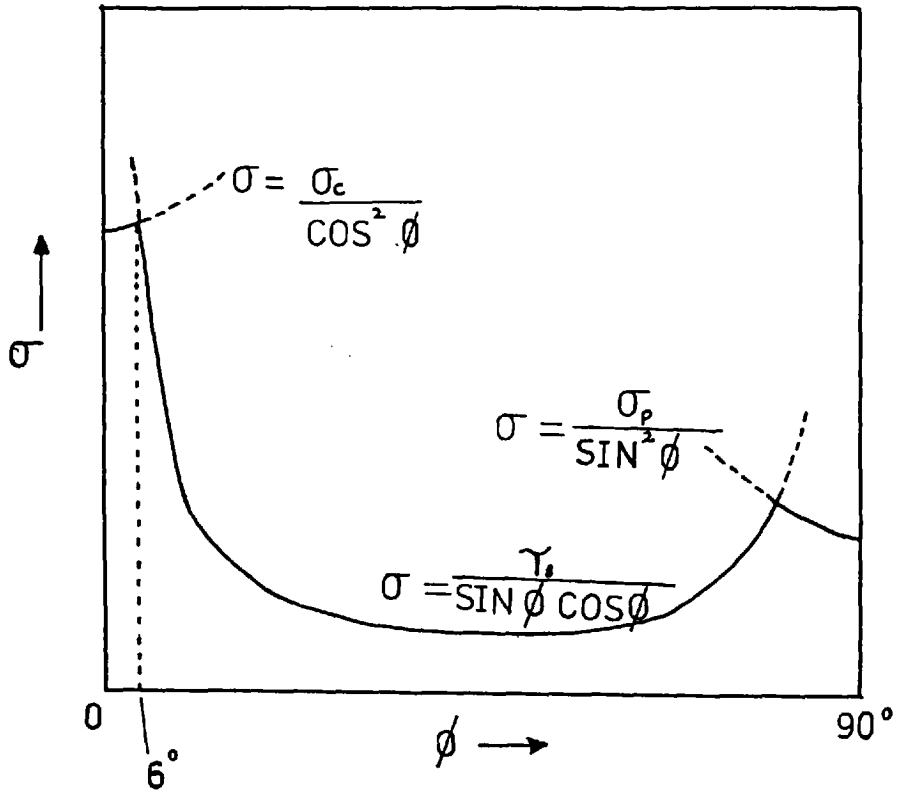
FIG. 22   Effect of fibre-stress axis inclination on composite strength

The curves in the figure are labelled:

$$\sigma = \frac{\sigma_c}{\cos^2 \phi}$$

$$\sigma = \frac{\sigma_p}{\sin^2 \phi}$$

$$\sigma = \frac{\tau_i}{\sin \phi \cos \phi}$$
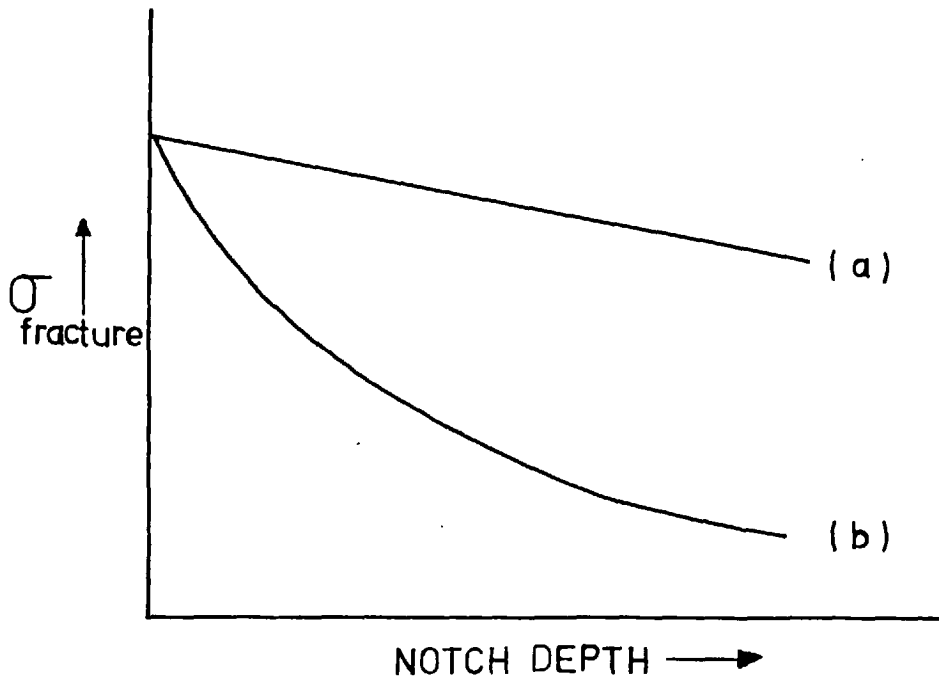
FIG. 23   Effect of notch depth on composite fracture toughness

Consider a brittle solid. We can set $\rho \simeq b$ the inter-atomic spacing and the theoretical strength as

$$\sigma_{th} = \sqrt{\frac{E\gamma}{b}} \qquad\qquad (59)$$

where γ = surface energy/unit area

  E = Young's modulus

Combining (58) and (59) we find:-

$$\sigma_A \simeq \tfrac{1}{2}\sqrt{\frac{E\gamma}{a}} \qquad\qquad (60)$$

This is the Griffith crack relation.

Now for a composite to be tough it can be seen that σ_A and/or ρ must be large. From (60) it can be seen that σ_A increases with surface energy. Both of these terms, σ_A and ρ , increase if the crack tip is blunted i.e. the radius increases and the effective value of γ increases by an amount which takes into account the plastic work done. Thus one method of producing a tough composite is to employ a ductile matrix so that plastic flow at or near the tip blunts the crack tip.

Considering the crack (parallel to the x axis) as a semi-ellipse with major axis length = 2a and minor axis length = 2b, Fig. 24 shows σ_y and σ_x as functions of the distance from the crack tip. Now σ_x has a maximum value at a distance of approximately 1 crack tip radius ahead of the crack. For a composite material with relatively weak fibre-matrix bonding Fig. 25 shows how a crack may be deflected parallel to the fibre causing delamination of the fibre. Once again this produces a high fracture toughness in the composite.

Thus we can expect a composite with a ductile matrix and relatively weak bonding to exhibit reasonably high fracture toughness values.
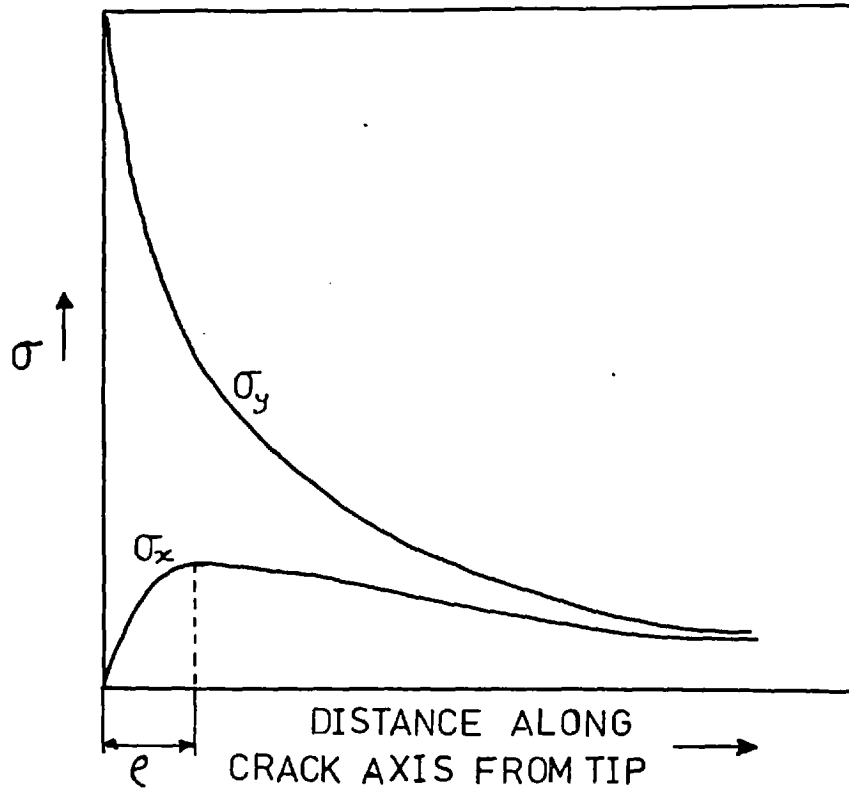
FIG. 24 Stress distribution as a function of distance from crack tip
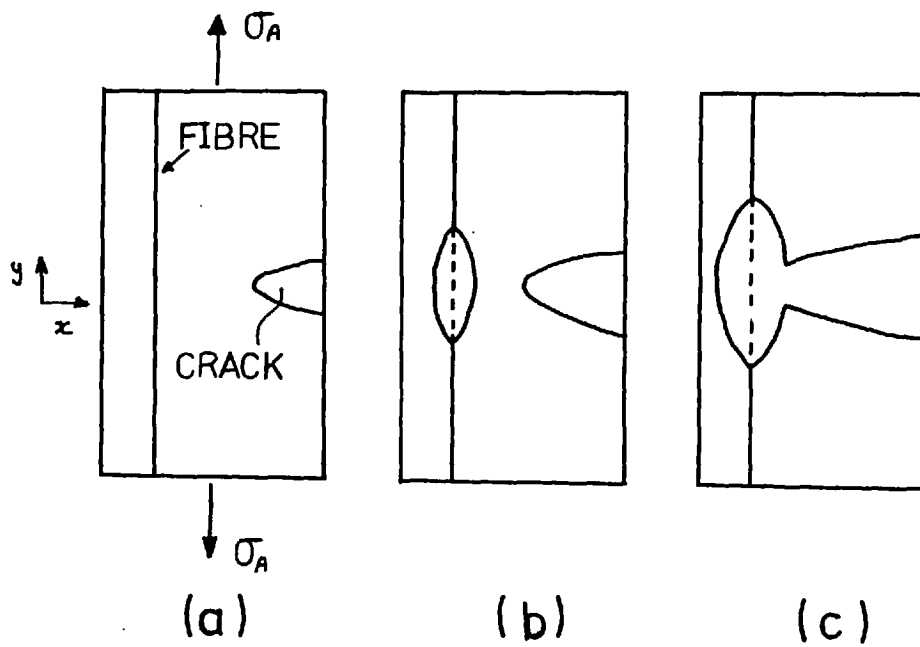
FIG. 25 Three stages in fibre delamination by crack propagation

3.8.1 Effect of temperature on extrude flow stress

The flow stress of most materials ia made up of two components:-

1) The athermal component i.e. the stress needed to enable dislocations to overcome long range obstacles such as precipitate particles and other dislocations on parallel slip planes.

2) The thermally activated component i.e. the stress needed to overcome short range obstacles such as solute atoms and lattice friction effects.

The opposition to dislocation motion may be represented as in Fig. 26. Consider a dislocation of length 1 and Burgers vector $\underline{b}$. The product $\underline{b}$ d 1 is termed the activation volume, V. N.B. This is not truly a volume as $\underline{b}$, d and 1 are coplanar but it gives an estimate of the size of the obstacle to be overcome. If the applied stress is K_s the force per unit length on the dislocation is $K_s \underline{b}$. Therefore the work done by the applied stress in overcoming the obstacle is $K_s \underline{b} l d$ i.e. $K_s V$. We can write[109]

$$u_o = u + K_s V \qquad (61)$$

However, part of K_s is occupied in overcoming other long range obstacles which interfere with this considered obstacle. Let this part $= K_A$. Therefore

$$u_o = u + (K_s - K_A)V \qquad (62)$$

we know that strain rate = dislocation density x $\underline{b}$ x velocity of dislocation movement. Also the velocity of dislocation = rate of overcoming obstacles x distance apart of obstacles.
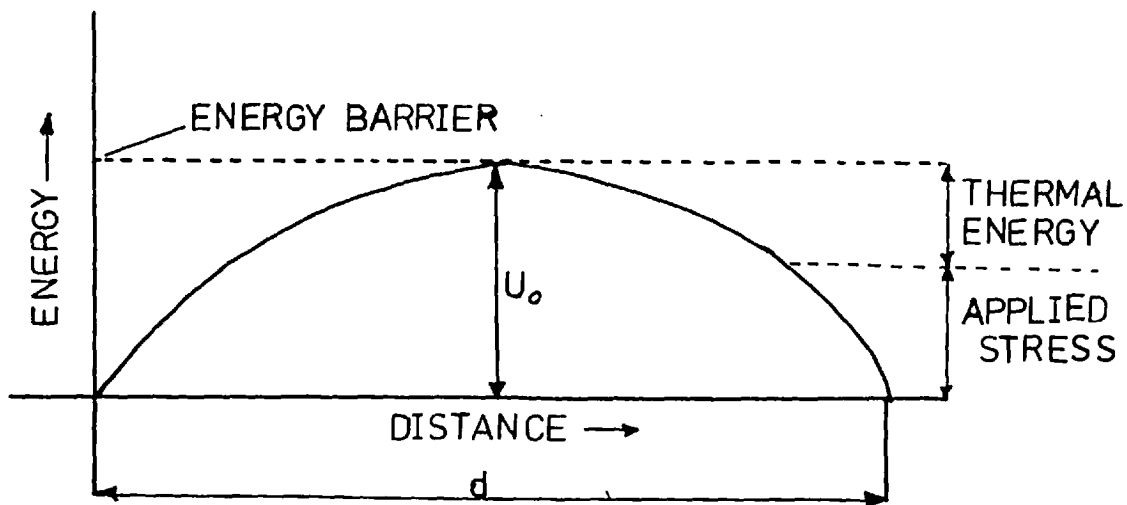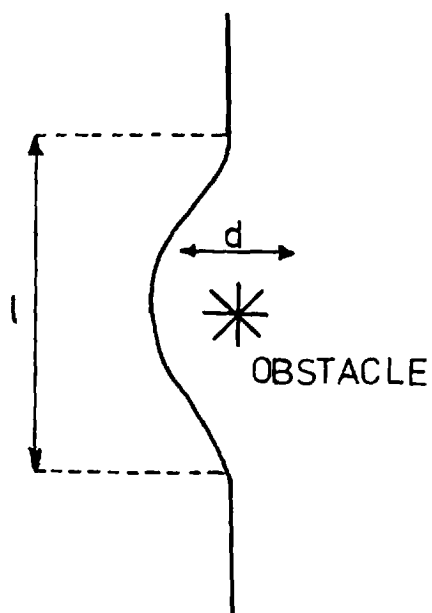
FIG. 26   Schematic representation of obstacle to dislocation
movement as an energy barrier
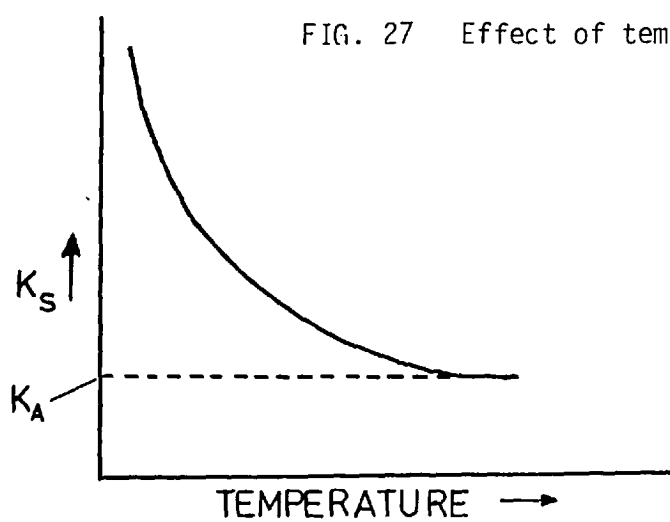
FIG. 27   Effect of temperature on flow stress

Therefore

$$\text{Velocity} = \nu_o \ \exp(-\tfrac{u}{KT}) \times D \qquad\qquad (63)$$

where:- ν_o = frequency of attempts to overcome obstacles

$\exp(-\tfrac{u}{KT})$ = fraction of successful attempts

D = distance apart of obstacles

Hence $\qquad \dot{\varepsilon} = \rho \ \underline{b} \ D \ \nu_o \ \exp(-\tfrac{u}{KT}) \qquad\qquad (64)$

Now $\qquad u = u_o - (K_s - K_A)V \qquad\qquad (65)$

Therefore $\dot{\varepsilon} = D \rho \ \underline{b} \ \nu_o \ \exp\left[\dfrac{V(K_s - K_A)}{KT}\right] \exp(-\dfrac{u_o}{KT}) \quad (66)$

Let $\qquad D \rho \ \underline{b} \ \nu_o = \dot{\varepsilon}_o$

Therefore $K_s = \dfrac{u_o - KT \ \ln(\dot{\varepsilon}_o/\varepsilon)}{V} + K_A \qquad\qquad (67)$

Fig. 27 shows the form of this relationship schematically.

3.9.1 Temperature change during extrusion

During extrusion the billet temperature is usually raised by the work done upon it. (Except for very high initial temperatures and slow ram speeds). It is estimated that 90% of this work is converted to heat energy. Heat flow from the billet to the container, tools and ram also occurs. A mean temperature of the billet may be predicted at any time after the beginning of extrusion by use of an integral profile method proposed by Sheppard and Raybould [34], assuming an initial uniformity of temperature between billet and container. However, if the initial billet temperature is different from that of the container the theory must be modified. Given below is the modified solution proposed by Sheppard and Wood [128].

The first step involves introducing a control volume around the deformation zone and equating the heat leaving this zone to the work put into it. Since the billet is also losing heat to the container outside this area, a second control volume may be used to include this heat loss in the overall volume equation. It is assumed that there is no conduction from control volume 1 to control volume 2 (see fig. 28). This is reasonable as the temperature gradient between them is small due to the high conductivity of aluminium. Back conduction into the pressure pad is considered. The heat flows are shown in (Fig. 28) and assuming 90% conversion of work done into heat we may write:-

$$0.9 \times L \times V \, t = Q_1 + Q_2 + Q_3 + Q_4 + Q_5 + Q_6 + Q_7$$

$$(68)$$

The interface temperature between deforming stock and tools is calculated in the usual way:-

$$\frac{T_B - T_I}{T_I - T_S} = \sqrt{\frac{K_S \, \rho_S C_A}{K_A \, \rho_A C_S}} \qquad (69)$$

Thus the temperature of the deformation zone is $T_B + \Delta T$ and the temperature differential $T_I - T_S$ is designated ΔT_D whilst in the deformation zone the temperature differential is $\Delta T + \Delta T_D$ designated ΔT^*. Q_1 to Q_7 cannot be estimated until the time/temperature profiles in the container, tools and billet have been estimated. The temperature profile around a heat source may be expressed:-

$$T(x,t) = a_o + a_1 x + a_2 x^2$$

where $T(x,t)$ is the (temperature - datum temperature) at a point a distance x from the source at a time t. The constants a_o, a_1, a_2 may be found by consideration
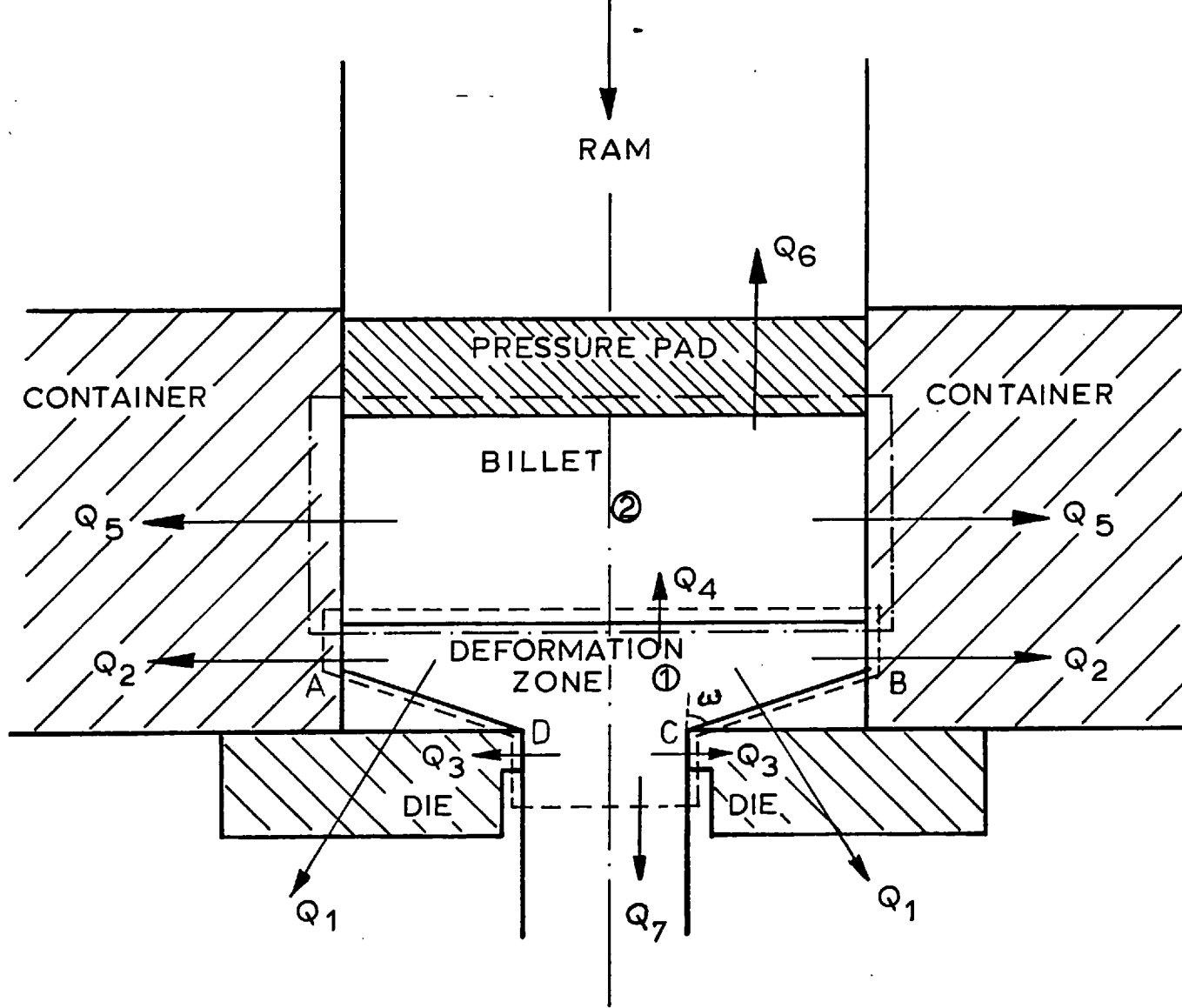
FIG. 28 Control volumes and heat losses employed in integral
profile temperature rise model

of the boundary conditions.

at $x = 0$ $\Delta T(x,t) = \Delta T^*$ and $a_o = \Delta T^*$

At distance s, the maximum penetration of the heat front:-

$$\Delta T(x,t) = 0$$

and $\dfrac{d\Delta T(x,t)}{dt} = 0$

hence $a_1 = -2a_2 s$

and $a_2 = \dfrac{\Delta T^*}{s^2}$

$$a_1 = -\dfrac{2\Delta T^*}{s}$$

$$\Delta T(x,t) = \Delta T^* - \dfrac{2\,\Delta T^*}{s}\,x + \dfrac{\Delta T^*}{s^2}\,x^2 = \Delta T^*(1 - \dfrac{x}{s})^2 \qquad (70)$$

If heat flows only in the x direction then the heat accumulated may be written:-

$$Q_{acc} = \int_0^s A\,C\rho\,\Delta T^*\,(1 - \dfrac{x}{s})^2\,dx$$

$$= A\,C\rho\,\Delta T^*\,\dfrac{s}{3} \qquad (71)$$

Hence $Q_{acc/sec} = \dfrac{A\,C\rho\,\Delta T^*}{3}\quad \dfrac{ds}{dt} \qquad (72)$

From the Fourier equation:-

$$\dfrac{dQ}{dt} = -KA\,\dfrac{dT}{dx} = -KA\left[\dfrac{d\Delta T(x,t)}{dx}\right]_{x=0} \qquad (73)$$

Equating (72) and (73) gives:- $\quad s = \sqrt{\dfrac{12kt}{\rho C}}$ $\qquad$ (74)

which will be valid where the contact area A does not vary with x.

For Q_2, Q_3 and Q_5, A will vary with x and

$$Q_{acc} = \int_{o}^{s} 2\pi \quad \ell \rho C\Delta T^* \left(1 - \frac{x}{s}\right)^2 dx$$

$$= \frac{\pi \, 1 \, \rho C\Delta T^* \, s^2}{6} \qquad (75)$$

Proceeding as before

$$\frac{dQ}{dt} = \frac{\pi \, 1 \, \rho C\Delta T^* s}{3} \frac{ds}{dt}$$

and

$$s = \sqrt[3]{\frac{18kAt}{\pi \rho 1 \, C}} \qquad (76)$$

The heat losses from each control volume may now be calculated

Q1 The surface contact area of the cone A B C D

$$= \frac{\pi}{\cos\omega}\left\{\frac{D_B^2 - D_E^2}{4}\right\}$$

hence $Q_1 = \Delta T^* \dfrac{\pi(D_B^2 - D_E^2)}{\cos\omega} \left(\dfrac{K_s \rho_s C_s}{12}\right)^{\frac{1}{2}} t^{\frac{1}{2}}$ $\qquad$ (77)

Q2 The depth of the zone of working is approximately:-

$$\left(\frac{D_B - D_E}{2}\right) \tan 45°$$

hence $l_D = \left(\dfrac{D_B - D_E}{2}\right)(1 - \tan\omega)$

ω being obtained from an upper bound solution.

The heat accumulated in the radial direction is given by (75) which assumes the heat source to be at the centre of a large cylinder. In fact the heat source is distance R_B from the billet centre. Hence

$$Q_{acc} = \frac{\pi}{6} l_D \, \rho C \, \Delta T^* \, (R_B + s)^2$$

which includes the heat stored in the material. Hence heat loss is given by:-

$$Q_2 = \frac{\pi}{6} \Delta T^* l_D \left[\{ 18 K_s \, D_B (\rho_s C_s)^{\frac{1}{2}} t \}^{\frac{2}{3}} \right.$$

$$\left. + \{ 18 \, K_s D_B^{\,4} (\rho_s C_s)^2 t \}^{\frac{1}{3}} \right] \qquad (78)$$

Similarly

$$Q_3 = \frac{\pi}{6} \Delta T^* l_1 \left[\{ 18 K_s D_E (\rho_s C_s)^{\frac{1}{2}} \}^{\frac{2}{3}} \right.$$

$$\left. + \, 18 K_s D_E^{\,4} (\rho_s C_s)^2 t \}^{\frac{1}{2}} \right] \qquad (79)$$

The heat losses due to back conduction Q_4 from volume 1 will be ignored. Tanner and Johnson[44] have justified this assumption and shown the losses to be negligible for normal ram speeds. The heat loss Q_6 will be significant when the ram approaches the deformation zone area. Following a similar derivation to that used to find Q_1 we may write:

$$\text{Surface area of contact } A = \frac{\pi D_B^{\,2}}{4}$$

$$Q_6 = \Delta T_D \, \pi D_B^{\,2} \, \lceil \frac{K_s \rho_s C_s}{12} \rceil^{\frac{1}{2}} \, t^{\frac{1}{2}} \qquad (80)$$

Q5

If the length l_T is the depth of control volume 2 in (Fig. 28) then l_T at any time Δt after start of extrusion will be

$$l_T - V \ \Delta t$$

and Q_5 may be written:-

$$Q_5 = \frac{\pi \Delta T_D}{6} \left[\{18K_s \ D_B \ l_T^{3/2} (\rho_s C_s)^{\frac{1}{2}}\}^{\frac{2}{3}} \{t^{\frac{2}{3}} - \frac{3V \ t^{5/3}}{5 l_T}\} \right.$$

$$\left. + \{18K_s \ D_B^4 \ l_T^3 (\rho_s C_s)^2\}^{\frac{1}{3}} \{t^{\frac{1}{3}} - \frac{3V \ t^{4/3}}{4 l_T}\} \right] \quad (81)$$

The heat loss Q_7 is straight forward and may be expressed:-

$$Q_7 = \Delta T \ \rho_{AL} C_{AL} \ RV \ t \ \frac{\pi D_E^2}{4} \quad (82)$$

hence
$$Q_1 = (\Delta T + \Delta T_D)(K_1 t^{\frac{1}{2}})$$

$$Q_2 = (\Delta T + \Delta T_D)(K_2 t^{\frac{2}{3}} + K_3 t^{\frac{1}{3}})$$

$$Q_3 = (\Delta T + \Delta T_D)(K_4 t^{\frac{2}{3}} + K_s t^{\frac{1}{3}})$$

$$Q_4 = 0$$

$$Q_5 = \Delta T_D \ K_6 t^{2/3} + K_1 t^{5/3} + K_3 t^{\frac{1}{3}} + K_9 \ t^{4/3}$$

$$Q_6 = \Delta T_D \ K_{10} \ t^{\frac{1}{2}}$$

$$Q_7 = \Delta T \ K_{11} t$$

Hence work done =

$$\Delta T \{ A_1 t^{\frac{1}{2}} + A_2 t^{\frac{1}{3}} + A_3 t^{\frac{2}{3}} + A_4 t \} + \Delta T_D \{ B_1 t^{\frac{1}{2}} + B_2 t^{\frac{1}{3}} + B_3 t^{\frac{2}{3}}$$

$$+ B_4 t^{4/3} + B_5 t^{5/3} \} \qquad (83)$$

Work done = $\Delta T \; C_1 (\text{Total}) + \Delta T_D \; C_2 (\text{Total})$

Hence temperature rise of extrude:-

$$\Delta T = \frac{0.9 \times L \times V \; t \qquad - \Delta T_D \; C_2 \{t\}}{C_1 \{t\}} \qquad (84)$$

The program given in appendix (4) uses this method to calculate the temperature change

3.10.1 Torsion testing

Generally, torsion tests are carried out to gain information about the flow stress of a material at various temperatures and strain rates. The equation most commonly used to obtain flow stress information from torsion data was first proposed by Nadai[105] :-

$$\tau = \frac{1}{2\pi a^3} (3M + \Theta \frac{dM}{d\Theta}) \qquad (85)$$

where τ = surface shear stress

M = torque

Θ = amount of twist

a = specimen radius

$\dfrac{dM}{d\Theta}$ = slope of torque—twist curve.

The shortcoming of this equation is that it assumes
the stress is not dependent upon the strain rate. This
may be acceptable for some materials which are virtually
strain rate insensitive but it is unacceptable for
aluminium and its alloys which show a marked strain
rate sensitivity. Fields and Backofen[106] suggested a
modified equation to incorporate strain rate effects:-

$$\tau = \frac{M}{2\pi a^3} (3 + n + m) \tag{86}$$

where:- n = the gradient of $\ln M$ v. $\ln \Theta$ at const.
           strain rate

        m = the gradient of $\ln M$ v. $\ln \dot{\Theta}$ at const. Θ
           ($\dot{\Theta}$ = rate of twisting).

The use of this equation permits the calculation of the
flow stress from the results of the minimum number of
torsion tests and removes the need for differential
torsion testing (i.e. the testing of specimens of
different diameter).

CHAPTER 4

EXPERIMENTAL PROCEDURE

4.1.1. <u>Introduction</u>

The following chapter describes the experimental methods used to :-

(1) Examine the starting materials.

(2) Prepare composites by extrusion.

(3) Monitor process conditions.

(4) Prepare specimens for testing and examination.

(5) Measure mechanical properties.

(6) Examine the extrude structure microscopically.

4.2.1. <u>Metal Powder Production</u>

The metal powders used in this research project were produced by one of two methods :-

(1) Air atomization. (horizontal air blast)
    (Aluminium Powder Co)

(2) Water atomization. (horizontal water jet)
    (Davy-Lowe Ltd.)

In both cases the feedstock to the atomizer furnaces was prealloyed cast ingots. The HE9 and HE30 were produced by the former method whereas the Al-Mg and Al powders were produced by water atomization in an attempt to increase the oxygen content. It was hoped that the increased oxygen content would improve the extrude mechanical properties.

4.2.2. Glass Powder Production

The glass used for reinforcement throughout this project was of nominal composition :-

$$B_2O_3 - 10\% \ SiO_2$$
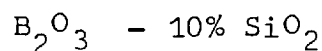
This particular glass was selected for three main reasons :-

(1) B_2O_3 has a low softening point which is much less than the temperatures obtained when extruding Aluminium or Aluminium Alloys. It is thus viscous at hot working temperatures.

(2) B_2O_3 forms a good bond with aluminium during extrusion. This is an essential feature, necessary to ensure that the fibres do not "pull-out" of the matrix when a load is applied to the composite.

(3) B_2O_3 with 10% SiO_2 is a glass with good mechanical properties. This is a necessity if a strong composite is to be produced.

The glass was manufactured at the Borax Research Laboratories. It was prepared by roller mixing carefully weighed amounts of the constituent oxides which were fused in fireclay crucibles and poured into steel mounds. The product was then crushed, ground and sieved to produce a glass powder.

4.2.3. Powder Size

There are a number of techniques available for the determination of the particle size distribution of a quantity of powder. The simplest technique is that of sieving. The end-point of a sieve test is specified[129] as either :-

(a) The end of a fixed time period.

or (b) The time at which the rate of particle
passage through a sieve has reached a
specified value.

Technique (a) was used to simplify matters as much as
possible. Powder samples were taken from each drum
after the contents had been thoroughly mixed by
rolling.

The sieving was carried out on . conventional
0.2M diameter B.S. wire mesh sieves. A weighed amount
(0.15 - 0.2 Kg) of the powder (glass or metal) was
placed on the uppermost of a stack of sieves. The
stack was then placed on an "Endrock" mechanical
sieve shaker. The sieving was then carried out by a
mechanical vibratory and rotary motion for one hour and
the separate fractions collected and weighed. Particles
trapped on a particular sieve were assumed to have a mean
size between that of the catching sieve and the one
before. In reality a wide range of sizes in between
these two mesh sizes existed.

4.2.4. Powder Shape and Structure

The shapes of the individual powder particles
within the powder mass were investigated using a
Cambridge stereoscan 600 scanning electron microscope.
Particles were distributed on small aluminium stubs
which had previously been painted with an electrically
conducting paint (silver Dag). The stubs were then placed
in the column of the microscope and the column evacuated.
The surfaces of the stubs were scanned at magnifications
ranging from 50 to 5000 times.

To investigate the powder structures, powder
particles were mounted in "met-set". The specimens
were then ground on silicon carbide paper and polished
with diamond paste and alumina powder (down to 0.05μ).
Finally the specimens were cleaned and then etched
in Keller's reagent. A Vickers' light microscope

was used to examine the specimens at magnifications of up to 400 times.

4.2.5. Chemical Analysis

The analysis of the atomised powder was carried out by the "analytical services" department within the College. They employed infra-red spectrophotometry on compacted powder pellets. A wet chemical analysis was also used to determine the magnesium content of the Al-Mg alloy.

4.3.1. Mixing and Compaction of Billets

Carefully weighed amounts of metal and glass powder were poured into screw-topped containers which were then rolled for two hours to ensure thorough mixing. The glass content of the billets was varied between 0 and 20 wt.%.

The process of cold compaction was carried out in a 0.075m diameter ram and die set made from boronised heat treated KEA 145 steel. The compaction set was designed so that the ram was the same length as the die to facilitate compact ejection. The ram was machined down to a push fit tolerance to ensure that little powder forced its way up between the ram and die during the compaction. Before the die was filled with powder, the walls and tool pieces were painted with a solution of stearic acid in chloroform to act as a lubricant. This ensured little pickup of aluminium on the tooling surfaces. Having filled the container with a weighed amount of powder,(0.77Kg), compaction was carried out using a "Tangye" 2MN (200 TON) press to a pressure of 14 MN/m^2. This gave a billet of 80-90 % theoretical density (depending on the alloy and glass content) of height 0.09m.

4.3.2. Strength of the Compacted Billet

The strength of the compacted billet was

investigated to discover if the billet was strong enough to withstand fairly rough handling on the factory floor prior to extrusion. This "post-compaction" billet strength was deemed important if the process was to be commercially viable.

These tests were carried out in the Borax Research Laboratories. In all cases the billets tested were $HE9$ alloy plus 10wt% of $B_2O_3 - S_1O_2$. The billets were compacted in a 0.0445 M long X0.0254 M diameter ram and die set, each billet weighing 0.05 Kg. These dimensions ensured that the shape factor of the billet was the same as that of the larger extrusion billet.

In theory it had been intended to study the toughness i.e. notch ductility, of the billets. Unfortunately as no impact testing equipment was available, at the time, the true toughness was not measured. From experience the billets were known to be most likely to shatter transversely, and so it was decided that the billets should be loaded transversely.

This applied load was increased gradually and continuously from zero. The experimental set up is shown in Fig.29. The billets were supported by two 45° "V" blocks with a 0.02 M gap between them. The load was applied by means of a "knife edge" (in fact of finite radius) to the middle of the billet. The load was produced by a sand crushing machine.

As the area of contact between block and billet was unknown, the actual fracture pressures were unknown. What was obtained was a comparison of the "relative" strengths of billets compacted at pressures ranging from 185 to $465MN/m^2$. The theoretical densities were found by measuring the weights and volumes of the billets and assuming a 100% density of 2580 Kg/m^3. The effect of sintering the billets after compaction at temperatures ranging from 150-450°C was also

FIG. 29 Apparatus used to determine compact strength
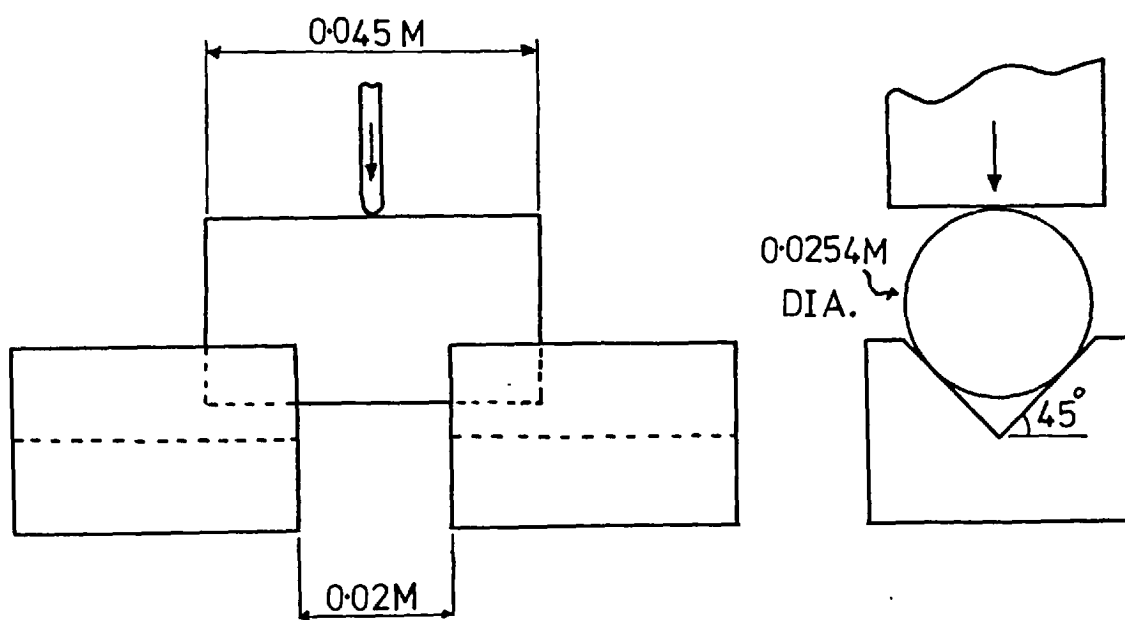
investigated. Billets compacted from different sieve fractions were also tested to find the effect of powder particle size on compact strength.

4.4.1. The Extrusion Press

The extrusion press used was a 5MN, vertically mounted, fast action ENEFCO press. It was situated over a run out pit thus permitting direct extrusion with the die fixed in position above the pit by a backing ring. The press layout is shown in plate 1 with operating controls on the right beneath the load indicating dial and oil pressure gauges.

The container, fixed onto two hydraulic rams via a cast housing, plate 2, was capable of accommodating billets of up to 0.075 m in diameter and 0.158 m in length.

An auxilliary pump enabled the ram approach speed prior to the commencement of extrusion to be increased greatly. This reduced the heat lost by the billet to its surroundings whilst the ram was being lowered to touch the pressure pad. Once the load exceeded 0.2 MN this pump "cut out" and the ram moved at the pre-set ram speed during the extrusion.

4.4.2. The Heaters

The container was heated by eight inconel heating elements placed around it and held in position inside the container holder casting. These heaters, with a total rating of 12 kilo-watts, had a maximum operational temperature of $700^{\circ}C$. To prevent overheating of the elements thermocouples, attached to eurotherm controllers, were braised onto each element. With the elements operating near their maximum temperatures the temperature of the container liner was maintained at $300^{\circ}C$.

4.4.3. Lubrication

Previously Chare[19] showed the use of graphite

PLATE 1

General layout of the extrusion press
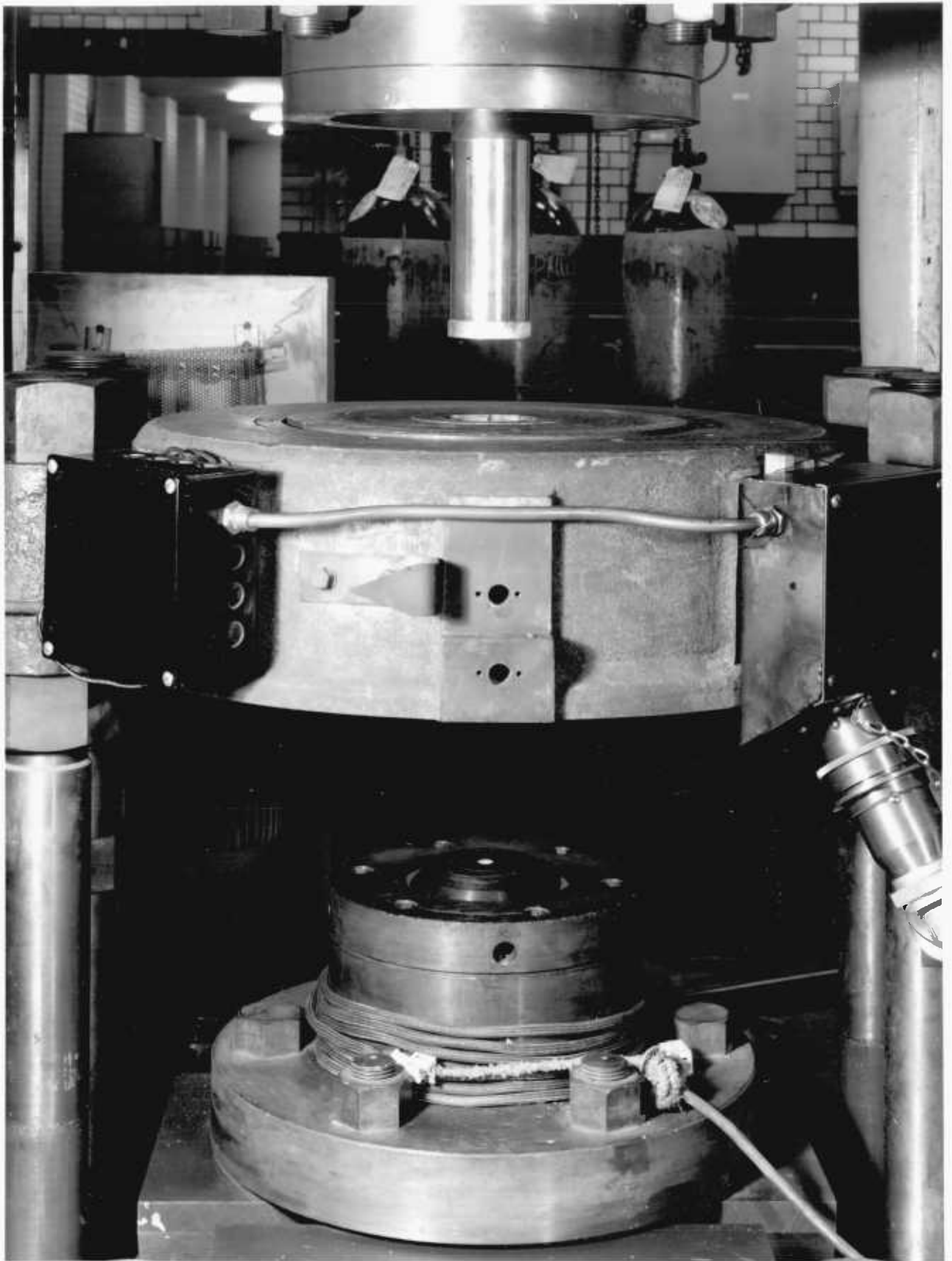
PLATE 2

Container, ram and die on extrusion press.

as a lubricant for powdered aluminium alloy extrusion
to be unsuccessful, producing a severe fir tree
defect due to excessive die pick up and friction. He
achieved satisfactory results using circular pads of
Aluminium 0.01m thick and 0.073m in diameter placed in
front of the billet before extrusion. These pads formed
dead metal zones for the powder billets and also
covered the extrudes with "sheaths" of solid material
during passage through the deformation zone and die.

In the present series of experiments a 0.01m thick pad
of solid HE9 of 0.073m diameter was used for each of the
HE9 powder extrusions and a similar pad of HE30 was
used for each of the remaining HE30, Al–Mg and Al powder
extrusions. In the case of composite extrusions the
sheath produced by the pad was of even greater
importance in that it protected the glass fibres from
the atmosphere and prevented hydrolysis from occurring.

4.4.4. Billet Preheat

The preheating of the billets to the desired
extrusion temperature was performed in an air circulating
furnace situated adjacent to the press. Temperatures in
the range 250 – 600° C were investigated. The furnace
was calibrated by means of a billet, drilled axially
to the centre, containing a thermocouple which was
connected to a digital voltmeter. The furnace temperature
control was set at various temperatures in the range
mentioned above and the furnace allowed to attain
these temperatures. The billet containing the thermocouple
was then placed in the furnace for 40 minutes and then
the D.V.M. reading was noted and converted to the true
billet temperature.

It was necessary for the heat losses, during the
transfer of the billet from the air circulating
furnace to the container, to be measured. The billet
containing the thermocouple was removed from the
furnace (at different temperatures) and transferred

to the container whilst a series of D.V.M. readings at
measured time intervals were noted. This gave cooling
curves for pre-heat temperatures. These curves are
shown in appendix (5).

Attempts to preheat billets in an induction
furnace situated above the press container proved
futile due to the voids and the high oxide content
of the compacted billets.

4.4.5. Reduction Ratio

The reduction ratios used in this series of
experiments were 5, 10, 30, 40, 60, 80 and 180:1.
These ratios were obtained by using interchangeable
dies in the die holder. Fig 30   shows the die
design used throughout. The die, held in place by the
holder and the retainer ring, is shown in Plate 2.

Changing the die involved the removal of the
retaining ring, which was held in place by 6 bolts,
followed by the removal of the die holder leaving the
die piece and backing ring. The new die was then
placed on the backing ring and the holder and the
retaining ring replaced.

4.4.6. Ram Speed

The ram speed was controlled by the adjustment
of the pumps to give a range of extrusion speeds varying
from 0.003 m/sec to 0.013 m/sec by contra flow direct
pumping. Higher speeds, of the order of 0.1 - 0.2 m/sec
were obtained by using the accumulator drive i.e.
discharging nitrogen filled pressure bottles. The speed
was measured by a rectilinear potentiometer with a 0.6m
stroke which was fixed between the cross head and the
base of the press. The voltage, which varied with ram
position, was fed into a Hewlett Packard 136A x-y recorder
and plotted against time, the slope of the line on the
chart giving the average ram speed.

FIG. 30   Extrusion die
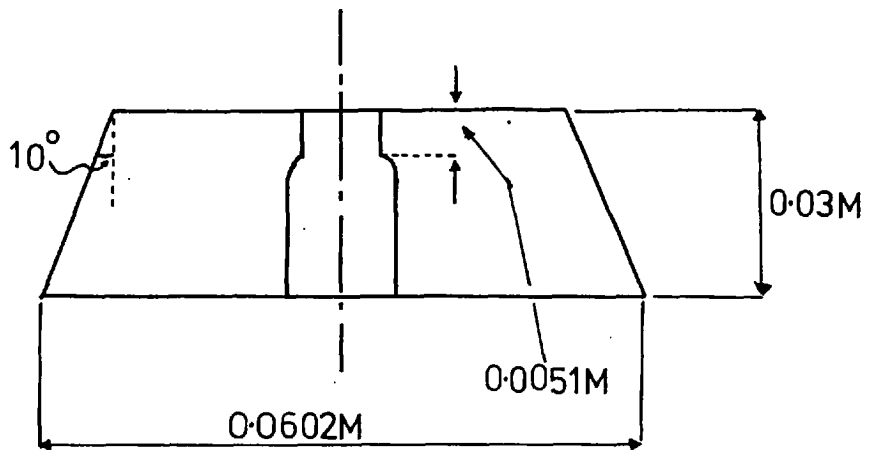
FIG. 31   Locations of samples taken from an extrude
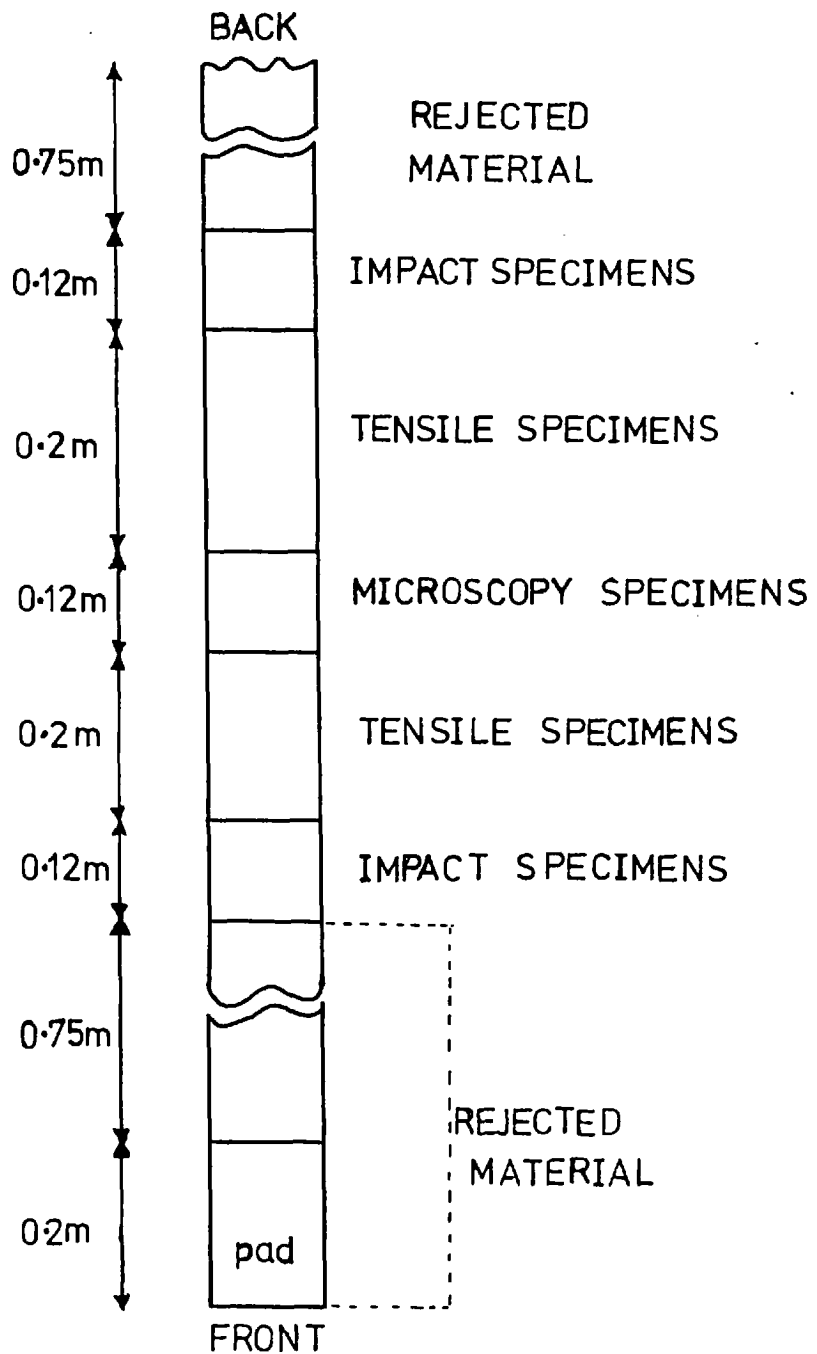
4.4.7. Extrusion Load

The extrusion load was measured by a Mayes load
cell situated directly above the ram stem. The output
was indicated on the dial gauge and recorded on the
X-Y recorder. The X-Y recorder pen speed was fixed
thus enabling a load/displacement curve to be drawn.

4.4.8. Extrusion Procedure

The billet with a pad taped on top was heated
in the air circulating furnace for 40 minutes at the
desired temperature. The billet was then removed
from the furnace with tongs, inverted so that the pad
sat directly on top of the die and then dropped into
the container. A pressure pad to prevent "skulling"
around the ram was placed behind the billet and the
extrusion initiated. The ram was lowered quickly via tne
fast approach mechanism until it reached the back of
the billet and the load reached 0.2MN. The fast
approach motor then cut out automatically and the ram
continued at the pre-set, desired speed. The load
and ram displacement were recorded on the X-Y recorder.
The extrusion was stopped when the ram made contact
with two protective steel ring segments placed on
top of the container. The stem was then raised and the
container lifted. The extrude was sawn through just
above the die. Then, with the discard and pressure
pad left in the container, the extruded rod was
punched out of the die into the pit below. The container
was then lowered onto two liner supports, placed on
the die holder, and the discard and pressure pad pushed
out by the ram, using a dummy stem. A scraper pad,
having an interference fit with the liner, was then
pushed through the container to clean the surface
of the liner. This insured a fairly uniform liner
surface condition for each extrusion and thus fairly
uniform friction conditions.

4.4.9. Heat Treatment

As both HE9 and HE30 are classical precipitation hardening alloys, the precipitate in question being Mg_2Si, the effect of heat treatments on the extruded rod was of some interest. Specimens cut from the extruded rod were soaked in the air circulating furnace at temperatures ranging from 500-580°C for times of 1 to 20 hours. The specimens were then quenched in water and aged at temperatures ranging from 160 to 195°C for times of 1 to 20 hours.

Some extrusions were subjected to a press quench followed by an ageing treatment to see if the preheat given to the powder billet had homogenised and dissolved the Mg_2Si phase.

4.5.1. Product Properties

Specimens for mechanical testing and for optical and electron microscopy were cut from each extrude. In each case these specimens were taken from the central region for the sake of consistency (see Fig 31) The central portion was taken because the beginning of each extrude contained pad material followed by a short length of "improperly" consolidated material and the end of each extrude might have suffered from "back-end" defect.

4.5.2. Hardness Tests

These tests were carried out on the mounted specimens used for optical microscopy. A standard Vickers hardness machine was employed using a load of 2.5 Kg. Hardness traverses across the section of the extrude were performed. A sectioned, partially extruded billet was also traversed longitudially through the deformation zone to find if there was any correlation between hardness and the extent of consolidation down through the deformation zone.

4.5.3. Tensile Tests

These tests were carried out using No.12
Hounsfield specimens on an Instron Universal Testing
Machine. During each test the cross head speed remained
constant. The approximate strain rate was calculated
from the constant cross head speed and the initial
specimen length. (Initial length ≈ length when plastic flow
commences). Tests were performed at strain rates varying
from 0.0005 - 0.02 sec^{-1}, the limiting strain rates
produced by the available cross head speeds.

Tests were also performed at temperatures
ranging from room temperature to 400°C. For the high
temperature tests the specimens and the nimonic rods
attached to the cross head were surrounded by a split
furnace. A thermocouple placed close to the tensile
specimen controlled the heating operation. When the
required temperature was reached, the specimen was
maintained at this temperature for ten minutes to attain
thermal equilibrium before commencing the test. In
each case two specimens were tested under each set of
conditions and the results averaged. (The small diameter
of the 180:1 extrude precluded the manufacture of
specimens for this particular extrusion ratio).

4.5.4. Impact Tests

Impact tests on notched specimens were carried
out using a Hounsfield balanced impact machine. The
notch cross-section, method of supporting the specimen
and direction of delivery of the blow were the same
as in the standard Izod impact test, but specimen
size and shape were different (0.008 mm dia. bar
0.0445m long, compared with 0.01m square bar 0.075m long
for an Izod specimen). The energy reading given by
this machine was multiplied by a factor of 2.4 in
order to obtain the corresponding Izod value.

4.5.5. Torsion Tests

Specimens for torsion testing were taken from extrudes of extrusion ratio 5:1 and 10:1. Plate 3 shows the torsion specimen used in these tests. The gauge length and diameter were such that the maximum strain rate attainable in the torsion machine, having a maximum motor speed of 1000 r.p.m., was 50 s^{-1}.

$$\text{Strain Rate} = \frac{2\pi rn}{L}$$

where r = specimen radius

L = specimen length

n = revs/sec

This was desirable as typical extrusion strain rates employed were of the order of 10-50 s^{-1}. The short gauge length used also increased the homogeneity of deformation during the test. The specimens were heated in situ by an induction heater with the temperature controlled by a thermocouple in the fixed end connected to a eurotherm. Specimens were tested at various temperatures between 250-500°C and at various strain rates from 0.5 - 50s^{-1}. After testing to failure, the specimen, enclosed in a sliding, sealed container, was quenched with a water jet to achieve rapid cooling. The torque was measured by a lever arm operating a load cell, the output being fed into a U.V. recorder. A calibration curve of torque versus deflection, was obtained by hanging a known weight on a rod, connected to the load cell, at known distances from the centre of the driving shaft and reading the U.V. deflections. The calibration curve is shown in appendix 6.

4.6.1. Optical Microscopy

Both longitudinal and transverse specimens were cut from the extrudes for examination. These were mounted in slow setting (24 hrs) met. set. This mounting fluid was used as it undergoes no exothermic reaction on

R = 0.5

20°

1·5 ⌀

17·5 max

3·0 ⌀

9/16" BSF

20·1
19·9

5/8" Flats

10·02
9·98

35·0
34·0

5·1
4·9

65 ± 0·2

12·5
12·4
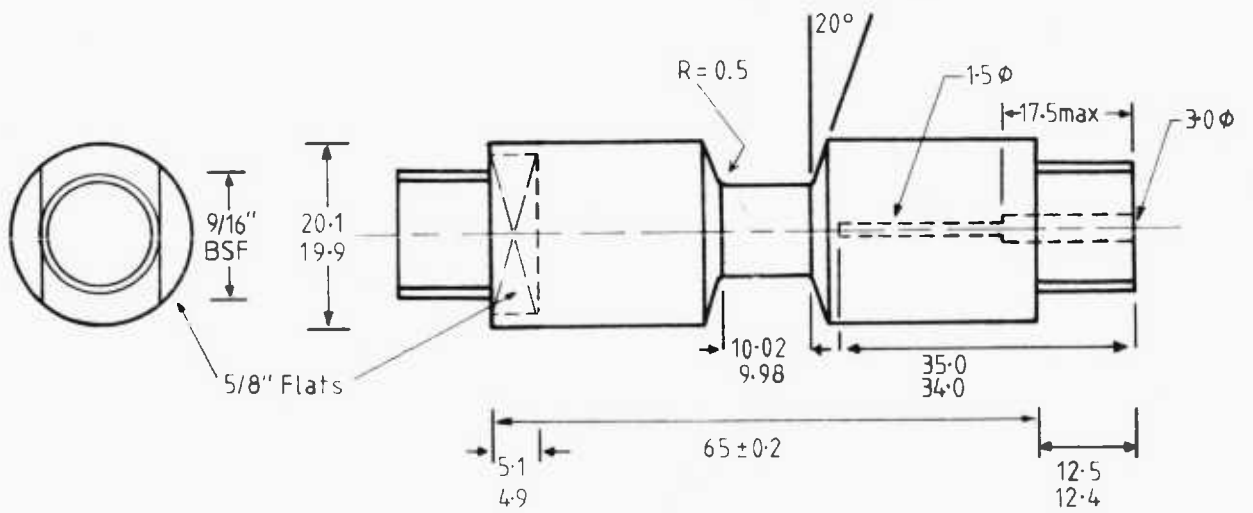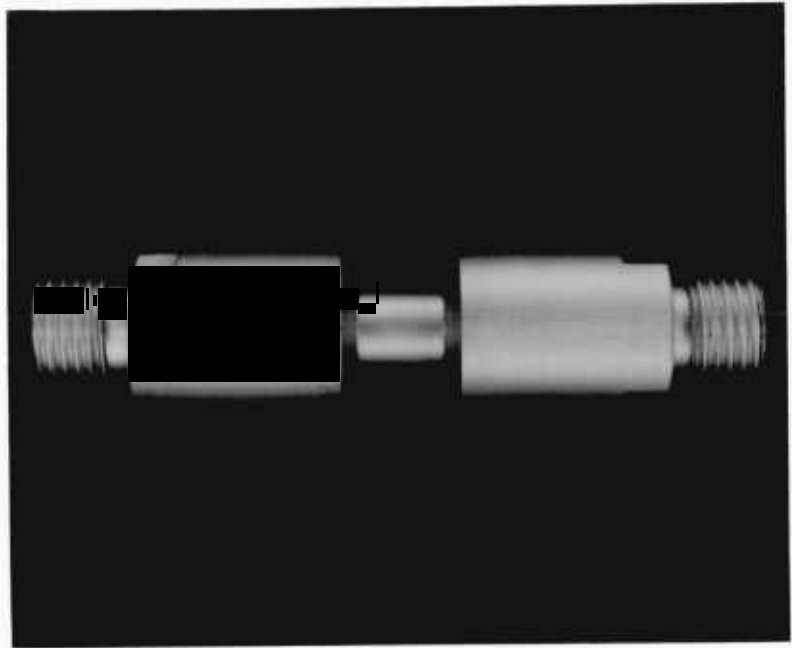
PLATE 3   Torsion Specimen

hardening. The specimens were then ground on silicon
carbide paper, polished on a brasso wheel and then
finished off on a vibromet automatic polisher containing
a slurry of 0.3μ alumina in distilled water.

The polished specimens of composite material
required no etching before examination under the
optical microscope. The specimens containing no glass
were etched in the usual Aluminium alloy etches ie.
Keller's reagent, Tuckers' reagent and 0.5% HF to show
the Mg_2Si precipitates.

4.6.2. Transmission Electron Microscopy

Longitudinal and transverse specimens were cut
from the extrudes using a fine piercing saw to avoid
too much heat generation. The specimens were then
ground on silicon carbide paper, using a steel
grinding block, to a thickness of 0.0001m. A standard
"window" technique was then employed to thin the
specimens down to foil thickness. A solution of 30%
Nitric Acid in methanol was used for the electro-
polishing. A potential difference of 15V and a temperature
of not greater than $-30^{\circ}C$ were found to give the best
results. A solution of perchloric acid, ethanol
and glycerol was also tried under different conditions
of temperature and potential differnece, and proved
to be unsatisfactory.

The reinforced specimens proved impossible
to thin properly as the holes left by the fibres
caused the foils to disintegrate. The unreinforced
HE9, HE30 and Al-Mg specimens thinned reasonably well
although some difficulty was experienced with the Al-Mg
specimens. The Al specimens were extremely difficult
to thin, probably due to their high oxide content.

The transmission microscopy was carried out on an
AEI EM6 100 Kv electron microscope fitted with a
tilting stage.

4.6.3. Scanning Electron Microscopy

As the type of fracture of the tensile specimens
was considered to be important, it was decided to
examine the fracture surfaces under the scanning
microscope. The fractured end of each tensile specimen
was sawn off and mounted upon an aluminium stub
with araldite. A spot of electrically conducting paint
(silver dag) was then used to prevent the specimen from
electrically charging up. The stub was then inserted
in the microscope and the fracture surface examined
as described in 4.2.4.

4.6.4. Partially Extruded Billets

Several extrusions under different conditions
were stopped after the "steady state" region of the
load-time graph had been reached. These partial billets
were then pushed out, sectioned, polished and etched
in an attempt to observe the flow pattern. However, it
was found that due to the very fine initial powder
particle size no flow pattern could be easily
distinguished.

To overcome this difficulty several powder
billets containing copper discs placed 0.01m apart
in the compaction die were compacted and partially
extruded. These billets, when sectioned and polished,
gave a much better representation of the flow pattern
existing during extrusion. One partial extrusion of a
composite billet containing no copper strips was
examined after sectioning and polishing. Etching
was unnecessary and the formation of the fibres through
the deformation zone was clearly visible.

Several partially extruded billets were sectioned
and a 0.0015m thick slice machined from one half of
each for preparation of electron microscope foils.

CHAPTER 5

RESULTS AND DISCUSSION

5.1.1 <u>Sieve analysis of metal powders</u>

The sieve analyses for the HE9, HE30, Al-Mg and
Al powders are given in tables 1-4 (see end of chapter
for tables), together with the median particle sizes.
The figures shown represent, on average, the results of
six sieving operations. As the particle size distribution
has such a marked effect on the subsequent extrude
structure and properties, a knowledge of this distribution
is vital. It must also be remembered that a meaningful
comparison of results with those obtained by other workers
in the powder metallurgy field is possible only if the
size distribution for each powder used is available.

5.1.2 <u>Sieve analysis of glass powder</u>

The sieve figures for the B_2O_3-10% SiO_2 glass powder
used throughout the investigation are given in table 5.
The median particle size of the glass is much smaller
than that of the metals (74μ compared to 110-150μ). This
is advantageous as smaller glass particles have a greater
tendency to elongate without fracturing in the deformation
zone during extrusion.

5.1.3 <u>Chemical analysis</u>

The chemical analyses of the metal powders are
given in table 6. The most surprising feature is the
large difference in oxygen content between the Al-Mg and
Al powders, both of which were produced by water atomi-
zation. Considerable differences must have existed in
the atomizing conditions to produce this effect. From
the sieve figures given in tables 3 and 4 it is evident
that the Al powder is somewhat coarser. Now as smaller
particles cool faster it is reasonable to assume that the
longer "flight path" of the larger Al particles, during

the atomization process, allows a greater amount of
oxidation to occur. i.e. the larger particles cool
more slowly and therefore enjoy a greater time at
temperatures which permit oxidation. It should also
be remembered that smaller particles have a greater
surface area: volume ratio (i.e. $4\pi r^2/\frac{4}{3}\pi r^3$ ↑ as r ↓)
and therefore have more surface area available for
oxidation. Clearly, from the figures in table 6, the
surface area consideration is far out-weighed by the
cooling rate effects causing the Al powder oxide content
to be far larger than that of the Al-Mg. The higher
melting point of the Al ($60^{\circ}C$ higher than that of Al-
3 wt.% Mg) may also have necessitated a higher atomi-
zation temperature, leading to even greater oxidation.

5.1.4 Shape of powder particles

The scanning electron micrographs in Plate 4 show
the shape of the individual powder particles of the four
types of metal powder investigated. All four materials
exhibit "tailing" which is a feature commonly produced
by atomization processes using horizontal blasts. Chare[19]
found this effect in aluminium powders produced in a
horizontal blast air atomizer. He also noted an absence
of "tailing" in powders produced using a vertical air
blast.

The shape and size of powder particles produced by
atomization depend upon the nature of the impinging gas
or water jet and on the geometrical configuration of the
apparatus. Long cooling times are required to produce
spherical powders. Slow cooling rates permit surface
tension forces to minimize the surface area, producing
spheres. However, to prevent particle coalescence, the
cooling rate must be great enough to ensure sufficient
solidification prior to deposition. Gurney et al[24] pro-
duced remarkably spherical 7075 aluminium alloy powder
using a rotating electrode process. In fact, for compacting
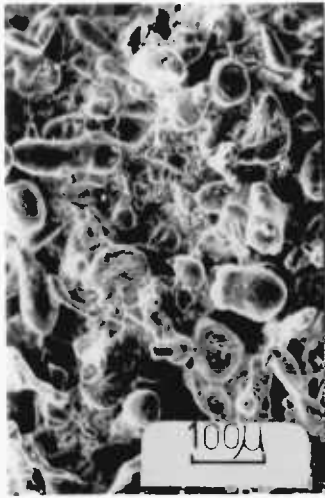
(a)
HE9
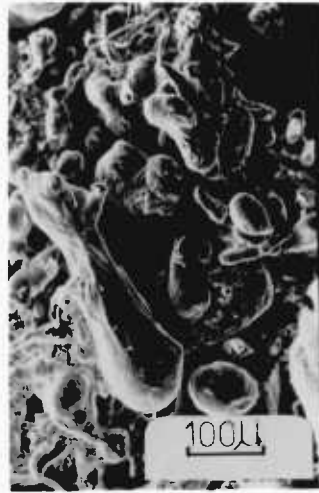
(b)
HE30
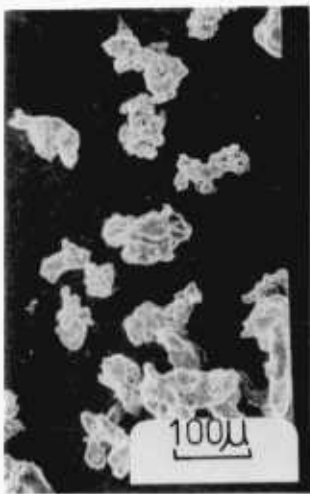
(c)
Al
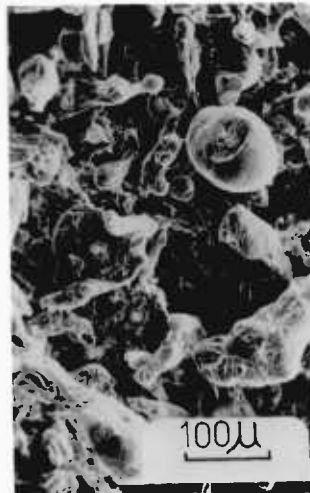
(d)
Al-Mg

PLATE 4

Scanning electronmicrographs of powders

purposes, spherical particles are less desirable than
irregularly shaped particles with "tails". This is
because spherical particles provide the minimum surface
area for interparticle bonding. Irregularly shaped
particles compact to a higher density due to bridging
effects i.e. particle "tails" fill irregularly shaped
voids. Thus compacts made from irregular particles are
stronger. On the other hand sintering rates for spherical
particles are believed to be higher than for irregular
particles. Thus, for compacts produced by pressing and
sintering, the optimum particle shape lies somewhere
between the two extremes of completely spherical and
completely irregular.

5.1.5 Structure of powder particles

The presence of a very fine structure, dendritic
in nature, in the HE9, Al-Mg and Al powders is revealed
by optical micrographs (a), (b), and (c) respectively in
Plate 5. This structure (also present in the HE30 powder)
is caused by the high solidification rate present in the
atomization process. Gurney et al[24] found similar structures
in 7075 aluminium alloy powder produced by the rotating
electrode process.

5.1.6 Strength of compact

The results of the experiments to determine the
effects of:-

(1) compaction pressure
(2) sintering temperature
(3) powder particle size

on compaction strength are given in tables 7-9. The
theoretical densities mentioned in table 7 are calculated
by expressing the density of the compact, found from
volume and weight measurements, as a percentage of the
density of cast HE9 + 10 wt.% glass (2850 kg m^{-3}).

(a)

HE9

(b)

Al-Mg

(c)

Al

PLATE 5   Optical micrographs of powders
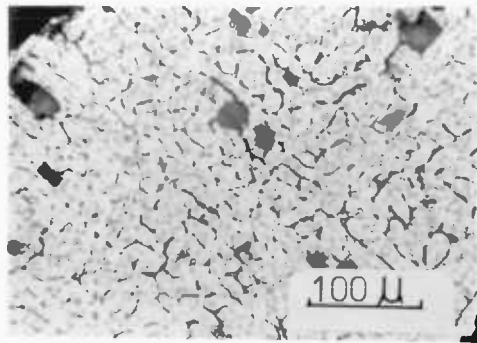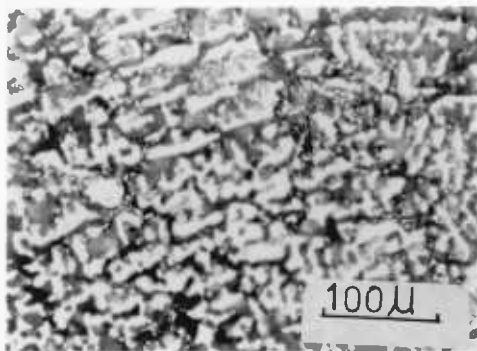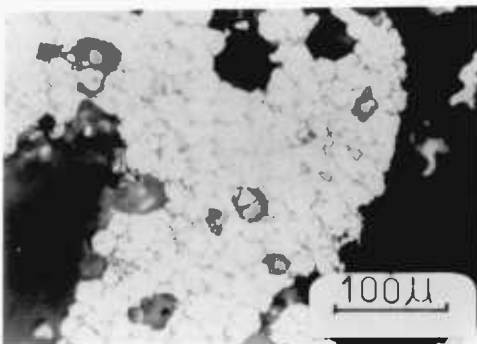
A linear relationship between theoretical density and
"fracture force" (see 4.3.2) is demonstrated in Fig. 32.
However, a correlation coefficient of 0.948 indicates
that the experimental points fit an equation of the form

Force = const' + density x const'',

only approximately. The results are replotted in Fig.33
in a form which tests the applicability of the relation-
ship suggested by Konopicky[5]:-

$$\ln \left(\frac{1}{1-D}\right) = K'P + \text{constant} \tag{1}$$

where D = relative density
      P = compact pressure
      K' = constant.

In this case the equation is:-

$$\ln \left(\frac{1}{1-D}\right) = 0.293 \times 10^{-2} P + 1.349$$

A correlation of 0.985 indicates that the data points fit
equation (1) quite well. Over the range of pressures
investigated the traditional three stages of compaction
(see 2.1.1) are not discernible. Stage 1 compaction i.e.
a decrease in volume without particle deformation, is not
present as this involves lower pressures than those inves-
tigated. Chare[19] encountered stage 1 compaction only at
pressures of less than 50 MN/m^2, for Al-Fe alloy powder.
The absence of stage 3 compaction i.e. bulk compression
of the compact, is due to the relatively low pressures
used. Thus Fig. 33 represents stage 2 compaction only
i.e. the elastic-plastic deformation of particles.

Several billets, compacted at the same pressure,
were sintered at various temperatures. The effect of
sintering temperature on compact strength is shown in
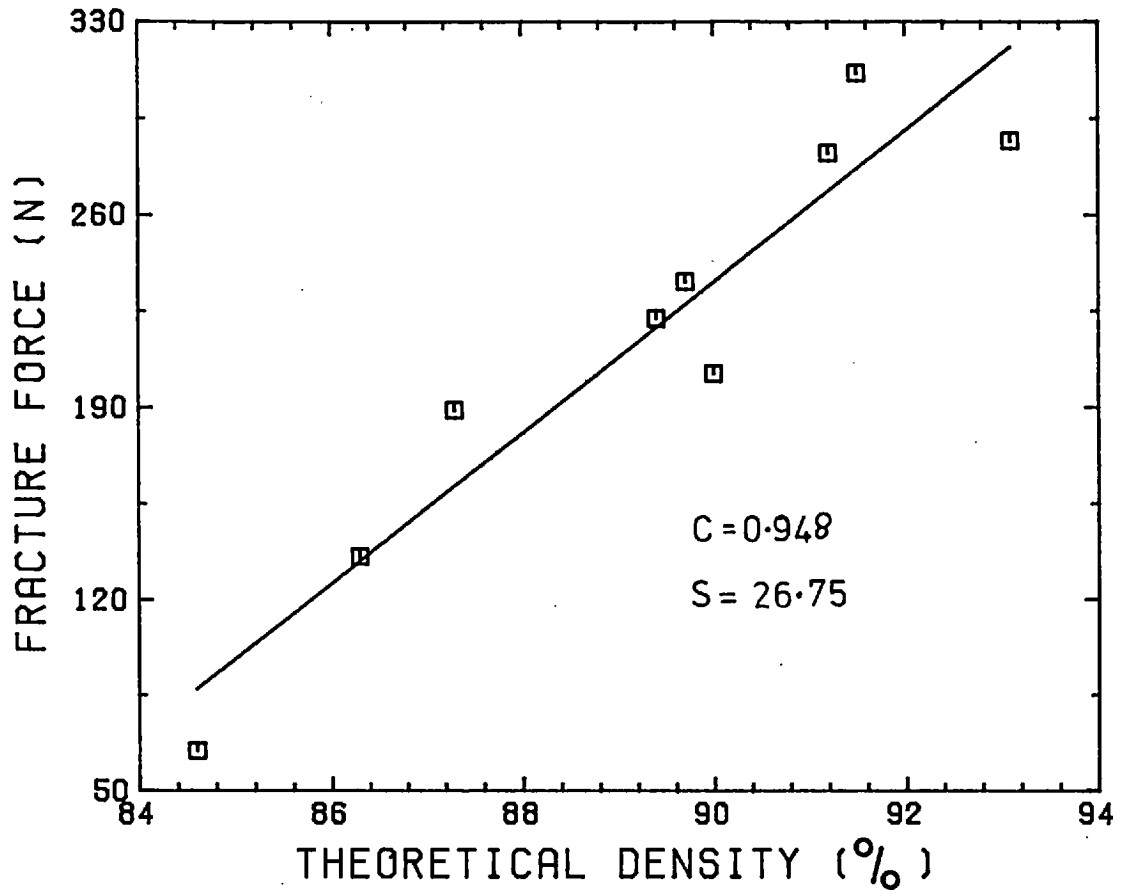
FIG. 32 Compact fracture force as a function of theoretical density
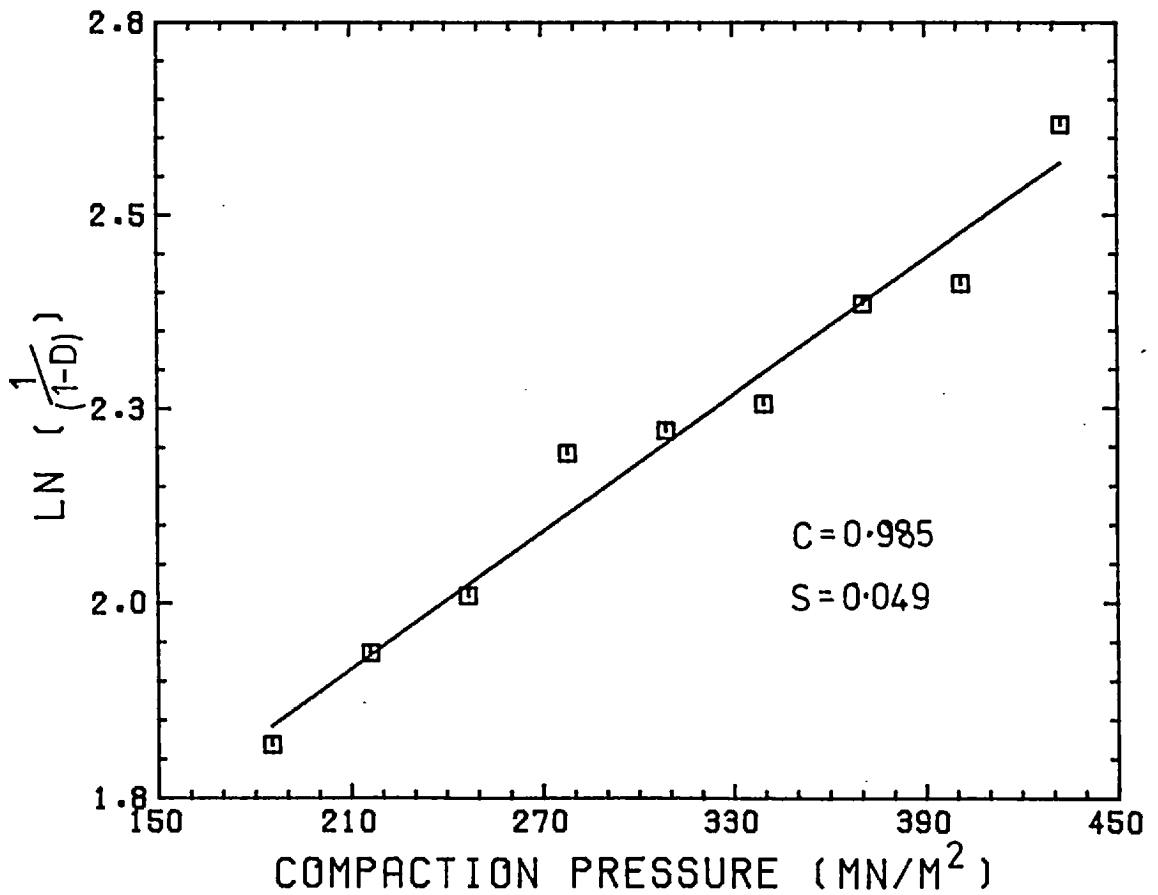
FIG. 33 Relative density of compact as a function of compaction pressure

Fig. 34. Billet strength increases rapidly with sintering temperature in the range 250-450°C. Below 250°C the rate of increase is considerably less. This temperature dependence is to be expected as the rate of diffusion increases rapidly with temperature according to Darken's equation[108]:-

$$J_i = -B_i \, kT \, \frac{dC_i}{dx}$$

where T = temperature

J_i = rate of self-diffusion

k = Boltzman's constant

B_i = mobility

$\frac{dC_i}{dx}$ = concentration gradient

The effect of particle size on compact strength was also investigated. A decrease in compact strength with increasing particle size is evident in Fig. 35. The rate of decrease in strength diminishes with increasing particle size. This behaviour is fairly easily explained. As the particle size decreases the surface area/volume ratio increases thus providing more surface area for interparticle contact. Thus the total interparticle bonding area increases, improving the compact strength.

As mentioned in Chapter 2, previous investigators have not attempted to relate compact strength directly to compaction pressure. In the present work although only a limited amount of data was avilable, it was decided that an attempt to relate fracture force to compaction pressure would be useful. Fig. 36 reveals that a second degree polynomial fits the data points reasonably well. The equation of the line is:-

$$F = -326 + 2.77P - 0.003P^2$$

where F = fracture force

P = compaction pressure
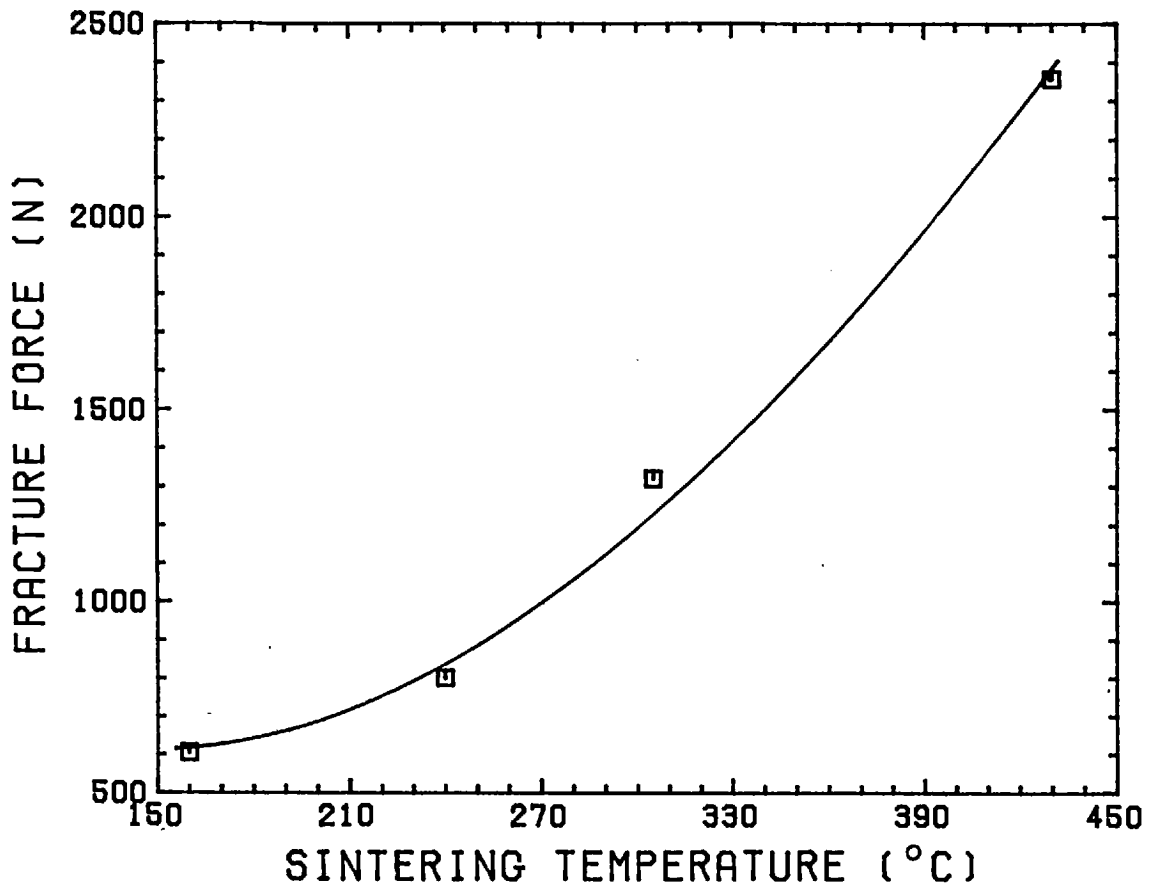
FIG. 34 Relationship between compact fracture force and sintering temperature
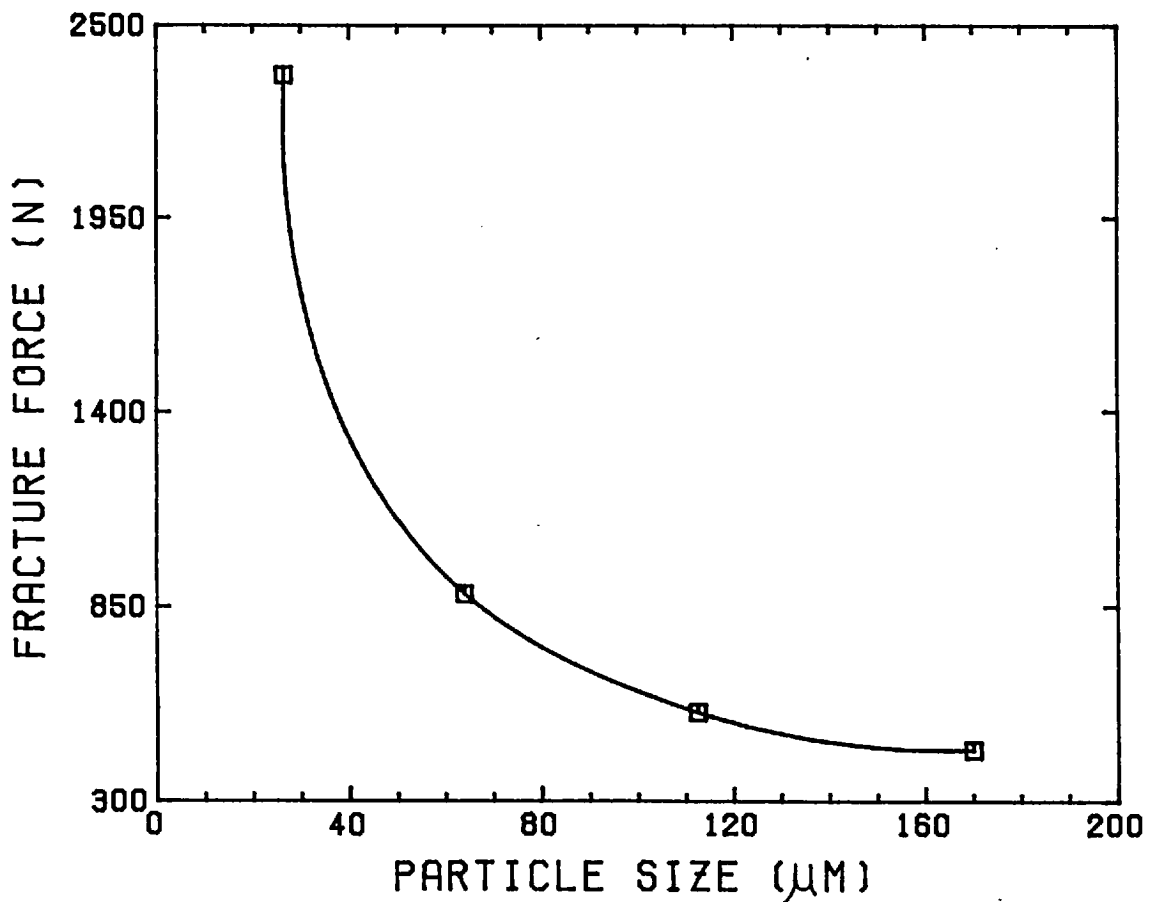
FIG. 35 Dependence of compact fracture force on powder particle size
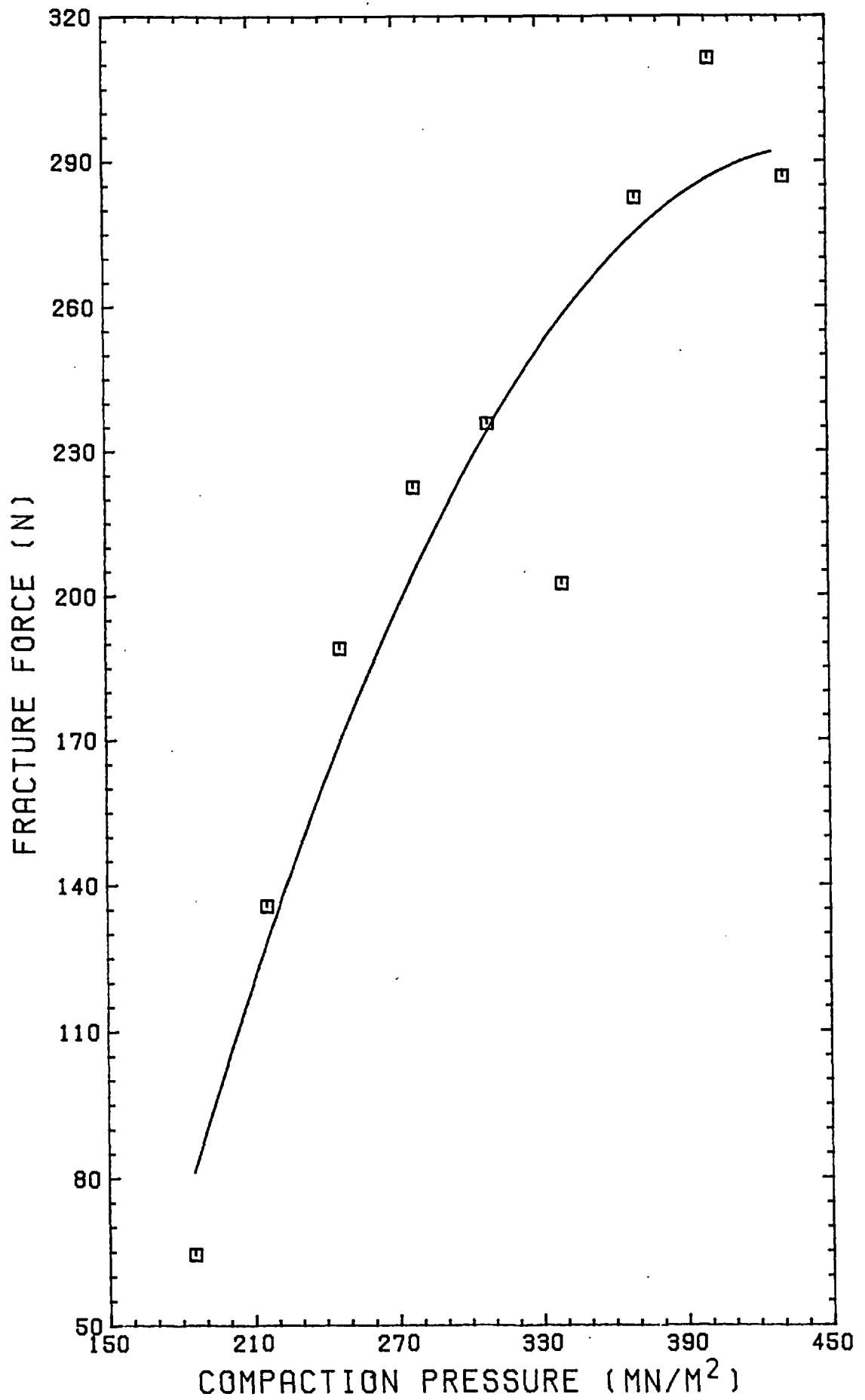
FIG. 36 Relationship between compact fracture force and compaction pressure

It must be emphasised that this equation is the result
of only seven compactions carried out at room temperature.

5.2.1 Theoretical prediction of extrusion loads

The theory discussed in (3.2.3) enables the extru-
sion load to be predicted by the use of one of two
solutions:-

either   (a) a minimised plane strain upper bound solution
or   (b) a minimised plane strain solution modified
             for axisymmetric extrusion.

From the results of torsion tests (5.5.1) and tensile tests
(5.9.1, 5.9.3 and 5.9.4) equation (17) becomes:-

$$K_{ij} = \frac{40}{\sqrt{3}} \; \overset{.}{\varepsilon} \, 0.1 \; \overset{-}{\varepsilon} \, 0.21$$

Extrusion pressure plotted as a function of extrusion
ratio, in Fig. 37, enables the loads predicted by the two
solutions mentioned above to be compared to the experi-
mental results for a series of HE9 extrusions. A very
large discrepancy exists between the pressures predicted
by the modified solution for axisymmetric extrusion and
those observed in practice. The predicted values are
generally 50% less than the experimental values.
Clearly this method is of little use. In fact the plane
strain solutions give more reasonable results. The pre-
dicted slope of this curve is, however, manifestly incorrect.
For both high (> 55:1) and low (< 25:1) extrusion ratios
the theory is unacceptable. When extruding cast billets
this method usually predicts pressures which are ∿20%
above those actually obtaining. One of the main reasons
why the two methods mentioned above give such unsatisfactory
results is that although the general form of equation (17)
is correct, the strain and strain rate exponents cannot
be accurately determined by simulated tensile and/or torsion
tests in the case of powder extrusion. This is because:-
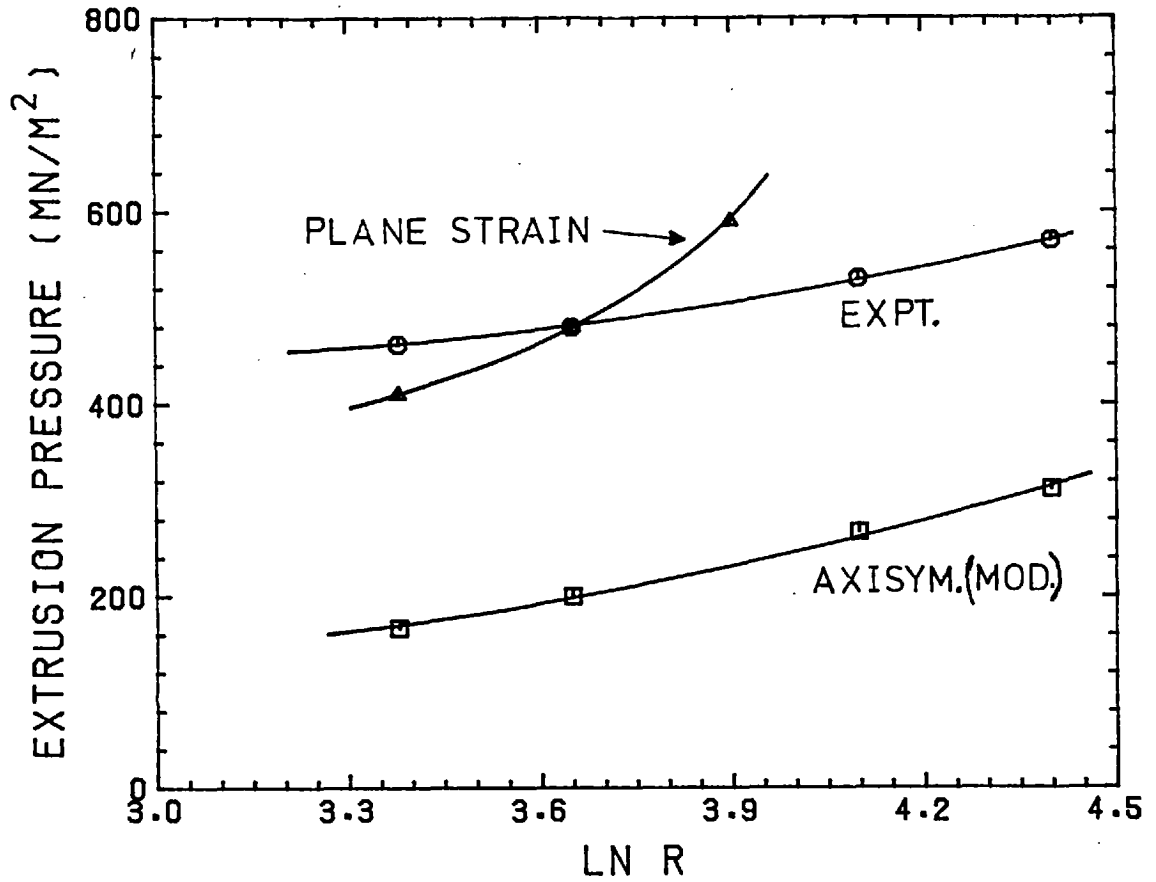
FIG. 37 Comparison between experimentally measured HE9 powder extrusion pressures and theoretically predicted values (plane strain upper bound)
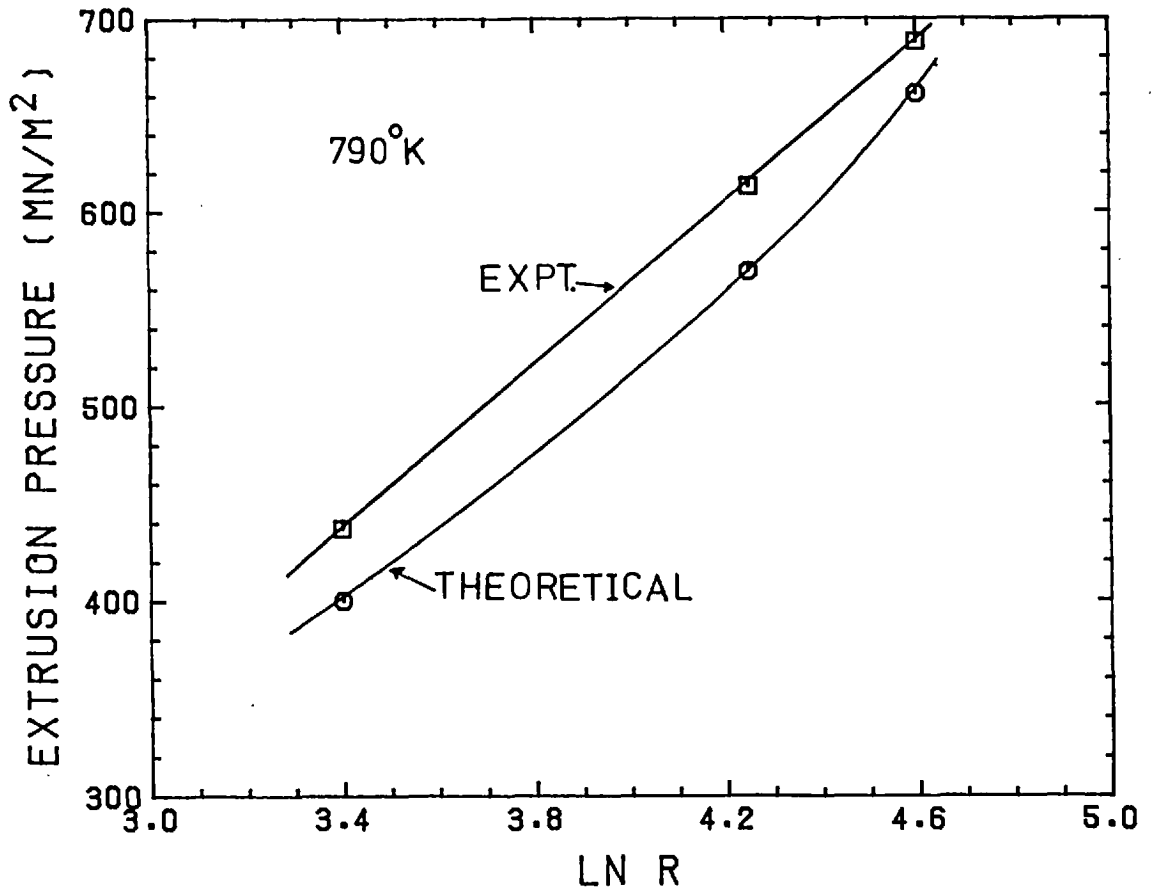
FIG. 38 Comparison between measured extrusion pressures for cast aluminium alloy and theoretically predicted values (elemental axisymmetric upper bound)

(1) The compressive and shear stress must be
    simultaneously present in order to achieve
    the welding and rewelding processes associated
    with consolidation of the material.

(2) The material used in laboratory tests is the
    extruded product and possesses properties
    different to those of the powder compact
    before it negotiates the deformation zone.

For these reasons the exponent values in (17) must be
calculated as part of the optimization procedure associated
with the upper bound approach.

This is possible using the theory in 3.4.1. Before
applying this theory to powder compact extrusion it is
necessary to establish that it adequately predicts extru-
sion pressures for known flow stress conditions. Wood
and Sheppard[128] have shown that for an as-cast aluminium
copper alloy subjected to torsion testing the flow stress
is given by

$$\bar{\sigma} = 62.5 \ln \left[(0.087\dot{\varepsilon})^{0.23} + \{(0.087\dot{\varepsilon})^{0.46} + 1\}^{\frac{1}{2}} \right]$$

(at 790°K)

This equation was substituted in the program given in
appendix 3 to calculate the flow stress. The predicted
pressures thus obtained are compared with the experimental
results of Wood in Fig. 38. It can be seen that the axi-
symmetric upper bound approach, when used in conjunction
with a suitable optimization process, predicts pressures
which are fairly near the experimental values.

Earlier workers[35,36,117] have assumed a constant
mean flow stress when evaluating the rate of internal
energy dissipation although Halling and Mitchell[36]
suggested a method enabling the effects of work hardening
to be considered. In the present study the rate of energy

dissipation is determined for each element since the
flow stress is considered to be both strain and strain
rate sensitive. The deforming region was divided into
50 elements representing a 10 x 5 matrix after ascertaining
the fact that a 800 element matrix improved the answer
by only 1.2%. The use of the coarser matrix results in
a considerable saving in computer time.

The experimental powder extrusion pressures for HE9
are compared with those predicted by this theory over a
range of extrusion ratios from 10:1 to 180:1 in Fig. 39.
The optimum values of A, n and m (equation 17) are 45,
0.02 and 0.05 (at $780^{\circ}K$). Clearly excellent agreement
exists between predicted and experimental pressures over
a wide range of extrusion ratios (5:1 to 180:1). For
most aluminium alloys the value of the strain rate
exponent, n, varies from 0.18 to 0.25 in the hot working
region. The present value of 0.02 indicates that powder
compacts are very much less strain rate sensitive than
their cast counterparts. This is further evidence in
support of the thesis of Sheppard and Chare that the
predominant consolidation mechanism in the deformation
zone is welding of particle necks, shearing and rewelding
as a continuous process resulting in final product properties
being achieved only near the exit of the zone . Fig. 40
demonstrates that the theory works equally well for HE30.
In this case the optimum values of A, n and m are 55, 0.03
and 0.05 respectively (at $800^{\circ}K$). The low n value once
again re-emphasies the argument concerning the consolidation
mechanism.

Other workers have shown that for Al powder[123] and
7075 Al alloy powder[24] extrusion a natural strain of 2.3
is required for complete densification and consolidation
of the product. The computer program which calculates
the theoretical extrusion pressure also predicts that
70% of the deformation zone experiences a total strain
of less than 2.3, even at an extrusion ratio of 80:1
(Fig. 41). This also indicates that final product properties
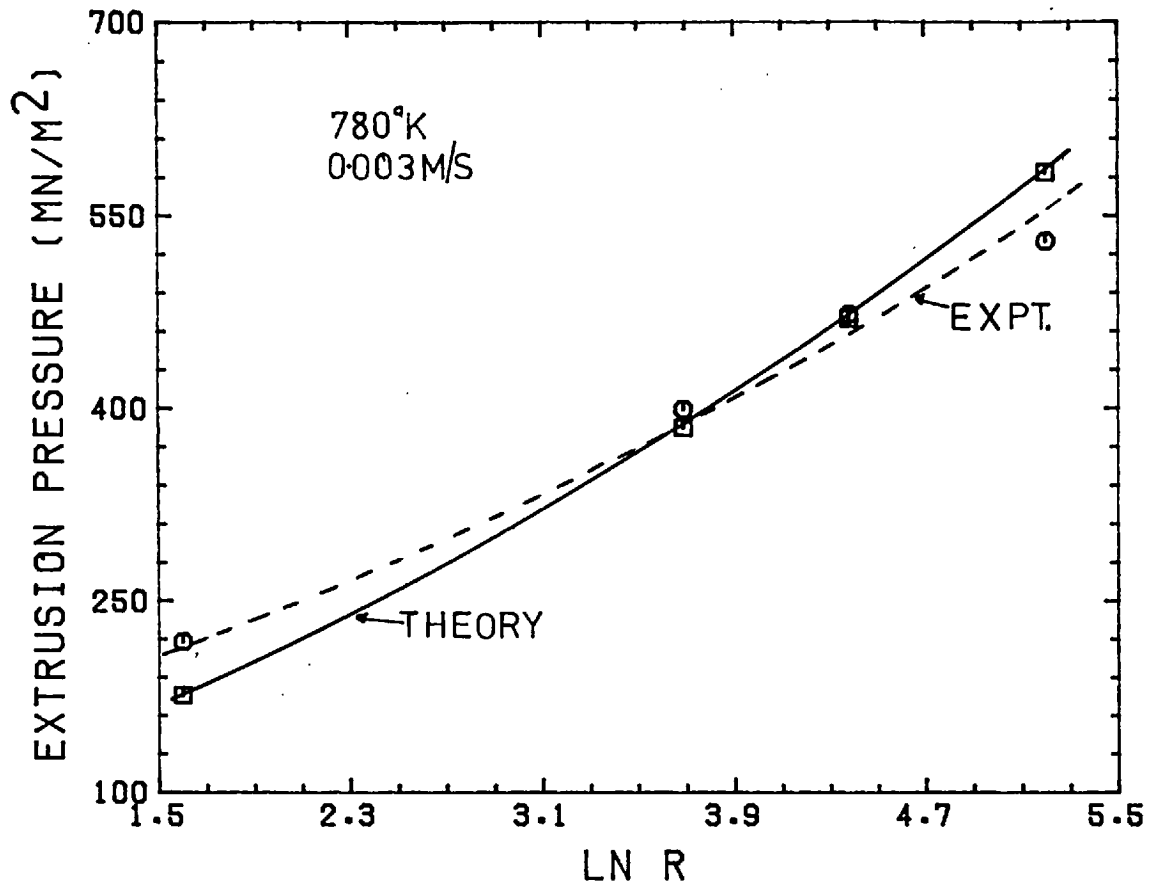
FIG. 39 Comparison between measured HE9 powder extrusion pressures
and theoretically predicted values (elemental axisymmetric
upper bound)
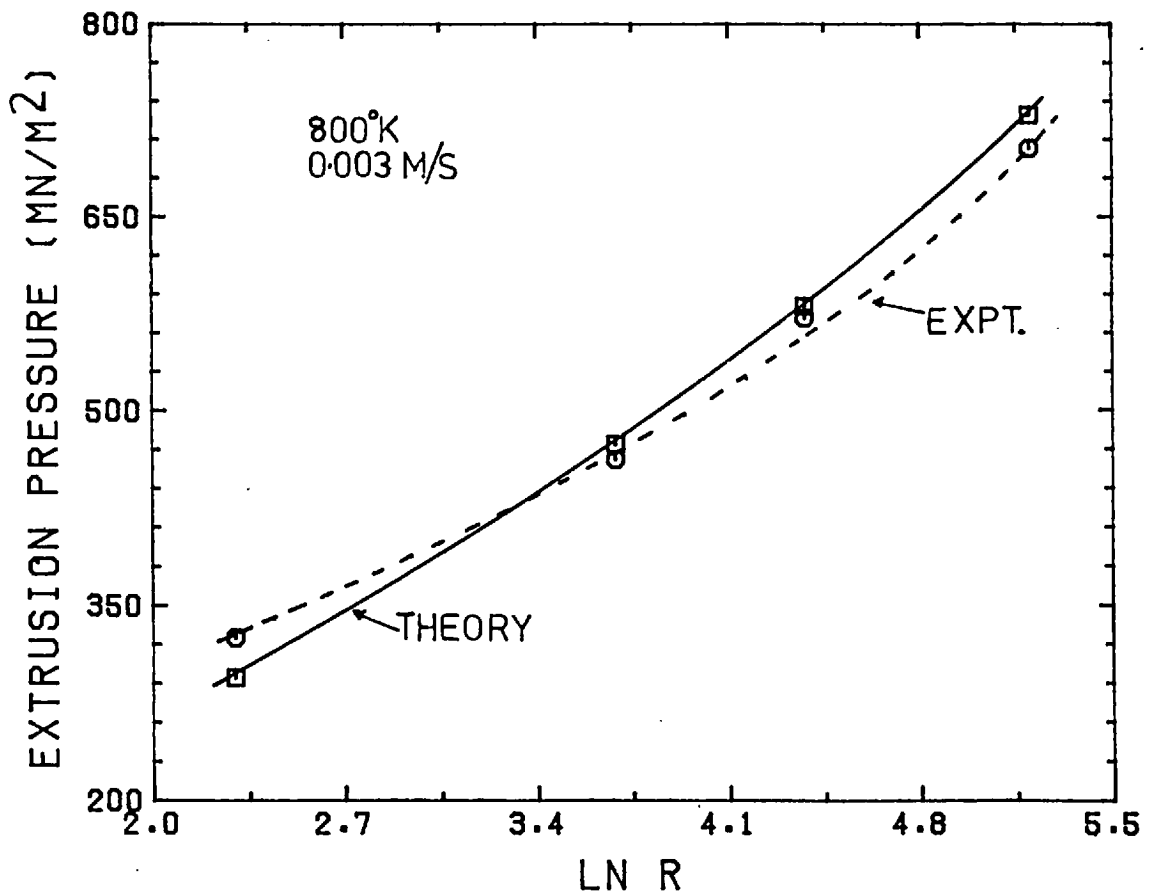
FIG. 40 Comparison between measured HE30 powder extrusion pressures
and theoretically predicted values (elemental axisymmetric
upper bound)
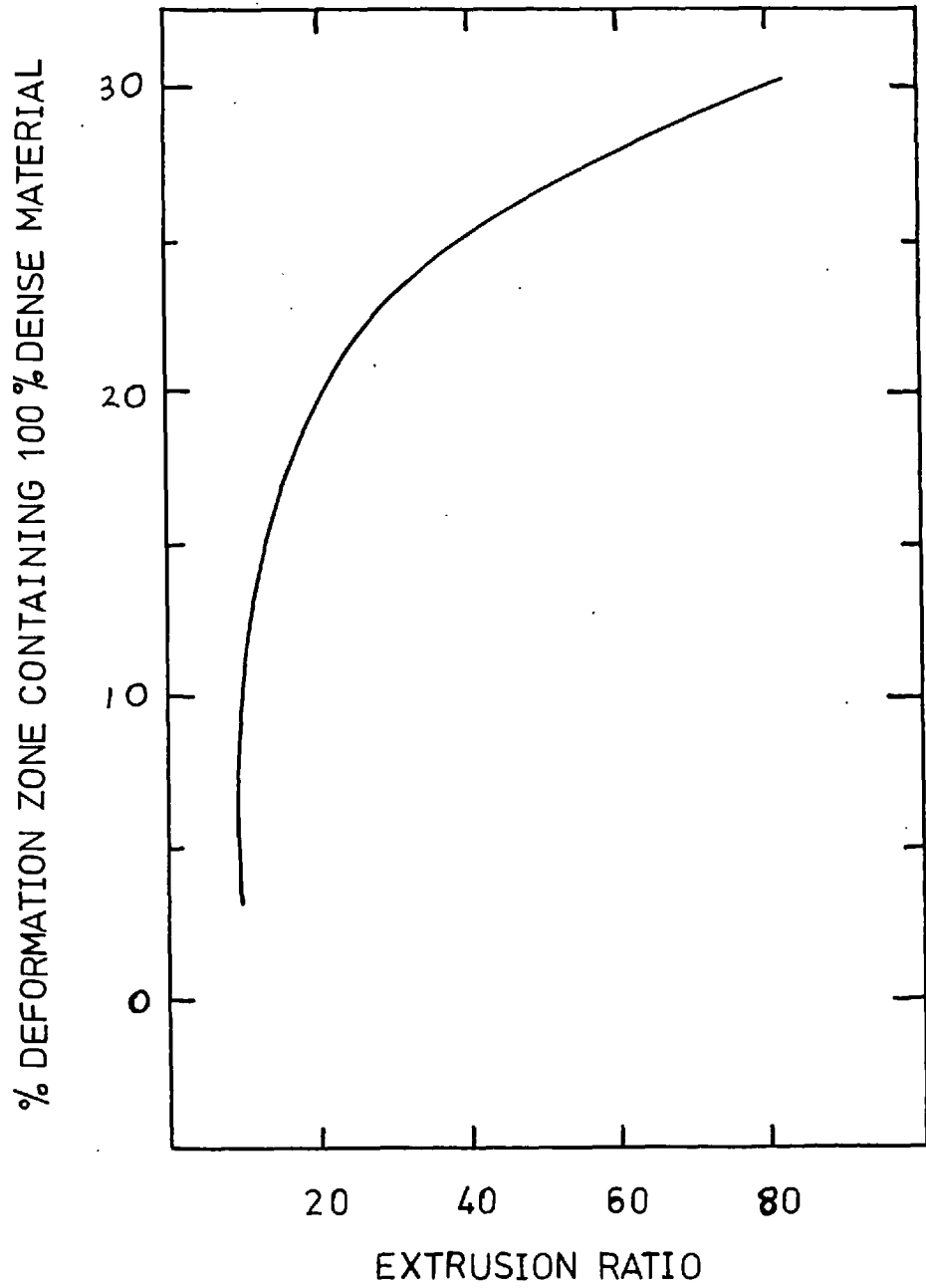
FIG. 41 Theoretically predicted effect of extrusion ratio on densification

are not achieved until far into the deformation zone.
Fig. 42 shows how the predicted values of angles α and
δ (Fig. 11) vary with extrusion ratio. The value of δ
increases continuously with extrusion ratio but α behaves
in a more mysterious way, falling to a minimum value at
40:1 and then increasing again.

The program may also be used to predict P/K values
at various extrusion ratios by equating A, n and m to √3̄,
0 and 0 respectively. In Fig. 43 the values thus predicted
are compared with those produced by Halling and Mitchell's
single triangle field axisymmetric solution and with the
values produced by the plane strain, double triangle field
solution. Clearly the P/K values given by the present
analysis are slightly better than those of the axisymmetric
analysis, over the entire range of ratios from 5:1 to 180:1.
The plane strain solution does yield lower P/K values at
ratios below 20:1. However, above this ratio the P/K
values predicted increase alarmingly, until at 180:1,
the value is 100% larger than the answers given by the
other two analyses.

5.3.1 Strain rate prediction (from upper bound solution)

The program in appendix 3 calculates the strain
rate within each element of the deformation zone (in
addition to the strain rate at each discontinuity).
Therefore by introducing print statements into the program
the strain rate at the centroid of each element may be
obtained. For a 10x5 matrix, an average strain rate
acting along each of five stream lines can be calculated.
(The stream line is assumed to pass through the centroids
of a row of elements). i.e.

$$\overline{\dot{\varepsilon}}_1 = \sum_{1}^{10} \dot{\varepsilon}_i \, d \, l_i \, /L_1 \quad \text{(see fig. 44)}$$

A mean overall strain rate, $\overline{\dot{\varepsilon}}_T$, may then be obtained thus:-

$$\overline{\dot{\varepsilon}}_T = \sum_{1}^{5} 2\pi \, r_i \, d_r \, \overline{\dot{\varepsilon}}_i \, /\pi R_B^2$$
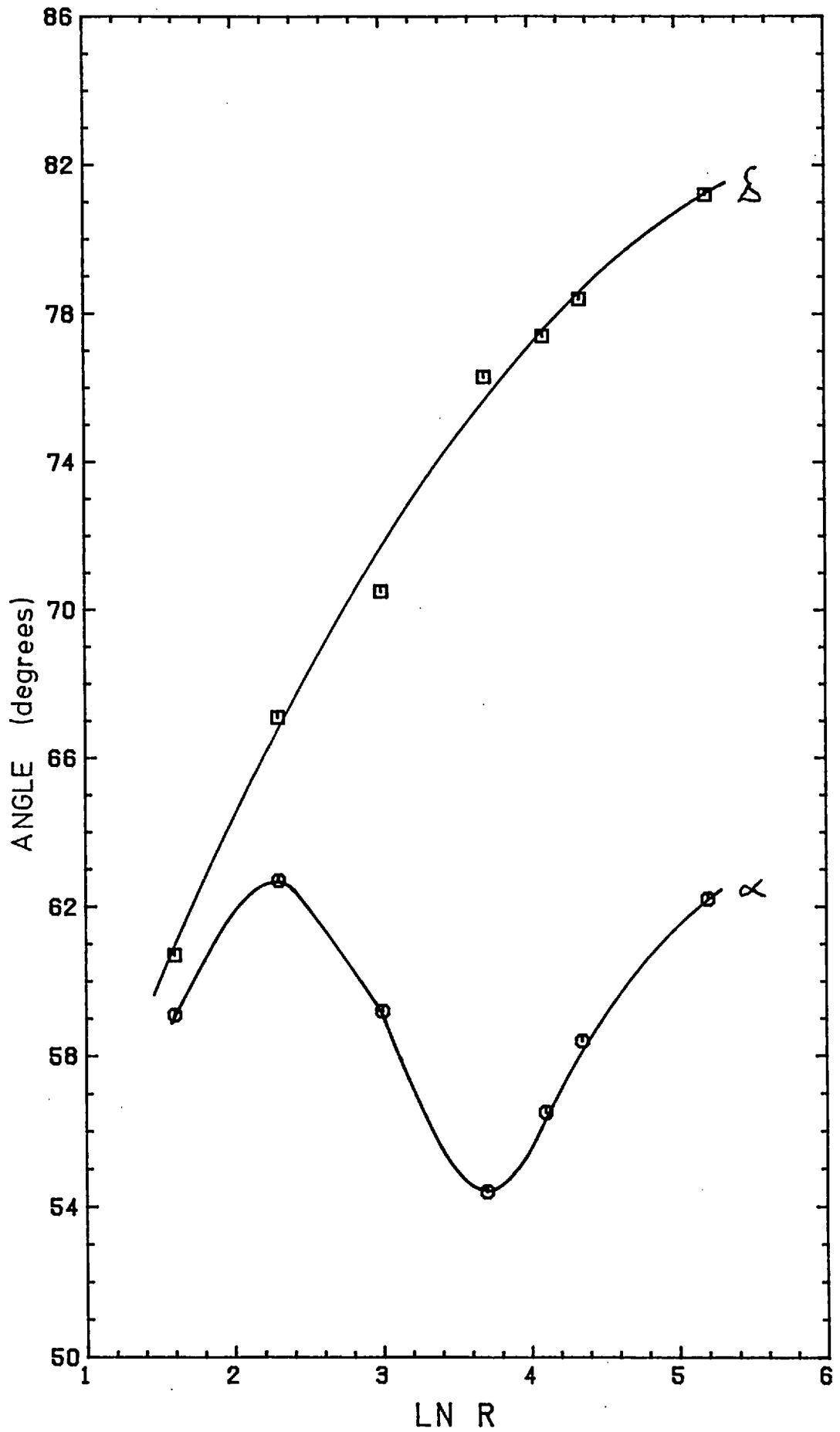
FIG. 42 Theoretically predicted variation in velocity field angles with extrusion ratio
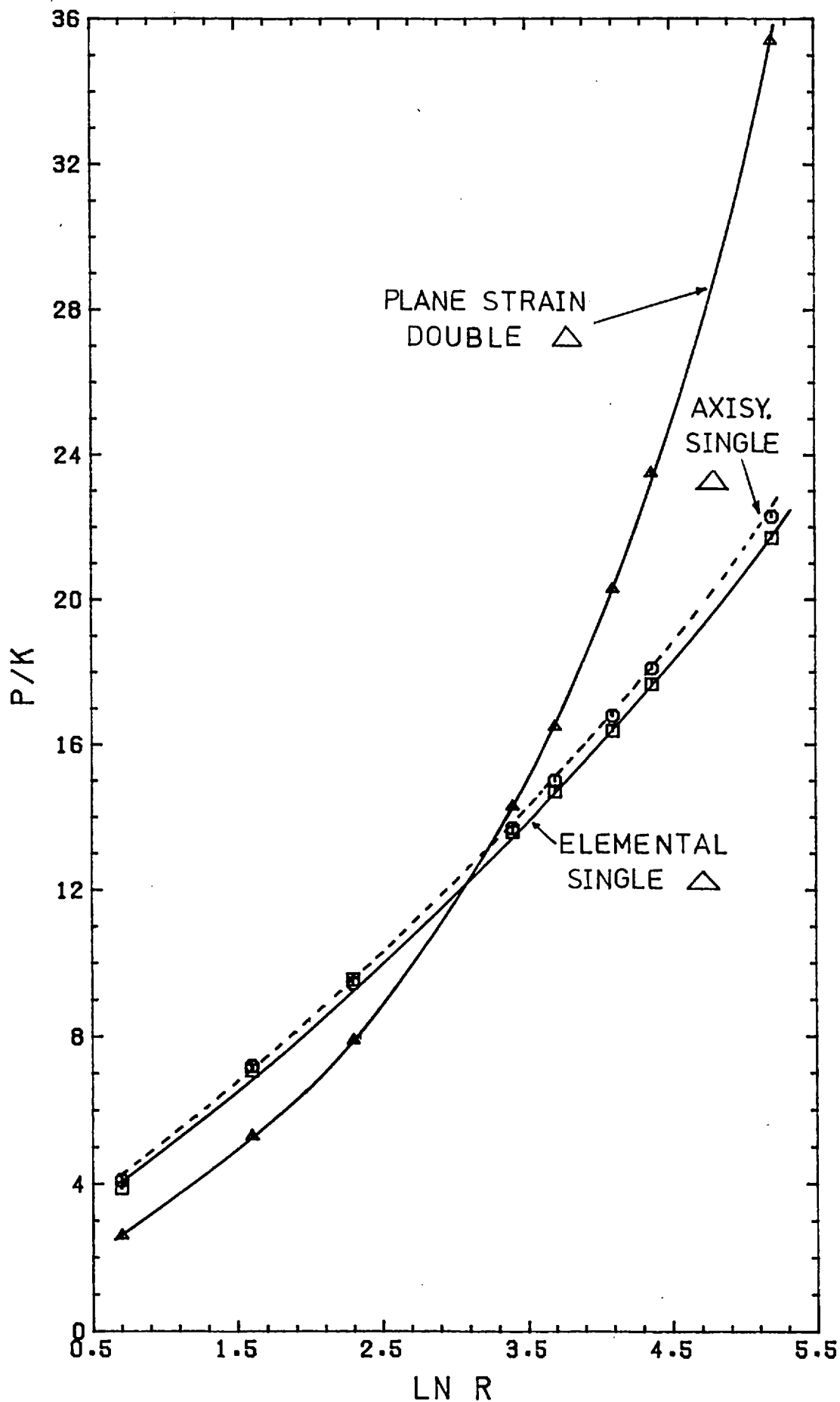
FIG. 43 Variation in predicted P/K values with extrusion ratio for the three upper bound solutions

R_B

d_T

r_i

dl_i

L_i

$\dot{\varepsilon}_1$

$\dot{\varepsilon}_2$

$\dot{\varepsilon}_3$

$\dot{\varepsilon}_4$

$\dot{\varepsilon}_5$

streamline
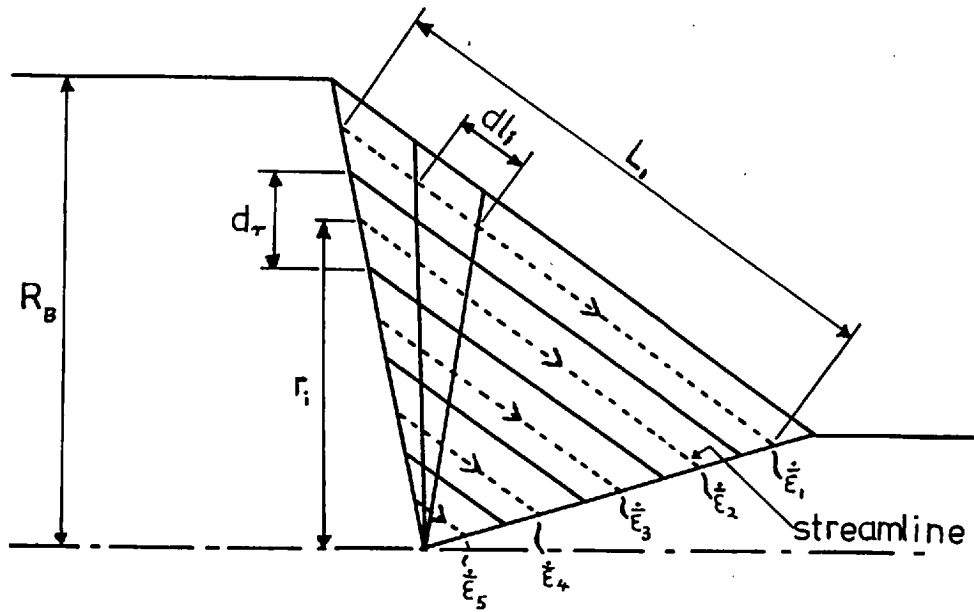
FIG. 44 Upper bound model for strain rate prediction

The results obtained by this method are plotted against
ln R in Fig. 45. They are compared with those predicted
by Feltham's equation at two ram speeds, 0.003 m/sec
and 0.013 m/sec. At both speeds the strain rate predicted
by the upper bound solution is smaller at all ratios
below 180:1. The agreement between the two theories
seems to be relatively independent of the ram speed but
clearly improves with increasing extrusion ratio. (At
some ratio in excess of 180:1 the curves seem destined
to intersect).

5.4.1 Extrusion parameter measurements

The following parameters were measured for each
extrusion and are given in table 10:-

1) Extrusion ratio
2) Ram speed
3) Billet temperature
4) Glass content
5) Extrusion pressure

The calculated values of flow stress, strain rate and
final extrude temperature are also listed.

Typical load-displacement curves for two HE9 powder
billets and a solid billet of the same alloy composition
(excluding Al_2O_3 content) are shown in Fig. 46. The curves
differ significantly in the initial stages of the process
i.e. while the quasi-static deformation zone is being
established. The cast billet, B, exhibits the normal
linear region during upsetting prior to the achievement
of the peak load. The powder billets, A and C, show non-
linear compaction zones. Sheppard[123] reasoned that this
corresponded to the compact obtaining 100% density. It
should be clearly understood that the attainment of the
theoretical density does not coincide with the attainment
of optimum mechanical properties. In fact, at this stage,
the billet is brittle and has practically no resistance to
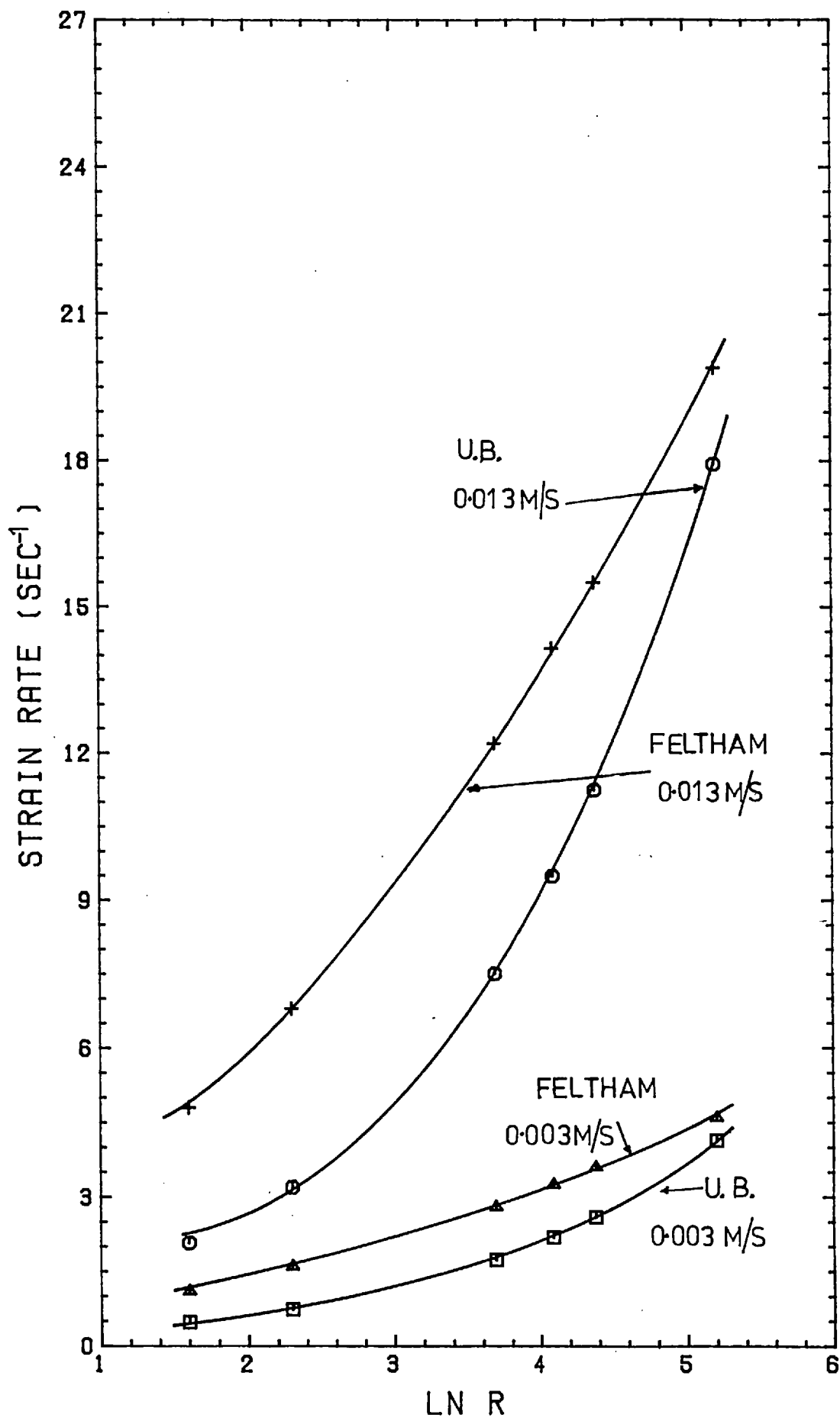
FIG. 45 Comparison between upper bound and Feltham strain rates predicted for various ram speeds and extrusion ratios
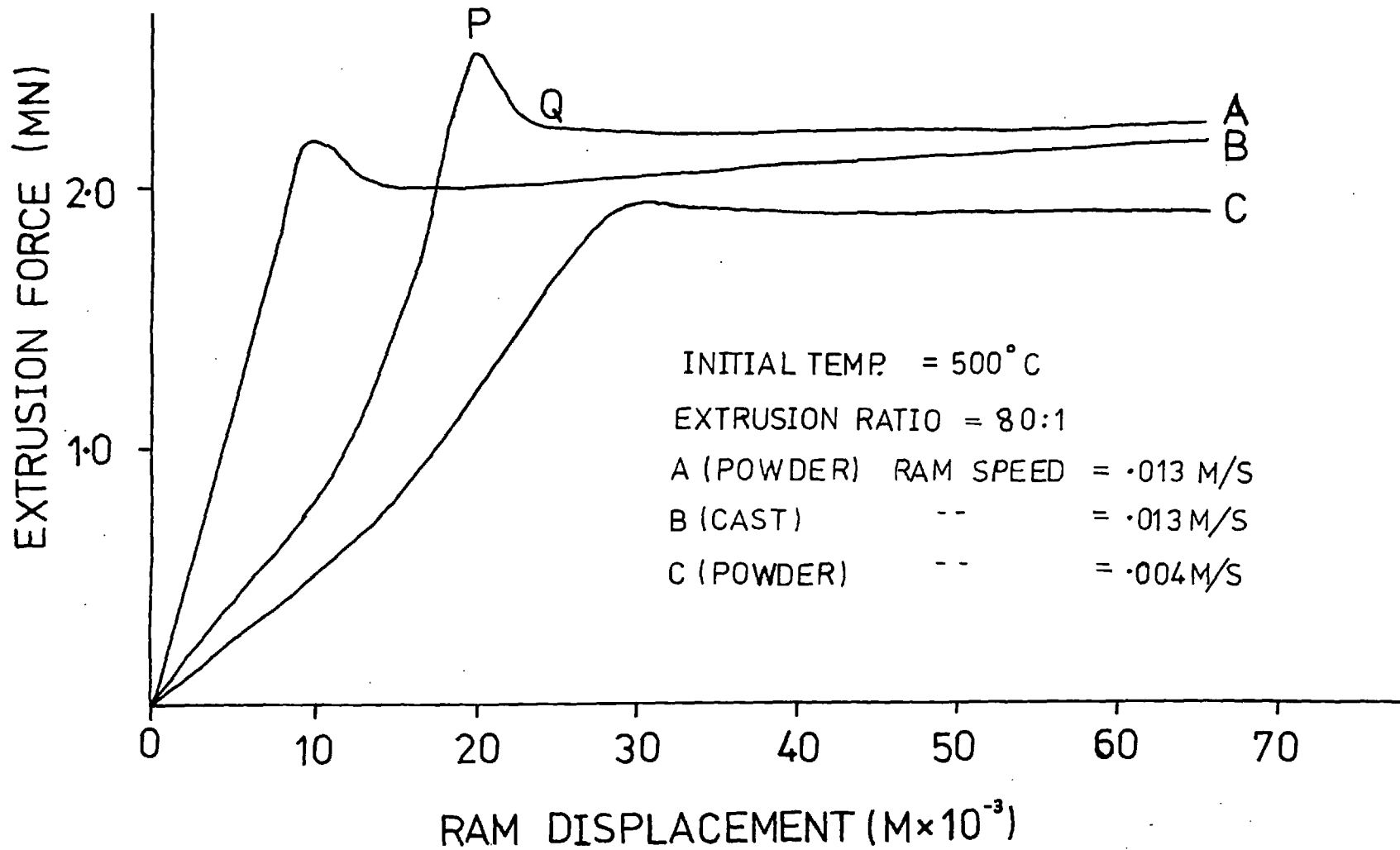
FIG. 46   Experimentally recorded extrusion load vs. ram displacement curves

shear. The mechanical properties of forged[120] metal
powder billets are generally much inferior to those of
extruded powder billets. This evidence is clearly in
agreement with the thesis[135] that deviatoric deformation
(only a limited amount of which is present in forging) is
a prerequisite for the achievement of acceptable properties
and the powder billet cannot obtain optimum properties
until it has completely traversed the deformation zone
present during extrusion.

The fact that a peak exists on curve A but not on
curve C is interesting and is discussed in some detail
in the next section (5.4.2).

On first examining the curves A and B, in Fig. 46,
the hypothesis that powder compacts require lower extrusion
loads than cast billets of the same composition seems
improbable. However, it must be remembered that the cast
billet, B, does not possess the high Al_2O_3 content of the
powder compact. The flow stress of extruded material
containing this oxide dispersion is increased considerably
by its presence. In Fig. 47 the curves A and B are re-
plotted in a different form to allow for this variation
in flow stress. The extrusion pressure readings are made
dimensionless by dividing them by the 0.2% proof stress
values. The "dimensionless pressure" required to extrude
the cast billet is clearly much higher. This tends to
support the thesis that a cast billet with the same oxide
content as the powder would require much higher extrusion
loads than those shown by curve A in Fig. 46.

5.4.2 Effect of extrusion parameters on load

The most widely used relationship between load
and extrusion ratio was first suggested by Johnson:-

$$P/2K = A + B \ln R \qquad (3)$$

where P = pressure   K = shear flow stress
       R = extrusion ratio   A,B = constants.
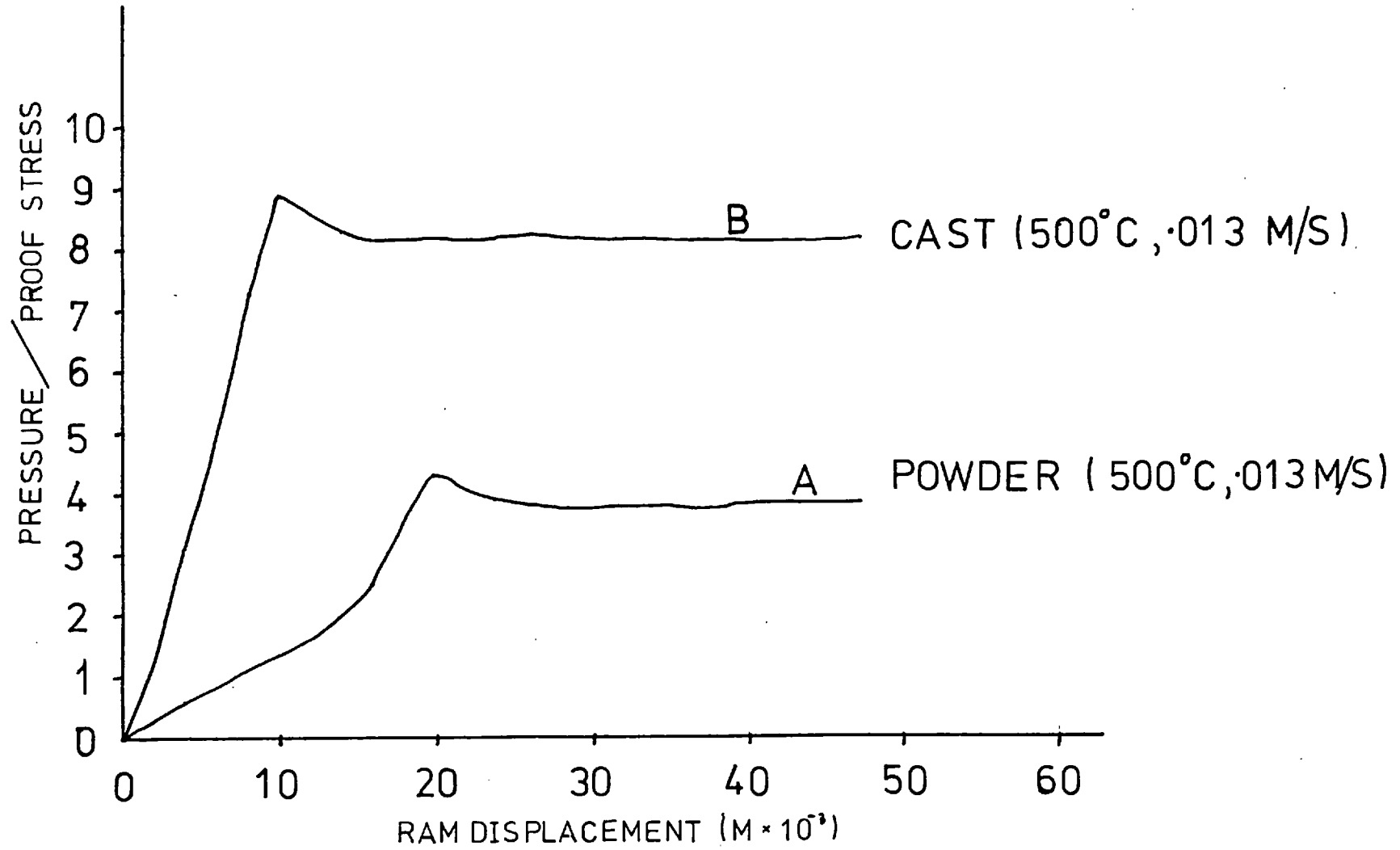
FIG. 47   Dimensionless extrusion pressures vs. ram displacement curves for powder and cast billets

This relationship has been shown to hold for solid billet extrusion of many alloys. However, in the case of powder extrusion, the value of K varies throughout the deformation zone. In order to use equation (3) a mean value of K must be employed. The equation may be written:-

$$P = A' + B' \ln R$$

where A', B' contain a mean shear stress term.

Figs. 48-50 demonstrate that linear relationships between extrusion pressure and extrusion ratio do exist for the extrusion of HE9, HE30 and HE9-5% glass powders, at various temperatures, over the extrusion ratio range 5:1 to 180:1. Volmer[121] discovered a similar relationship for iron powder compact extrusion. Various workers have found that this relationship breaks down at ratios of less than ∿5:1 for aluminium alloy powders[123,124] and for high speed steel powders[22]. This breakdown is due to incomplete consolidation of the extrude at these low ratios.

For cast billets of HE9 alloy the relation between pressure and extrusion ratio at 540°C is:-

$$P/\sigma = 0.52 + 1.32 \ln R \qquad (87)$$

The equation for HE9 powder compact extrusion, at 540°C, is:-

$$P = 71.8 + 82.5 \ln R \qquad (88)$$

For comparative purposes it is convenient to write equations (87) and (88) in the form:-

$$P/B' = 0.39 + \ln R \qquad \text{cast billet} \qquad (89)$$

$$P/B' = 0.87 + \ln R \qquad \text{powder billet} \qquad (90)$$
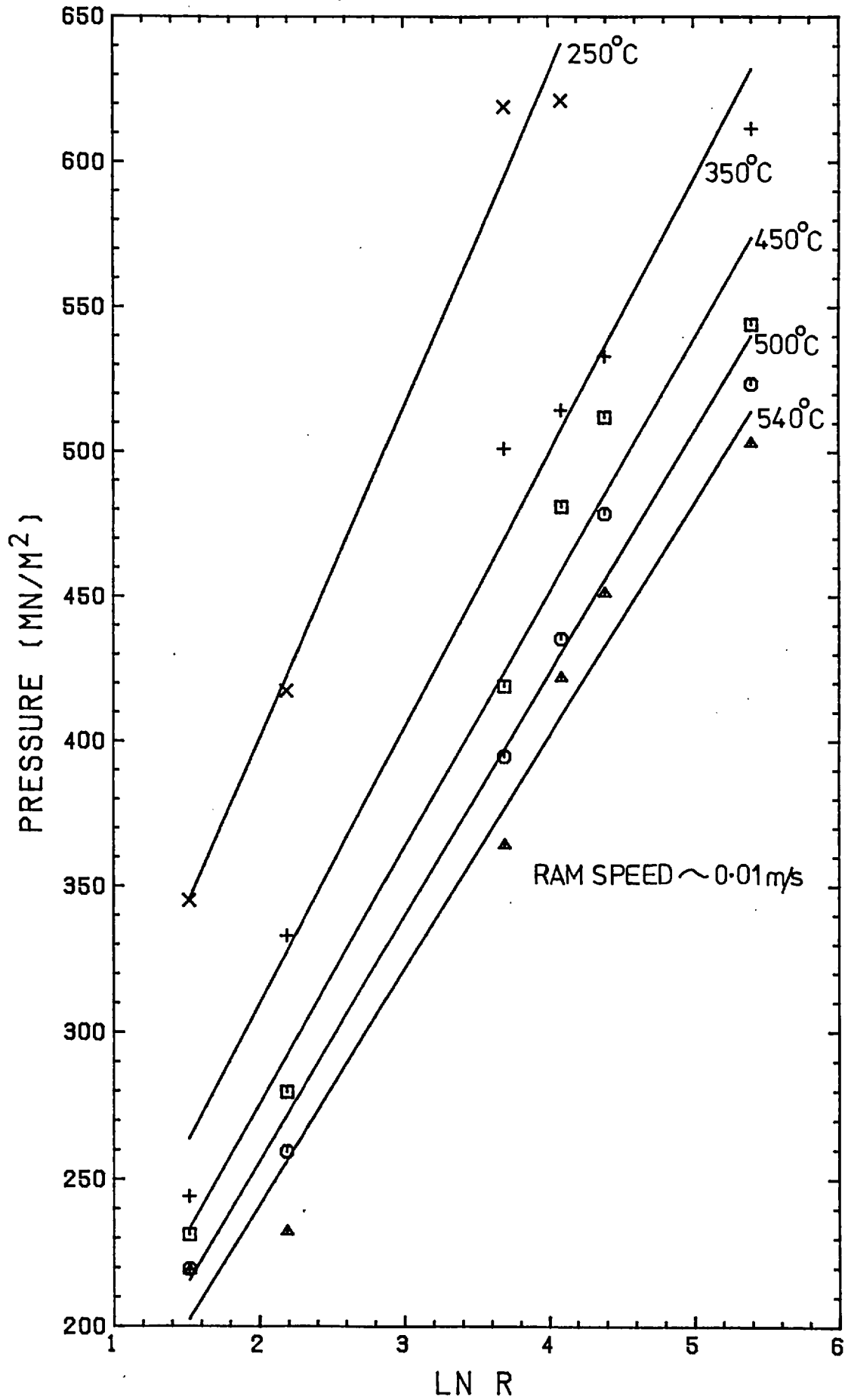
FIG. 48   Effect of temperature on extrusion pressure vs. ln R
relationships for HE9 powder extrusion
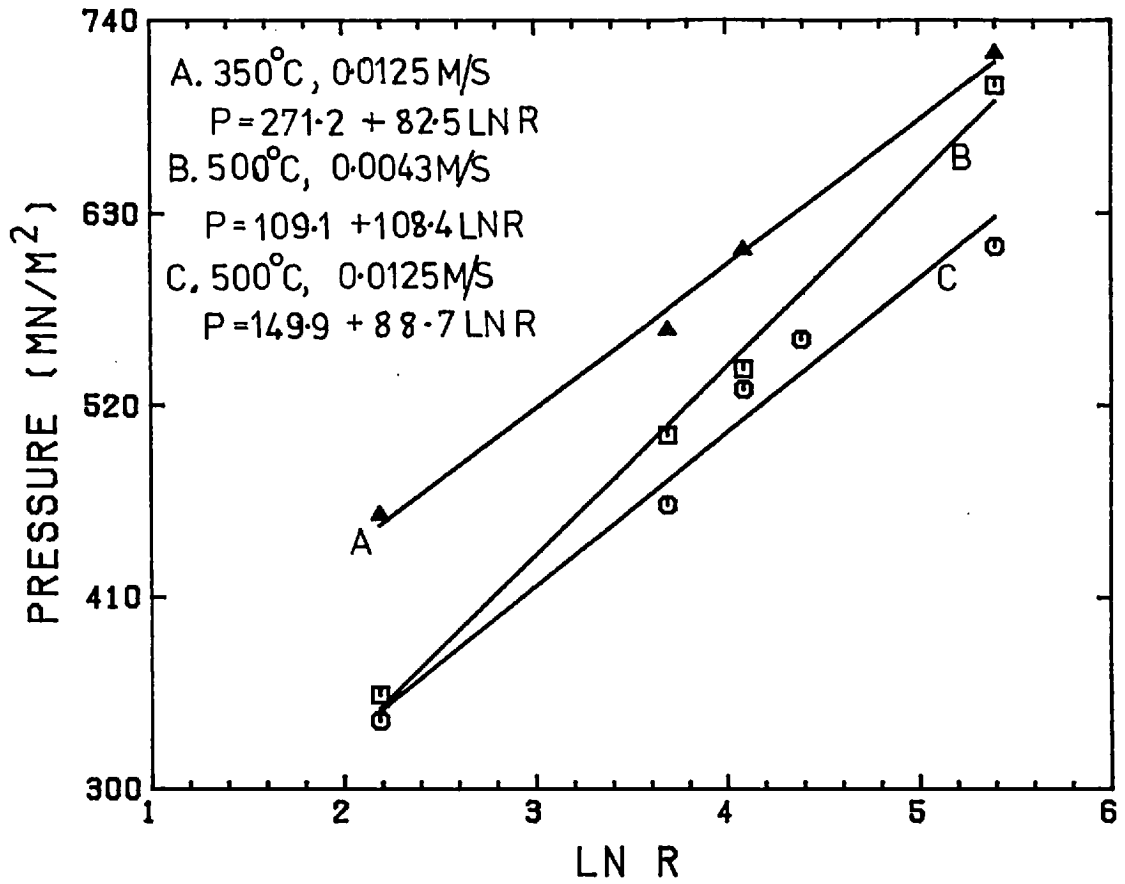
FIG. 49 Extrusion pressure vs. ln R relationships for HE30 powder extrusions
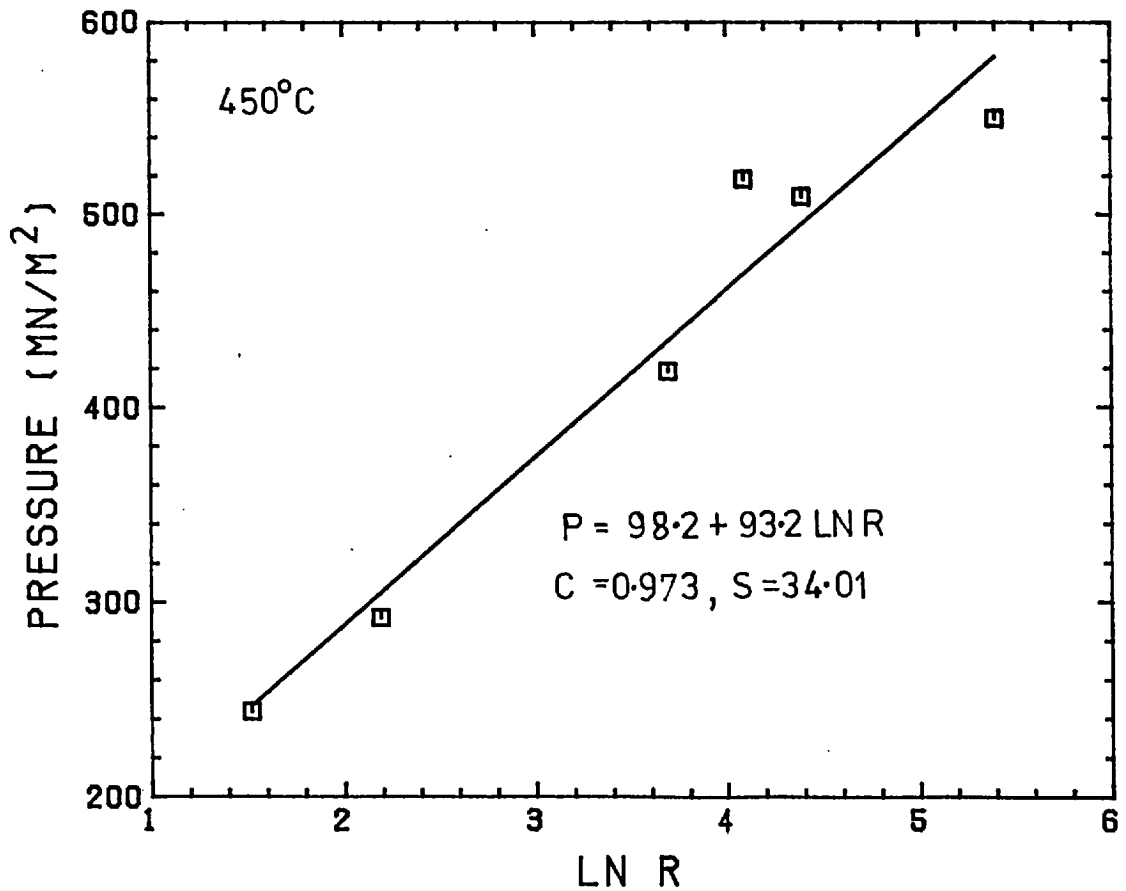
FIG. 50 Extrusion pressure vs. ln R relationship for HE9 + 5wt.% glass billet extrusion

The significant feature here is the relative magnitudes of the constants on the right hand sides of these equations. This constant is generally recognised to be a measure of the so-called 'redundant' work i.e. work not directly contributing to a shape change. This constant represents the redundant portion of the total energy of extrusion. At a ratio of 40:1 this redundant work represents 19% of the total for powder extrusion compared to only 10% in the case of cast extrusion. This is consistent with the concept of 'building' the extrude as the powder traverses the deformation zone; weld necks being continuously broken and rewelded until the compact as a whole can withstand the applied deviatoric stresses. Thus the actual construction of the product (normally achieved by sintering) is performed by the portion of the extrusion pressure normally termed redundant – clearly a misnomer for powder extrusion processes.

Equations similar to (88) and (90) may be written for HE9 at all the temperatures investigated in the range 250-540°C. These equations are listed in table 11. The effect of extrusion temperature on this 'redundant work' term is shown in Fig. 51. A rapid decrease in this term with increasing extrusion temperature is apparent. The results of Ashcroft and Lawson[112] exhibit a similar trend for commercially pure aluminium extrusion. However, their results for an Al-Mg-Zn-Cu alloy do not exhibit any correlation between redundant work and extrusion temperature. These results of Ashcroft and Lawson together with the present findings suggest that the correlation between temperature and redundant work depends on the alloy content. The temperature dependence suggests that extrusion is more efficient at higher temperatures as less 'redundant work' is required for consolidation. In fact the 'redundant work' term represents 30.4% of the total work done at 250°C (for a 40:1 ratio) decreasing to 15.4% of the total at 500°C. This improvement in efficiency with increasing temperature is probably due to enhanced softening at the higher temperatures producing the familiar decrease in
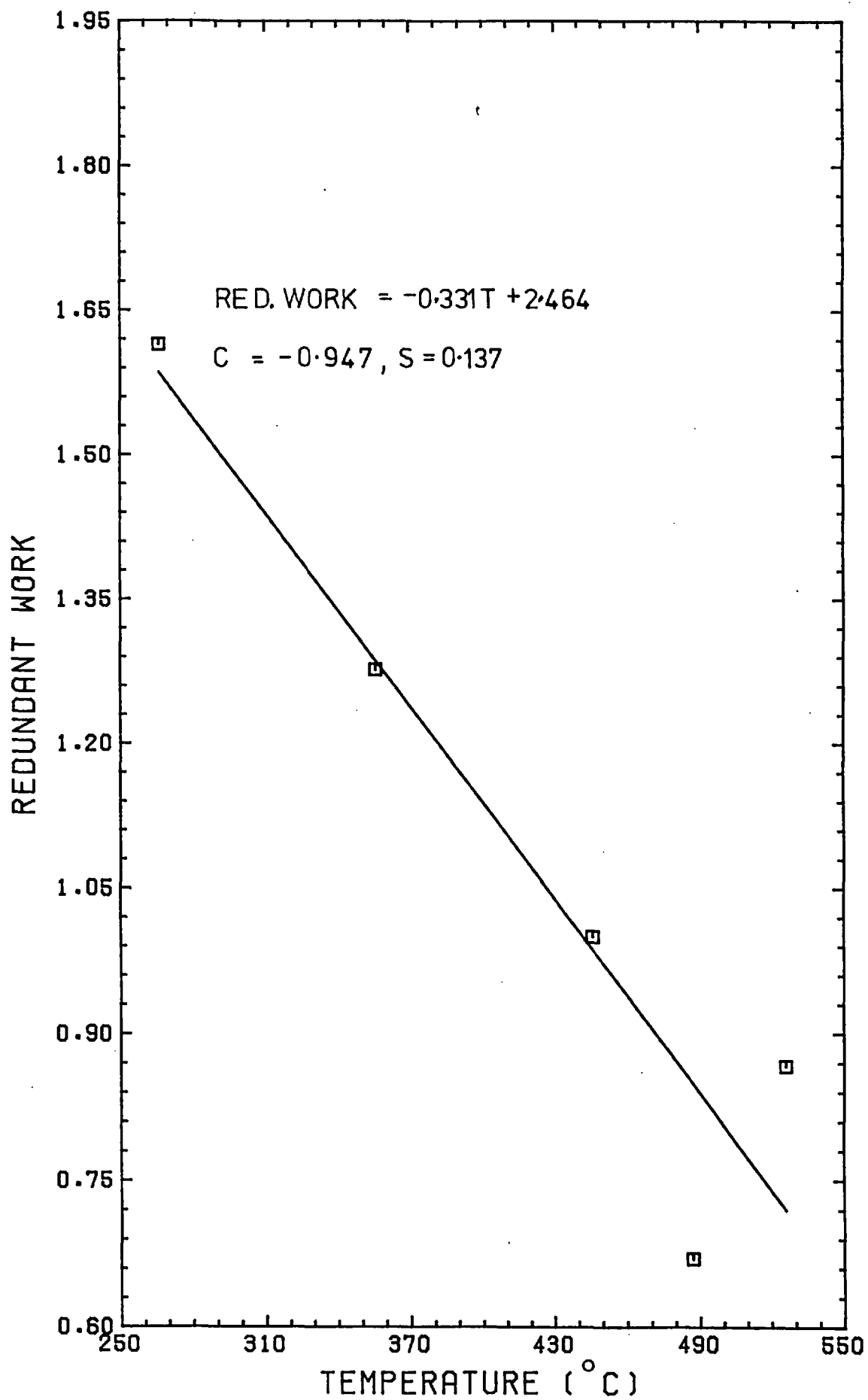
FIG. 51   Effect of extrusion temperature on redundant
           work term (For HE9)

flow stress. It would seem reasonable to assume the
consolidation of a powder during extrusion to be a thermally
activated process, as in sintering. If this is the case
the 'redundant work', employed in consolidating the powder,
and the temperature ought to obey an Arrhenius type of
relation i.e. redundant work α exp(1/T). Fig. 52 shows
such a relationship to exist. The correlation coefficient
of 0.954 indicates that the experimental points fit the
relationship quite well. The effect of a 5% glass content
on the extrusion pressure vs. lnR relationship is very
small indeed (Fig. 50). The redundant work term only
changes from 1.03 to 1.05.

Peak extrusion pressure is plotted against temperature
in Fig. 53 , for the four metals investigated. The cor-
relation coefficients, given in Fig. 53, indicate that
linear relationships definitely exist for these materials.
This suggests that the flow stress is directly related to
the extrusion temperature.

The existence of a peak (denoted by PQ in Fig. 46)
in one of the powder billet load-ram displacement curves
is contrary to evidence reported on the extrusion of Ni-
rich alloys[113] but agrees with work carried out on high
speed steel[122] powder extrusions. During the latter
investigation the removal of the peak was achieved by
using a soft, iron powder "nose" placed in front of the
billet. This break through pressure is quite obviously
more than that necessary to overcome friction between the
compact and the container liner and has been attributed to
temperature quenching at the die/billet interface[114].

In the present series of experiments billets extruded
at the same temperature as the tools also exhibited peaks
in the load-displacement curve, proving the quenching
theory to be inadequate. Sheppard and Castle[13] have
presented an explanation based on dislocation dynamics
but for cast billets their experimental evidence suggests
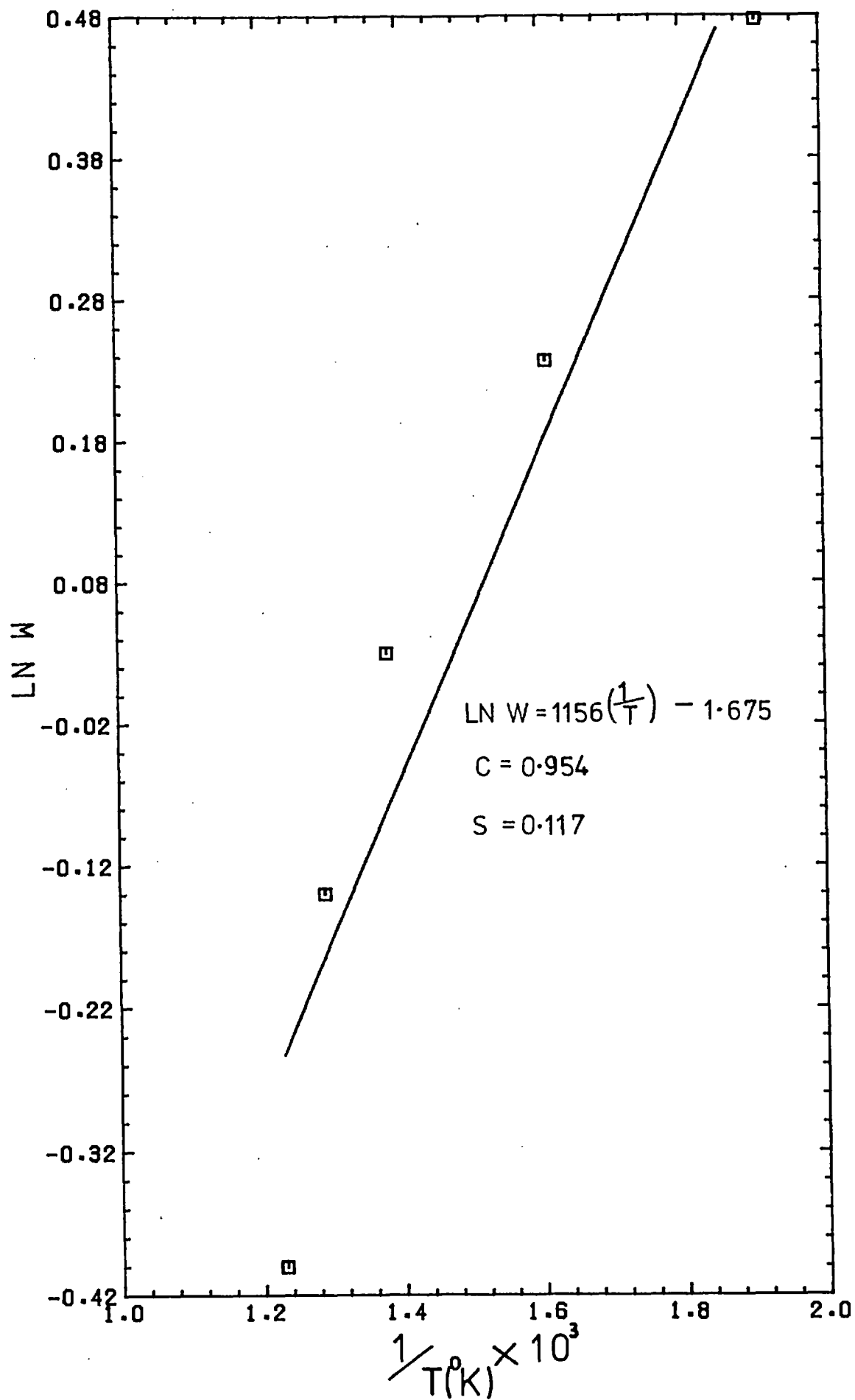
FIG. 52   Logarithm of redundant work as a function of
reciprocal of extrusion temperature
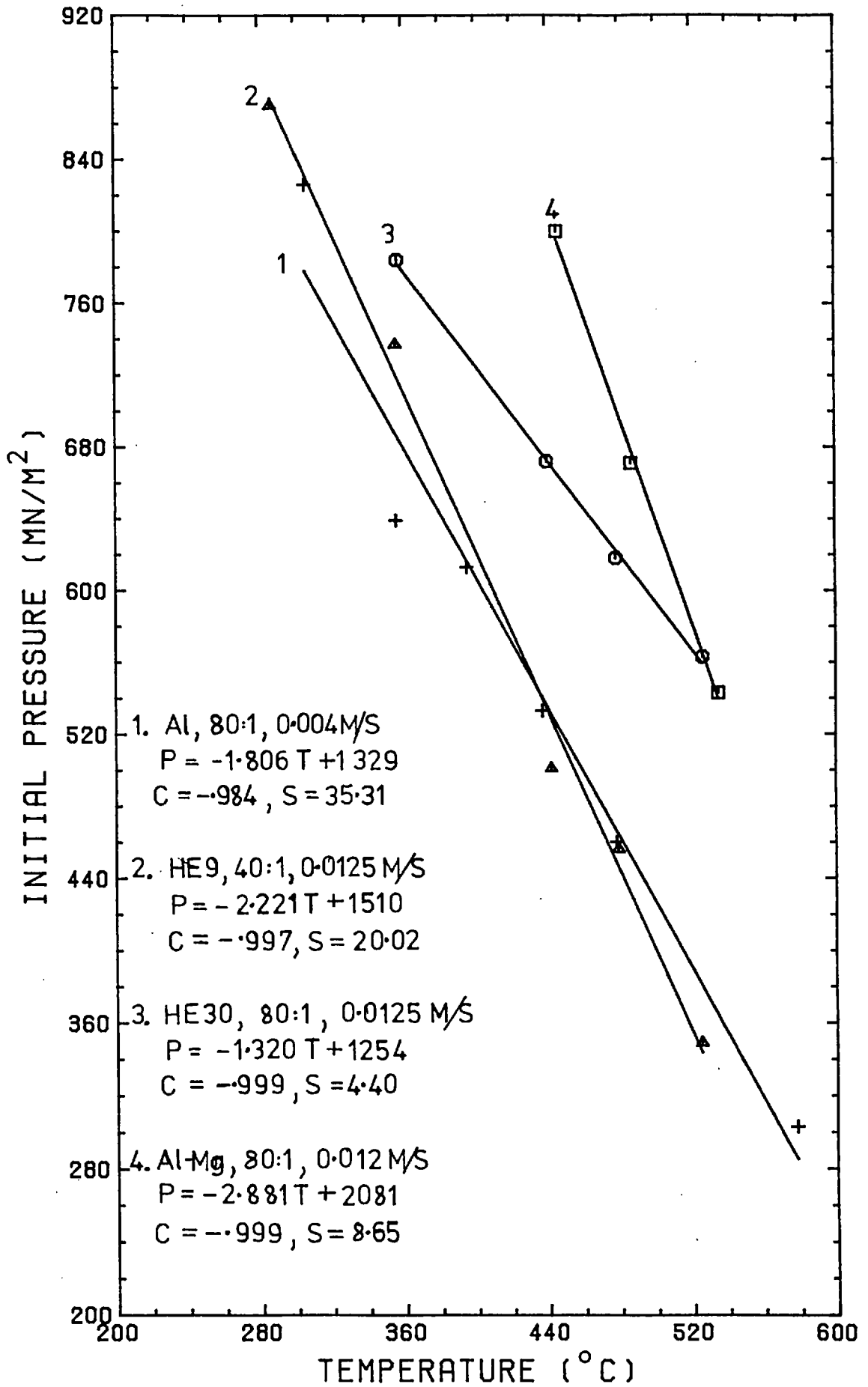
FIG. 53   Initial extrusion pressure as a function of
            extrusion temperature

that the strain rate has little effect. Fig. 46 is in disagreement with this finding since the only variation in extrusion conditions between A and C is in the strain rate. (It should be noted that during extrusion, with a nominally constant ram speed, the ram in fact slows down while the load reaches a peak and then accelerates until the steady state phase begins). However, the maximum load in extrusion C is also lower in this experiment and existing evidence suggests the existence of a threshold load below which these pressure peaks either do not occur or cannot be detected. (In the present series of experiments several compacts, extruded without lubricating pads, also exhibited peaks).

The evidence, then, supports the view that this phenomenon is connected with a dynamic process. At high strain rates an excess of dislocations is generated immediately after the compaction phase and before dynamic softening processes, such as recovery, commence operating. At this early stage in the extrusion cycle the continuous oxide coatings of the powder particles act as barriers to dislocation motion and annihilation causing high dislocation densities within the particles. With fine powders (as in the present case) many particles of 2-3μm exist. Thus the actual sub-grain size is limited, in many cases, by the size of the particles. Limiting the subgrain size increases the flow stress and thus the extrusion load i.e.

$$\sigma \; \alpha \; (\text{subgrain size})^{1/x}$$

As the extrusion proceeds the oxide layers are fragmented allowing the dislocations to move more freely and reduce their number by annihilation. Thus the dislocation density decreases and the flow stress is lowered causing a drop in extrusion load.

When lower strain rates are employed in extrusion the rate of dislocation production is balanced by the rate of the dynamic softening processes. The same argument

could be applied to those extrusions in which the maximum
load is low. This thesis is supported by the experimental
points in Fig.54 . The difference between peak pressure
and steady state pressure increases with strain rate in
HE9, HE30 and HE9 + 5 wt.% glass compact extrusions.
From this argument it would follow that extruding at
higher temperatures should reduce both the magnitude and
the dependence of peak height on strain rate due to increased
dynamic softening rates. The curves for HE9 at 350°C and
540°C (in Fig. 54) support this thesis. It should be
recalled, however, that increasing the strain rate increases
the temperature rise obtaining as well as increasing the
flow stress in the absence of a temperature rise. Hence
the pressure required may be greater or less depending upon
the balance of these variables.

5.5.1 Torsion test results

The primary reason for performing torsion tests was
to obtain flow stress-strain rate relationships over a range
of temperatures. From such information the values of α, the
hot working equation constant and ΔH, the activation energy
of the material may be calculated.

Fig. 55 depicts a schematic representation of the
shape of torque-twist curves obtained, at various temperatures,
for HE9 and HE30 extrudes. As the temperature decreases
the maximum in the torque-twist curve occurs at larger strains.
Jonas[115] and Sellars[131] encountered similar behavour in
commercially pure aluminium. The maximum becomes less well
defined with decreasing temperature until, at 300°C and
below, no maximum exists.

During deformation the flow stress increases as the
dislocations multiply until softening processes begin to
operate. The flow stress is then governed by a balance
between the rates of work hardening and dynamic softening.
If these rates are equal in magnitude (i.e. rate of dislocation
multiplication = rate of dislocation annihilation) a steady
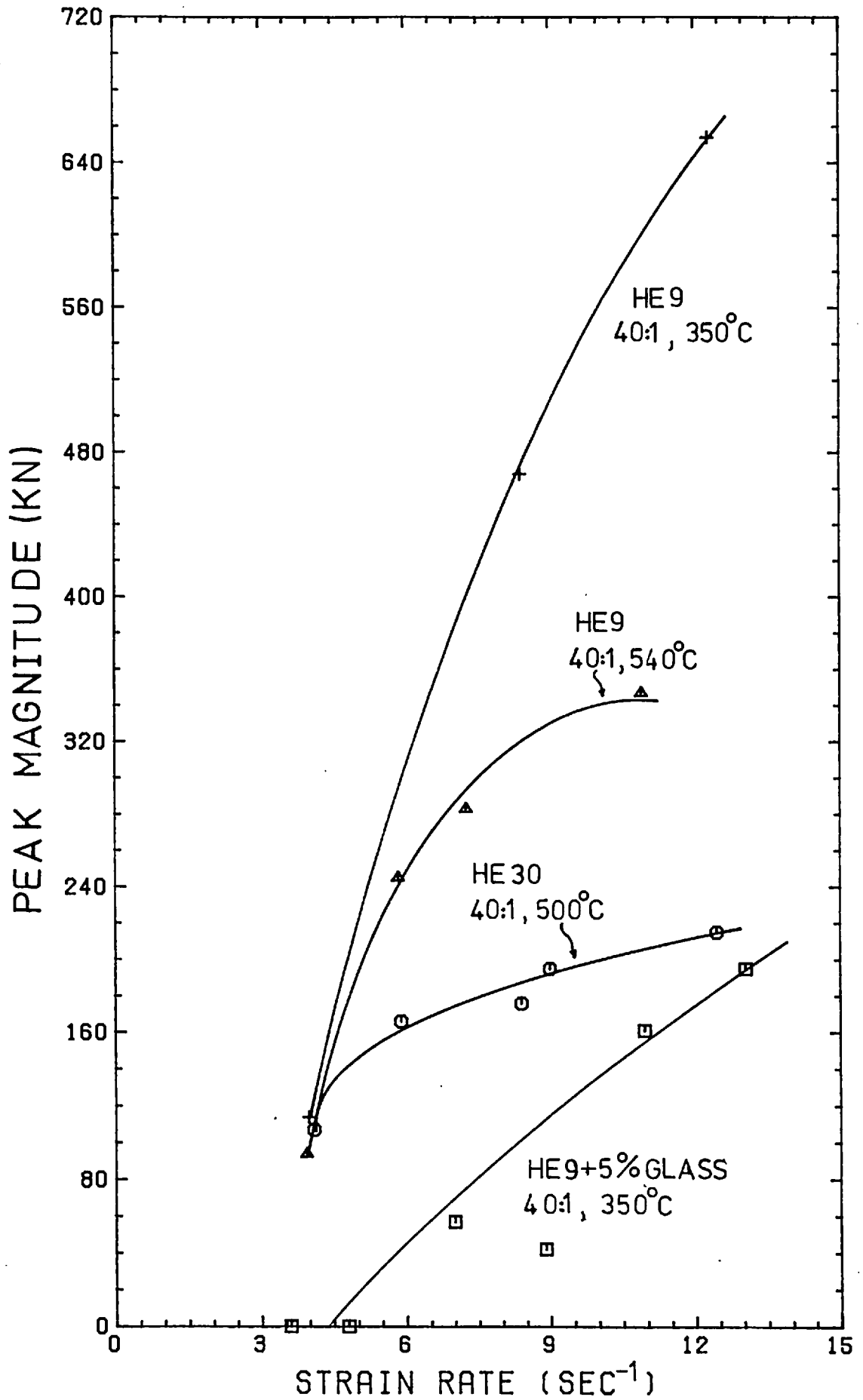
FIG. 54   Effect of strain rate on magnitude of extrusion
            load curve peak
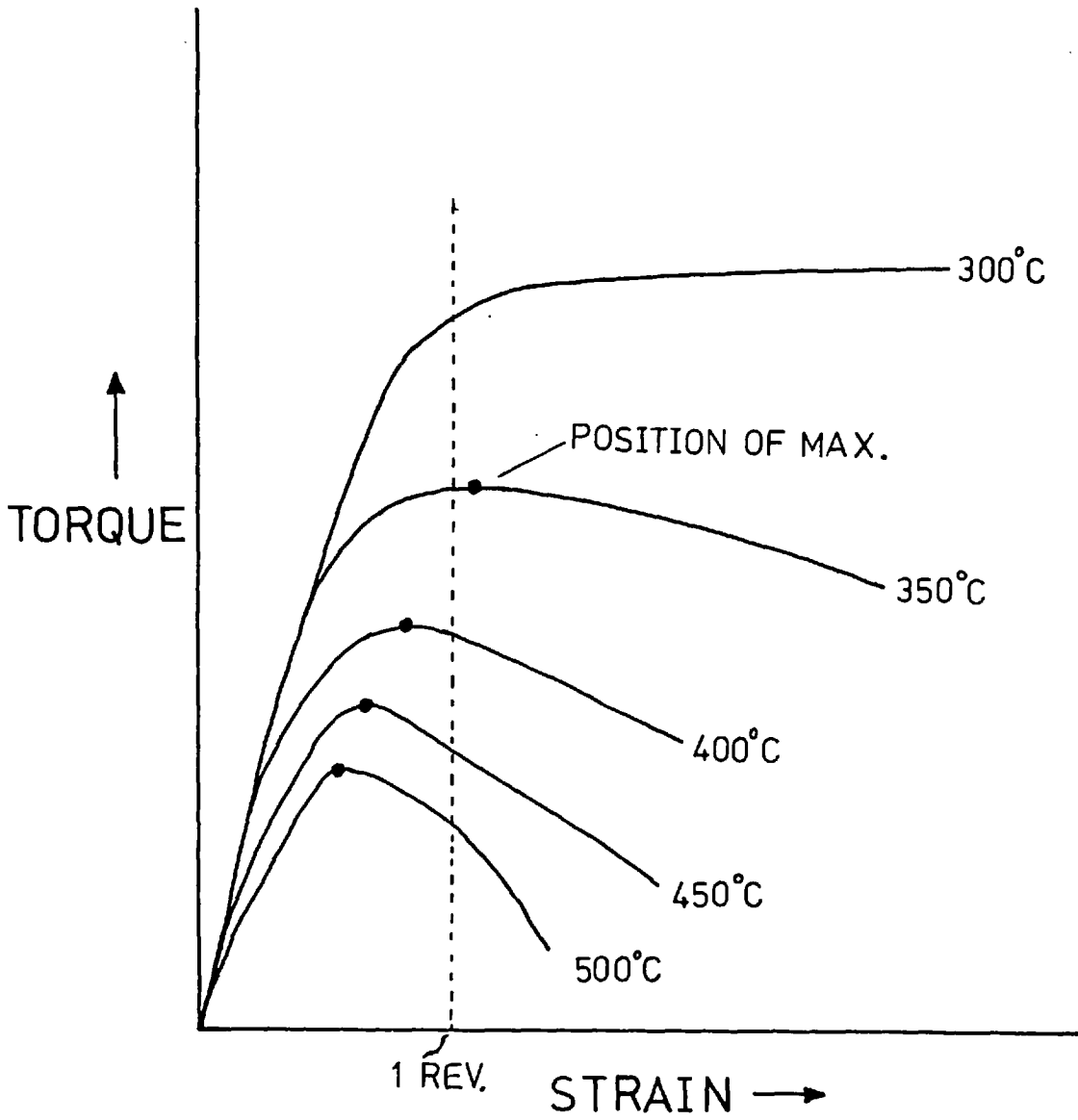
FIG. 55   Schematic representation of torsion curves
at various temperatures

state is reached with the flow stress remaining constant.
If the softening rate is predominant a decrease in flow
stress occurs. In Fig. 55, the position of the maximum
marks the strain at which the softening rate becomes
dominant. As the test temperature is increased, the
critical strain required to initiate softening processes,
such as dynamic recovery, decreases. This causes a shift
in the maximum towards smaller strains.

Tables 12 and 13 give the maximum torque value for
each HE9 and HE30 specimen together with the twist rate.
Plots of maximum torque vs. ln Twist rate (revs/sec) are shown
in Figs. 56 and 57. From the correlation coefficients
given it is clear that linear relationships definitely
exist for both materials at all the temperatures inves-
tigated. Sellars also found similar linear relationships
for several aluminium alloys as did Ormerod[139] for high
purity aluminium.

The Backofen analysis detailed in 3.10.1 was used
to determine flow stresses from the torque values measured.
The m and n values used were calculated and are listed in
tables 14 and 15. The shear flow stress was calculated
(at a constant strain $\sim$ 1/4 rev.) for each specimen and
is listed in tables 16 and 17. (At such an early stage
in the test the effects of temperature rise may be dis-
counted).

Figs. 58 and 59 show the linear relationships between
ln shear flow stress and ln shear strain rate at the various
temperatures. From the correlation coefficients given it
is obvious that both HE9 and HE30 obey a law of the form:-

Flow stress = constant x (strain rate)^n

i.e. $\sigma = C \dot{\varepsilon}^n$
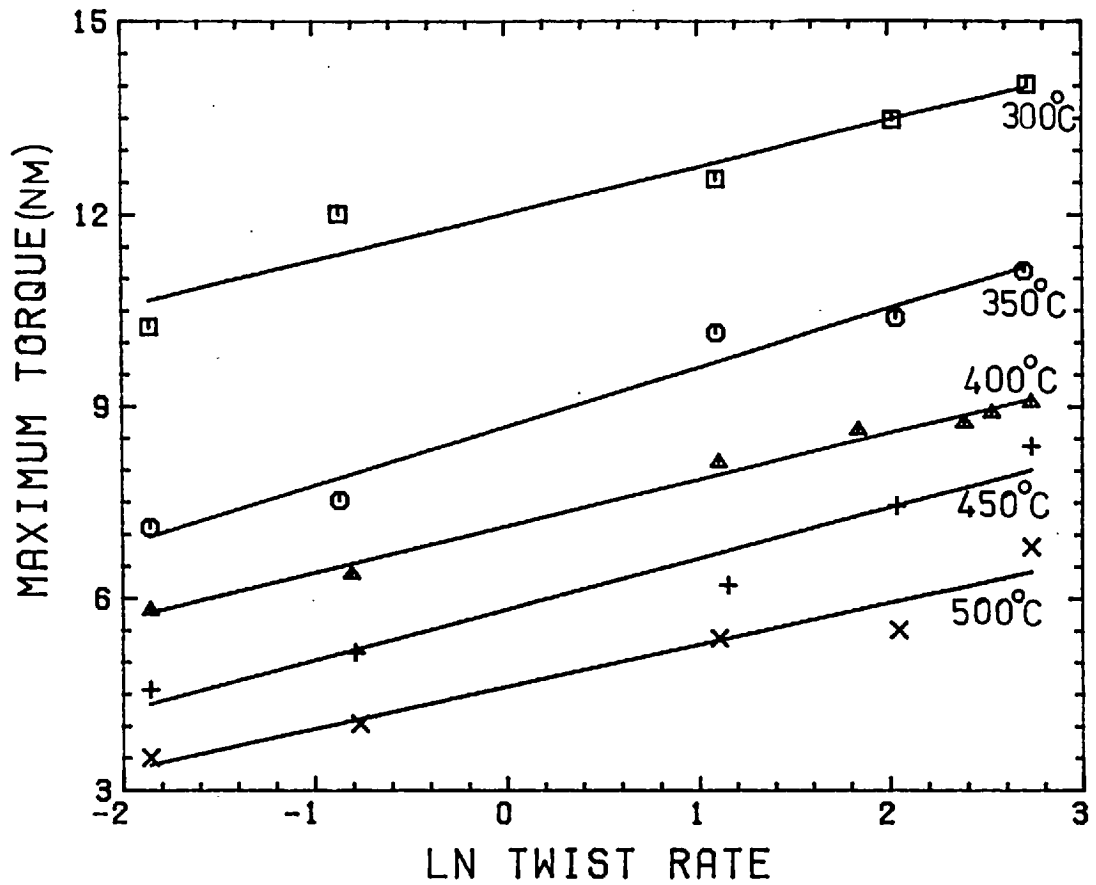
FIG. 56 Maximum torque as a function of twist rate at
various temperatures (HE9)
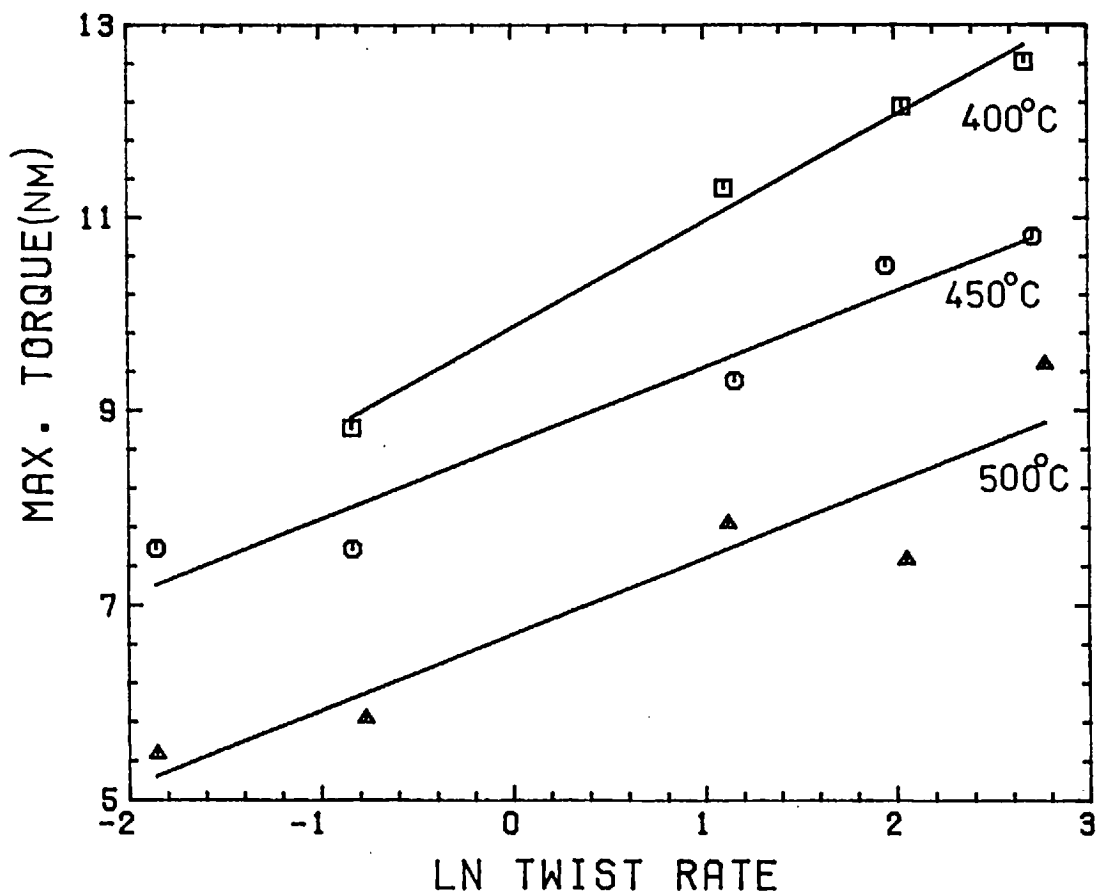
FIG. 57 Maximum torque as a function of twist rate at
various temperatures (HE30)
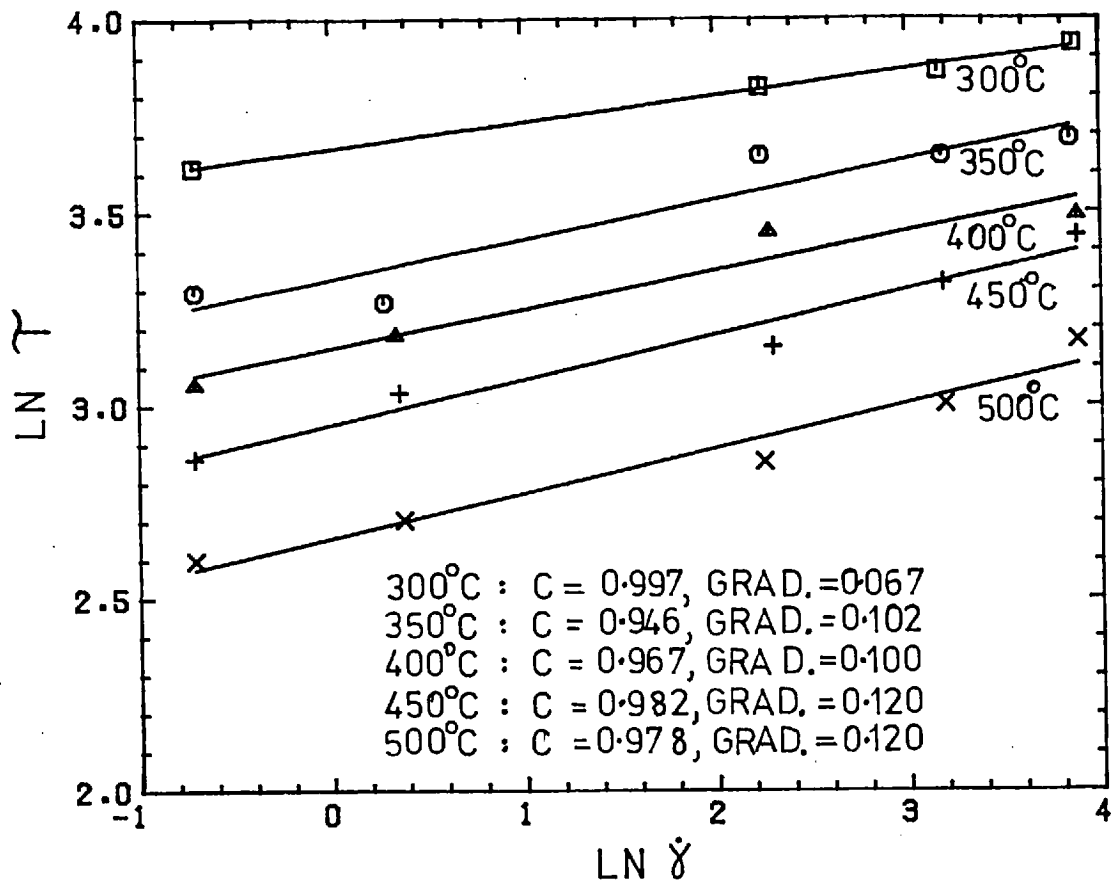
FIG. 58   Relationship between ln τ and ln γ̇ at different
temperatures (HE9)
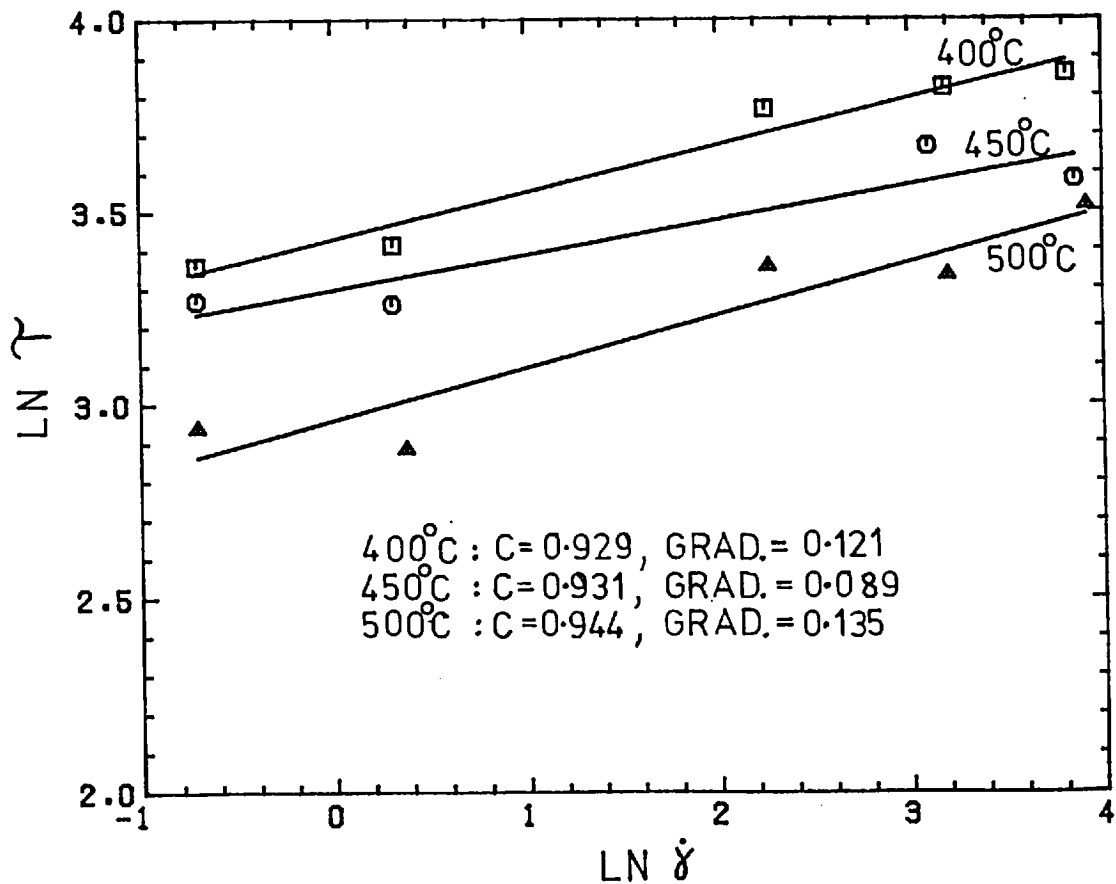
FIG. 59   Relationship between ln τ and ln γ̇ at different
temperatures (HE30)

For HE9 the strain rate exponent n, given in Figs. 58
and 59, varies from 0.07 at 300°C to 0.12 at 500°C.
Lack of data prevents conclusions being drawn about the
effect of temperature on the strain rate exponent for
HE30.

Alder and Philips[134] found that the strain rate
exponent of aluminium decreased dramatically with tem-
perature from 550-20°C (for compression to 40% reduction).
The strain rate exponent, n, was found to very from 0.16
to 0.02 over this temperature range. Thus it can be seen
that the present torsion results agree well with the com-
pression results of Alder and Philips.

5.6.1 Determination of the hot working constants and the activation energy

According to the theory in 3.6.2 the constant, α,
may be obtained from the gradients of ln σ vs. ln $\dot{\varepsilon}$ plots
at high stress levels and ln σ vs. $\dot{\varepsilon}$ plots at low stress
levels. i.e. β and n_2 values. Values of β, n and α,
for HE9 and HE30, at each torsion test temperature are
listed in tables 18 and 19. Apparently α varies signi-
ficantly with temperature. (Fig. 60 shows that α increases
with temperature.) As α, in fact, is defined as a temperature
independent constant it is quite obvious that this method
is unsatisfactory. In order to use this method properly,
high and low stress levels must be defined clearly. For
this purpose a value of α is required, which defeats the
object. An alternative approach must be adopted.

$$\dot{\varepsilon} = A_1 (\sinh \alpha\sigma)^n \exp(-\frac{\Delta H}{RT}) \qquad (32)$$

by definition: $Z = A_1 (\sinh \alpha\sigma)^n$

substituting: $(\frac{Z}{A_1})^{1/n} = \sinh \alpha\sigma$

$\therefore \qquad \alpha\sigma = \sinh^{-1} (\frac{Z}{A_1})^{1/n}$
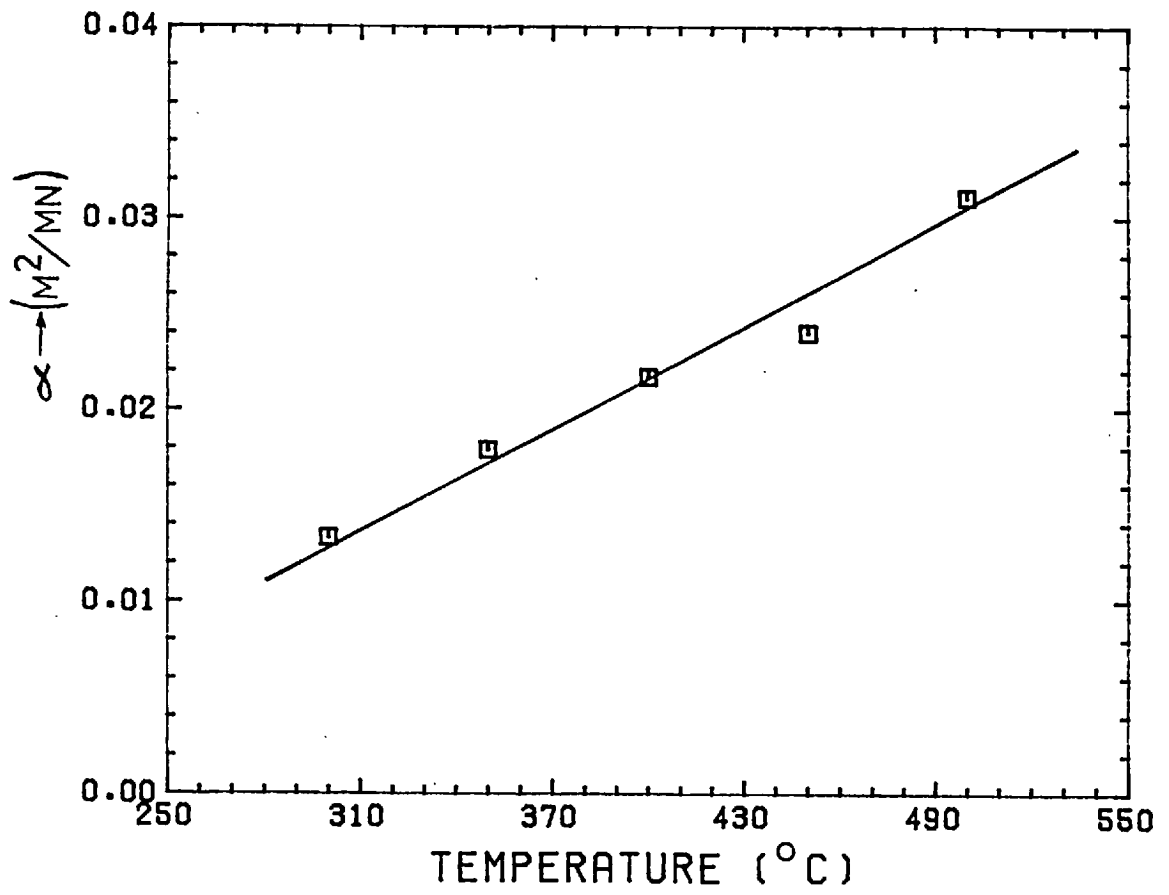
FIG. 60   Effect of temperature on alpha

substituting for $sinh^{-1}$

$$\alpha\sigma = \ln \left[(\frac{Z}{A_1})^{1/n} + \sqrt{(\frac{Z}{A_1})^{2/n} + 1} \right]$$

$$\therefore \quad \sigma = \frac{1}{\alpha} \ln \left[(\frac{Z}{A_1})^{1/n} + \sqrt{(\frac{Z}{A_1})^{2/n} + 1} \right] \quad (91)$$

Equation 91 contains four variables: α, ΔH, A_1 and n. If guesses of α, ΔH, A_1, and n are supplied, the minimization routine described in 3.4.1 can be used to minimize the difference between experimental flow stresses and theoretical values calculated using (91) by changing α, ΔH, A_1 and n. The values of these variables which give the minimum difference between theoretical and experimetnal stresses are the best which can be obtained from this data.

The results for the HE9 and HE30 torsion test data are listed in table 20. The activation energies of 167, 224 and 170,881 J/mole for these alloys are somewhat higher than the value for extruded commercially pure aluminium powder of 155,000 found by Sheppard and Chare[135] and the value of 156,000 found by Wong and Jonas[68], also for aluminium. (The values obtained by these other investigators are equivalent to the energy of self diffusion for aluminium). This difference is probably caused by the alloy content of the HE9 and HE30 together with the oxide dispersion obstructing dislocation motion and therefore increasing the energy barrier to be overcome for recovery processes to occur. The α values found in the present investigation (0.038 and 0.040) compare very well with those found by Wong and Jonas (0.040) and by Sheppard and Chare (0.031-0.042). The n values of 5.16 and 3.87 also compare well with those of Wong and Jonas (4.2). Figs 61 and 62 show ln Z vs. ln sinh $\alpha\sigma$ plots for the HE9 and HE30 torsion data. The correlation coefficients of 0.988 and 0.976 respectively, indicate that the general hot working equation fits the experimental data rather well. Using the activation energy and α values obtained from the torsion results, plots of ln Z vs. ln sinh$(\alpha\sigma)$,
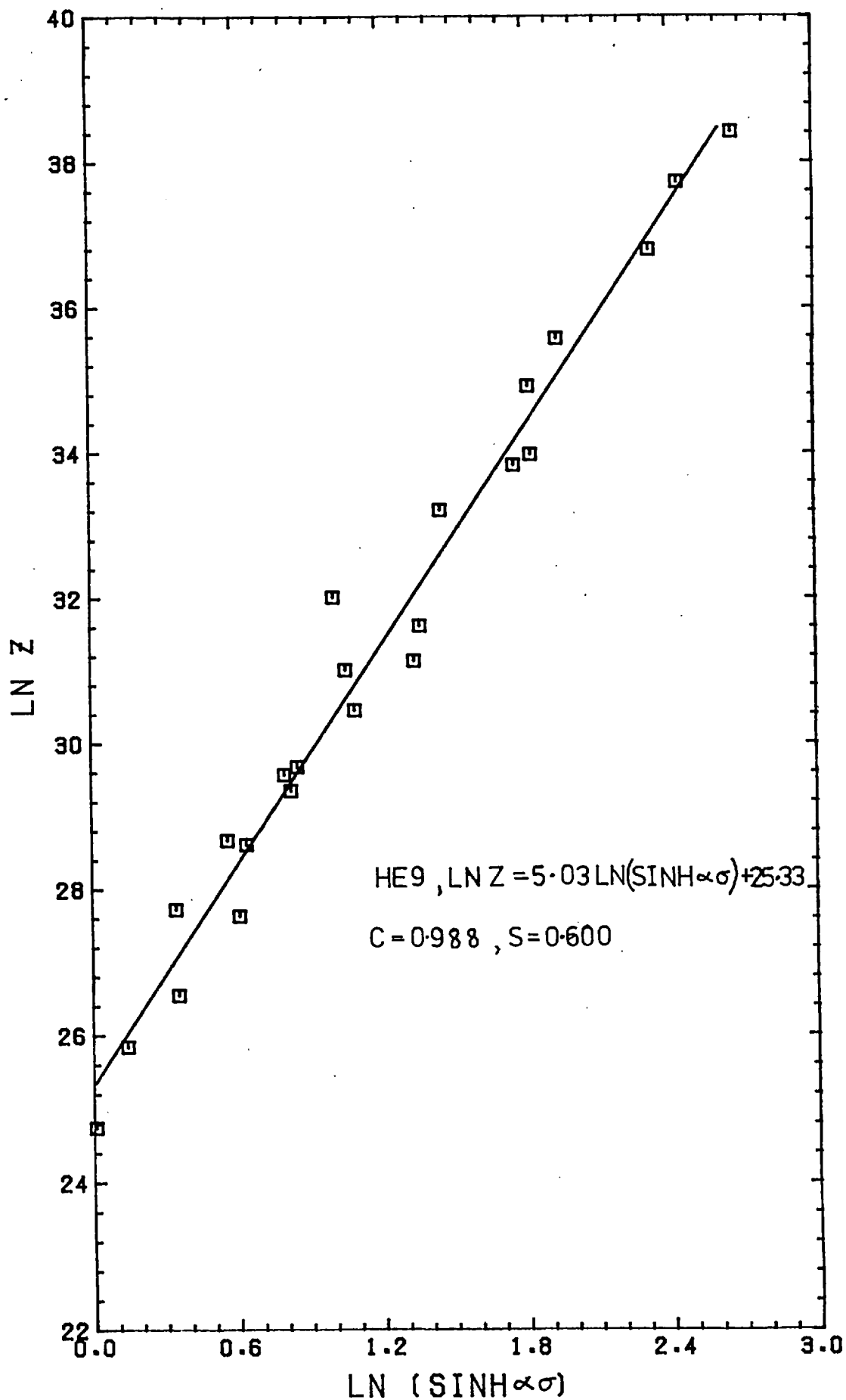
FIG. 61 ln sinh(ασ) vs. ln Z   (HE9 Torsion Tests)
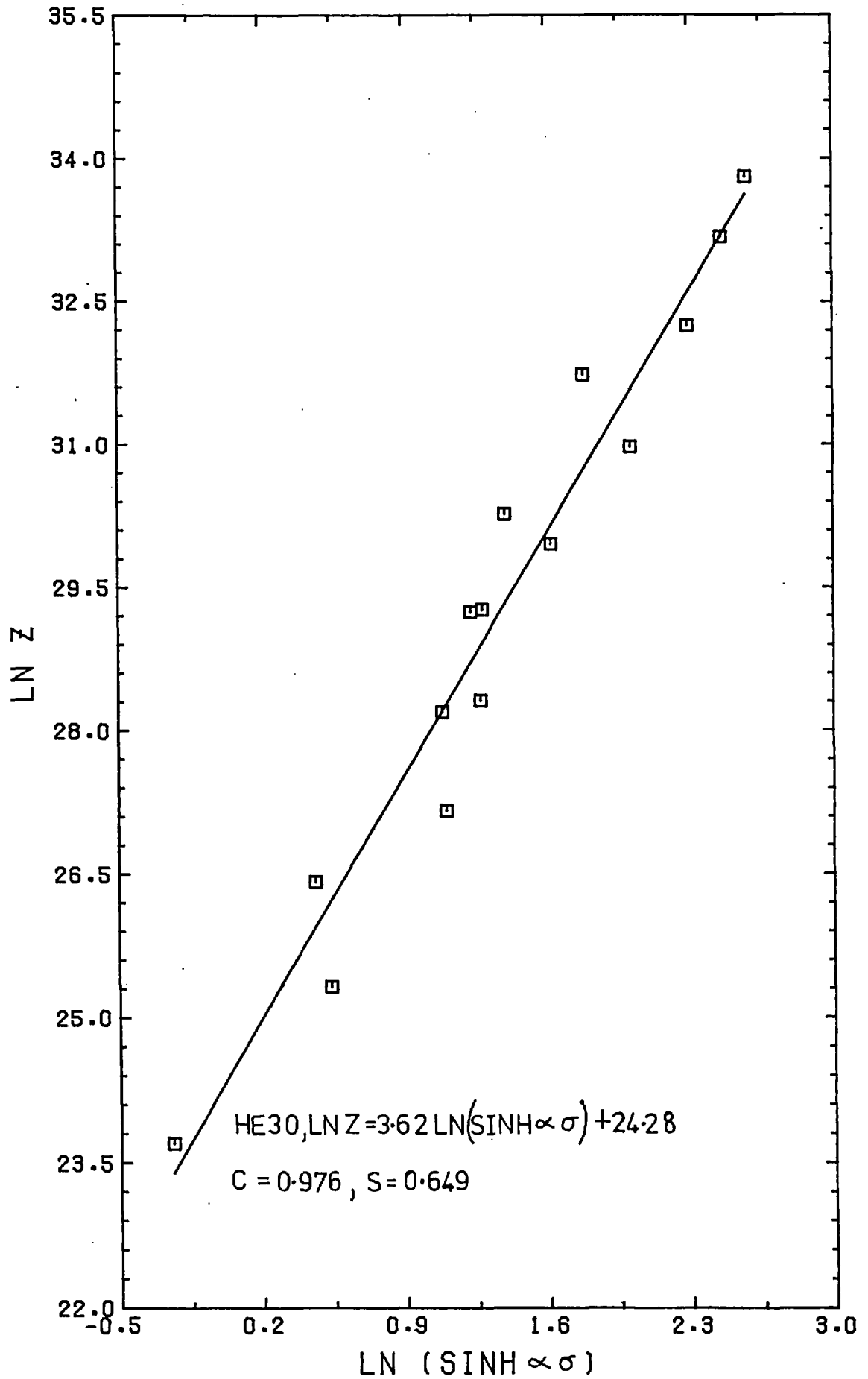
FIG. 62   ln sinh(ασ) vs. ln Z (HE30 Torsion Tests)

for extrusion data, are shown in Figs. 63, 64 for HE9
and Fig. 65 for HE30 (The extrusion temperatures were
calculated using the integral profile technique).
Clearly, the extrusion data points do not fit the hot
working theory nearly as well as the torsion results.
Obviously, the flow stress, strain rate and extrude
temperature values derived from extrusion results are
much less accurate than values derived from torsion
data. Therefore greater inaccuracies must be expected
when working with extrusion data. The gradients of the
plots in these three figures give n values of 3.74 and
2.98 for HE9 and 5.07 for HE30, respectively, compared
to the values of 5.16 and 3.87 obtained from the torsion
results. Now the strain rate sensitivity of a material
is proportional to 1/n. Therefore the higher the n
value the lower the strain rate sensitivity. If the
thesis that powder compacts are less strain rate sen-
sitive than solid billets is correct one would expect
n values derived from the extrusion of powder billets
to be higher than n values derived from torsion tests
on the consolidated extrude. This appears to be the
case for HE30 but not for HE9. Thus some doubt must
exist as to the relative magnitudes of the strain rate
sensitivities of powder and cast material. One possible
explanation for this discrepancy between the two powders
is outlined below. The flow stress values obtained from
the torsion tests were calculated from the torque-twist
curves after 1/4 of a revolution. The readings were
taken at this early stage on the assumption that the
temperature rise of the specimen could be neglected.
This is a reasonable assumption at the higher temperatures
where the flow stress is small. During the low temperature
experiments, especially at high strain rates, the tem-
perature rise may not be negligible, due to the larger
flow stress of the material. Thus data points, in Figs
61 and 62 at the top end of the ln sinh $\alpha\sigma$ scale, should
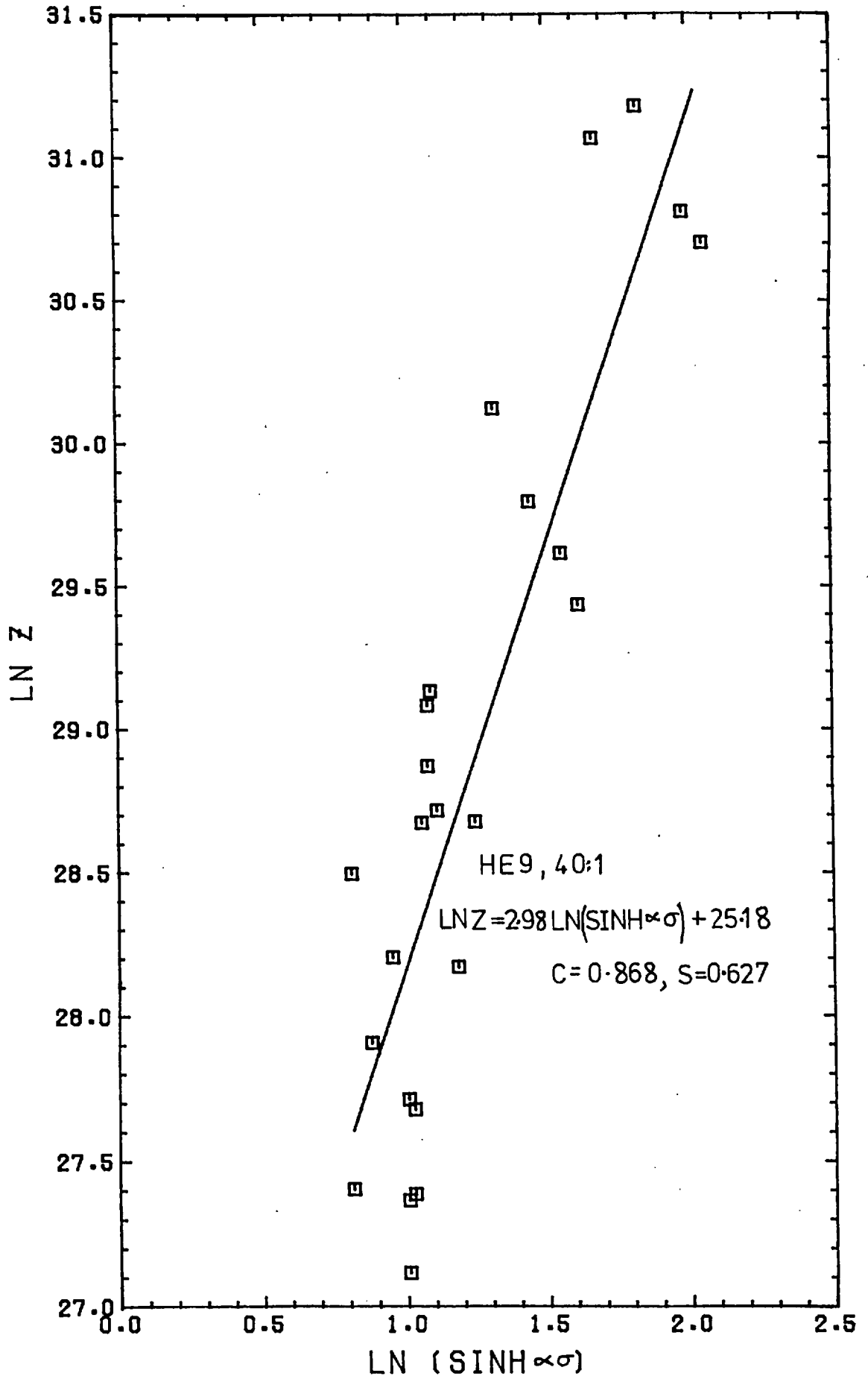
FIG. 63 ln sinh(ασ) vs. ln Z (HE9 40:1 Extrusions)

FIG. 64 ln sinh(ασ) vs. ln Z (HE9 80:1 extrusions)

HE30, 40:1

LNZ = 2·92 LN(SINH ∝ σ) + 23·91

C = 0·900, S = 0·388
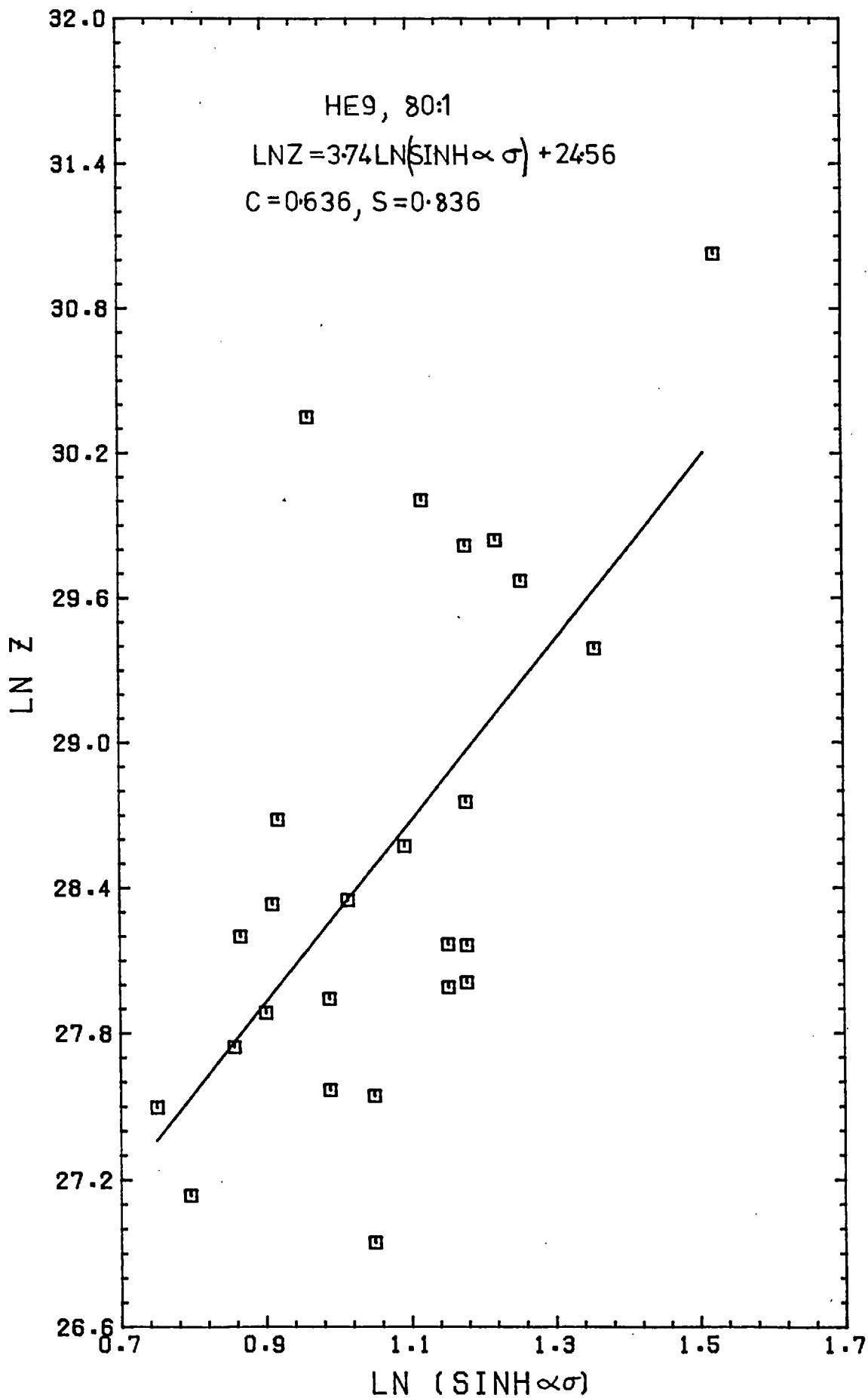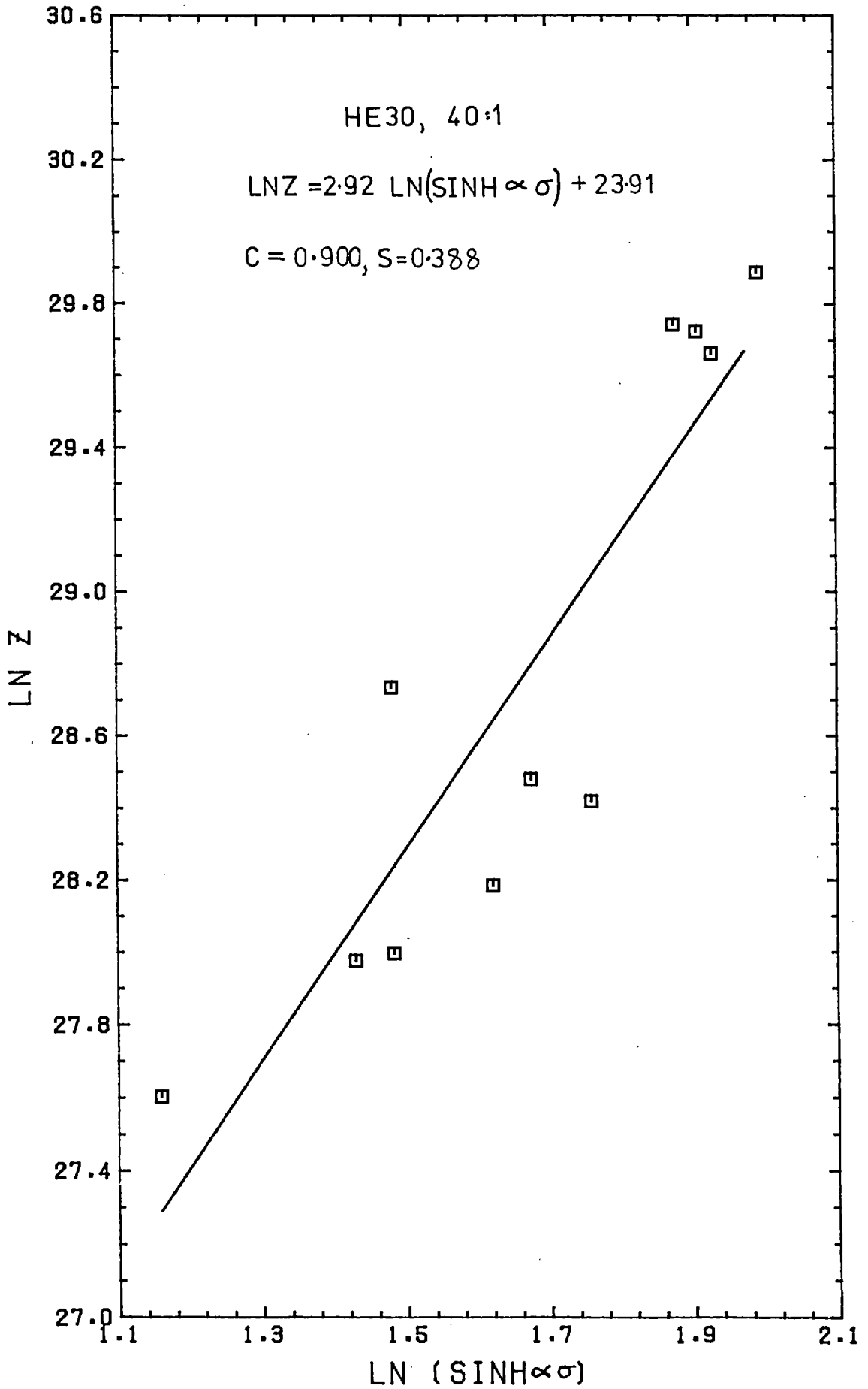
FIG. 65 ln sinh(ασ) vs. ln Z (HE30 40:1 extrusions)

really be moved to slightly lower ln Z values. This in
turn would produce a lower gradient and thus a lower n
value, indicating a larger strain rate sensitivity in
the consolidated extrude used in the torsion tests.
Thus the strain rate sensitivities of consolidated HE9
and HE30 may be more than $\sim$ 1/5.16 and 1/3.87 respectively.

5.7.1 Partial extrusions - flow patterns

The flow patterns obtained for extrusion ratios
of 40:1 and 180:1 (both at 450°C) are shown in Plate 6(a)
and (b) respectively. In both cases the dead metal zone,
consisting of the pad material, is clearly visible. Conical
deformation zones including semi-angles of 66° and 69°
respectively are fairly distinct. For ratios of 40:1
and 180:1 the minimized axisymmetric single triangle upper
bound solution predicts semi-angles of 54° and 56°, an
error of approximately 17%. Several workers including
Childs[136] have used grids machined on split billet faces
to study flow patterns and to estimate strain rates during
extrusion. Obviously this technique cannot be applied to
powders.

Plate 7 shows a fibre composite billet, partially
extruded at 450°C ($\sim$ 170°C above the softening point tem-
perature) at a ratio of 10:1. The formation of the fibres
in the deformation zone is clearly shown. The elongation
of the fibres near the extrude surface is much greater
than that of the central fibres. This confirms the concept
of greater deformation occuring near the billet surface
during extrusion. As previously mentioned in 2.3.1 this
greater deformation can produce a surface layer of recry-
stallised material in the extrude giving undesirable
product properties. The degree of fibre misalignment
in the extrude in Plate 7 is negligible and so an assump-
tion of uniaxially aligned fibres is quite reasonable.
Drawn on the micrograph, in Plate 7, is one half of the
upper bound field predicted, for a 10:1 extrusion ratio,
by the axisymmetric solution discussed in 3.3.1. Clearly

(a)

(40:1)

(b)

(180:1)

PLATE 6   Partial extrusions

(10:1)
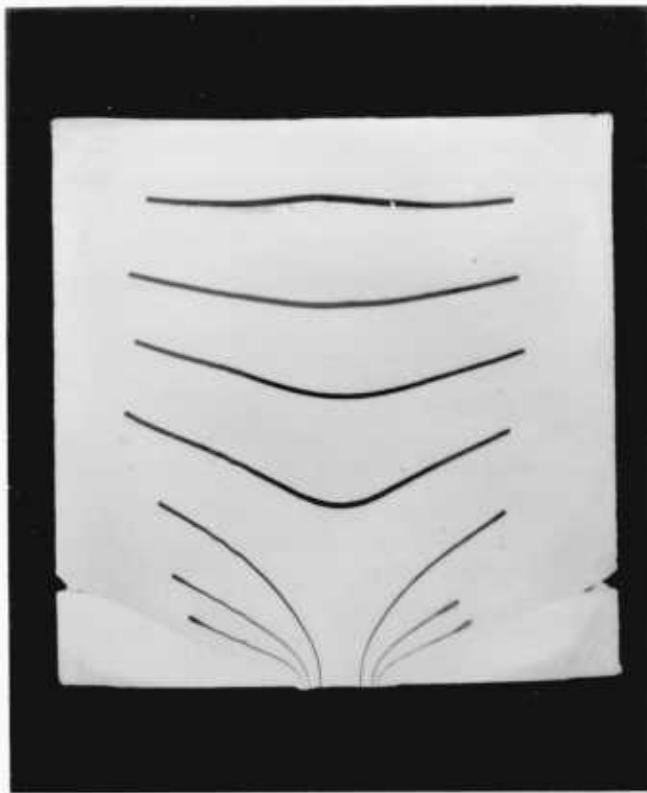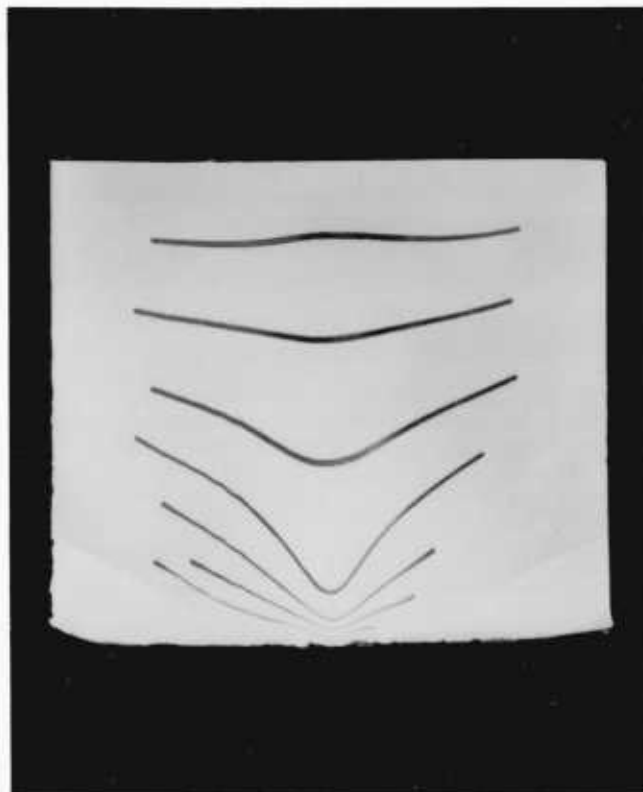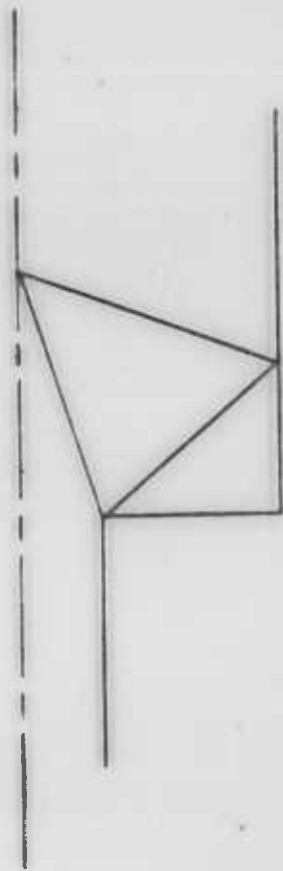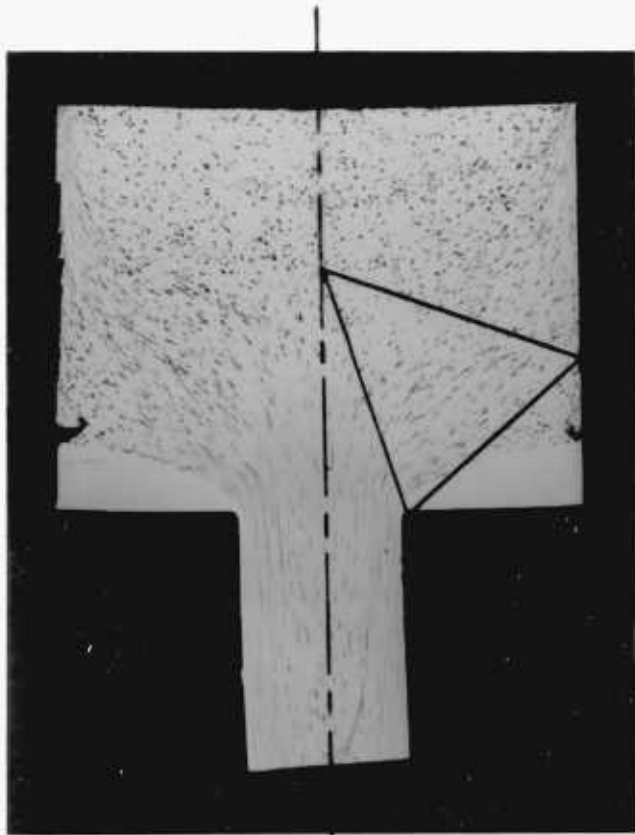
PLATE 7

Partial extrusion showing fibre formation

(10:1)
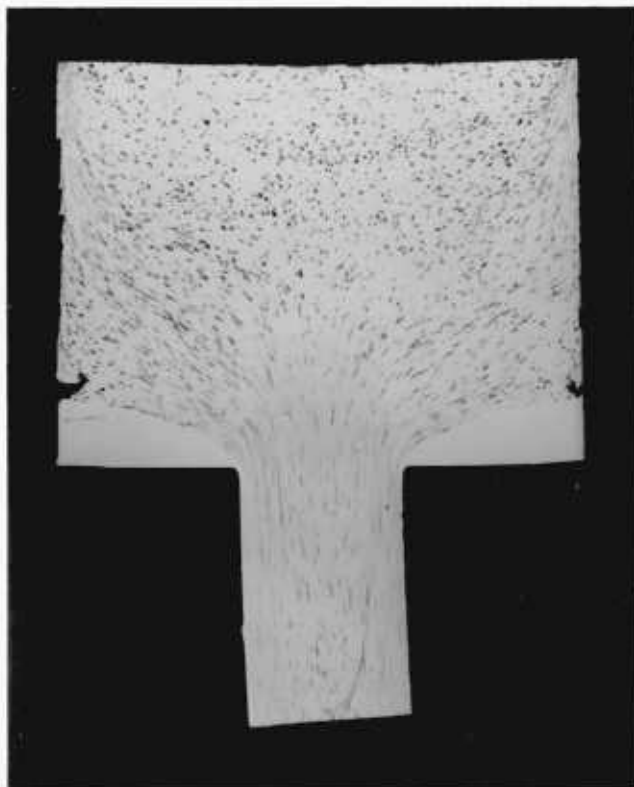
PLATE 7

Partial extrusion showing fibre formation

the theoretically predicted field agrees quite well with
the actual deformation obtaining and the fibres are not
fully elongated until they have almost reached the final
(theoretical) velocity discontinuity AB. The calculation
in 3.7.5 predicted a critical aspect ratio i.e. (fibre
length/fibre diameter) of ~ 40 and a minimum extrusion
ratio of 10:1, for ideal fibres of 2412 MN/m^2 tensile
strength. In practice the fibres are far from ideal and
so their tensile strength is considerably less than 2412
MN/m^2. Thus the true critical aspect ratio is $<<40$.
(In 5.9.6 the tensile strength is estimated ~ 890 MN/m^2
giving a critical aspect ratio ~ 15). Thus in practice
the fibres attain the critical amount of elongation some
time before reaching AB. Due to variations in deforma-
tion across the section, the outer fibres attain this
critical aspect ratio at an earlier stage than the central
fibres.

5.8.1 Effect of extrusion conditions on extrude surface finish

A good product surface finish is essential if any
extrusion process is to be commercially successful. Surface
defects can provide sites for crack initiation, leading to
reduced mechanical strength, and also lower resistance to
degradation by the elements. If the extrude is to be
successfully anodized a homogeneous, good quality surface[119]
is vital. Even if the extruded product is not subjected
to loading or exposed to the elements, the surface finish
must have an acceptable appearance.

Table 21 used in conjunction with Plates 8 and 9
summarises the effects of extrusion temperature, ram
speed and glass content on the surface finish of the
various materials. Each combination of ram speed (or
glass content) and extrusion temperature is represented
by a letter which refers to a micrograph in Plate 8 or 9.

HE9 extrude,with a good surface finish, is fairly easy to produce over a wide range of extrusion conditions. The only defects occurring are scoring, due to die pick-up, (Plate 8b),and disintegration of the surface layer of pad material (Plate 8c). Generally the surface finish improves with increasing ram speed and temperature. For ram speeds from 3-8 mm/sec temperatures in excess of 500°C must be employed. However, at 13 mm/sec any temperature, between 250 and 540°C, is satisfactory.

HE30 behaves in a similar manner. However, the surface finish appears to be more dependent on ram speed and less on temperature. A satisfactory finish is produced using any ram speed from 8-13 mm/sec over the temperature range 350-540°C. Pearson[116] recommends a temperature of 450-490°C and a ram speed of approximately10mm/sec for cast 51S alloy (similar in composition to HE30). Neither HE9 or HE30 suffer from "hot shortness" at the higher extrusion temperatures. Although, generally, the ductility of aluminium increases with temperature its flow stress decreases and thus high speed - high temperature deformation tends to cause tearing in the weakened aluminium. Many aluminium alloys are especially susceptible to hot shortness. A typical example of such an alloy is any of the strong Al-Mg-Cu-Zn alloys which contain the $Al-CuAl_2$ eutectic. During extrusion the surface "layers" of the extrude heat up more than the central core. In many cases the eutectic temperature is exceeded and "regions" of eutectic composition begin to melt i.e. incipient melting. (Even if no actual melting occurs, these regions become so weak that their flow stress is $\sim$ zero). Secondary tensile stresses acting in the die neck, elastic expansion stresses exerted on emergence from the die and thermal stress due to cooling cause cracking and tearing in the extrude surface. This is the defect known as "hot-shortness". The use of the powder extrusion process ensures a fine, homogeneous distribution of second phase particles minimizing the occurence of segregation. This, in turn,

reduces the likelihood of hot shortness cracking.

In the case of Al-Mg the surface finish - ram speed dependency is reversed. A satisfactory extrude is only obtained with lower ram speeds of 3-8 mm/sec. The effect of temperature over the range investigated, 400-500°C, appears to be very slight. Al-Mg alloys are notoriously strain rate sensitive during extrusion. Extruding too rapidly often produces a poor quality extrude due to surface checking and/or die pick-up.

Extrusion of the Al powder compacts is more difficult. A satisfactory surface finish is only obtained if high temperatures, ∿ 600°C, and fast ram speeds, ∿13mm/sec, are used. Other extrusion conditions produce a "fir-tree" type defect (Plate 8d). This type of defect is usually associated[11] with hot shortness. In this case, however, this defect occurs when low temperatures and ram speeds are used. Remembering the absence of lubricating pads, the defect may be caused by die pick-up. Secondary tensile stresses, generated in the region of the die, may also play a part. At the lower temperatures the flow stress of the Al is higher and it becomes brittle and may thus suffer cracking due to these stresses. Thus the extrude might be said to suffer from "cold shortness". Wilcox and Whitton[132], while extruding duralumin and Parsons et al[133], while extruding aluminium[133] (both at low temperatures and ram speeds) encountered a "fir-tree" defect due to "cold shortness".

Additions of 5 wt.% glass have little effect on the surface finish of HE9 extrudes. An acceptable product is obtained over a wide range of extrusion conditions. Once again the faster ram speeds, 8-13 mm/sec, give the best results in the temperature range 350-550°C. The maximum amount of glass which can be successfully incorporated in an extrude is approximately 6-7 wt.%. Extrudes

(a)

(b)

(c)

(d)

PLATE 8   Surface finish of HE9 extrudes

(e)

(f)

(g)

(h)

PLATE 9   Surface finish of HE9 +5 wt.% glass extrudes
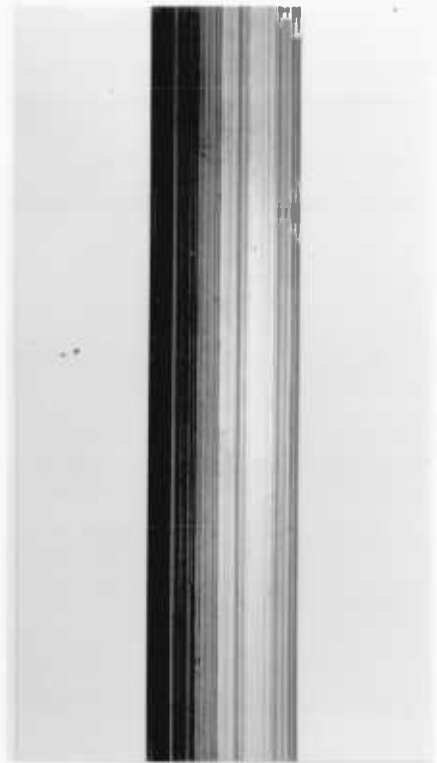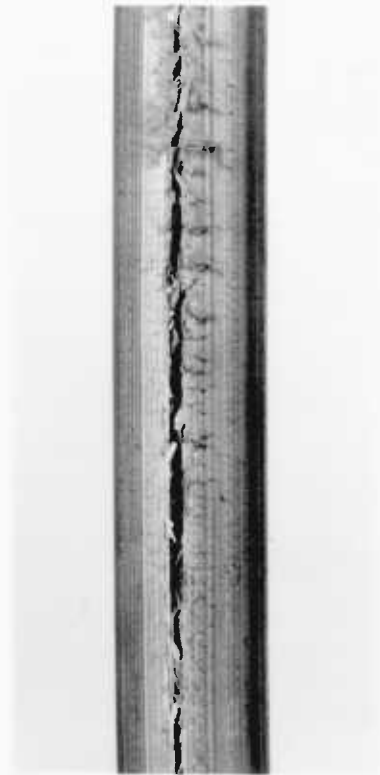
containing more than this amount suffer from splitting
(Plate 9 (g) and (h)) due to elastic expansion of the
glass.

The limited number of glass reinforced Al-Mg
extrusions produced also exhibit an improvement in
surface finish with increasing ram speed. This trend
is the reverse of that exhibited by the unreinforced
Al-Mg extrudes.

Over the temperature range 375-550°C all of the
reinforced aluminium extrudes are unsatisfactory. A
"fir-tree" defect due to cold shortness and die pick up
is common at the lower ram speeds. Increasing the ram
speed produces only a very slight improvement.

5.9.1 Stress-strain behaviour of the extrude

The results of the tensile tests are given in
table 22 . Great difficulty was experienced in testing
the glass reinforced specimens at elevated temperatures
due to a tendency for the specimens to fracture in the
grips. The shapes of the load-extension curves for the
different materials are represented schematically in
Figs. 66 and 67.

Unreinforced HE9 and HE30 specimens display a fairly
linear elastic region followed by an extended plastic
region in which the load increases steadily up to a
maximum value at which point necking occurs. The load
then gradually decreases until fracture occurs, usually
after quite large elongations. The glass reinforced HE9
behaves similarly in the elastic region. However, during
plastic deformation the curve is significantly steeper (in
this region the glass still behaves elastically) as predicted
in 3.7.2. A very limited amount of necking occurs, after
the maximum load is reached, quickly followed by fracture.
The elongation to fracture is noticeably reduced by the
presence of the brittle glass.
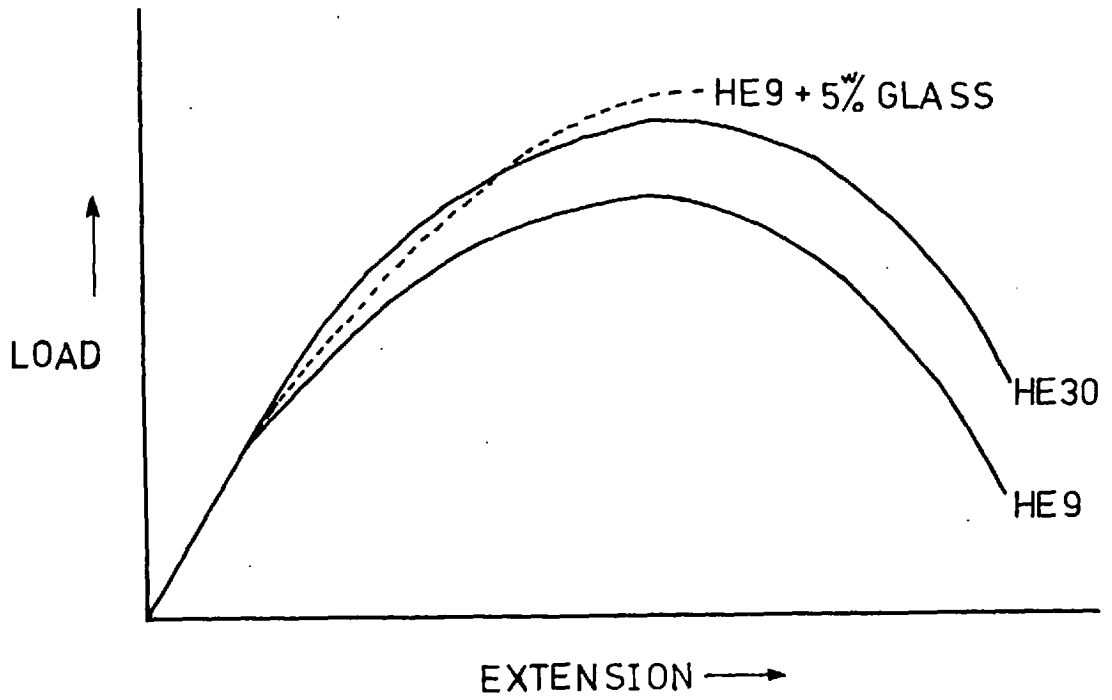
FIG. 66 Load vs. extension curves from tensile
tests (HE9, HE30, HE9 + 5wt.% Glass)
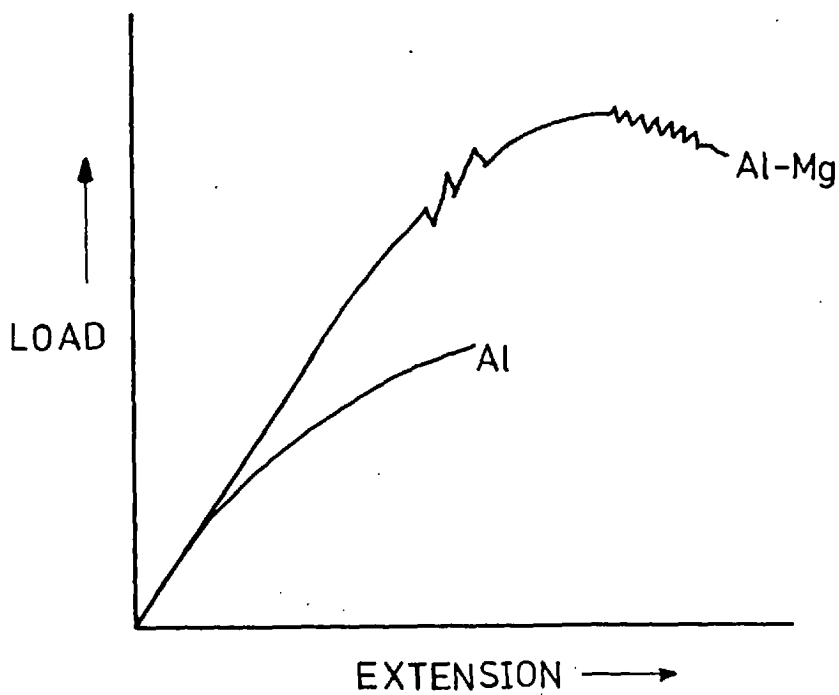
FIG. 67 Load vs. extension curves from tensile
tests (Al, Al-Mg)

Several tests were performed on larger HE9,
HE9 + 5 wt.% glass and HE30 tensile specimens using a
standard 50mm strain gauge, to obtain values of elastic
moduli.   The results are given below

	HE9	HE9+5 wt.% glass	HE30	Al (Published)
Elastic Modulus (MN/m^2)	67.3	61.2	72.8	71

The values for HE9 and HE30 are in good agreement with
the published value for aluminium.   The elastic modulus.
of the reinforced HE9 is about 13% less than that of
aluminium.   Theoretically the modulus of the material
should remain unaffected by the addition of fibres of
similar modulus.   However, cracks introduced by the glass
addition may well cause this reduction in modulus. Although
the presence of such cracks in the matrix reduces the
modulus of the composite, the U.T.S. is still higher than
that of unreinforced material.   This is because the tensile
strength of the fibres has a much larger influence on the
U.T.S. than the strength of the matrix does, within reason.
i.e. as long as the matrix does not disintegrate .

The Al specimens (Fig. 67) possess a very limited
elastic region.   Brittle fracture occurs after small plastic
strains before the gradient of the curve ever reaches zero ·
i.e. no necking occurs.

The Al-Mg alloy exhibits a fairly well defined elastic
region.   During plastic deformation (room temperature tests
only - not at 400°C) the phenomenon of serrated yielding
occurs (manifested by the saw-tooth curve in Fig. 67).
Al-Mg alloys are prime examples of metals subject to this
strain ageing phenomenon which, basically, involves three
stages (See 5.9.4):-

   1) dislocations are pinned by solute atoms
   2) the flow stress increases until the dislocations
      are torn free
   3) the flow stress decreases again.

Necking occurs in the Al-Mg specimens leading to fracture, usually at fairly high strains.

Listed below are the optimum tensile properties of the various materials investigated together with the properties of some commercially produced alloys.

(all as extruded)	Extru-sion Temp °C	0.2% P.S.	U.T.S.	% Elongation
HE9 (powder)	250	132	160	23
HE9+8wt.% glass	450	92	223	28.4
HE30 (powder)	350	141	193	32
Al-Mg (powder)	400	176	308	22
Al-Mg+1wt.% glass	450	158	307	20
Al (powder)	600	74	160	10.5
Al+9wt.% glass	550	73	140	4
25 Alcan Aluminium (Solid)		--	60	18
Al-3Mg-Mn (solid)		100	215	14
Al-4.5Mg-Mn (solid)		130	280	11
HE9 (solid)		55	100	12

(For unreinforced HE9, HE30 and Al-Mg the extrusion temperature giving the optimum properties is fairly low i.e. dynamic softening is minimized at low temperatures. Reinforced HE9, Al-Mg and Al require higher extrusion temperatures i.e. the glass viscosity is reduced at high temperatures and fibre formation improves).

From the figures the advantages of glass reinforcement and the powder route are fairly obvious. Unreinforced HE9 powder extrude has a proof stress $2\frac{1}{2}$ times that of conventional "solid" HE9. The U.T.S. is also 60% greater and the elongation twice as large as the corresponding "solid" extrude value . The U.T.S. of the Al powder extrude is $2\frac{1}{2}$ times that of its conventional "solid" counterpart

although its elongation is significantly less due to the high oxide content of the powder material. HE9 + 8wt.% glass extrude has proof stress and U.T.S. values which are the equal of Al-3%Mg-Mn "solid" extrude, plus a much better elongation. The properties of unreinforced HE30 are comparable to those of Al-3%Mg-Mn "solid" although once again, the powder derived material has a much better elongation value. Finally, the properties of Al-3%Mg powder extrude are superior in everyway to those of Al-4.5%Mg-Mn "solid" extrude.

It must be stated that the temperatures employed during the extrusion of the reinforced materials were probably higher than necessary for good fibre formation. Thus the figures given for the reinforced materials are probably not the optimum values attainable. i.e. HE9 + 8 wt.% glass could probably be extruded at 350°C giving even higher proof stress and U.T.S. values.

5.9.2 Analysis of fracture behaviour

The type of fracture experienced by the various materials during tensile testing at room temperature and 400°C is listed in table 34.

Both the HE9 and HE30 specimens exhibit necking prior to fracture. At room temperature and 400°C transparticle, cup and cone, ductile fracture occurs (Plate 19(a) and (b)). Glass additions cause embrittlement of the HE9 extrude although a cup and cone type of fracture still takes place (much less necking occurs prior to fracture). Plate 19(e) shows the fracture surface of a glass reinforced HE9 extrude. The ends of the fibre channels are clearly visible.

The Al and Al+glass extrudes experience a very brittle type of fracture with a complete absence of necking. On examination of the surfaces the fracture appears interparticle in nature, probably due to the high oxide content present.

(Plate 19(c) and (d)). A large crack, probably initiated at an oxide fragment, is also visible in 19(c).

The Al-Mg alloy undergoes a fairly ductile type of fracture at both test temperatures. At room temperature, some necking precedes a 45° shear, transparticle, ductile fracture. At 400°C transparticle, cup and cone, ductile fracture occurs. Once again, the addition of reinforcing glass causes embrittlement.

5.9.3 Effect on extrude properties of variations in extrusion conditions

The variation in mechanical properties, with initial billet temperature, is shown for the various materials in Figs 68-72.

In the case of HE9 (Fig. 68) the room temperature proof and ultimate stresses show the expected decrease with increasing billet temperature (in the range $250-480^{\circ}$C) which is due to softening, probably by dynamic recovery. However, from 480 to 540°C the trend is reversed: the material becomes stronger and elongation continues to improve. This may be because, at the higher temperatures, a limited amount of magnesium silicide (Mg_2Si) is taken into solution and on subsequent air cooling after extrusion a supersaturated solution with a non-equilibrium vacancy concentration is formed. A natural[73] ageing process at room temperature might then produce a fine precipitate of Mg_2Si. The room temperature proof stress varies from $75-125$ MN/m^2 over the temperature range investigated which compares with an as-extruded strength of $50-55$ MN/m^2 for the normal cast alloy. In fact this strength compares well with that of the heat treated alloy, quoted as $130-160$ MN/m^2. The elongation varies from approximately 22-27%, which is remarkable since the normal as-extruded product is assigned a value of 12% for this property and the heat-treated alloy only 7%. These excellent elongation figures are most
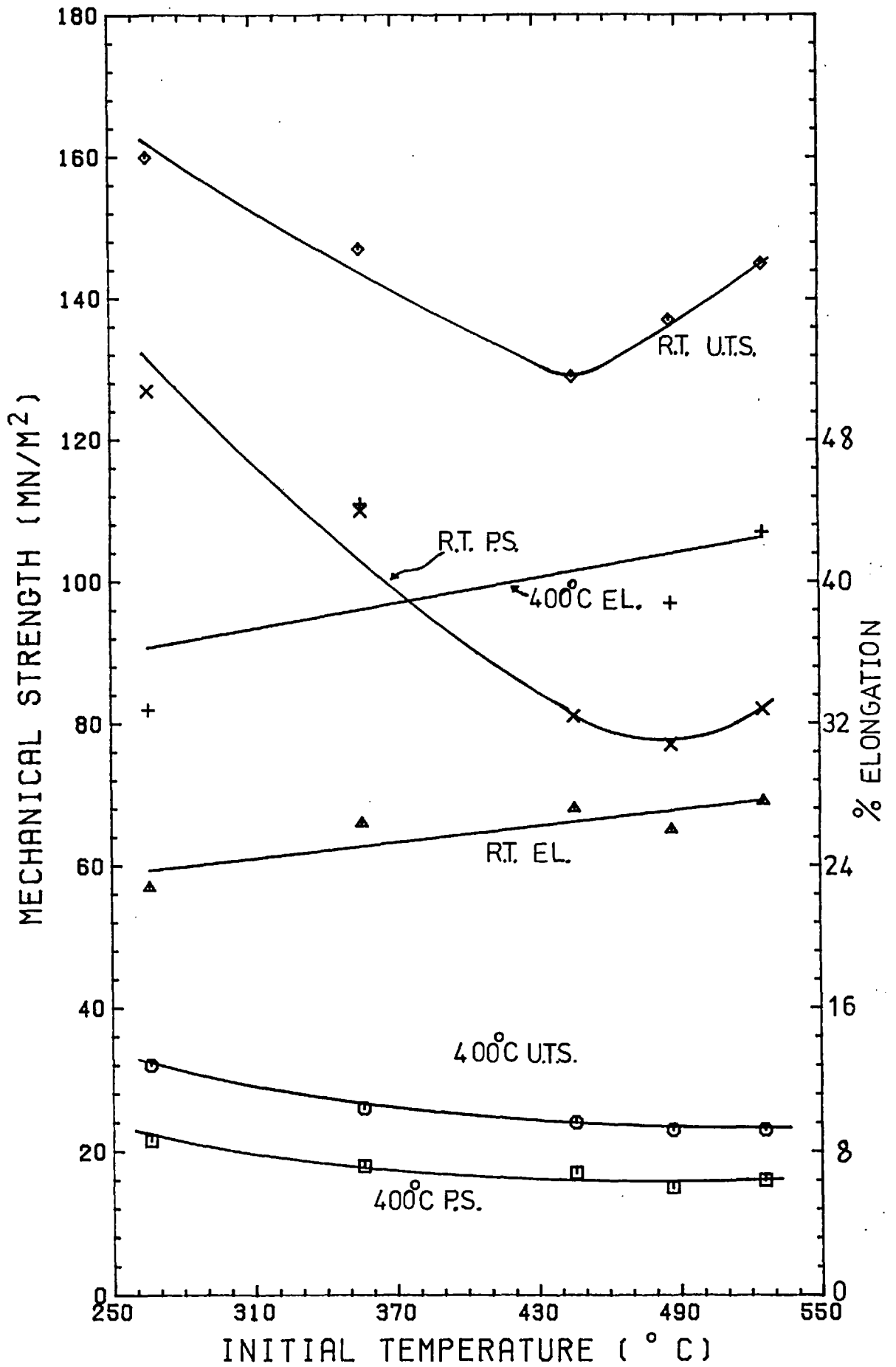
FIG. 68 Effect of extrusion temperature on HE9 mechanical properties

probably due to the inherently fine structure and small particle size of the atomized powder. The increase in elongation with billet temperature is also due to enhanced recovery at the higher temperatures causing more efficient dislocation elimination.

The strength of the extrude at 400°C decreases slightly with increasing billet temperature. This indicates that at the higher test temperature the form and distribution of precipitate have little effect on resistance to deformation. This alloy is therefore unsuitable for high-temperature applications.

Fig. 69 shows the effect of billet temperature variation on the properties of HE30. Generally, the behaviour is similar to that of HE9. However, the room temperature proof and ultimate stresses also decrease, with increasing billet temperature, from 480-540°C. This behaviour is the reverse of that exhibited by HE9 in the same temperature range. This is somewhat surprising as HE30 is more responsive to conventional heat treatments. The excellent elongation values (32-44%) may once again be attributed to the structure and particle size of the atomized powder. In fact the HE30 elongation values are even better than those of HE9. This is probably due to the HE30 powder median particle size (122μ) being finer than the HE9 powder (141μ). Fig. 70 clearly demonstrates that the strength of extruded Al-Mg decreases with increasing billet temperature over the range 400-550°C. (The minimum temperature investigated was dictated by the press capacity). The elongation is little affected by this parameter and remains approximately 21-22%.

In the case of the Al powder extrusions (Fig. 71) the proof and ultimate tensile stresses decrease with temperature from 300-400°C and then increase as the temperature is raised from 400-600°C. This increase in U.T.S. at temperatures above 400°C is particularly marked.
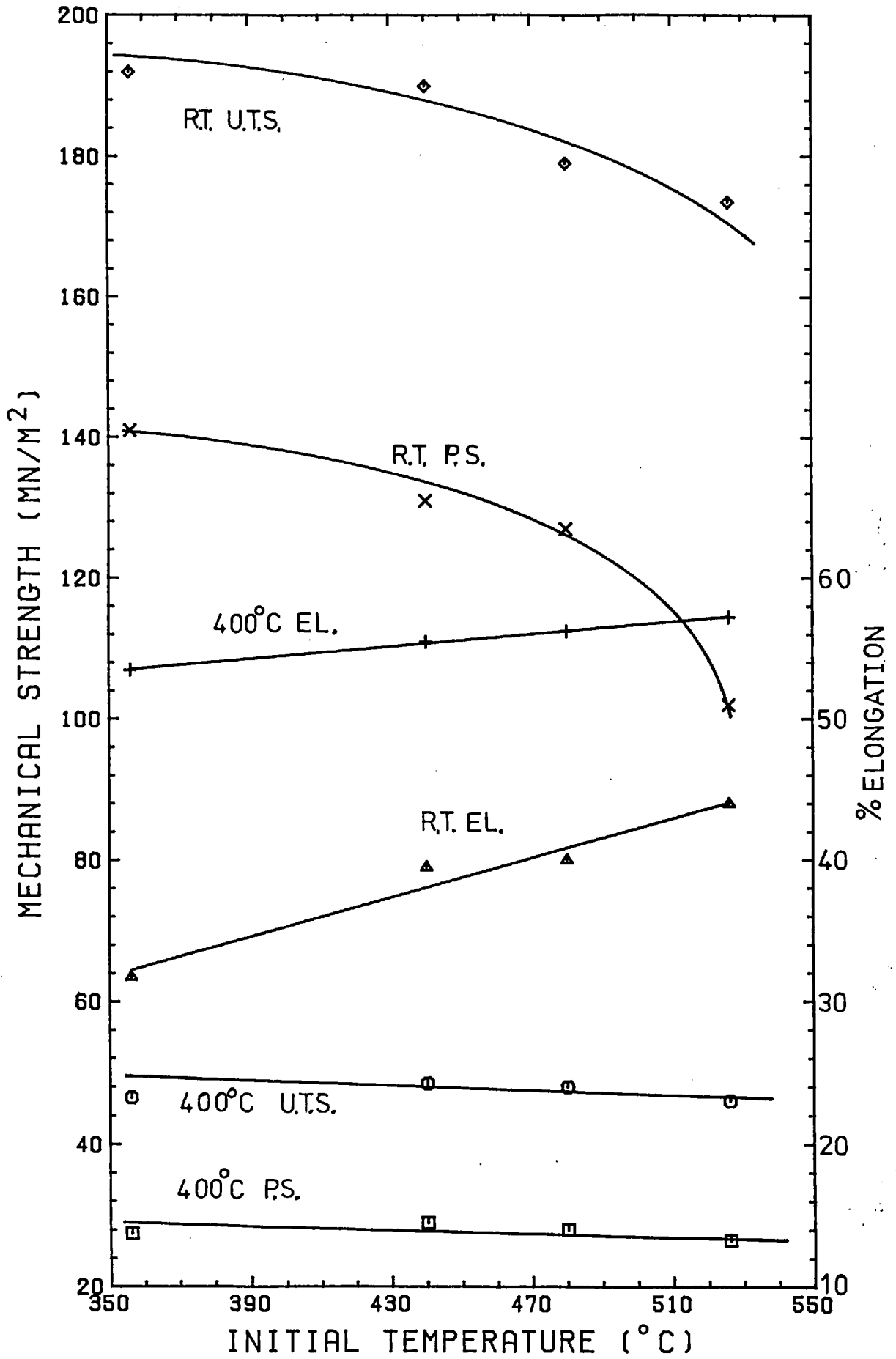
FIG. 69   Effect of extrusion temperature on HE30
         mechanical properties
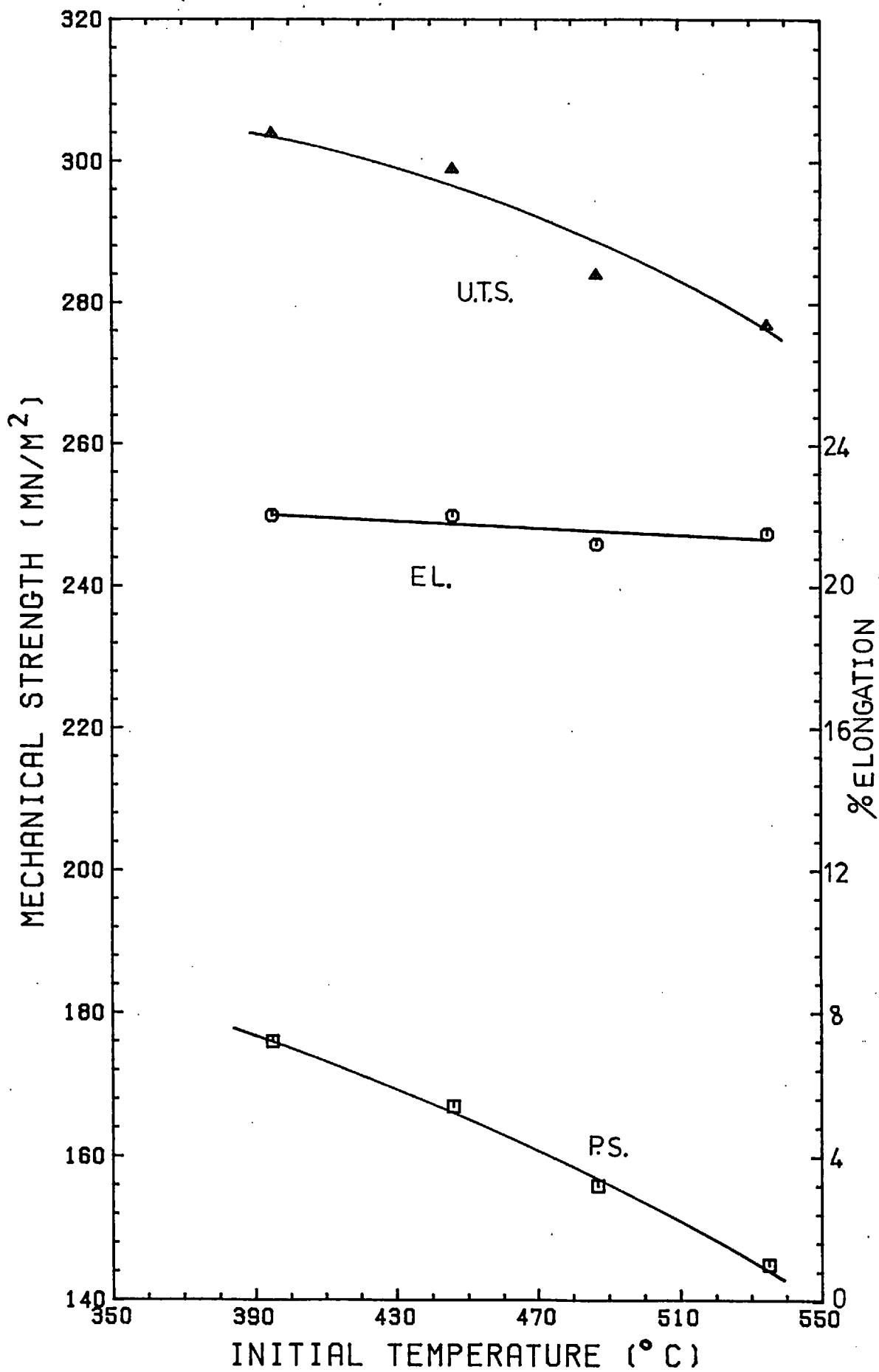
FIG. 70 Effect of extrusion temperature on Al-Mg
mechanical properties
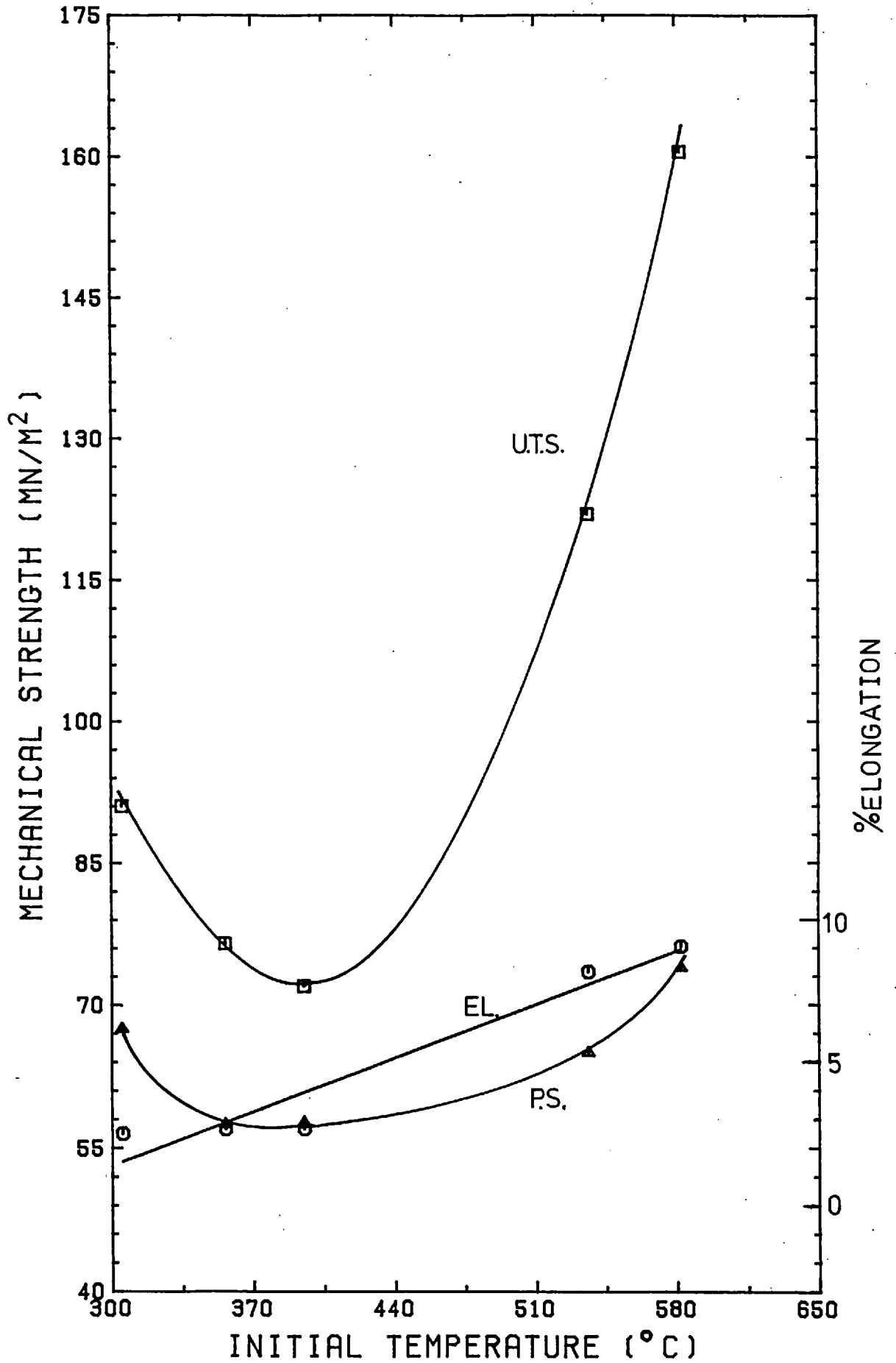
FIG. 71 Effect of extrusion temperature on Al
mechanical properties

The decrease in strength with increasing temperature over the initial range may once again be due to improved dynamic softening. As mentioned in 5.6.1 increasing the temperature up to approximately 600°C increases the ductility and improves the extrude quality by preventing cracking due to secondary tensile stresses. This may in turn increase the extrude strength. In general the elongation is much lower than that of HE9, HE30 or Al-Mg due to the high oxide content of the Al powder ($\sim$ 7wt.%).

The effect of varying the billet temperature on the properties of a HE9 + 5 wt.% glass composite is shown in Fig. 72. The U.T.S. increases, almost linearly with temperature from 400-550°C. This increase in U.T.S. is caused by improved matrix-fibre bonding and by an increase in fibre perfection. (At higher temperatures the glass viscosity is lower making fibre formation easier). This effect more than compensates for the softening of the metal matrix by dynamic recovery. The proof stress decreases from 90-70 MN/m^2, with increasing temperature, due to enhanced softening mechanisms. As fibre reinforcement theory predicts, the proof stress is little affected by the addition of the glass. This is because the metal flows plastically before any effective reinforcement occurs. (The very slight decrease in proof stress is probably due to stress concentrating effects and is also within the range of experimental error). Once again the elongation increases with temperature.

The effect of varying the extrusion ratio is shown in Fig. 73. Over the range from 5:1 to 80:1 the proof stress increases steadily for both HE9 and HE30. Gurney[24] found that for extrusion ratios above 10:1 the mechanical strength of 7075 powder extrudes deteriorated. He suggested that this was due to cracking caused by excessive deformation and to the large grain size produced by recrystallisation. He further proposed that extrusion ratios above. 10:1 produced cracks resulting from excessive amounts of shear during the extrusion

(continued...)
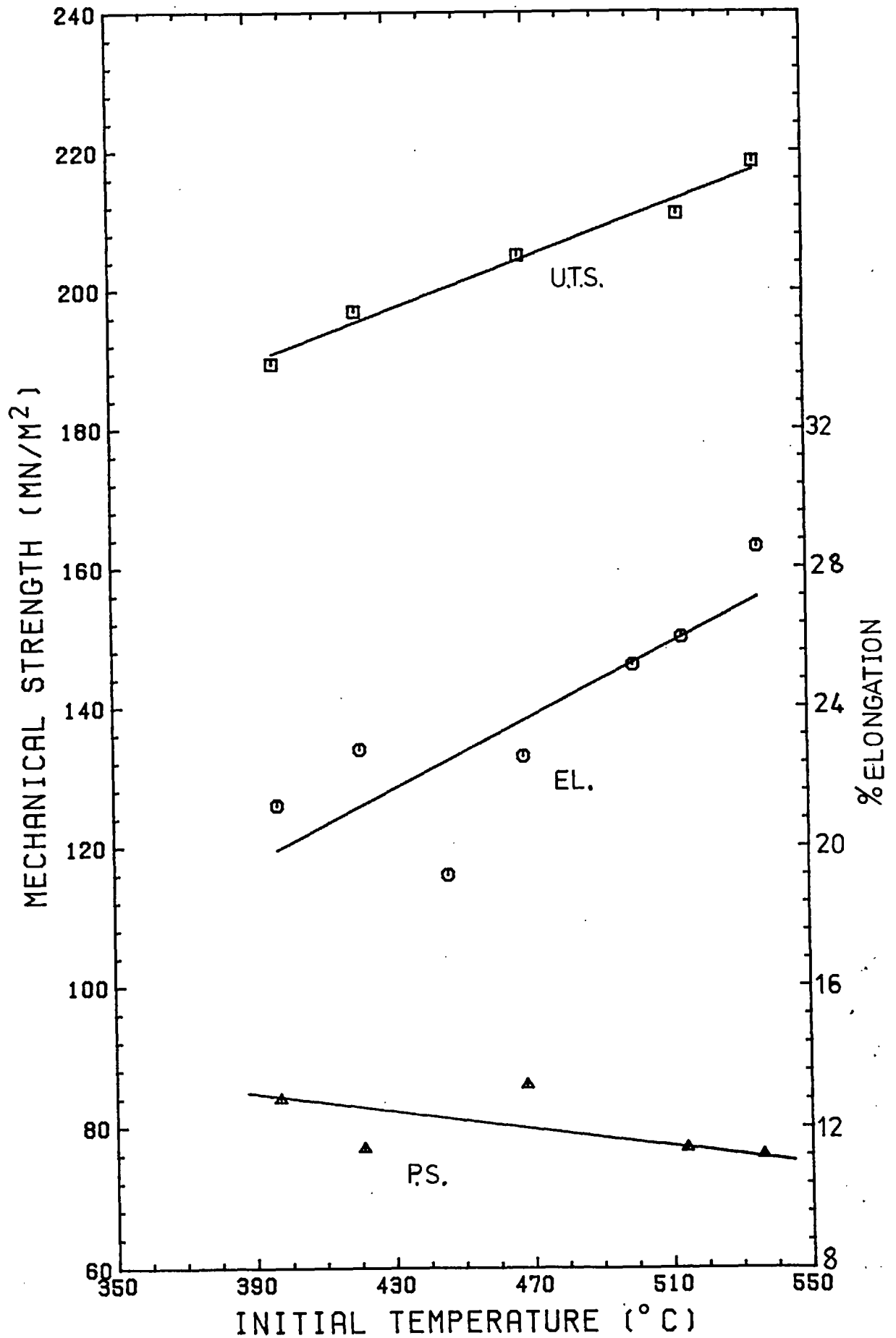
FIG. 72 Effect of extrusion temperature on HE9 + 5wt.%
glass mechanical properties
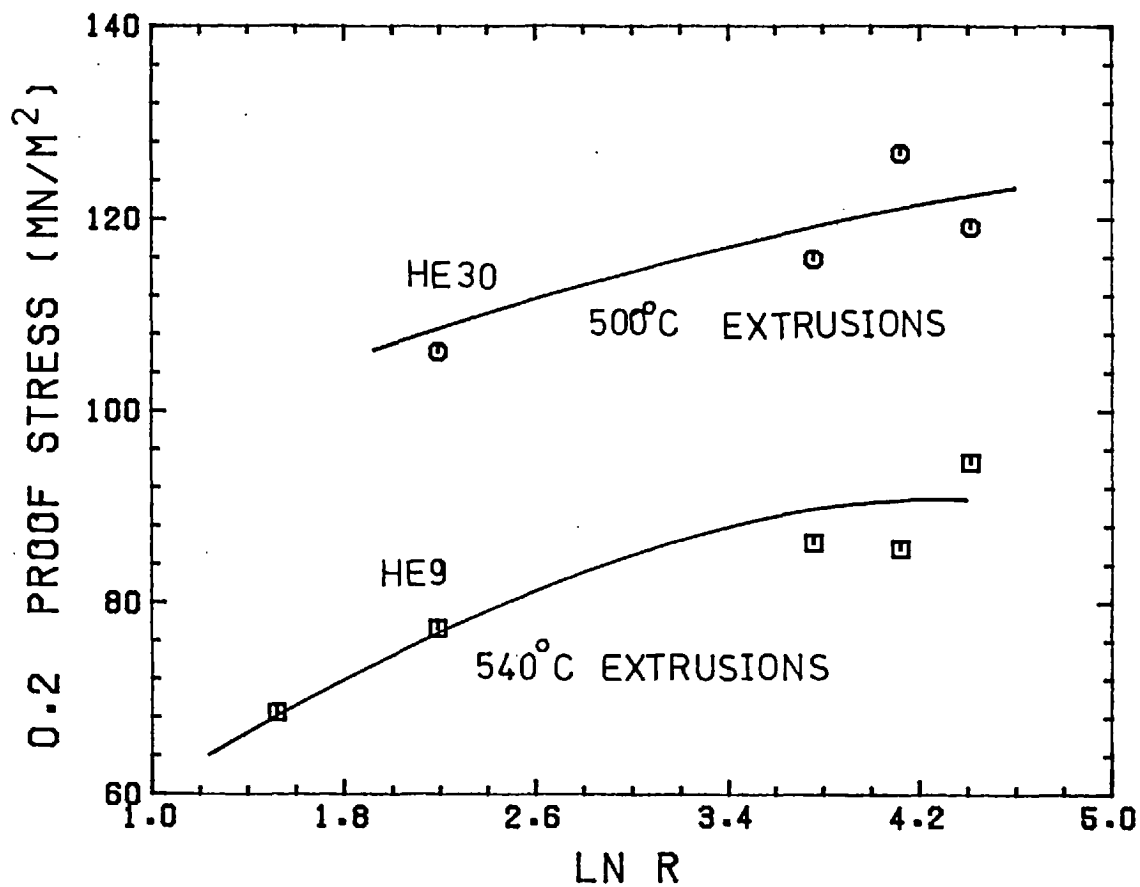
FIG. 73 Effect of extrusion ratio variation on the strength of HE9 and HE30 extrudes
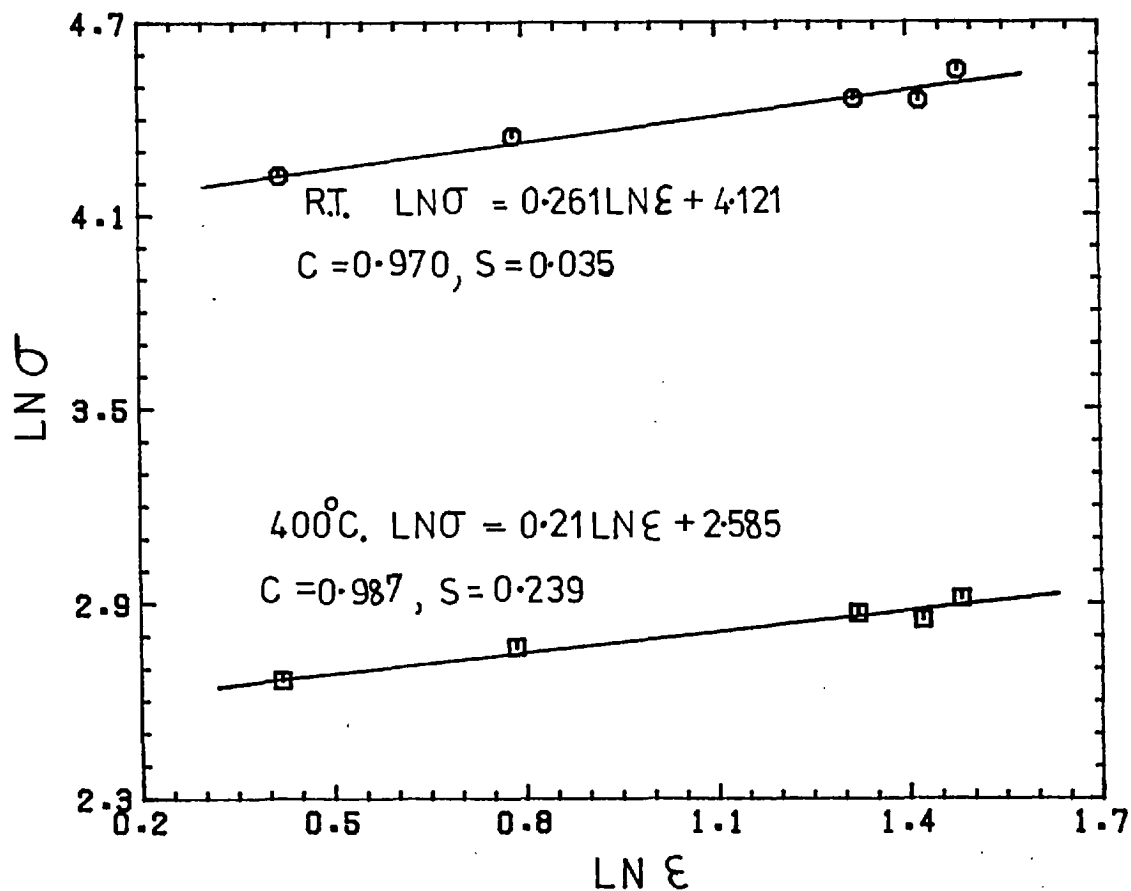
FIG. 74 Tensile test lnσ vs. lnε relationships at different temperatures (HE9)

process which could not be accomodated in the matrix near the hard particles of fragmented oxide. As no such cracks were found in the present investigation, or by other workers such as Chare[23], this theory must be questioned. Fig. 74 demonstrates the applicability of a law of the form:-

$$\sigma = \text{const. } \varepsilon^m$$

The relatively high correlation coefficients indicate that the experimental points fit the law quite well. The strain or work hardening exponent, m, varies from 0.26 at RT. to 0.21 at 400°C. This also indicates that an extrusion ratio of 5:1 produces fully consolidated material i.e. if a 5:1 extrude were not fully consolidated m would decrease with increasing extrusion ratio over the range 5:1 to 80:1.

5.9.4 Dependence of extrude properties on test conditions

The variation in the proof stress of HE9 with tensile test temperature is shown in Fig. 75. As expected, the strength decreases rapidly with increasing temperature. This curve very closely resembles that depicted in Fig. 25. (predicted by Seeger's[109] analysis 3.8.1). Therefore the curve may be represented by an equation of the form:-

$$K_s = \frac{[U_o - KT \ln (\frac{\dot{\varepsilon}_o}{\varepsilon})]}{V} + K_A \qquad \text{(See 3.8.1 for symbols)} \qquad (67)$$

The athermal component of the flow stress, due to long range obstacles such as oxide dispersions, precipitates etc. is designated as K_A in (67). From Fig. 75 the value of K_A is 16 MN/m^2. For the normal cast alloy K_A is quoted as 7-8 MN/m^2. The discrepancy is caused by the presence of fragmented oxide particles in the powder extrude.

Fig. 76 indicates the effect of strain rate on the proof stress of HE9 and HE30. Both alloys obey a law of
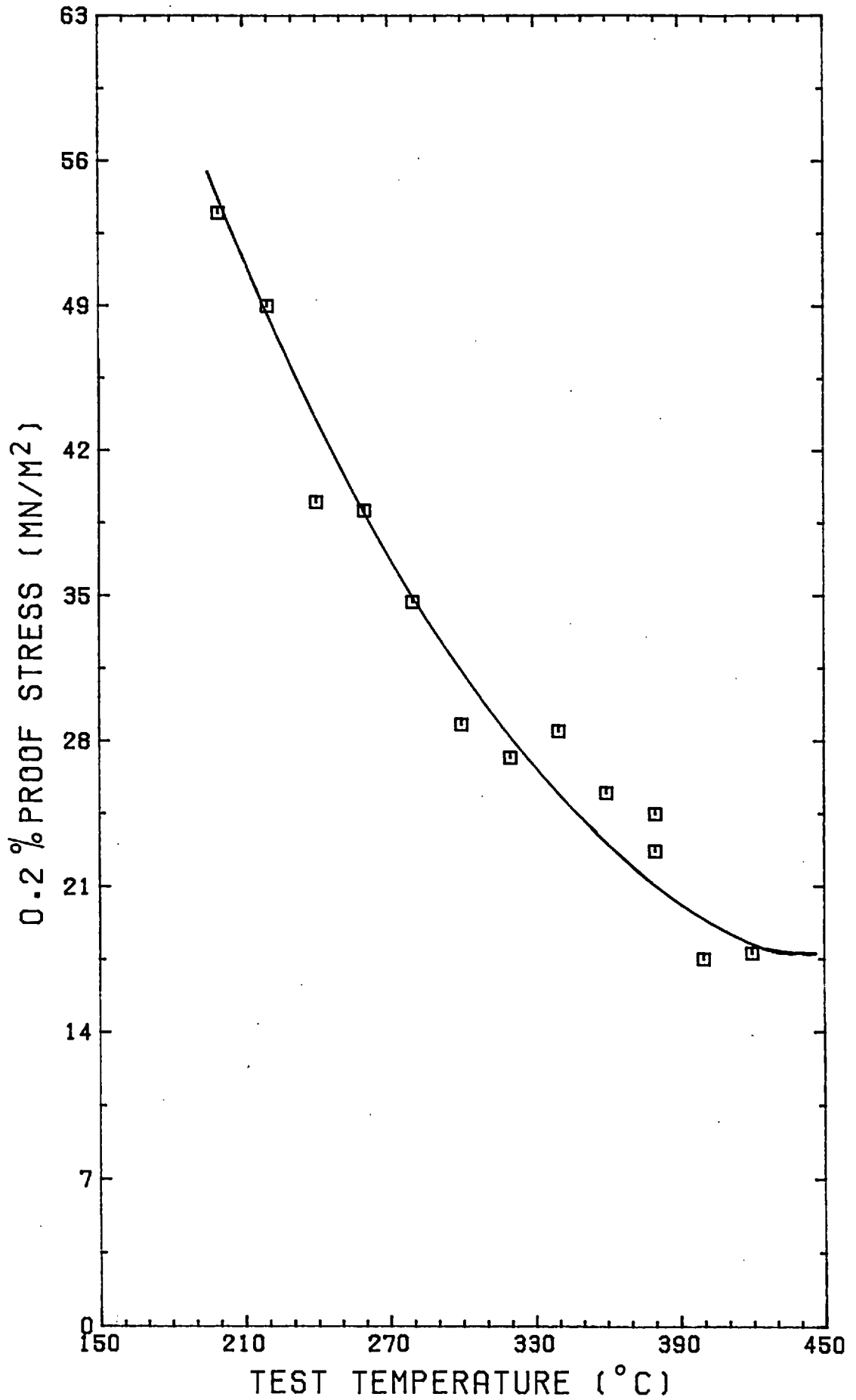
FIG. 75 HE9 proof stress as a function of temperature
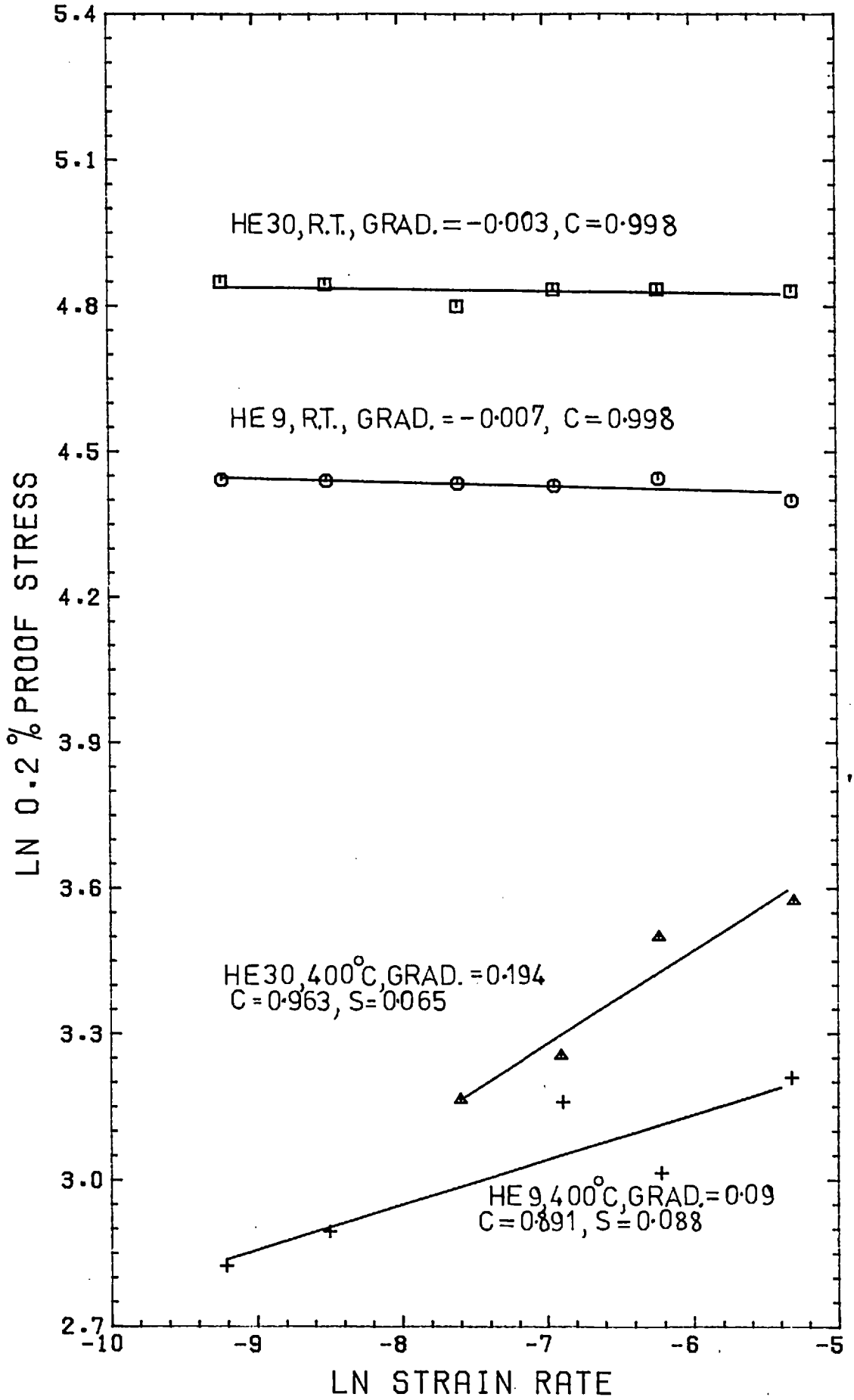
FIG. 76 Effect of strain rate on proof stress of HE9 and HE30

the form:-

$$\sigma = \text{const. } \dot{\varepsilon}^n$$

The reasonably high correlation coefficients indicate
a good fit between the experimental points and the theory.
Raising the test temperature from room temperature to 400°C
has a dramatic effect on the strain rate exponent of both
alloys. The value of n changes from -0.007 to +0.09 for
HE9 and from -0.003 to 0.19 for HE30. This trend was also
found in 7075 aluminium alloy by D'Antonio et al[110] and
by Alder and Philips[134] in commercially pure aluminium.
In particular D'Antonio discovered variations in the
strain rate exponent over similar temperature and strain
rate ranges (i.e. < 10^{-2}/sec) to those investigated in the
present work. The increase in proof stress with strain
rate at 400°C occurs because the work hardening rate exceeds
the recovery rate by an ever increasing amount as the strain
rate rises. The negative exponent at room temperature is
not so easily explained. Lubahn[111] has reported that the
strain rate exponent of 61S alloy (Al-0.6%Mg-Si) attains
a minimum, negative value at room temperature. He suggests
that this phenomenon is due to strain ageing which is most
prevalent in 61S at room temperature. Some materials, during
plastic deformation, suffer dislocation pinning by solute
atom clusters. As the load increases the stress acting
on the dislocations builds up and eventually the dislo-
cations are torn free. The stress needed to maintain
dislocation motion is less than that needed to initiate
it and so the load falls slightly. However, the solute
atoms diffuse rapidly and "repin" the dislocations. Thus
the cycle is complete. Repetitions of this cycle cause
the "saw tooth" effect in the load extension curve (Fig. 67).
If the strain rate is increased a stage is reached when
the diffusion rate of the solute atoms is not great
enough to permit this "repining" to occur and this in
turn lowers the flow stress. This mechanism may be
operating in the HE9 and HE30 alloys although no serrated

yielding is apparent in their tensile test curves.
Strain ageing does not occur at higher temperatures
(i.e. 400°C) because the increased solute atom diffusion
rate affords the atoms insufficient time to repin dis-
locations.

This n value of 0.09 for HE9 at 400°C agrees well
with the value of 0.1 found from torsion results (5.5.1).
This is quite interesting considering that the torsion
tests were performed at strain rates several orders of
magnitude higher than those used in the tensile tests.

5.9.5 Dependence of extrude properties on powder particle size

The mechanical properties of extruded HE9 greatly
depend on the initial powder particle size, as seen in
Fig. 77. The U.T.S., 0.2% proof stress and elongation
all deteriorate with increasing powder particle size.
Chare[23] found, for Al powder, that the proof stress
increased linearly with (initial particle diameter)$^{-\frac{1}{2}}$,
the effect being more pronounced at room temperature
than at 400°C. (The greater amount of thermal energy
possessed by dislocations at 400°C enables them to over-
come obstacles, such as subgrain boundaries, more easily).
Al-Fe, Al-Mn and Al-Mg-Zn alloy powders were found to
behave in a similar manner although the overall strengthen-
ing effect, produced by decreasing the particle size, was
much smaller. Chare also found the extrude subgrain size
to increase linearly with the initial powder particle
size. Therefore he suggested that the proof stress was
also proportional to (subgrain size)$^{-\frac{1}{2}}$. Hansen[84] extruded
aluminium powder and found that the Al_2O_3 behaved like
a three-dimensional network of dispersoids. He also
suggested a Hall-Petch equation of the form:-

$$\tau = \tau_s + \text{const.} \ \lambda^{-\frac{1}{2}} \qquad\qquad (9)$$

to relate flow stress to oxide interparticle spacing .
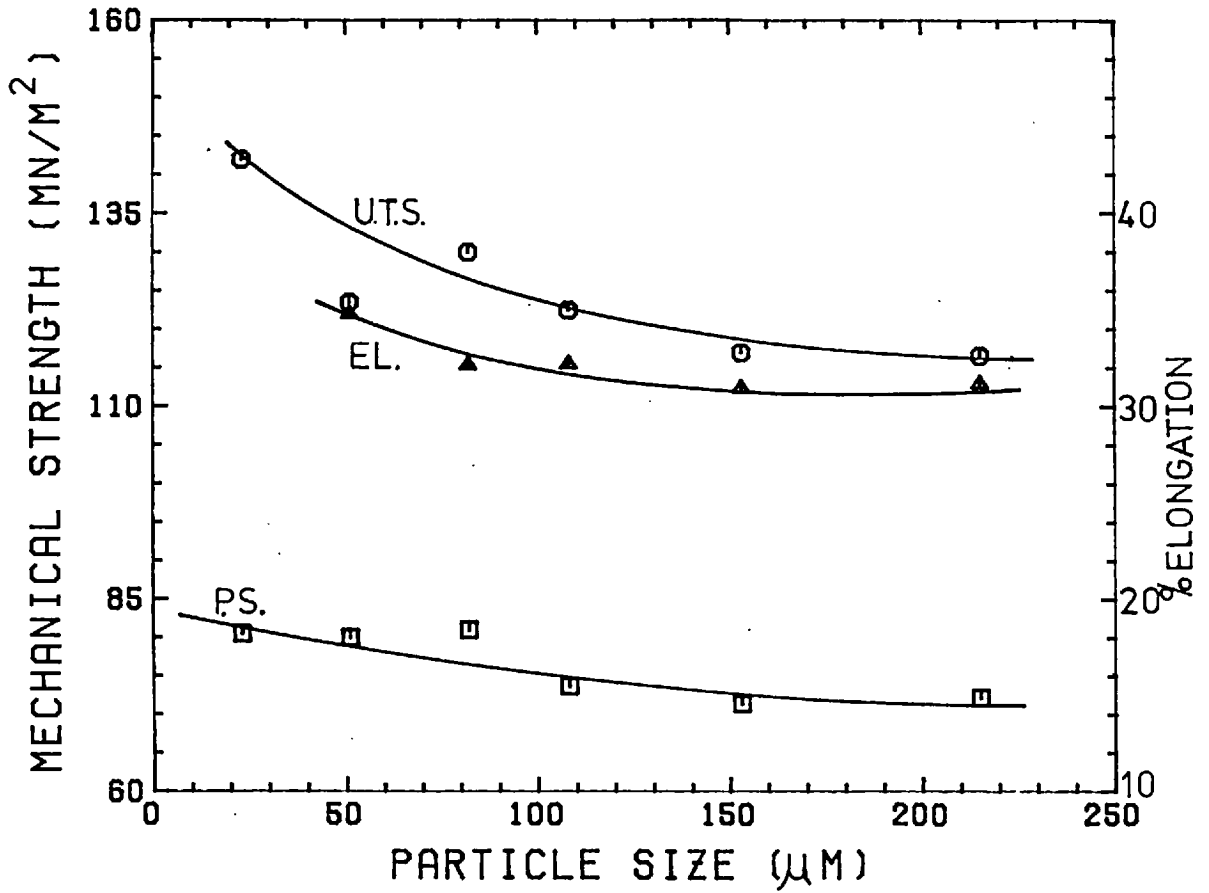
FIG. 77 Mechanical properties of HE9 extrude as a function
of powder particle size

FIG. 78 Relationship between HE9 extrude strength and
(powder particle size)$^{-\frac{1}{2}}$

$$U.T.S. = 157 \cdot 8 \frac{1}{\sqrt{\mu}} + 107 \cdot 0$$
$$C = 0 \cdot 923, \ S = 3 \cdot 782$$

$$P.S. = 84 \cdot 8 \frac{1}{\sqrt{\mu}} + 65 \cdot 9$$
$$C = 0 \cdot 791, \ S = 3 \cdot 781$$
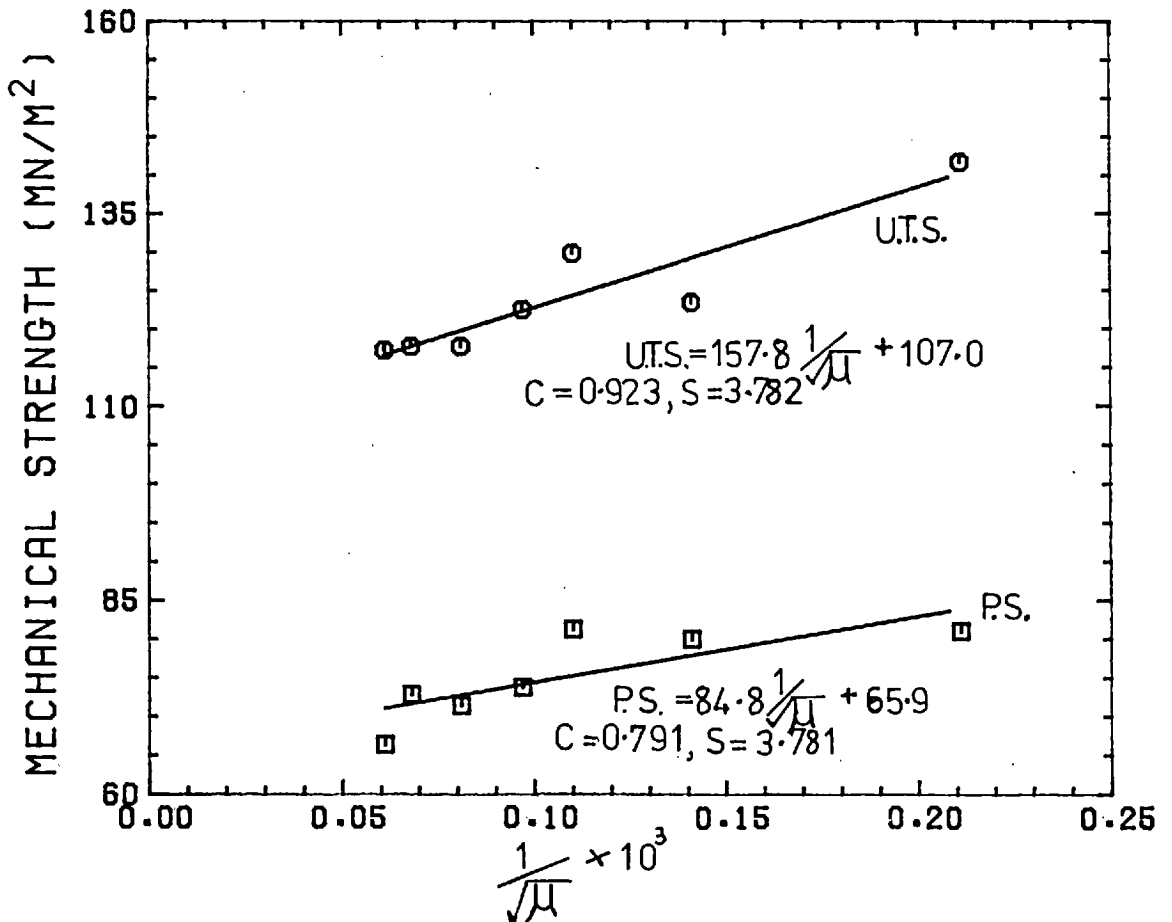
In fact λ is approximately equal to the mean powder
particle diameter.

Fig. 78 shows the application of this relationship
to the HE9 results giving an equation:-

$$\tau = 65.9 + 84.8 \; \lambda^{-\frac{1}{2}} \tag{87}$$

However, the low correlation coefficient of 0.79 casts
some doubt on the applicability of the relationship.
More experiments are required before definite conclusions
can be drawn. (In fact the U.T.S. data fits the relation-
ship rather better giving an equation:-

$$\tau = 1070 + 157.8 \; \lambda^{-\frac{1}{2}} \tag{88}$$

correlation coefficient = 0.92.)

This Hall-Petch type relation between powder
particle size (or indeed subgrain size) and proof stress
corresponds to the relation in solid materials between
grain size and flow stress.

This latter relation is often expressed in the
equation:-

$$\tau_y = \tau_i + k \; D^{-\frac{1}{2}}$$

where D = grain size
       τ_y = flow stress

The term τ_i is the lattice friction stress and k is a
term, the magnitude of which is proportional to the difficulty
a dislocation experiences in traversing a grain boundary.

5.9.6 Effect on extrude properties of variations in glass content

The significant effect of glass content on mechanical properties is illustrated in Figs. 79-81 for HE9, Al-Mg and Al respectively. Equation (44) in 3.7.3 i.e.
$\sigma_c = \sigma_m(1-V_F) + \sigma_F V_F$, predicts a linear increase in U.T.S. with volume fraction of glass. This is observed for HE9 over the range 0-8 wt.% glass. Further increases in the glass content rapidly weaken the composite. By applying equation (44) the U.T.S. of the glass fibres may be obtained from a knowledge of the composite strength. e.g. at 5 wt.% glass i.e. 9.2 vol % glass (Density of glass = 1410 kg/m^3)

$$\sigma_c = \sigma_m V_m + \sigma_F(1 - V_m) \qquad (44)$$

$$\therefore \quad 200 = 130 \times 0.91 + \sigma_F(1 - 0.91)$$

$$\therefore \quad \sigma_F = 891 \text{ MN/m}^2.$$

This value is much lower than quoted values for commercially available glasses such as E - glass (3700 MN/m^2) silica (4600 MN/m^2) and B_2O_3-10% SiO_2 (2412 MN/m^2). This indicates the poor quality of the fibres formed during extrusion.

The decrease in strength with increasing glass content above 8 wt.% is probably due to the difference in bulk modulus between the glass and metal. ($K_{matrix} = 26.2 \times 10^3$ MN/m^2, $K_{glass} = 13.8 \times 10^3$ MN/m^2). The elastic expansion of the glass fibres is much greater than that of the metal matrix. At typical extrusion temperatures the matrix is weak and the force exerted by the glass, on emerging from the extrusion die, produces cracks leading to drastic weakening of the composite.

Plate 10(a) is a transverse section of a HE9 + 5 wt.% glass extrude showing cracks in the matrix surrounding a
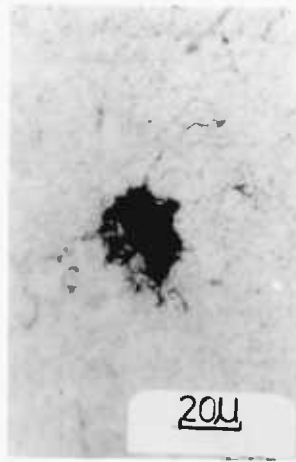
(a)

Transverse optical micrograph
of fibre channel
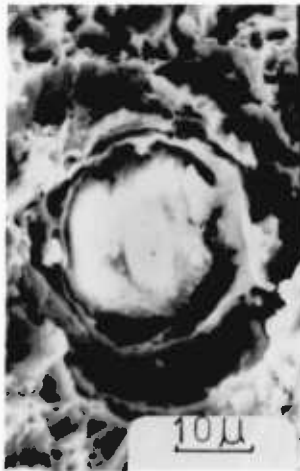
(b)

Transverse scanning electron
micrograph of fibre

PLATE 10   Micrographs of HE9 + 5 wt.% glass
extruded at 450°C
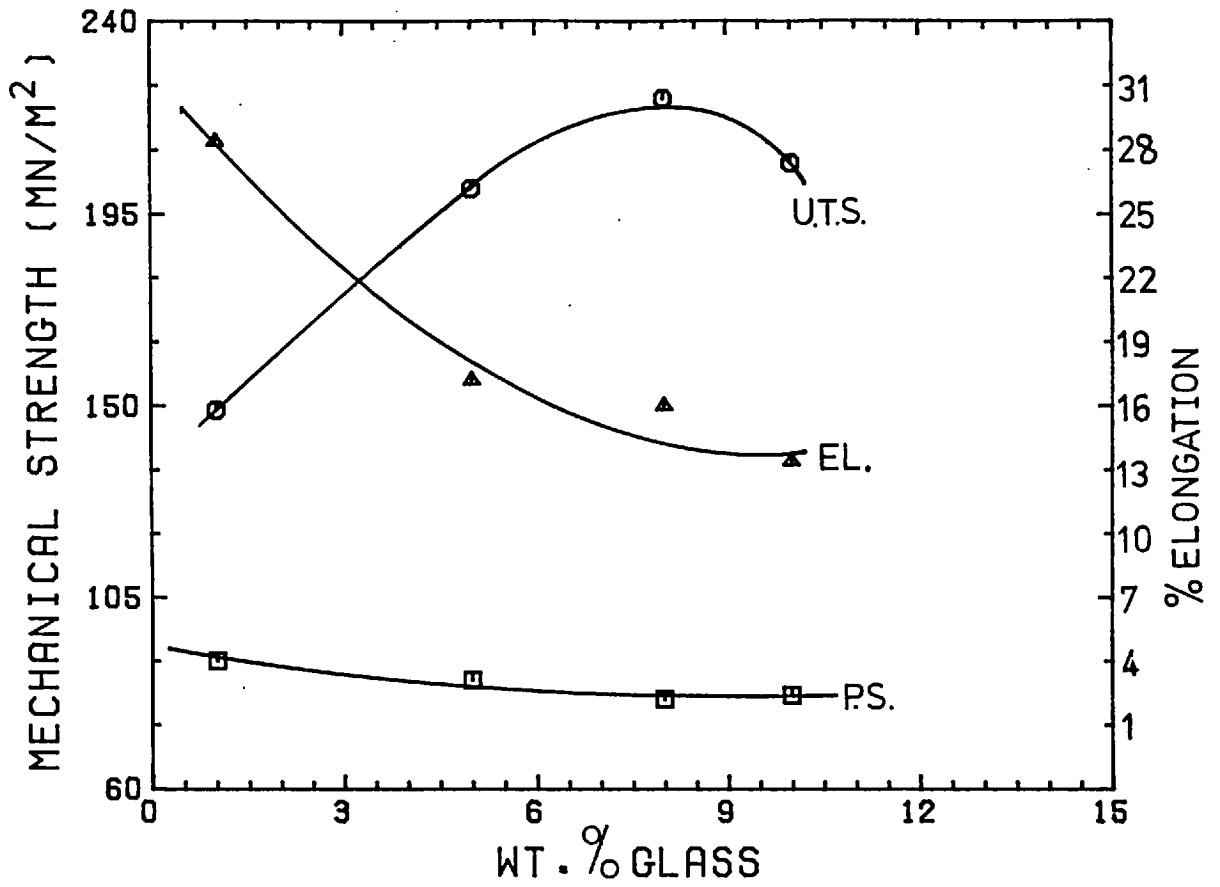
FIG. 79   Effect of variations in glass content on
mechanical properties of HE9-glass extrudes
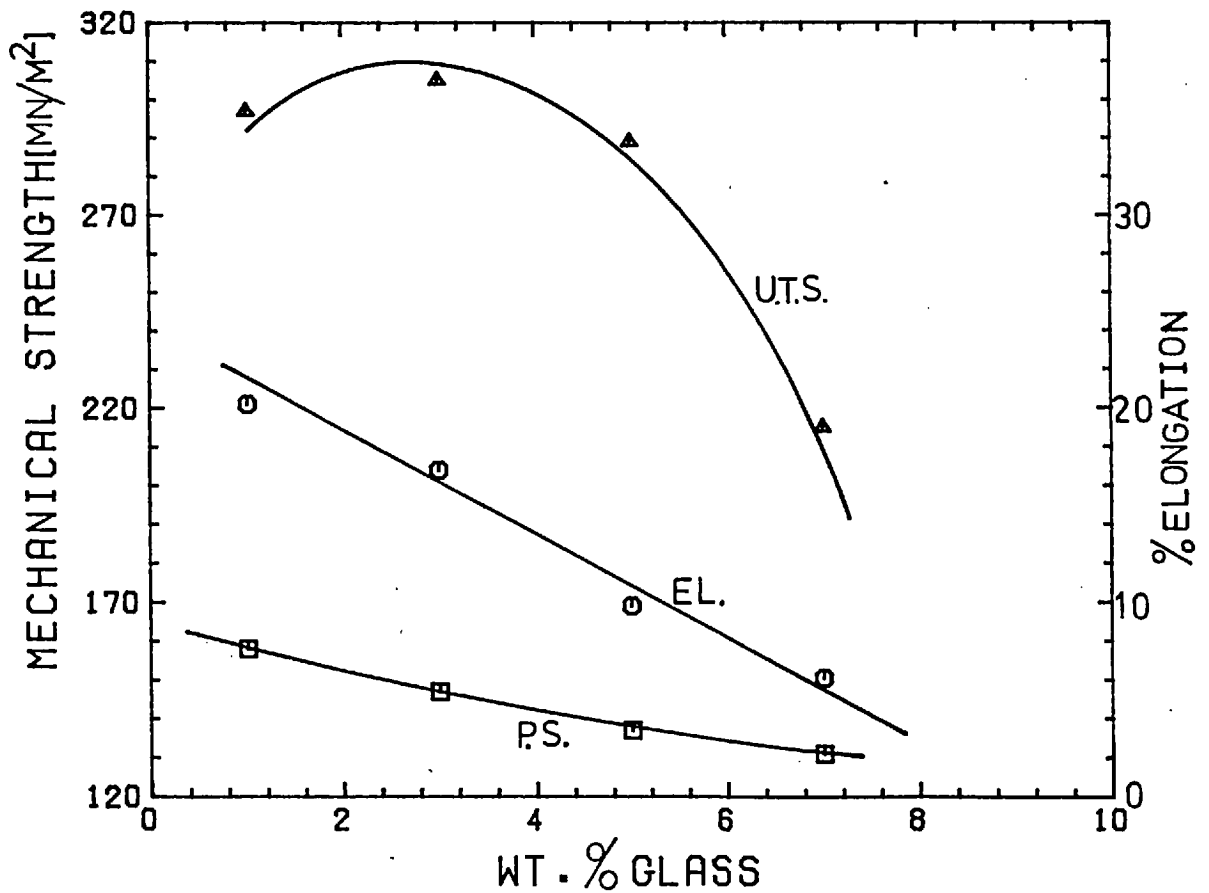
FIG. 80   Effect of variations in glass content on mechanical
properties of Al-Mg-Glass extrudes

fibre. When the glass content is raised to 12-15 wt.%
disintegration of the extrude results (Plate 9(h)).
The optimum glass content of 8 wt.% improves the U.T.S.
of the HE9, extruded at the same temperature, by 71%.
The proof stress decreases with glass content due to
matrix cracking and the stress concentrating effect of
fibre ends. (In theory the proof stress should be unaffected
by glass fibres because the metal yields before any
reinforcement occurs). The addition of glass reduces
the elongation value because of the inherent brittleness
of the glass and the presence of matrix cracks.

Similar behaviour is observed for Al-Mg glass
composites in Fig. 80. As Al-3wt.%Mg is a much stronger
alloy than HE9 the peak in the U.T.S. curve might be
expected to occur at a glass content in excess of 8 wt.%.
In fact the peak U.T.S. occurs at only 3 wt.% glass.
Further additions reduce the strength significantly.
This shift in peak U.T.S. is probably due to adverse
effects, on the fibre strength, of chemical reactions
between the glass and the abundant supply of Mg present
in this alloy. As in the case of HE9 both the proof
stress and the elongation decrease significantly with
increasing glass content. (Extrudes containing more
than 7 wt.% glass are impossible to machine due to dis-
integration). Overall, the properties of Al-Mg-Glass
composites are very disappointing.

The U.T.S. of the Al-glass composite increases
continuously, though non-linearly, with glass content
as depicted in Fig. 81. Extrudes containing more than
9 wt.% glass disintegrate on machining and so it must be
assumed that 9 wt.% is the optimum glass content. The
U.T.S. of the 9 wt.% is only 14% greater than that of
the unreinforced aluminium (extruded at the same tempe-
rature, 558C). In fact at glass contents below
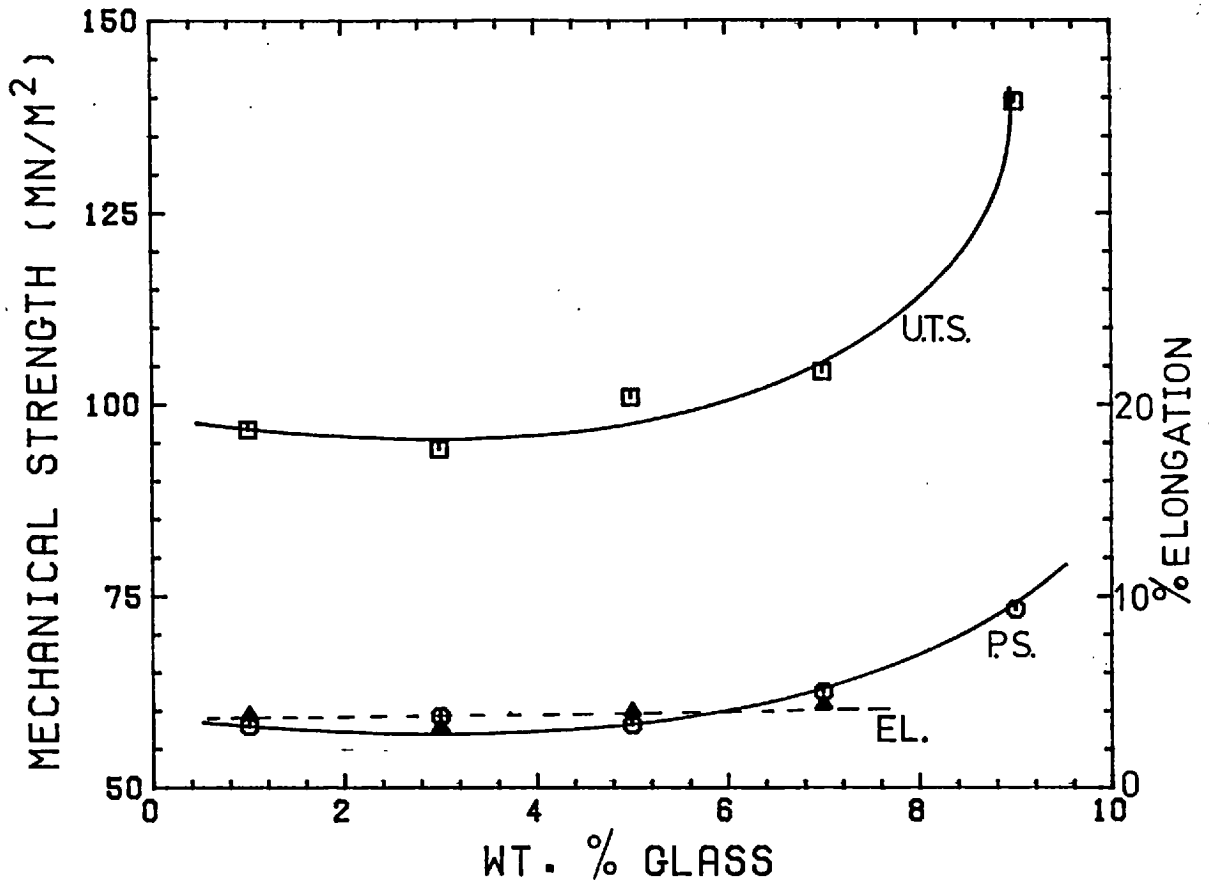
FIG. 81   Effect of vairations in glass content on mechanical
properties of Al-Glass extrudes

FIG. 82   Effect of variations in glass particle size
on mechanical properties of HE9-Glass extrudes
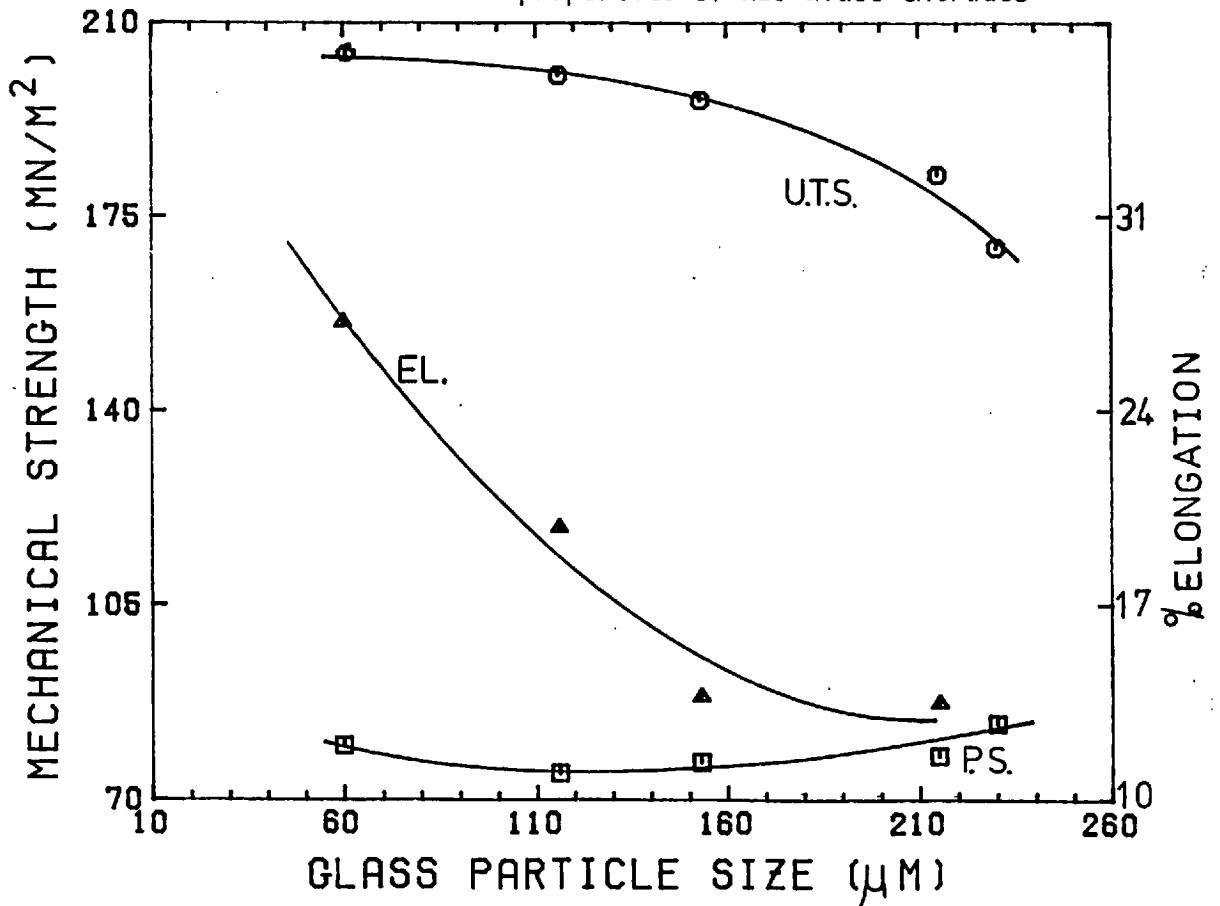
∿ 9wt.% the composite is weaker than the unreinforced
matrix. The elongation value of about 4% remains
largely unaffected by the glass content although the
Al is very brittle due to its large oxide content and
the measurement accuracy of such small values must be
in some doubt. The proof stress appears to increase
with glass content although this conclusion is based
on only one data point at 9 wt.% glass. Thus it is more
likely that no significant change, in fact, occurs in
proof stress. Overall, the results for Al-glass com-
posites are disappointing.

The effect of varying the initial glass particle
size is shown in Fig. 82. The U.T.S. decreases rapidly
with increasing particle size. This is fairly easy to
explain. For a given weight of glass a reduction in
particle size increases the surface area/volume ratio
producing more metal-glass interfacial area. This
leads to better bonding, better load transfer and higher
U.T.S. values. As expected, the proof stress is largely
unaffected by the glass particle size. The elongation
decreases rapidly with increasing glass particle size
because large fibres suffer more damage, during forma-
tion in the die, than small ones. (This may also contri-
bute to the reduction in U.T.S.).

5.10.1 <u>Hardness results</u>

The results of hardness tests carried out on the
various extruded materials are given in table 23. Generally
the hardness is governed by the alloy content such that
the materials, in order of hardness are:

1) Al-3wt.%Mg   3) HE9
2) HE30   4) Al

(This is also the order in terms of tensile strength).
No correlation exists between extrude hardness and extrusion

speed. Some of the results indicate a trend towards a
decrease in hardness with increasing extrusion temperature.
Chare[19] found a definite decrease in the hardness of
extruded Al powder with increasing extrusion temperature.
The only definite trend in the present results involves
an increase in hardness with decreasing glass content.
This is shown clearly in Fig. 83. Once again this is
due to expansion of the glass causing cracking in the
matrix. Increasing the glass content increases the
number and size of these cracks thus lowering the overall
hardness of the extrude.

A series of hardness measurements taken longitudinally
across the deformation zone of a sectioned partially extruded billet
revealed only a 5% variation in hardness and no correlation
between hardness and position. This is to be expected
because although the strength of the compact increases
as it passes through the quasi-static deformation zone
by a process of building and rebuilding interparticle welds,
the hardness of the individual particles is almost unaffected.
(Dynamic recovery eliminates work hardening effects). For
this reason a danger lies in predicting tensile properties
from hardness results for materials fabricated from powder.

5.11.1 Fracture toughness

Extruded HE9 and HE30 powders exhibit no correlation
between extrusion process parameters and notch ductility
(IZOD) values. The results from over 30 tests show little
scatter (Tables 24 and 25) and give an average impact
energy value of 42.2 J for HE9 which is almost identical
to that reported for the cast and wrought material (42.0 J
nominal). The average value for HE30 is 38.7 J. In all
cases the fracture surfaces are fibrous in nature. (None
of the unreinforced HE9 and HE30 specimens fractured com-
pletely in any of the tests). Ansell and Kim[137] encountered
similar fracture behaviour in Al-Al_2O_3 S.A.P. alloys tested
at temperatures in the range 20 to $-170^{\circ}C$
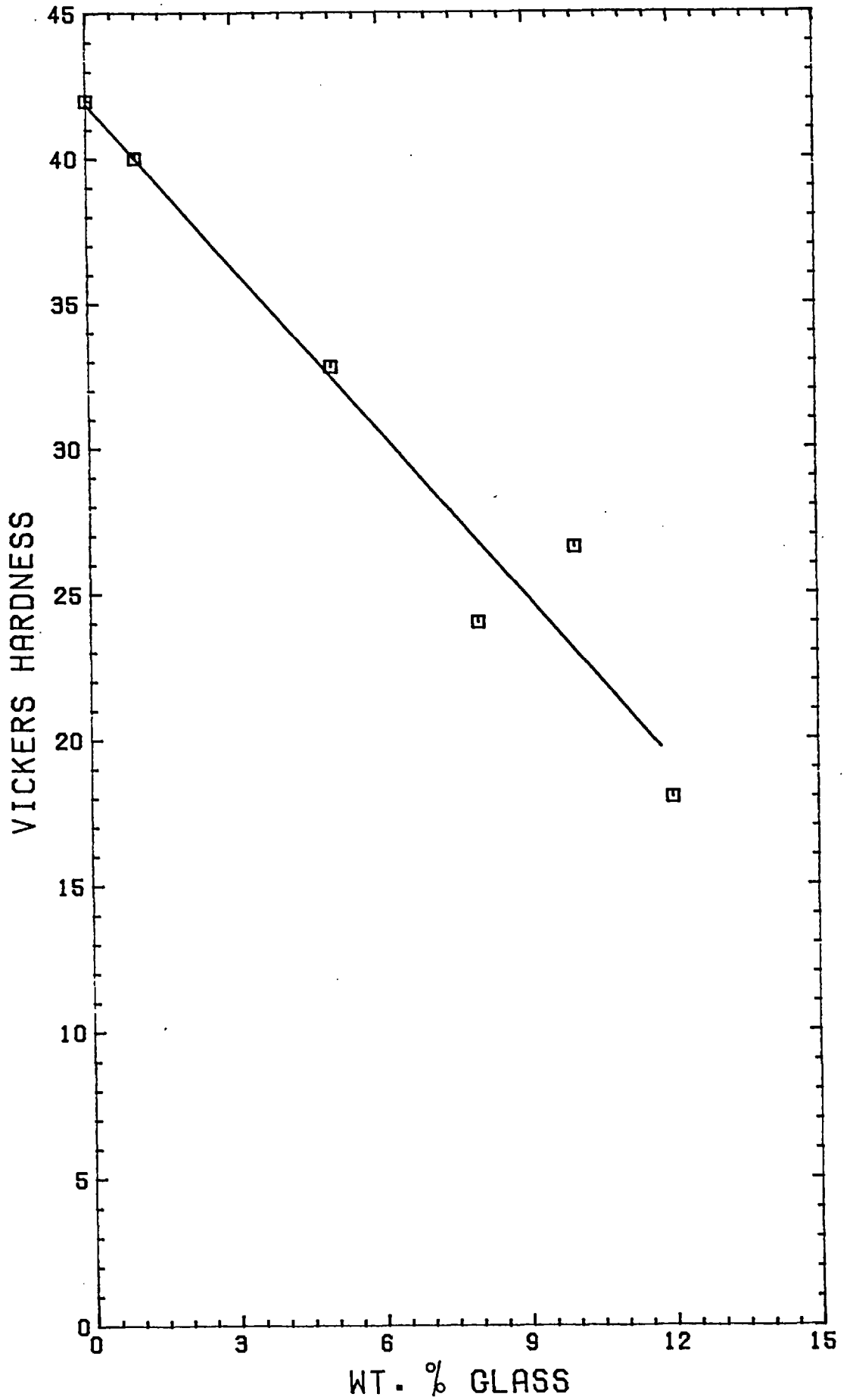
FIG. 83   Hardness of HE9 + glass extrudes as a function
of glass content

Bryant[141] found a marked decrease in the toughness
of H19 (Al, 0.4-1.4Mg, 0.6-1.3Si) with increasing extru-
sion temperature (for cast extrusion). He suggested that
this was due to large grain boundary Mg_2Si precipitates
in the recrystallised structure causing intergranular,
brittle fracture. On adding 0.4-1.0 wt.% Mn (in effect
changing H19 to HE30) the extrude structure changed from
recrystallised to fibrous and the sharp decrease in tough-
ness was prevented. Therefore it is to be expected that
the extrusion temperature should not significantly affect
the extrude toughness in the present investigation as
the HE9 extrudes (containing Mn) exhibit a fibrous, cold
worked structure.

The theory in 3.7.8 predicts quite high fracture
toughness values for composites having ductile matrices.
It predicts the occurrence of crack tip blunting which
consequently prevents inter-fibre crack propagation. On
the basis of this theory the results shown in Fig. 84 are
rather disappointing. The fracture toughness decreases
rapidly with increasing glass content. In fact an addition
of only 3 wt.% glass (6 vol %) lowers the toughness by
50%. Once again these low toughness values may be partly
attributed to excessive cracking in the matrix caused by
elastic expansion of the fibres. In addition a chemical
reaction between the glass and metal at the interface may
also have a deleterious effect on the extrude toughness.
The Mg present in the HE9 reacts with the glass forming
$Mg\ Al_2O_4$ spinel at the interface (see 5.13.1). The
presence of this spinel may well cause embrittlement of
the matrix. Fig. 84 also shows the effect on the fracture
toughness,of heating the test specimens to $200^{\circ}C$. A very
slight decrease (smaller than the experimental error) is
the result.
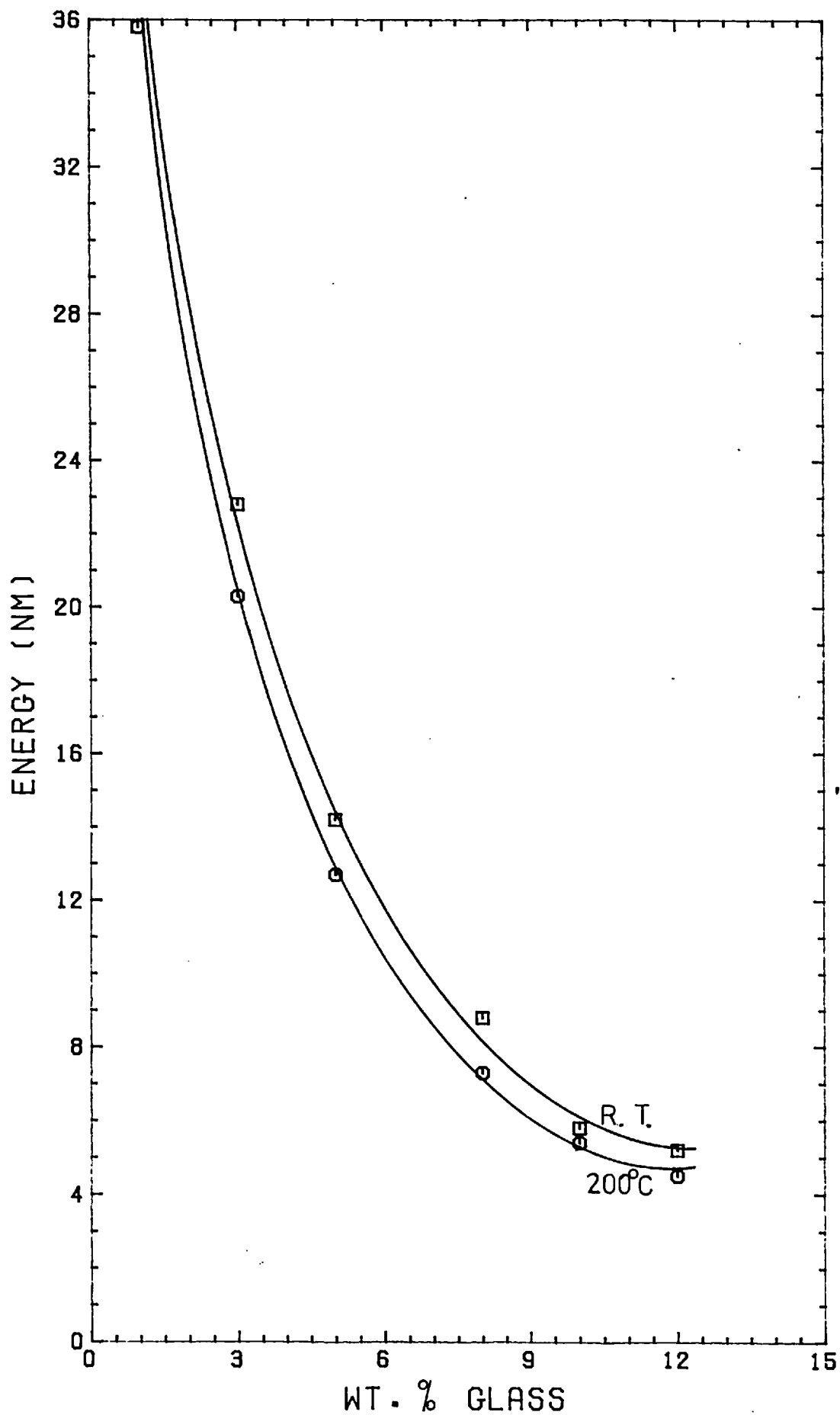
FIG. 84   Fracture toughness of HE9 + glass extrudes
as a function of glass content

5.12.1 Heat treatment results

The results of tensile tests carried out on heat treated HE9 and HE30 extrudes are given in tables 26-31. Listed in these tables are the various heat treatments employed.

These alloys are the most widely used precipitation hardening alloys and are frequently subjected to one of three differing heat treatments designated:-

T_B: solution heat treated only i.e. soaked at 500-560°C and quenched

T_E: solution heat treated, quenched, cold worked and naturally aged

T_F: solution heat treated, quenched and subsequently aged for several hours at 180 -200°C. A transformation of the type: needle-shaped zones → rods → platelets of equilibrium Mg_2Si occurs with increasing ageing time (see 2.9.1).

Typical properties for the cast and wrought alloy subjected to the differing heat treatments are given in Table 32.

The most commonly used industrial heat treatment involves a compromise. The extrude is press-quenched (i.e. the heating and extrusion of the billet replaces the solution treatment stage) and subsequently aged. A homogenisation treatment before extrusion serves two main purposes:-

1) It organises the precipitate ensuring that it is taken into solution during the extrusion cycle.

2) It helps minimize the die pick up.

In the case of HE9 the cast billet is first heat
treated to refine the Mg_2Si particles to the optimum
size of $\sim 0.5\mu$. The billet is then reheated quickly to
the extrusion temperature of $450-480^{\circ}C$. The reheat
operation must be rapid to avoid coarsening of the Mg_2Si
particles. The best method of reheating the billet
involves the use of an induction heater. A typical heater
can heat a 0.18 m diameter -0.7 m long billet to $450^{\circ}C$ in
3 minutes. In this short time precipitate coarsening is
negligible. During the actual extrusion procedure the
work done on the metal raises the temperature in the die
neck to $490-530^{\circ}C$. In this temperature range all of the
Mg_2Si redissolves. The extrude is then cooled at approxi-
mately $60^{\circ}C$ per minute to avoid rejection of the Mg_2Si.
Finally the extrude is artifically aged for 6 hours at
$175^{\circ}C$ to give a fine, homogeneous precipitate (<0.25 μm).

On comparing the results for HE9 and HE30 powder
extrudes subjected to a T_F type of heat treatment (tables
26-31) with those for cast and wrought 50S (table 32)
it can be seen that, given the correct heat treatment,
the powder extrudes are superior in U.T.S., proof stress
and elongation. (The following sections 5.12.2 and 5.12.3
describe the effect of variations in the T_F type of heat
treatments). Some powder billets were heated at $450^{\circ}C$,
extruded and artifically aged at $180^{\circ}C$ i.e. a press-quench
operation. The results in table 31 show that this pro-
cedure actually weakens the product. This is almost
certainly due to the lack of success of the homogenisa-
tion treatment, before extrusion i.e. very little of the
silicide precipitate is dissolved. Thus only a small
percentage of Mg_2Si precipitate is available for strengthening
purposes. This low level of activity is indicated by the
total variation in strength shown over the range of ageing
times, from 2 to 6 hours, in table 31. Unfortunately
this problem is not easily solved by subjecting the billets
to different homogenisation treatments because the Al_2O_3

layers surrounding the particles greatly hinder silicide dis-
solution. It might be possible to overcome this effect by
compacting to higher densities (thus, it is hoped, breaking
up the Al_2O_3 layer) and carrying out a pre-extrusion solu-
tion soak. However, it is very doubtful whether sufficient
disintegration of the oxide layers would occur. Even if .
such action succeeded it might prove difficult to prevent
reoxidation during the soak.

The results of attempts to heat treat HE9-5wt.%
glass reinforced extrudes are given in table 33. (It had
been hoped to combine fibre reinforcement with precipitation
hardening). Unfortunately, these results are very dis-
appointing, with the heat treatments having little effect
on the product properties. This is due to chemical reactions
occurring between the B_2O_3 and the magnesium. Most of the
magnesium reacts with the B_2O_3 leaving very little to combine
with silicon for precipitation strengthening. Indeed the
B_2O_3-Mg reaction degrades the fibre-metal interface[138], in
some cases actually weakening the product.

5.12.2 <u>Effect of soaking temperature variation on extrude</u>
<u>properties</u>

The important effect on the mechanical properties
of HE9 and HE30, of varying the soaking temperature is
shown in Fig. 85. (and table 26). The specimen extrudes
were given a T_F-type heat treatment. The U.T.S. and proof
stress increase with temperature up to about 555°C and then
begin to deteriorate. At the optimum temperature, 555°C,
the U.T.S. is increased by 28% and the proof stress by 60%.
Increasing the soaking temperature increases the amount of
Mg_2Si taken into solution which, in turn, produces more
precipitate on ageing. This produces the increase in
strength. Eventually, at about 555°C, a 5 hour soak
effectively dissolves all the Mg_2Si. Above this temperature
a slight weakening occurs probably due to subgrain growth.
(At elevated temperatures the subgrains tend to grow to
minimize the total subgrain boundary area and thus the
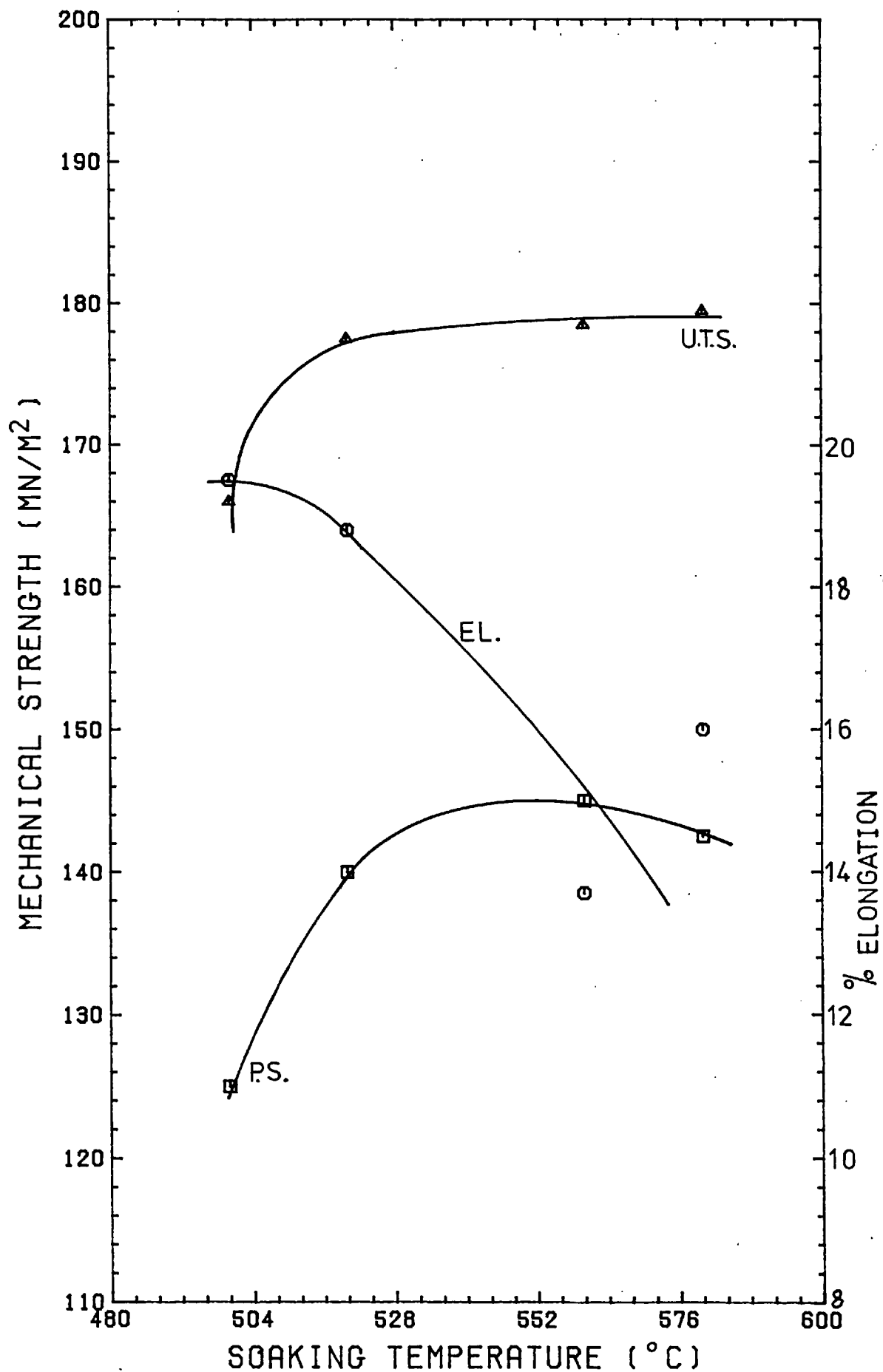
FIG. 85   Effect of variations in soaking temperature
on mechanical properties of heat treated
HE9 extrude

total free energy). The elongation decreases steadily
with increasing soaking temperature due to the increased
amount of precipitate and to the subgrain growth.

5.12.3 Effect of ageing time/temperature variation on extrude properties

The results from tables 27 and 28 are plotted in
Figs. 86 and 87. These demonstrate the effects of ageing
temperature and time variations on HE9 powder extrudes
subjected to a T-F type of heat treatment. The optimum
ageing temperature (for a 6 hour treatment) appears to
be $\sim$ 160°C (Fig. 86). The recommended ageing temperature
for conventionally extruded HE9 is 175°C. Using this
ageing temperature a 35% increase in U.T.S. and a 65%
increase in proof stress are obtained. Ageing for 6 hours
at temperatures above $\sim$ 160°C causes overaging i.e. the
precipitate particles grow larger than the optimum size.
The interparticle spacing therefore increases and the
mechanical strength deteriorates. The behaviour of the
HE9 powder extrude at different ageing temperatures is
represented schematically in Fig. 88, which explains the
relative magnitudes of points A, B and C in Fig. 86. The
decrease in elongation to a minimum of 13%, at an ageing
temperature of $\sim$ 167°C coincides with an increase in the
volume fraction of Mg_2Si precipitate. However, after
precipitation ceases and the existing particles begin
to grow, the elongation value increases again to about 21%
at an ageing temperature of 220°C. It appears that:

1) Elongation $\downarrow$ as volume fraction of precipitate $\uparrow$
2) Elongation $\uparrow$ as preciptate particle size $\uparrow$

The effect of varying the ageing time, at a constant
temperature of 180°C, is shown in Fig. 87. Initiallly
the U.T.S. and proof stresses increase and the elongation
decreases with ageing time as expected. However, from
Fig. 86 and 88 we would expected the peak strength to
correspond to an ageing time of less than 6 hours.
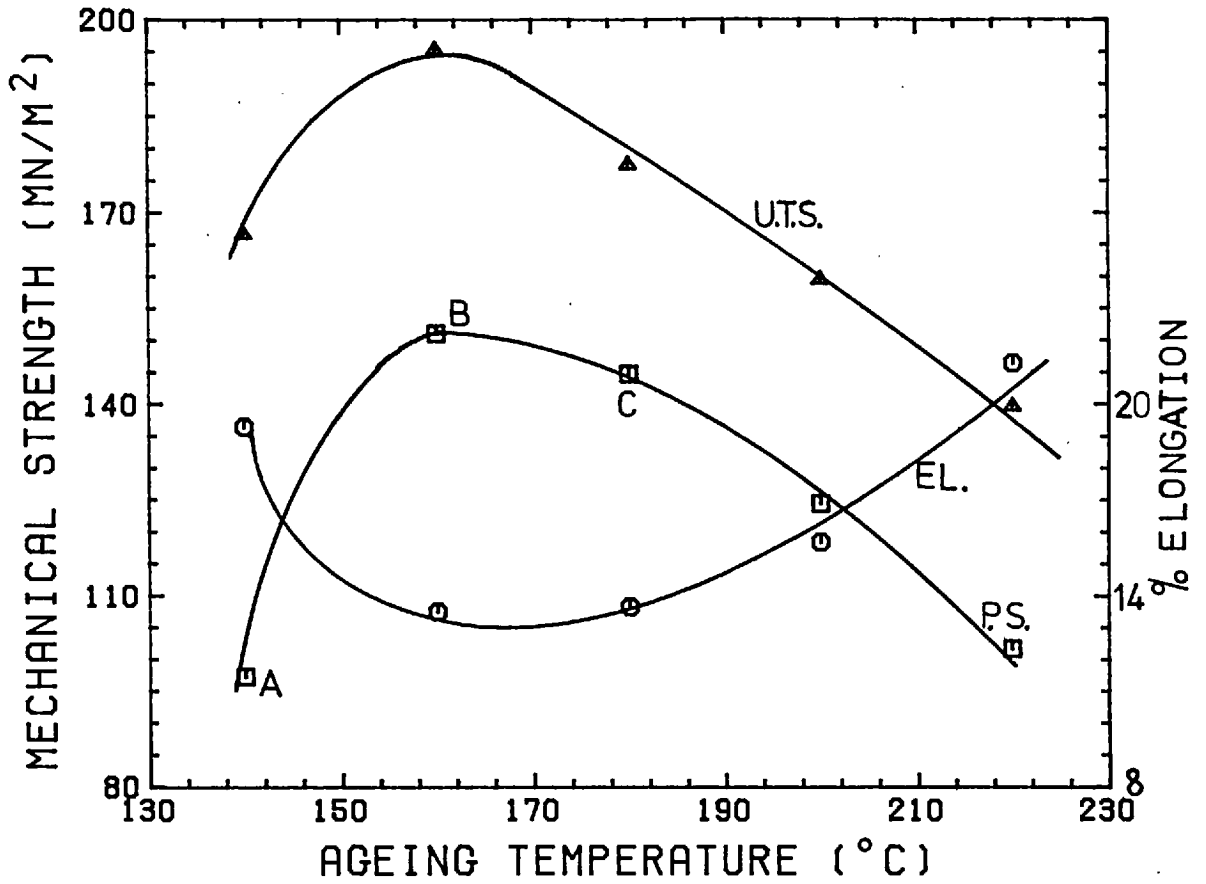
FIG. 86 Effect of variations in ageing temperature on
mechanical properties of heat treated HE9 extrude
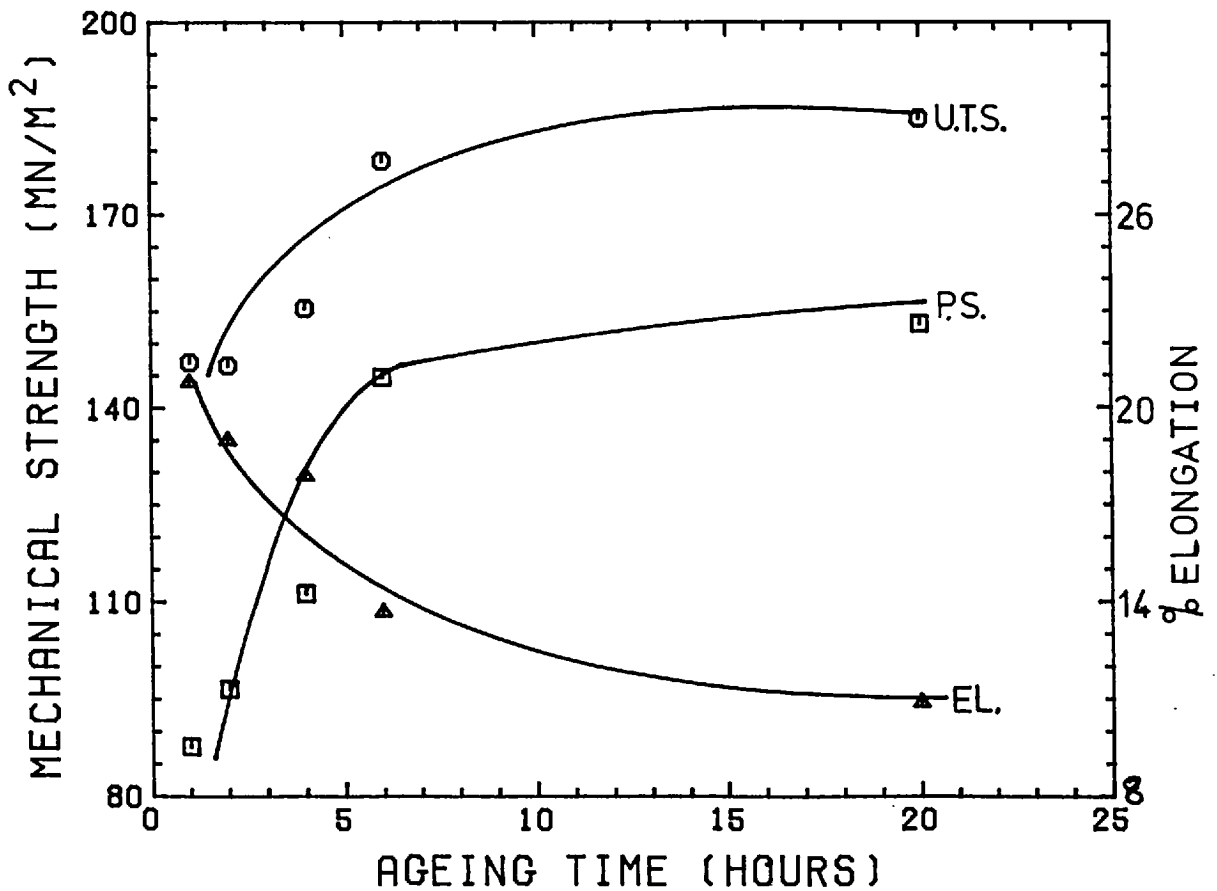
FIG. 87 Effect of variations in ageing time on
mechanical properties of heat treated
HE9 extrude
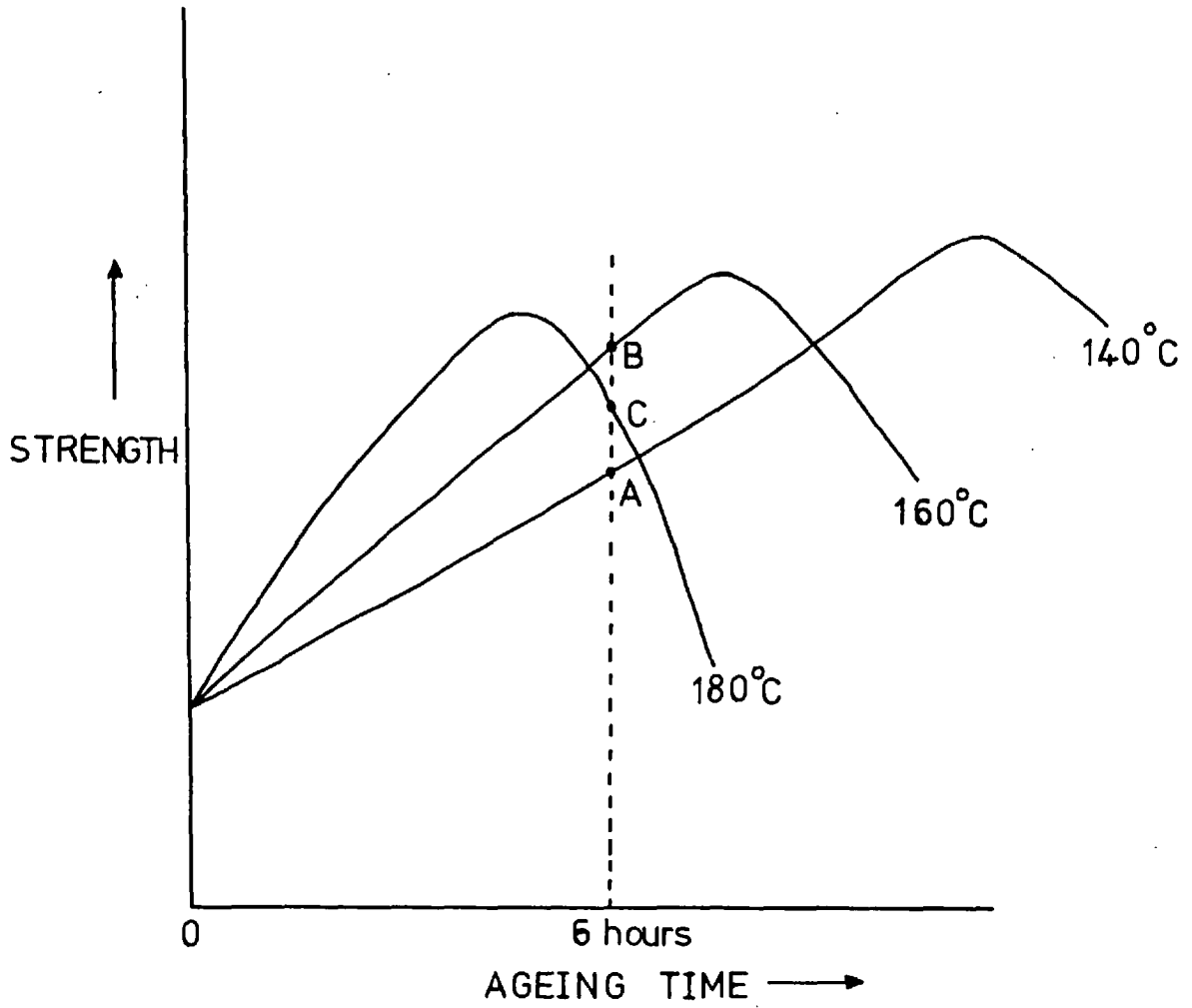
FIG. 88   Schematic representation of HE9
ageing curves at different temperatures

Fig. 87 indicates that the optimum strength may not be obtained for ageing times of less than 20 hours. However, this anomaly is based on the data points of only one specimen. (i.e. at 20 hours). Therefore it is more likely that the results for this specimen are erroneous.

HE30 behaves similarly to HE9 as can be seen in Figs. 89 and 90. In this case, however, the optimum ageing temperature for a 6 hour treatment is $180^{\circ}C$ (Fig. 89). The response to heat treatment is even better than that of HE9, the U.T.S. increasing by 40% and the proof stress by 85% on ageing for 6 hours at $180^{\circ}C$. The improved response is caused by the greater quantity of Mg_2Si available for precipitation hardening. The temperature sensitivity is greater than the time sensitivity as manifested by the curve in Fig. 90 being "flatter" than that in Fig. 89. Overageing does not seem to occur, at $180^{\circ}C$, until heating times of approximately 10 hours are employed. The elongation of HE30 appears to be much less affected by heat treatment than that of HE9 although prolonged ageing (16-24 hours) at $180^{\circ}C$ does cause a noticeable decrease. The reason why the elongation of HE30 powder extrude is less sensitive to heat treatment than that of HE9 is not obvious. Clearly the elongation of HE30 might be expected to decrease even more than that of HE9 because of the greater quantity of Mg_2Si available for precipitation. However, the fact that the initial powder particle size of the HE30 powder (median = 122μ) is smaller than that of the HE9 powder (median = 141μ) may have some bearing on the matter.

5.13.1 Structure of extrudes (optical micrographs)

The optical micrographs shown in Plate 11 reveal the structure of a typical HE9 extrude. The longitudinal micrograph (11(a)) shows a fibrous, cold-worked structure. The original powder particles have been elongated in the direction of extrusion. This "cold-worked" microstructure is the result of extruding at a temperature ($450^{\circ}C$) above

(a)
Longitudinal

(b)
Transverse

PLATE 11   Optical micrographs of HE9 extrude (450°C, 80:1)
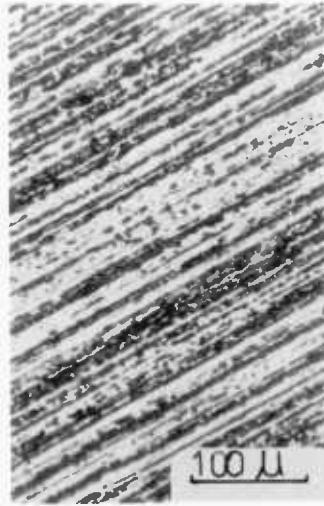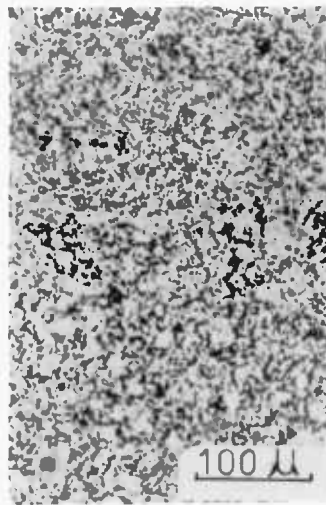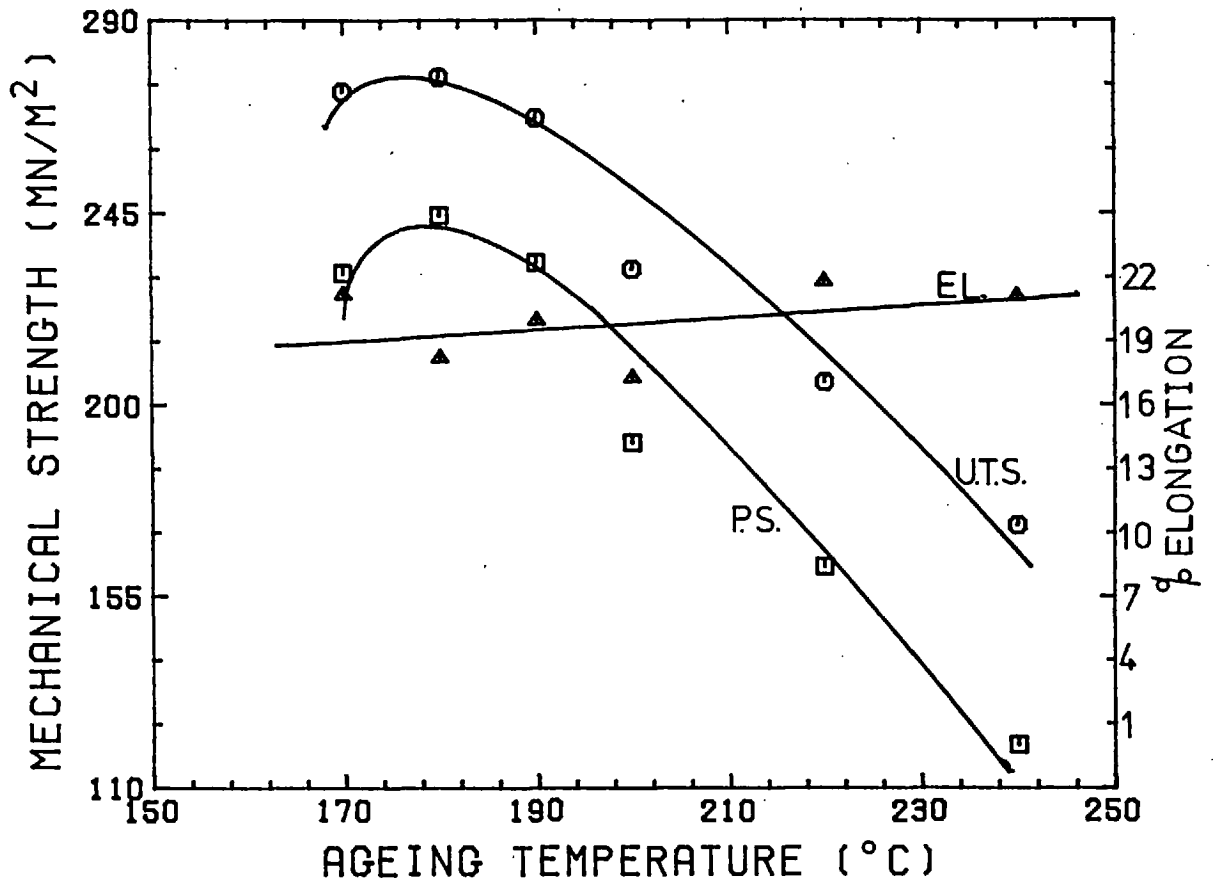
FIG. 89 Effect of variations in ageing temperature on
mechanical properties of heat treated HE30
extrude
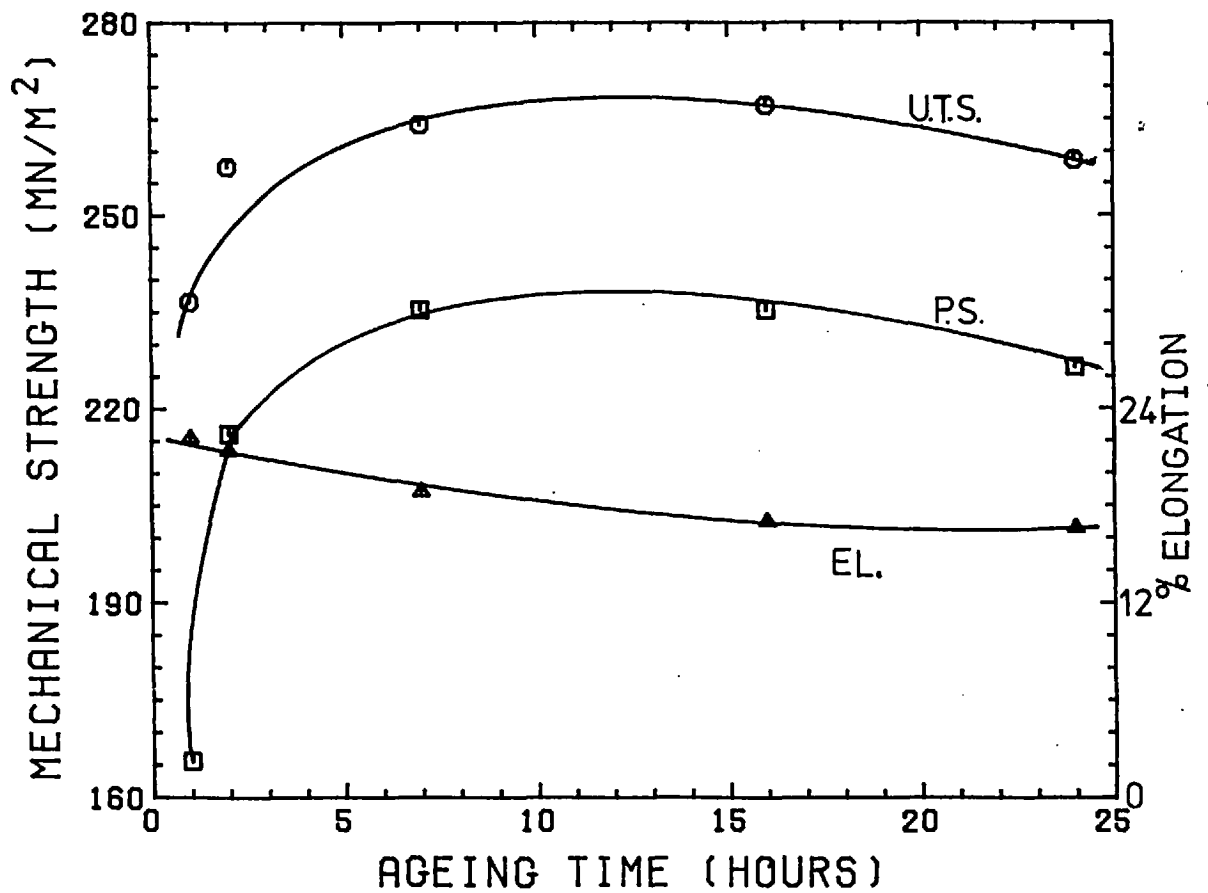
FIG. 90 Effect of variations in ageing time on mechanical
properties of heat treated HE30 extrude

the nominal static recrystallisation temperature ($350^{\circ}C$).
The transverse micrograph (11b) reveals the equiaxed
nature of the structure. This structure is typical of
extrusions produced over the entire range of temperatures
and strain rates investigated. Optical microscopy reveals
no evidence of recrystallisation in any of the extrudes.
Chare[19] and Ansell and Kim[137] found no evidence of recry-
stallisation in Al, Al-Fe & Al-Mn and S.A.P. powder extrudes,
respectively. This evidence supports the thesis that
dynamic recovery is probably the prevailing softening
mechanism although the presence of sub-grains cannot be
detected at these magnifications, except by the use of
polarized light. Jonas[49] found a similar "cold-worked",
fibrous structure in aluminium extrudes produced at $400^{\circ}C$
i.e. $50^{\circ}C$ above the recrystallisation temperature. However,
he discovered that extrusions produced at $500^{\circ}C$ and
above were fully recrystallised. Plumtree[58] has suggested
that the ability of aluminium to recrystallise is directly
related to its purity. The question that must now be
answered is: if impurities retard recrystallisation in
Aluminium why then do many of the stronger aluminium alloys
i.e. the 7000 and 5000 series recrystallise? Humphreys[140]
found that second phase particles, such as $CuAl_2$ particles,
help to nucleate recrystallisation if they are larger than
a critical size, which is strain dependent. He states that
the critical size, for a 45% reduction, is 1-2 μm. Thus
the second phase particles present in the stronger aluminium
alloys actually aid recrystallisation which originates
within zones of high dislocation density adjacent to the
particles. Now in the present series of experiments no
second phase particles of 1-2 μm size exist (see electron
micrographs in next section 5.13.2). In fact the precipitate
and fragmented oxide particles are $\ll$ 1-2 μm. Thus the
high oxide content of the HE9 powder together with the
Mn[141] alloying addition actually prevent recrystallisation,
even at the highest extrusion temperatures, the oxide particles
together with solute atom clusters preventing new, high
angle grain boundaries from sweeping through the material.

All the HE30, Al-Mg and Al extrudes exhibit similar structures for the same reasons. Plate 12(a) and (b) show longitudinal and transverse micrographs of a typical Al extrusion (550°C, 90:1). Again the longitudinal micrograph shows a fibrous structure consisting of elongated particles; the transverse micrographs revealing an equi-axed structure. The micrographs in Plate 12(c) and (d), show the structure of an Al 80:1 extrude produced at 300°C. The obvious cracking is due to the lack of ductility of the Al at this lower temperature. At this low temperature the material is fairly rigid and difficult to work due to the low rate of dynamic softening.

The imperfection of the fibres formed during extrusion is demonstrated in Plate 13. Micrographs (a) and (b) represent, respectively, longitudinal sections near the surface and at the centre of a HE9 + 5 wt.% glass extrude. The fibres near the surface are much more elongated than those at the centre. This is a manifestation of the variation in strain which occurs across the section of an extrusion. Micrographs (c) and (d) show the corresponding transverse structures . Clearly the fibres, in practice, are far removed from the theoretically ideal, uniform cylinders discussed in 3.7.1. This is the reason that the fibre strengths, estimated in 5.9.6, are so much less than values commonly available from industrially drawn glasses.

Extrusion of Al-glass and Al-Mg-glass composites produce similar fibres. Plate 14(a) and (b) show longitudinal sections, near the surface and at the centre of an Al-Mg-5 wt.% glass extrude, produced at 450°C (80:1). Micrographs (c) and (d) show the corresponding sections of an extrude of the same composition produced at 500°C, (80:1). Clearly the increase in temperature produces larger, better quality fibres. This is because the glass flows more easily, in the deformation zone, at the higher temperature.

(a)
Longitudinal   (550°C)   (b)
                                   Transverse

(c)   (300°C)   (d)
Longitudinal   Transverse

PLATE 12   Micrographs of aluminium extrudes
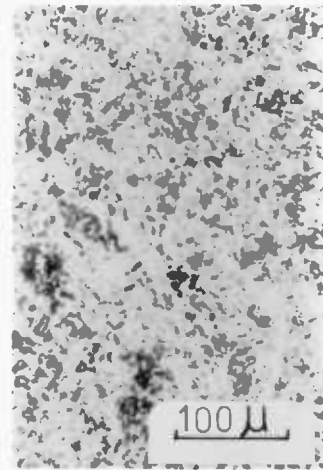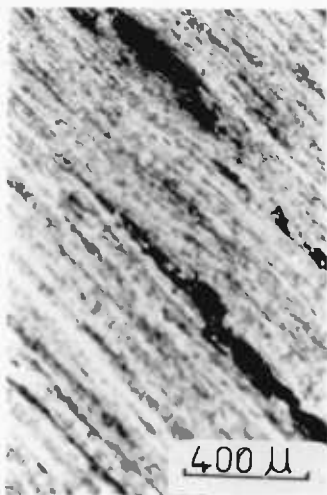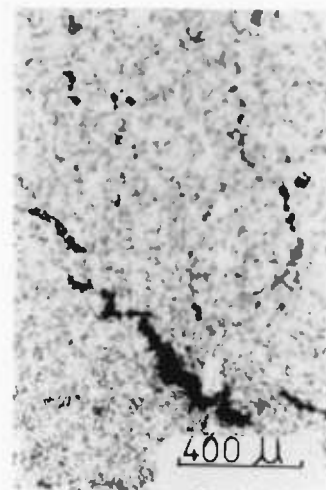
(450°C)

(a)

Longitudinal
(near surface)

(40:1)

(b)

Longitudinal
(at centre)
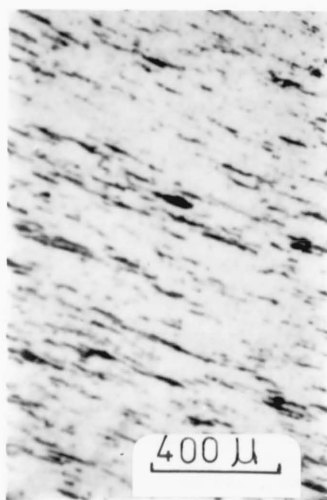
(c)

Transverse
(near surface)

(d)

Transverse
(at centre)
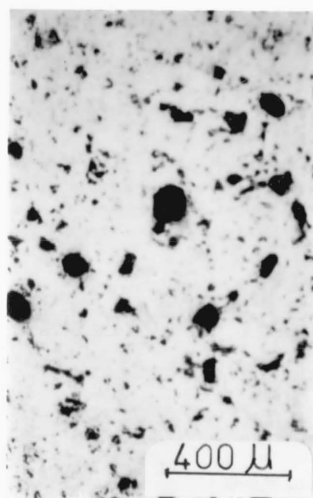
PLATE 13   Optical micrographs of an HE9 + 5 wt.% glass extrude

(a)
Longitudinal
(at centre)

(450°C)

(b)
Longitudinal
(near surface)
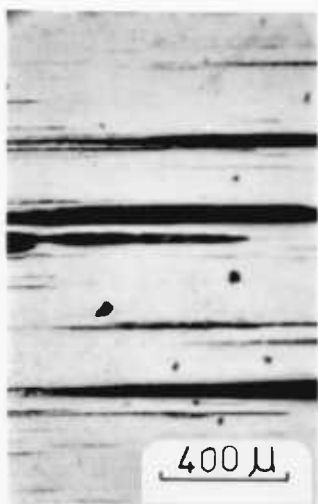
(c)
Longitudinal
(at centre)

(d)
Longitudinal
(near surface)

PLATE 14   Optical micrographs of Al-Mg + 5 wt.% glass extrudes
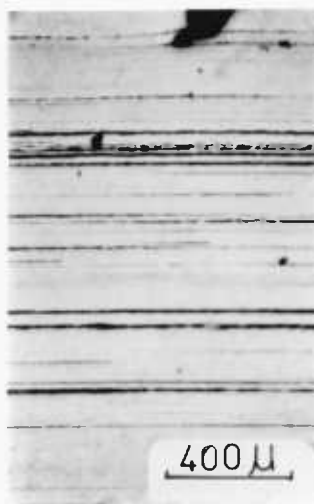
5.13.2 Structure of extrudes (transmission electron micrographs)

The electron micrographs in Plates 15-18 show clearly that dynamic recovery occurs during the extrusion of HE9, HE30, and Al-Mg alloys. (The absence of electron micrographs of reinforced extrudes and Al powder extrudes is due to the difficulty encountered in thinning these materials). Subgrains, elongated in the extrusion direction, constitute the substructure in the longitudinal sections of HE9 40:1 extrudes formed at 250°, 350° and $450^\circ C$. (Plate 15 (a), (b) and (c) respectively). Transverse micrographs (a) and (b) in Plate 16 reveal the "equi-axed" nature of the subgrains in this plane, in 40:1 extrusions produced at 450 and $540^\circ C$ respectively. The fact that the sub-grains are elongated in the extrusion direction but "equi-axed" in the plane perpendicular to this is evidence that the operating softening mechanism is dynamic recovery. The structure of HE30 extrudes is very similar to that of HE9. Plate 17(a) and (b) ($350^\circ C$, 60:1) demonstrate the dynamically recovered structure. Once again the sub-grains are elongated in the direction of extrusion (a) and "equi-axed" in the perpendicular plane (b). A similar substructure also exists in the Al-Mg extrudes ($500^\circ C$, 80:1) as shown in Plate 18(a). The main variation in structure over the temperature range investigated is an increase in subgrain size and perfection with temperature. In addition, at the higher extrusion temperatures the sub-grains tend to be "equi-axed" in three-dimensions i.e. the elongation in the extrusion direction disappears (Plates 15(a) and (c). At the higher extrusion temperatures the dislocation mobility increases and cell walls migrate tending to form "equiaxed" subgrains. Once again the driving force for this migration is the need to minimize the total grain boundary area and thus reduce the free energy of the structure.

Fig. 91 demonstrates an approximately linear relationship between subgrain size and extrusion temperature. Wong et al[118] discovered a similar relationship in extruded, commerically pure Al. They also noticed a tendency for the subgrains to become elongated in the extrusion direction at the lower temperatures. Raybould and Sheppard[32] found an approximately linear relationship between lnZ and subgrain size^{-1} for Al-7%Zn (for subgrain sizes > 2.5µ). The present results, plotted in this form (Fig. 92), do not fit a linear relationship. (N.B.Alinear relationship cannot be totally ruled out due to the lack of data points). However, a smooth curve may be drawn through the points giving quite a good fit. The divergence from linearity occurs at the higher Z values i.e. high strain rate, low temperature extrusions. Plate 15(d) shows a S.A.D.P. for a typical HE9 extrude (250°C, 40:1). A <111> orientation is associatedwith the fibrous texture produced by dynamic recovery during aluminium extrusion.

Oxide particles, remnants of the layers covering the original powder particles, are clearly visible in Plate 15(a) and (b). These fragments indicate the original powder particle boundaries. (Some of the particles which appear very close together represent boundaries parallel to the foil surface). Chare[14] found his original particle boundaries to be similarly outlined. The history of the formation of these oxide particles is unfolded in Plate 18 (b) and (c). Micrograph (b) shows the structure of the compact at position Y (Fig. 93) during the extrusion of an Al-Mg powder billet (350°C, 80:1). (The extrusion was stopped before completion, the billet sectioned and specimens taken). At this early stage in the deformation process the oxide layers between two adjacent particles are still almost completely continuous. Micrograph (c) shows the structure at position Z (Fig. 93) of an HE30 partial extrude (450°C, 80:1). At this later stage the oxide layers have been broken up and the original boundaries are clearly revealed by "chains" of oxide fragments.
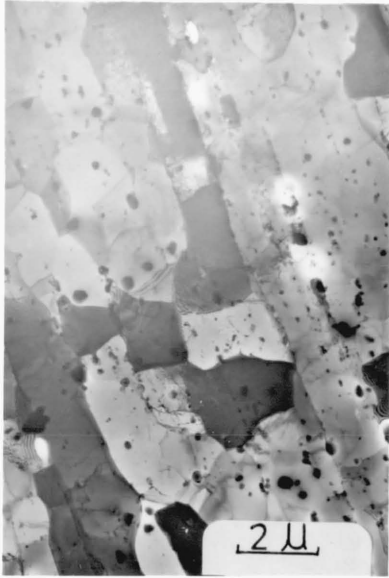
(a)
250°C
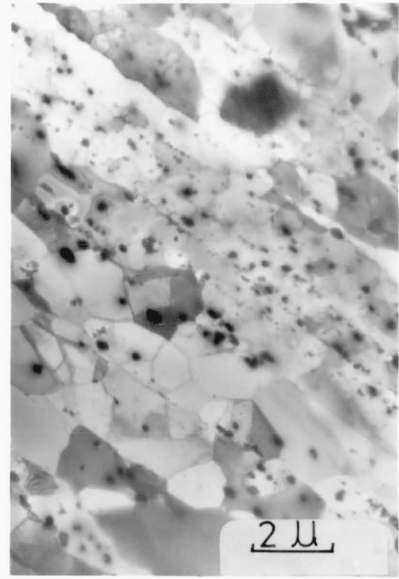
(b)
350°C
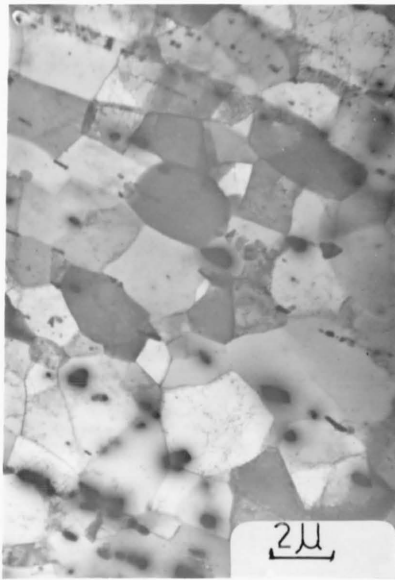
(c)
450°C

(d)
diffraction pattern

PLATE 15   Longitudinal transmission electron micrographs
of HE9 extrudes
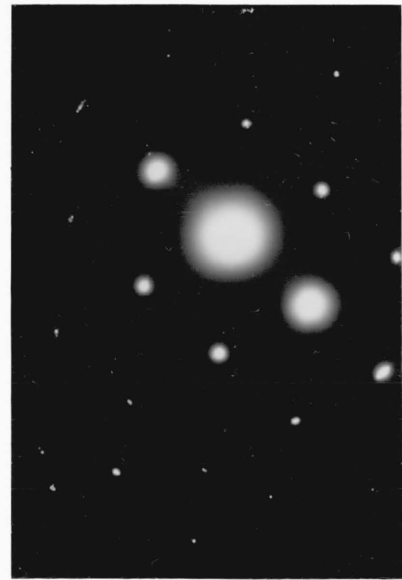
(a)
(450°C)
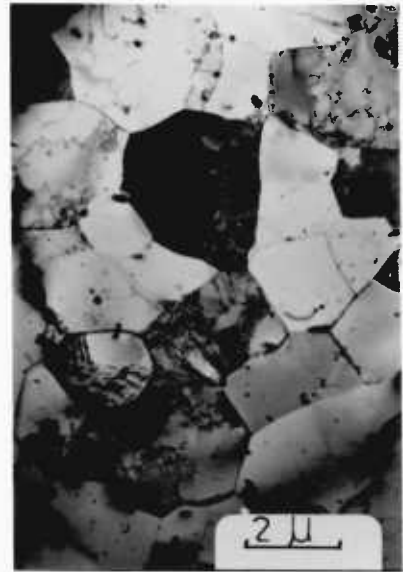
(b)
(540°C)

PLATE 16

Transverse electron micrographs of HE9 extrudes
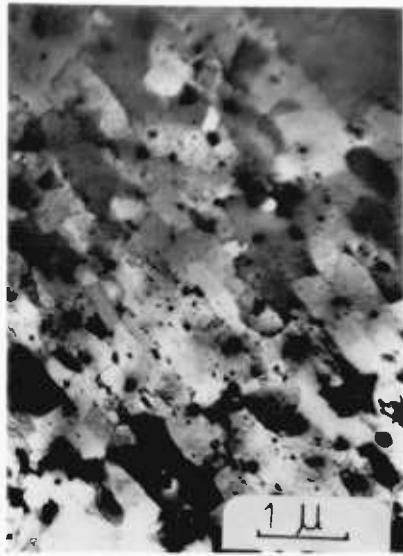
(a)

Longitudinal

$(350^{o}C)$

(b)

Transverse

(c)

$(550^{o}C)$

(taken from partial extrusion)

PLATE 17   Transmission electron micrographs of HE30 extrudes
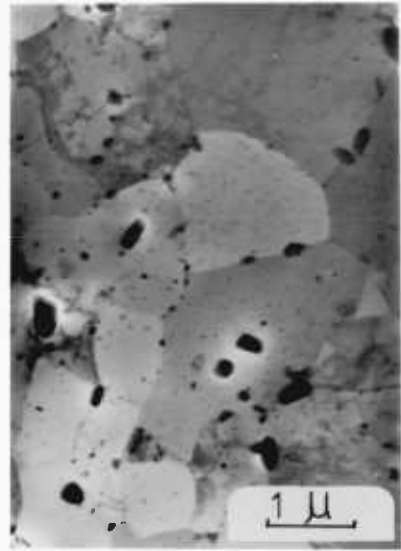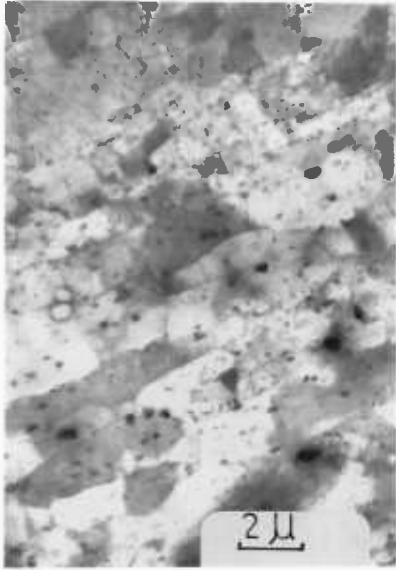
(a)
Al-Mg (500°C)
Longitudinal
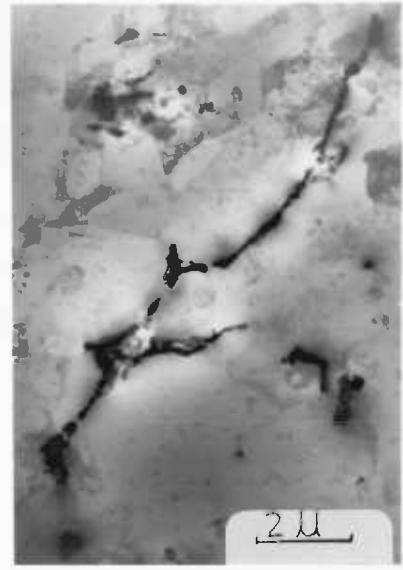
(b)
Al-Mg (350°C)
(Taken from partial extrusion)
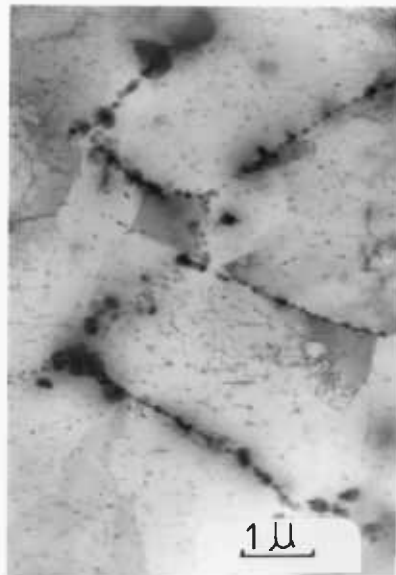
(c)
HE30 (450°C)

Taken from a partial extrusion)

PLATE 18   Transmission electron micrographs of Al-Mg and
HE30 extrudes.
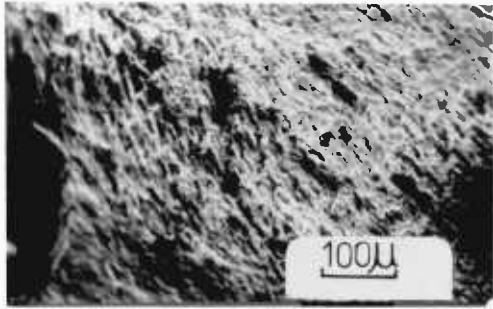
(a)

Room temperature test　　　HE9　　　400°C test

(b)
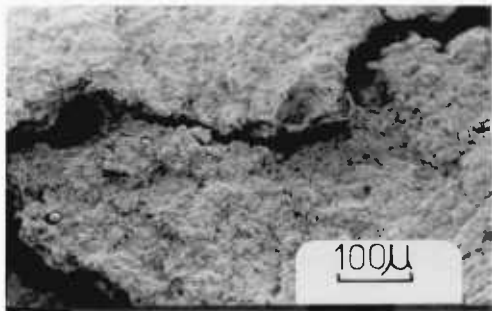
(c)

Room temperature test　　　Al　　　Room temperature test

(d)
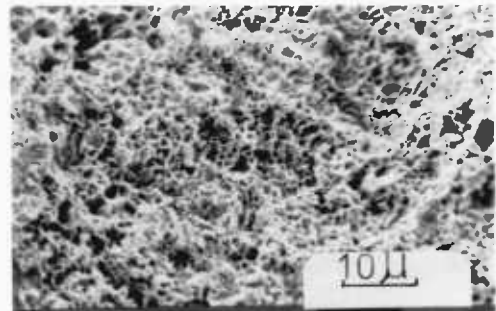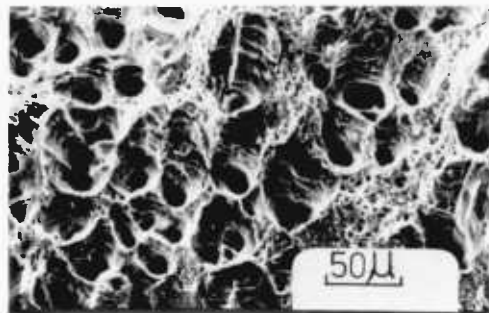
(e)

HE9 + 5 wt.% glass
Room temperature test

PLATE 19　　　Scanning electron micrographs of fracture surface
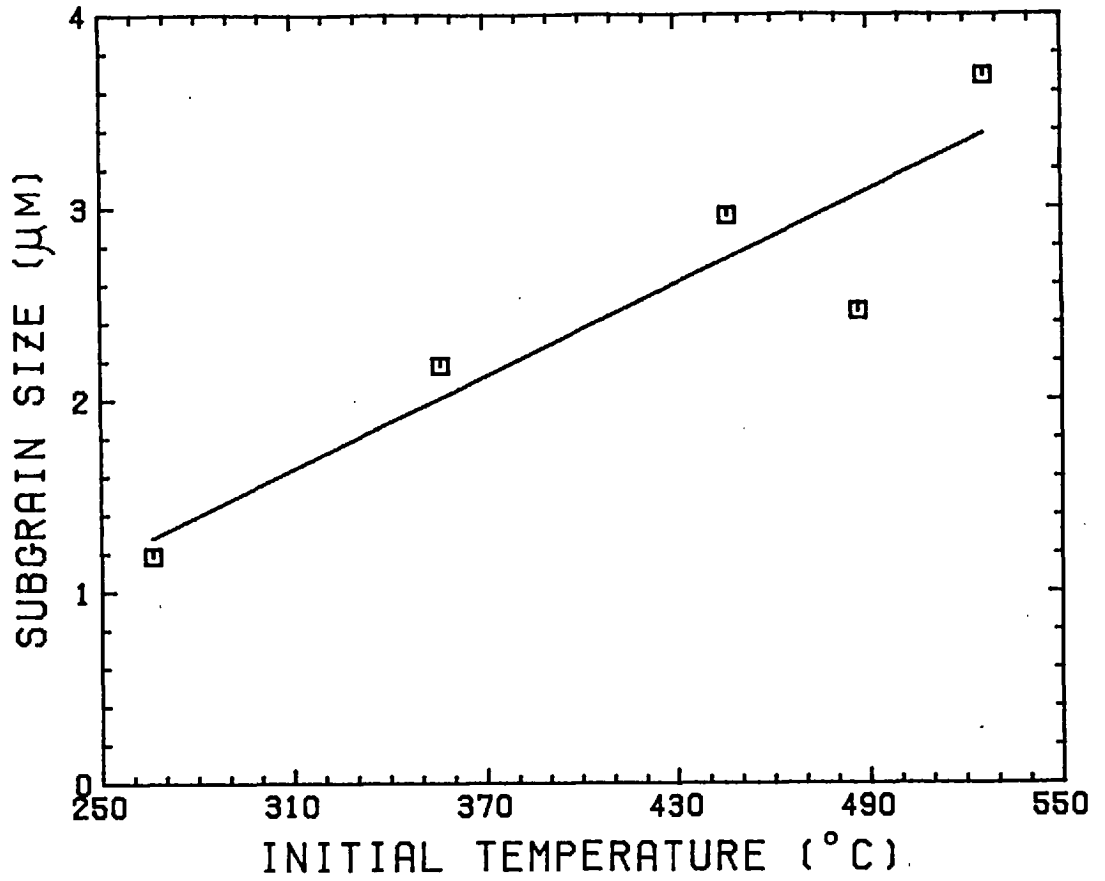
FIG. 91 HE9 extrude subgrain size as a function of extrusion temperature
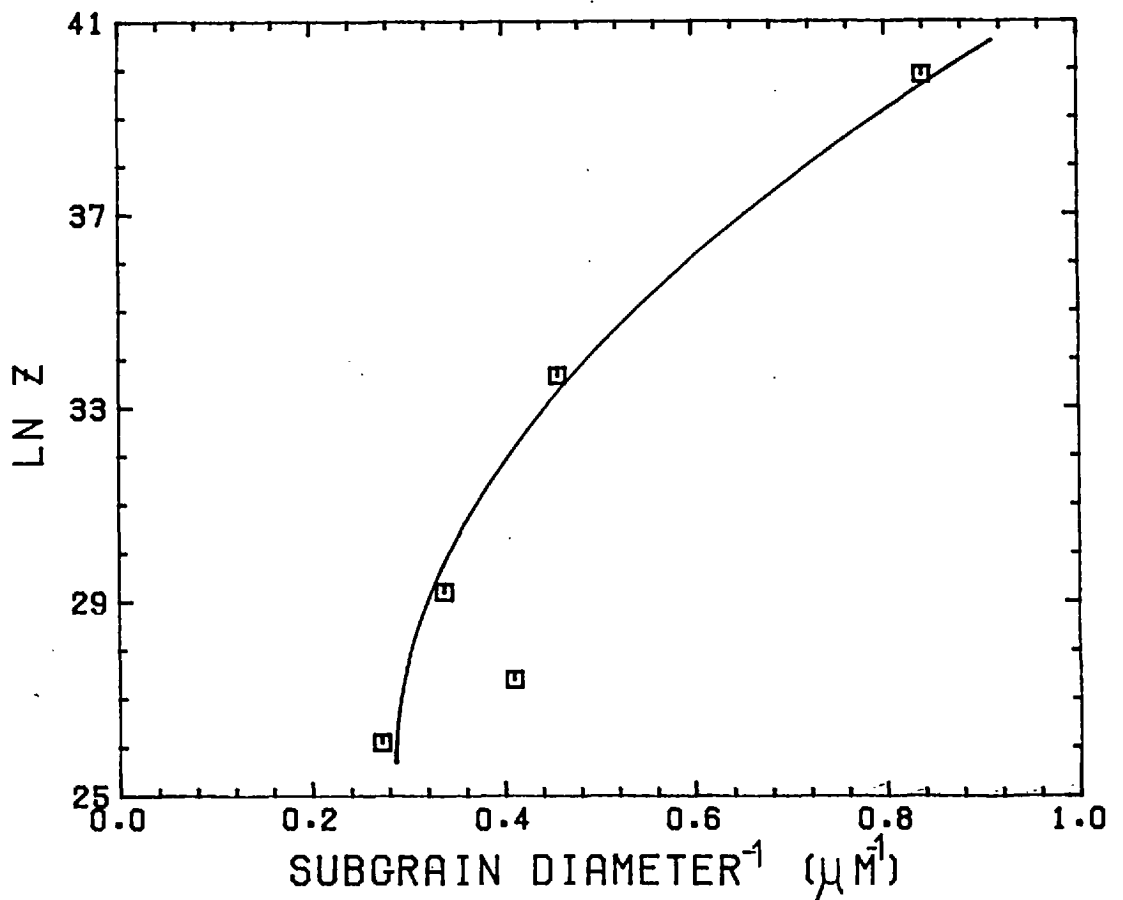
FIG. 92 ln Z vs. reciprocal subgrain size relationship for HE9 extrudes
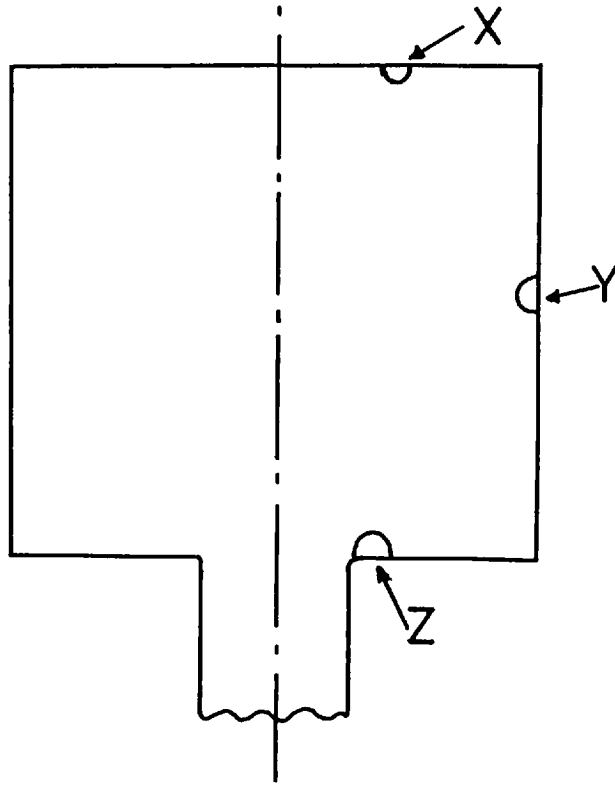
FIG. 93   Locations of electron microscope foils
         taken from partial extrusions

Thomas[72] found Mg_2Si precipitate particles, in
Al-Mg-Si alloys, occurring as rods along the <100>
directions in the aluminium matrix. Plates 17(c),
taken fromposition x in a partial extrusion (See Fig. 93)
and 18(c) reveal rod like particles which are mutually
perpendicular and thus may be considered as evidence in
support of Thomas's findings.

5.14.1 Nature of the glass-metal interface

Plate 10(b) is a scanning electron micrograph of
the end of a fibre channel in a fractured HE9 + 5 wt.%
glass tensile specimen produced from a 80:1, 450°C extru-
sion. The shell around the crater is fairly distinct.
This shell consists of the products of the glass-metal
chemical reaction. Research into the composition of these
products was carried out at Borax Consolidated Limited[138].
(A knowledge of the composition of these products is
important as the composite strength is dependent on the
strength of the metal-glass interface). HE30 + 5 wt.%
glass extrude specimens were dissolved in a NaOH solution
leaving behind the glass-metal interaction products as a
very fine suspension. Precipitates were produced by
centrifuging this suspension. An x-ray diffraction
examination revealed the presence of the spinel $MgAl_2O_4$.
Several extrudes were also heated at 550°C for several
hours before dissolution in the NaOH solution. The x.R.D.
pattern revealed the presence of a magnesium alumino-
silicate, probably $4MgO. 5Al_2O_3. 2SiO_2$. No magnesium
silicide was detected. This explains the lack of response
to heat treatments (see 5.12.1) shown by the reinforced
HE9 extrudes. (The lack of Mg_2Si in the matrix prevents
precipitation hardening from occurring).

HE9	
Particle size, μm	wt. per cent
+355	2.87
+180	36.42
+106	63.56
+90	68.91
+75	73.80
+63	79.06
+53	83.55
-53	16.26

Median Particle Size
= 143 μm

TABLE 1

Sieve analysis of HE9 powder

HE30	
Particle size, μm	wt. per cent
+355	2.91
+180	29.26
+106	55.61
+90	61.88
+75	67.77
+63	74.54
+53	80.38
-53	19.51

Median Particle size
= 121.8 μm

TABLE 2

Sieve analysis of HE30 powder

Al-3 wt.% Mg	
Particle size, μm	wt. per cent
+355	2.35
+250	15.77
+180	26.52
+125	42.72
+106	52.18
+75	65.49
+45	81.59
-45	18.21

Median Particle Size
= 110.4 μm

TABLE 3

Sieve analysis of Al-3wt.% Mg
powder

Al	
Particle size, μm	wt. per cent
+355	13.31
+250	31.25
+180	42.26
+125	58.52
+106	67.41
+75	77.93
+45	88.67
-45	11.28

Median Particle Size
= 153.8 μm

TABLE 4

Sieve analysis of Al powder

B_2O_3-10% SiO_2	
Particle Size, µm	wt. per cent
+250	8.13
+180	17.67
+125	30.09
+90	46.71
+75	49.29
+53	60.38
+45	64.65
-45	32.61

Median Particle Size = 74 µm

TABLE 5

Sieve analysis of B_2O_3-10% SiO_2 glass

	O	Si	Mg	Zn	Cu	Ni	Fe	Mn	Cr	Ti
HE9	0.062	0.120	0.330	0.025	0.014	0.004	0.150	0.100	0.010	0.014
HE30	0.062	0.330	0.350	0.020	0.040	---	0.310	0.530	0.013	0.019
Al-3wt.% Mg	0.120	---	3.000	0.100	0.078	0.006	0.300	0.510	0.040	0.040
Al	3.300	---	---	0.041	0.040	0.003	0.200	0.009	0.006	0.006

<u>WEIGHT PERCENTAGE OF ALLOYING ADDITIONS AND IMPURITIES</u>

TABLE 6

Chemical analysis of metal powders

Compaction Pressure (MN/m)	Theoretical Density (%)	Fracture Force (N)	$\ln(\frac{1}{1-D})$
185.3	84.6	64.5	1.8689
216.2	86.3	135.7	1.9863
247.1	87.3	189.1	2.0596
278.0	89.4	222.4	2.2424
308.9	89.7	235.8	2.2721
339.83	90.0	202.4	2.3066
370.7	91.2	282.5	2.4350
401.6	91.5	311.4	2.4616
432.4	93.1	286.9	2.6679

TABLE 7

Results of mechanical tests on cold compacts

Sintering Temperature (°C)	Fracture Force (N)
500	+2358
430	2358
375	+2358
305	1321
240	801
160	605

TABLE 8

Results of mechanical tests on sintered compacts

HE9 PARTICLE SIZE μm	FRACTURE FORCE (N)
26.5	2358
64	885
112	552
+150	445

TABLE 9

Results of mechanical tests on compacts
produced from different sieve fractions

TABLE 10   235

Extrusion parameters

No	Extrusion Ratio	(°C) Initial Temp.	(°C) Final Temp.	(m/sec) Ram Speed	(MN/m²) Peak Load	(MN/m²) Final Load	P/K	(MN/m²) Peak Flow stress	(MN/m²) Final Flow Stress	(sec⁻¹) Strain Rate	(sec⁻¹) ? x 10^?
(HE9)											
1	30	526	536.3	0.009	350.7	417.3	13.767	44.01	52.50	7.59	0.4648
2	30	526	509.7	0.005	345.1	408.2	13.767	43.42	51.56	4.64	0.6711
3	30	526	534.3	0.0135	394.7	338.3	13.767	49.66	42.56	11.39	0.7539
4	30	526	514.6	0.007	313.5	376.7	13.767	39.44	47.39	5.91	0.7285
5	30	526	472.3	0.003	313.5	394.7	13.767	39.08	49.66	--	--
6	30	526	--	--	310.6	394.7	13.767	39.08	49.66	--	--
7	40	432	482.3	0.0010	446.6	410.5	14.996	51.58	47.41	9.41	3.4590
8	40	426	464.5	0.0065	475.9	410.5	14.996	54.98	47.41	6.11	4.2716
9	40	439	491.3	0.0014	466.9	412.8	14.996	53.92	47.68	10.72	4.4906
10	80	437	517.2	0.0126	550.4	516.5	18.176	52.45	49.22	15.08	1.7091
11	80	438.5	493.8	0.0097	570.7	455.6	18.176	54.39	43.42	11.61	2.8605
12	80	432	459.9	0.0031	545.9	523.3	18.176	52.01	49.87	3.71	3.0770
13	80	432	483.1	0.006	527.8	500.7	18.176	50.30	47.72	7.18	2.5650
14	80	437	--	0.101	543.6	--	18.176	51.79	--	120.9	--
15	80	356	461.2	0.0094	581.9	523.3	18.176	55.46	49.87	11.25	8.8905
16	80	356	427.5	0.0043	577.4	466.9	18.176	55.03	44.56	5.14	15.1648
17	80	356	434.3	0.004	581.9	507.5	18.176	55.44	48.37	4.79	10.7293
18	80	355.5	472.9	0.0125	620.3	543.6	18.176	59.12	51.81	14.96	7.6905
19	80	355	--	0.094	660.0	--	18.176	62.98	--	112.51	--
20	80	265.5	432.4	0.0103	821	615.8	18.176	78.24	58.68	12.33	29.8140
21	80	265.33	--	--	--	--	18.176	--	--	--	Stuck
22	80	356	474.5	0.010	669	570.7	18.176	63.84	54.39	11.97	5.8065
23	40	356	454.5	0.0091	514.3	489.5	14.996	59.24	56.42	8.56	8.7057
24	40	478	478.2	0.0043	376.7	433.1	14.996	43.51	50.02	4.04	1.7177
25	80	471	489.8	0.0042	469.1	516.5	18.176	44.70	49.22	5.06	1.4304
26	80	520	501.8	0.0042	388	473.7	18.176	36.98	45.14	4.99	0.9580
27	40	526	490.8	0.0042	387.8	394.7	14.996	44.79	45.59	3.98	1.0876
28	5	526	490.8	0.0042	--	221	7.083	--	54.04	1.57	1.1639
29	10	527	469.8	0.0044	232.3	259.4	9.507	42.33	47.27	2.32	1.3343
30	60	527	493.5	0.0043	365.4	406	16.818	37.64	41.81	4.72	1.1752
31	180	526	506.5	0.0041	597.7	503	22.304	46.42	39.06	6.18	0.9933
32	40	526	485.7	0.0043	354.1	367.7	14.996	40.89	42.47	4.05	1.5206
33	80	526	496.1	0.0041	383.4	439.8	18.176	36.53	41.92	4.91	1.1185
34	40	525	492.3	0.0043	428.5	399.2	14.996	49.49	46.11	4.05	1.0913
35	80	479	480.5	0.0043	453.4	453.4	18.176	43.22	43.22	5.14	2.0135
36	80	477	504.3	0.0066	475.9	473.7	18.176	45.35	45.14	7.90	1.3661
37	80	478	495.3	0.0063	421.8	442.1	18.176	40.20	42.12	7.54	1.7665
38	40	525	511.9	0.0062	417.3	399.2	14.996	48.20	46.11	5.83	0.7850
40	40	479	495.8	0.0083	421.8	383.4	14.996	48.72	44.29	7.71	1.7747
41	40	478	485.5	0.0077	372.2	354.1	14.996	42.99	40.89	7.24	2.4108
42	80	526	521	0.0073	394.7	412.8	18.176	37.62	39.34	8.74	0.8737
43	80	526	537.8	0.0071	484.9	489.5	18.176	46.21	46.64	8.50	0.5046
44	80	480	536	0.0122	545.8	489.5	18.176	52.01	46.64	14.60	0.9157
45	80	478	525.3	0.0123	462.4	451.1	18.176	44.06	42.99	14.72	1.2892
46	40	526	530.7	0.0116	349.6	354.1	14.996	40.37	40.89	10.90	0.7895
47	40	525	539.8	0.0114	457.9	394.7	14.996	52.90	45.59	10.72	0.5897
48	180	479	528.4	0.0109	611.2	489.4	22.304	47.46	38.00	16.64	1.3215
49	10	527	511.7	0.0109	611.2	259.4	1.507	47.27	47.27	5.73	0.7762
50	60	527	551.6	0.0129	415.5	421.8	16.818	43.18	43.44	14.04	0.5503
51	5	527	511	0.0125	205.3	218.8	7.083	50.21	53.50	4.64	0.6431
52	10	526	510.6	0.0130	230.1	232.3	9.507	41.92	42.35	6.84	0.9605
53	180	528	569.6	0.0130	618	503	22.304	48.00	39.06	--	--
54	180	--	--	--	--	--	--	--	--	--	--
55	80	--	--	--	--	--	--	--	--	--	--
56	60	--	--	--	--	--	--	--	--	--	--
57	40	--	--	--	--	--	--	--	--	--	--
58	10	--	--	--	--	--	--	--	--	--	--
59	5	--	--	--	--	--	--	--	--	--	--
60	40	--	--	--	--	--	--	--	--	--	--
61	40	--	--	--	--	--	--	--	--	--	--
62	40	--	--	--	--	--	--	--	--	--	--
63	40	526	--	0.137	360.9	--	14.996	41.69	--	128.85	--
64	80	479	--	0.141	455.3	--	14.996	50.28	--	132.62	--
65	80	526	--	0.128	473.7	--	18.176	45.14	--	155.20	--
66	40	440	--	0.137	475.9	--	14.996	54.98	--	128.85	--
67	40	442	462.3	0.0043	523.3	435.3	14.996	60.45	50.28	4.05	5.0702
68	40	356	429	0.0043	631.5	462.4	14.996	72.94	53.42	4.05	12.0731
69	40	266	406	0.0045	857	541.3	14.996	98.99	62.51	4.23	31.000
70	40	266.5	442.2	0.014	902.2	627	14.996	104.2	72.42	13.17	21.000
71	40	266	436.2	0.0123	895.4	611.2	14.996	103.42	70.60	11.57	24.000
72	80	266	--	--	--	--	--	--	--	--	Stuck
73	80	265.5	--	--	--	--	--	--	--	--	Stuck
74	40	266	426.7	0.0121	--	575.2	14.996	--	66.44	11.38	34.7083
75	40	266	--	--	--	--	--	--	--	--	Stuck
76	40	356	463.5	0.0089	715	527.8	14.996	82.58	60.97	8.37	6.6677
77	40	356	469.1	0.0131	737.6	514.3	14.996	85.20	59.41	12.32	7.2716
78	40	412	495.6	0.013	500.7	406	14.996	57.83	46.89	12.23	2.8518
79	40	441	464.3	0.0043	550.3	446.3	14.996	63.57	51.58	4.05	2.8519
80	40	442	472.8	0.0061	496.2	417.3	18.176	57.31	48.20	5.74	2.9623
81	80	441	499.9	0.0071	550.3	523.3	18.176	52.45	49.87	8.50	1.7040
82	80	442	523.1	0.0130	577.4	523.3	18.176	55.03	49.87	15.56	3.4608

Table 10 continued...

236

No	Extrusion Ratio	(°C) Initial Temp.	(°C) Final Temp.	(m/sec) Ram Speed	(MN/m) Peak Load	(MN/m) Final Load	P/K	(MN/m²) Peak Flow Stress	(MN/m²) Final Flow Stress	(sec⁻¹) Strain Rate	(sec⁻¹) Z x 10
(HE9)											
83	80	535	539.7	0.0091	381.2	424.0	18.176	36.32	40.41	10.89	0.6102
84	80	446	501.1	0.0089	469.	480.4	18.176	44.70	45.78	10.65	2.0503
85	80	350	459.1	0.0089	575.2	534.5	18.176	54.82	50.94	10.65	9.0973
86	60	350	455.8	0.0091	575.2	514.3	16.818	59.24	52.97	9.90	9.5785
87	60	446	504.4	0.0089	--	481	16.818	--	50.40	9.69	1.6699
88	60	258	422.7	0.0091	805.2	621	16.818	82.93	61.56	9.90	35.6082
89	60	487	514.8	0.0089	421.8	435.3	16.818	43.44	49.99	9.69	1.1867
90	180	487	532.6	0.0089	487.2	523.3	22.304	37.85	40.63	13.59	0.9468
91	180	446	511.7	0.0091	552.6	52412	22.304	42.92	41.15	13.89	1.8816
92	180	350	472.9	0.0091	648.8	611.5	22.304	50.39	46.42	13.89	7.1382
93	10	350	418.1	0.0094	388.0	333.8	9.507	70.69	60.81	4.94	21.5385
94	10	258	384.2	0.0091	595.5	417.3	9.507	108.50	76.02	4.79	95.7130
95	10	446	461.0	0.0091	293.2	279.7	9.507	53.42	50.96	4.79	3.8114
96	10	487	480.2	0.0091	248.1	259.4	9.507	45.21	47.27	4.79	1.8955
97	5	487	487.1	0.0091	259.4	219.5	7.083	63.43	65.09	3.37	1.0465
98	5	446	453.1	0.0093	236.8	231.2	7.083	57.91	56.53	3.45	3.6987
99	5	350	397.4	0.0093	309.0	243.6	7.083	75.57	59.57	3.45	36.9470
100	5	258	368.4	0.0091	558.2	345.1	7.083	136.30	84.39	3.37	140.1234
(HE30)											
1A	80	440	540.3	0.0128	672.1	597.7	18.176	64.05	56.95	15.32	1.4477
2A	80	478	554.7	0.0129	618	559.4	18.176	58.89	53.31	15.44	0.9599
3A	80	526	594.7	0.0131	563.9	516.5	18.176	53.73	49.23	15.68	0.5515
4A	40	479	534.3	0.0132	516.5	462.4	14.996	59.65	53.42	12.41	1.4148
5A	60	479	550.2	0.0133	584.2	530	16.818	60.17	54.58	14.48	1.0097
6A	180	479	565.9	0.0129	726.3	611.2	22.304	56.40	47.46	19.69	0.8605
7A	180	479	529.2	0.0041	834.5	703.7	22.304	64.81	54.65	6.26	0.8392
8A	10	480	468.1	0.0042	387	354.1	9.507	70.51	64.52	1.28	1.4187
9A	10	479	509.2	0.0132	345.1	338.3	9.507	62.87	61.63	6.95	1.7958
10A	40	479	521.4	0.0089	530	473.7	14.996	61.21	51.72	8.37	1.4454
11A	40	480	493.6	0.0042	577.4	503	14.996	66.68	58.09	3.95	1.7042
12A	60	479	490.7	0.0038	581.9	541.3	16.818	59.93	55.76	4.13	1.7756
13A	60	356	492.	0.00131	744.3	609	16.818	76.66	62.76	14.26	6.6451
14A	60	356	463.1	0.0039	654.1	638.3	16.818	67.36	65.75	4.24	5.6736
15A	40	356.5	453.4	0.004	703.7	581.9	14.996	81.29	76.20	4.92	9.5542
16A	40	356	482.7	0.0133	739.8	563.9	14.996	85.44	65.13	12.51	8.1090
17A	80	356.5	--	0.0133	875.1	--	18.176	83.40	--	15.92	30.9790
18A	80	356.5	468.7	0.0039	764.6	669.9	18.176	72.87	63.84	4.67	5.0601
19A	180	356.5	--	--	--	--	22.304	--	--	--	Stuck
20A	180	357	517.5	0.0129	836.8	721.8	22.304	64.99	56.05	19.70	3.8587
21A	10	356	460.5	0.0127	600	457.9	9.507	109.31	83.42	6.68	9.8685
22A	10	--	--	--	--	--	--	--	--	--	--
23A	40	266.5	--	--	--	--	--	--	--	--	stuck
24A	80	266.5	436.7	0.0043	850.3	694.7	18.176	81.03	66.20	5.14	19.4351
25A	80	356.5	471.0	0.0044	872.9	660.9	18.176	83.17	62.98	5.27	5.2435
26A	40	356.5	462.4	0.0059	730.8	568.4	14.996	84.40	65.65	5.55	7.6215
27A	40	441	499.0	0.0068	611.2	514.3	14.996	70.60	59.41	6.40	2.3373
28A	80	440	514.6	0.0069	636.1	593.2	18.176	60.62	56.53	8.26	1.7807
29A	80	480	530.0	0.0068	581.9	570.6	18.176	55.46	54.37	8.14	1.0639
30A	40	479	513.1	0.0063	593.2	503	14.996	68.42	58.09	5.92	2.1990
31A	80	357	498.5	0.012	784.9	645.1	18.176	74.79	61.47	14.37	5.3387
32A	80	266.5	--	--	--	--	--	--	--	--	stuck
33A	40	266.5	--	--	--	--	--	--	--	--	stuck
34A	40	357	473.0	0.0095	755.6	557.1	14.996	87.28	64.55	8.94	8.2563
35A	40	440	502.8	0.010	581.9	473.1	14.996	67.20	54.62	9.41	3.0161
36A	40	480	530.8	0.0096	568.4	494	14.996	65.65	57.05	9.03	1.1688
37A	40	527	536.1	0.0096	475.9	406	14.996	54.98	46.89	9.03	0.9724
38A	80	479	547.1	0.0106	611.2	559.4	18.176	58.25	53.31	12.69	0.9824
39A	80	442	536.1	0.0106	694.7	604.5	18.176	66.20	57.61	12.69	1.3675
(Al-Mg)											
1N	80	258	--	--	--	--	18.176	--	--	--	stuck
2N	80	305	--	--	--	--	18.176	--	--	--	stuck
3N	80	350	--	--	--	--	18.176	--	--	--	stuck
4N	80	395	529.4	0.0086	--	721.8	18.176	--	68.73	10.30	
5N	80	446	559.2	0.0099	800.7	699.2	18.176	76.30	66.65	11.85	
6N	80	487	567.2	0.0096	671	639.4	18.176	63.95	60.93	11.49	
7N	80	535	581.1	0.010	543.6	57.29	18.176	51.81	54.59	12.00	
8N	80	487	566.9	0.0133	658.6	579.7	18.176	62.77	55.24	15.92	
9N	80	446	569.8	0.0131	823.3	687.9	18.176	78.46	66.20	15.68	
10N	80	446	546.5	0.0083	783.8	678.9	18.176	74.69	64.69	9.94	
11N	80	446	516.7	0.0043	817.6	687.9	18.176	77.91	65.56	2.97	
12N	80	446	519.7	0.0043	814.2	701.5	18.176	77.60	66.80	2.97	
13N	80	446	522.8	0.0041	--	727.4	18.176	--	69.32	4.91	
14N	80	446	551.3	0.0086	796.2	692.4	18.176	75.88	65.97	10.30	
15N	80	446	549.5	0.0090	775.9	676.7	18.176	73.94	64.49	10.77	
16N	80	487	561.0	0.0086	654.1	636.1	18.176	62.54	60.62	10.30	
17N	80	487	557.4	0.0080	647.3	636.1	18.176	61.68	60.62	9.57	
18N	80	487	531.6	0.0047	651.8	647.3	18.176	62.11	61.68	5.65	
19N	80	487	529.4	0.0043	665.4	660.9	18.176	63.41	62.98	5.11	
20N	80	487	534.5	0.0041	761.2	697.0	18.176	72.54	66.42	4.91	

Table 10 continued ...   237

No	Extrusion Ratio	(°C) Initial Temp.	(°C) Final Temp.	(m/sec) Ram Speed	(MN/m²) Peak Load	(MN/m²) Final Load	P/K	(MN/m²) Peak Flow Stress	(MN/m²) Final Flow Stress	(sec⁻¹) Strain Rate	(sec⁻¹) x 10
(A1)											
1A1	80	478	492.3	0.0043	439.8	509.7	18.176	41.92	48.57	5.14	
2A1	80	480	495.2	0.0041	469.1	530.0	18.176	44.70	50.51	4.91	
3A1	80	478	489.8	0.0057	475.9	534.5	18.176	45.35	50.94	4.43	
4A1	80	478	526.4	0.0083	180.4	521.0	18.176	45.78	49.64	9.94	
5A1	80	478	536.6	0.0106	475.9	507.5	18.176	45.35	48.36	12.68	
6A1	80	476	548.9	0.0159	536.8	530.0	18.176	51.15	50.51	16.64	
7A1	80	437	519.2	0.0123	534.5	527.8	18.176	50.94	50.30	14.72	
8A1	80	437	518.3	0.0107	536.8	543.6	18.176	51.15	51.81	12.81	
9A1	80	437	515.1	0.009	557.1	557.1	18.176	53.09	53.09	10.77	
10A1	80	437	491.0	0.0043	543.6	500.9	18.176	51.81	56.31	5.14	
11A1	80	437	46612	0.0041	527.8	484.9	18.176	50.28	46.21	4.91	
12A1	80	437	483.7	0.004	530.0	570.6	18.176	50.51	54.37	4.79	
13A1	80	395	471.9	0.0041	609.0	593.2	18.176	58.04	56.53	4.91	
14A1	80	265.5	--	--	--	--	18.176	--	--	--	stuck
15A1	80	305	--	--	--	--	18.176	--	--	--	stuck
16A1	80	305	447.3	0.0054	827.7	639.3	18.176	78.88	60.85	6.46	
17A1	80	356	463.4	0.0041	782.6	638.3	18.176	74.58	60.83	4.91	
18A1	80	356	502.0	0.00154	787.1	649.6	18.176	75.0	61.90	16.04	
19A1	80	395	514.1	0.0157	671.0	597.7	18.176	63.95	56.95	16.40	
20A1	80	395	762.4	0.0044	615.5	541.3	18.176	58.46	51.58	5.27	
21A1	80	533	532.1	0.0043	489.4	577.4	18.176	46.64	55.03	5.14	
22A1	80	536	567.0	0.0124	417.3	471.4	18.176	39.77	44.93	14.84	
23A1	80	582	589.0	0.0126	333.8	442.1	18.176	31.82	42.12	15.08	
24A1	80	582	534.7	0.0044	309.0	480.4	18.176	29.45	45.78	5.27	

No	% Glass	Extrusion Ratio	(°C) Initial Temp.	(°C) Final Temp.	(M/sec) Ram Speed	(MN/m) Final Load	P/K	(MN/m) Final Flow Stress	(sec⁻¹) Strain Rate
(HE9 + Glass)									
1C	1	80	446	482.4	0.005	500.7	18.176	47.72	5.96
2C	3	80	446	472.6	0.0044	480.4	18.176	45.78	5.29
3C	5	80	446	482.4	0.0047	512.0	18.176	48.79	5.63
4C	8	80	445	494.8	0.005	557.1	18.176	53.09	5.98
5C	10	80	447	487.0	0.0047	530.0	18.176	50.51	5.63
6C	12	80	446	488.1	0.0047	536.8	18.176	51.15	5.63
7C	15	80	446	499.8	0.0049	581.9	18.176	55.46	5.81
8C	17	80	446	502.5	0.0044	613.5	18.176	58.46	5.29
9C	15	80	446	494.2	0.0047	563.9	18.176	53.73	5.63
10C	20	80	444	496.7	0.0046	584.2	18.176	55.67	5.46
11C	1	40	446	472.3	0.0049	448.8	14.996	55.24	4.56
12C	3	40	446	476.3	0.0046	478.2	14.996		4.29
13C	5	40	446	482.9	0.005	498.4	14.996	56.33	4.69
14C	8	40	446	482.4	0.0047	498.5	14.996	57.57	4.42
15C	10	40	446	470.8	0.0046	453.4	14.996	52.38	4.29
16C	12	40	445	484.2	0.0051	489.4	14.996	56.53	4.83
17C	17	40	446	479.3	0.0049	478.2	14.996	55.24	4.56
18C	15	40	444	471.7	0.0043	469.1	14.996	51.18	4.02
19C	1	40	447	501.3	0.0131	417.3	14.996	48.20	12.32
20C	3	40	446	499.7	0.0131	410.5	14.996	47.41	12.32
21C	5	40	446	516.5	0.0125	480.4	14.996	55.50	11.80
22C	8	40	445	515.7	0.0124	480.4	14.996	55.50	11.66
23C	10	40	446	498.2	0.0128	406.0	14.996	46.89	12.07
24C	12	40	446	495.1	0.0125	408.3	14.996	47.16	11.80
25C	15	40	446	528.9	0.0121	530.0	14.996	61.21	11.39
26C	17	40	445	502.0	0.0128	421.8	14.996	48.72	12.07
27C	1	40	446	499.8	0.0087	466.9	14.996	52.91	8.18
28C	3	40	446	499.3	0.0088	462.4	14.996	53.42	8.31
29C	5	40	446	502.1	0.0086	478.2	14.996	55.24	8.01
30C	8	40	446	491.2	0.0088	428.6	14.996	49.50	8.31
31C	10	40	445	508.6	0.0087	503.0	14.996	58.09	8.18
32C	12	40	446	501.9	0.0086	475.9	14.996	54.98	8.04
33C	15	40	445	490.8	0.0088	428.6	14.996	49.50	8.31
34C	17	40	446	497.0	0.0088	448.9	14.996	51.86	8.31
35C	5	40	447	462.9	0.0040	444.3	14.996	51.32	3.75
36C	5	40	445	483.9	0.0070	435.3	14.996	50.28	6.57
37C	5	80	446	490.8	0.0070	475.9	18.176	45.35	8.35
38C	5	80	446	475.4	0.0037	530.0	18.176	50.51	4.44
39C	5	80	445	525.3	0.0113	541.3	18.176	51.58	13.47
40C	1	80	446	518.0	0.0131	489.4	18.176	46.64	15.69
41C	10	80	446	527.9	0.0125	530.0	18.176	50.51	15.01
42C	8	80	447	546.1	0.0125	609.0	18.176	58.04	14.68
43C	17	80	446	532.4	0.0123	552.6	18.176	52.65	14.68
44C	15	80	447	532.5	0.0120	557.1	18.176	53.09	14.33
45C	12	80	445	520.7	0.0120	512.0	18.176	48.79	14.33
46C	5	80	446	525.3	0.0120	532.3	18.176	50.75	14.33
47C	1	80	446	522.1	0.0094	557.1	18.176	53.09	11.20
48C	5	80	445	499.5	0.0088	473.7	18.176	45.14	10.58
49C	10	80	447	519.8	0.0095	548.4	18.176	52.24	11.00
50C	8	80	446	502.7	0.0091	509.7	18.176	48.57	10.92

No	% Glass	Extrusion Ratio	(°C) Initial Temp.	(°C) Final Temp.	(M/sec) Ram Speed	(MN/m) Final Load	P/K	(MN/m) Final Flow stress	(sec⁻¹) Strain Rate
(HE9 + Glass)									
51C	17	80	445	521.0	0.0094	548.1	18.176	52.24	11.26
52C	20	80	446	507.8	0.0086	509.7	18.176	48.57	10.24
53C	8.8	80	447	505.2	0.0088	496.2	18.176	47.29	10.58
54C	20	80	447	491.5	0.0040	586.4	18.176	55.88	4.78
55C	20	80	446	536.5	0.0120	570.6	18.176	54.37	14.33
56C	8.8	80	446	534.6	0.0128	554.9	18.176	52.88	15.36
57C	8.8	80	446	507.1	0.0047	622.5	18.176	59.32	5.63
58C	5	80	486	498.3	0.0039	548.1	18.176	52.24	4.61
59C	5	80	488	546.1	0.0128	500.7	18.176	47.72	15.36
60C	5	80	488	508.7	0.0050	527.6	18.176	50.30	5.98
61C	5	80	489	525.2	0.0067	534.6	18.176	50.94	8.02
62C	5	80	490	536.1	0.0084	534.6	18.176	50.94	10.07
63C	5	80	488	529.5	0.0084	507.5	18.176	48.36	10.07
64C	5	80	537	556.2	0.0083	507.5	18.176	48.36	9.90
65C	5	80	537	566.9	0.0128	462.4	18.176	44.06	15.36
66C	5	80	535	523.7	0.0040	557.1	18.176	53.09	4.78
67C	5	80	537	533.9	0.0049	543.6	18.176	51.81	5.81
68C	5	80	537	550.8	0.0076	505.2	18.176	48.15	9.04
69C	5	80	536	567.7	0.0083	557.1	18.176	53.09	9.90
70C	5	80	396	492.9	0.0086	568.4	18.176	54.16	10.24
71C	5	80	396	473.4	0.0043	593.2	18.176	56.53	5.12
72C	5	80	397	502.2	0.0135	545.8	18.176	52.01	16.21
73C	5	80	397	471.7	0.0050	557.1	18.176	53.09	5.98
74C	5	80	398	481.7	0.0066	557.1	18.176	50.51	7.85
75C	5	80	396	492.5	0.0114	530.0	18.176	56.95	13.65
76C	5	80	352	483.4	0.0117	597.7	18.176	56.95	14.00
77C	5	80	352	455.6	0.0044	597.7	18.176	56.95	5.29
78C	5	80	351	485.0	0.0134	590.9	18.176	56.31	16.04
79C	5	80	352	461.9	0.0054	597.7	18.176	56.95	6.49
80C	5	80	353	464.1	0.0076	566.1	18.176	53.95	9.04
81C	5	80	352	473.6	0.0091	584.2	18.176	55.67	10.92
82C	8.8	80	447	522.7	0.0097	550.3	18.176	52.45	11.60
83C	8.8	80	447	495.6	0.0044	581.9	18.176	55.46	5.29
84C	8.8	80	446	532.8	0.0133	543.6	18.176	51.81	15.86
85C	8.8	80	447	494.0	0.0051	543.6	18.176	51.81	6.14
86C	5	80	447	509.2	0.0064	566.1	18.176	53.95	7.67
87C	5	80	447	523.0	0.0112	530.0	18.176	50.51	13.31
88C	5	40	446	496.0	0.0113	412.8	14.996	47.68	10.59
89C	5	40	397	497.4	0.0125	525.5	14.996	60.69	11.80
90C	5	40	397	449.0	0.0043	473.7	14.996	54.72	3.89
91C	5	40	396	462.8	0.0047	514.3	14.996	59.41	4.42
92C	5	40	398	469.8	0.0068	489.4	14.996	56.53	6.43
93C	5	40	397	482.3	0.0097	496.2	14.996	57.31	9.12
94C	5	40	397	486.0	0.0117	489.4	14.996	56.53	10.99
95C	5	40	536	569.5	0.0107	496.2	14.996	57.31	10.06
96C	5	40	535	56.13	0.0125	437.6	14.996	50.54	11.80
97C	5	40	536	502.6	0.0043	424.8	14.996	49.07	4.04
98C	5	40	536	532.0	0.0053	499.2	14.996	57.66	4.98
99C	5	40	537	552.0	0.0071	511.4	14.996	59.06	6.72
100C	5	40	535	541.3	0.0091	415.3	14.996	47.96	8.60
101C	5	40	536	542.0	0.0113	378.7	14.996	43.73	10.62
102C	5	40	536	553.9	0.0127	404.4	14.996	46.71	11.96
103C	5	40	514	553.6	0.0093	512.7	14.996	59.22	8.74
104C	5	40	468	502.4	0.0096	411.2	14.996	47.49	9.00
105C	5	40	421	--	--	432.8	14.996	49.99	--
106C	5	40	468	--	--	428.7	14.996	49.52	--
107C	5	40	372	456.0	0.0094	453.2	14.996	52.34	8.87
108C	5	40	351	--	--	491.1	14.996	56.73	--
109C	5	40	351	421.4	0.0039	450.4	14.996	52.03	3.63
110C	5	40	351	438.7	0.0051	483.8	14.996	51.04	4.80
111C	5	40	350	437.4	0.0074	449.1	14.996	51.87	6.99
112C	5	40	351	--	--	480.3	14.996	55.46	
113C	5	40	352	452.4	0.0139	455.8	14.996	52.56	13.04
114C	5	40	446	505.9	0.0137	428.7	14.996	49.52	12.88
115C	5	5	447	--	0.0125		7.083		
116C	5	10	446	--	0.0129		9.507		
117C	5	80	446	--	0.0125		18.176		
118C	5	180	445	--	0.0123		22.304		
119C	5	60	446	--	0.0126		16.818		
120C	5	80	468	--	0.0093		18.176		
121C	5	80	421	--	0.0097		18.176		
122C	5	80	372	--	0.0090		18.176		
123C	5	80	514	--	0.0091		18.175		
(Al-Mg + Glass)									
1NR	1	80	446	541.2	0.0089	645.1	18.176	61.47	10.58
2NR	3	80	446	553.2	0.0091	687.9	18.176	65.56	10.94
3NR	5	80	445	548.9	0.0086	681.2	18.176	64.92	10.26
4NR	7	80	447	549.2	0.0083	687.9	18.176	65.56	9.92

Table 10 continued ...   239

No	% Glass	Extrusion Ratio	(°C) Initial Temp.	(°C) Final Temp.	(M/sec) Ram Speed	(MN/m²) Final Load	P/K	(MN/m²) Final Flow stress	(sec⁻¹) Strain Rate

(Al-Mg + Glass)

No	% Glass	Extrusion Ratio	Initial Temp	Final Temp	Ram Speed	Final Load	P/K	Final Flow stress	Strain Rate
5NR	9	80	446	554.3	0.0080	715.0	18.176	68.14	9.57
6NR	11	80	4??	549.1	0.0083	685.7	18.176	65.35	9.92
7NR	13	80	447	553.7	0.0080	710.5	18.176	67.71	9.57
8NR	15	80	445	558.0	0.0080	727.4	18.176	69.32	9.57
9NR	5	80	446	570.8	0.0127	701.5	18.176	66.86	15.21
10NR	5	80	446	505.9	0.0040	651.1	18.176	62.34	4.79
11NR	5	80	487	535.3	0.0043	687.9	18.176	65.56	5.13
12NR	5	80	487	563.1	0.0080	658.6	18.176	62.77	9.57
13NR	5	80	488	589.9	0.0130	672.1	18.176	64.05	15.56

(Al + Glass)

No	% Glass	Extrusion Ratio	Initial Temp	Final Temp	Ram Speed	Final Load	P/K	Final Flow stress	Strain Rate
1AlC	5	80	446	524.2	0.0139	507.5	18.176	48.36	16.59
2AlC	5	80	446	520.5	0.0089	559.3	18.176	53.30	10.61
3AlC	5	80	447	517.2	0.0083	557.1	18.176	53.09	8.92
4AlC	5	80	444	500.3	0.0041	624.7	18.176	59.53	4.95
5AlC	5	80	446	492.1	0.0044	568.4	18.176	54.16	3.30
6AlC	5	80	447	493.1	0.0043	579.6	18.176	55.24	5.13
7AlC	5	80	421	482.3	0.0013	581.9	18.176	55.46	5.13
8AlC	5	80	421	522.1	0.0129	570.6	18.176	54.37	15.39
9AlC	5	80	396	517.8	0.0135	611.2	18.176	58.25	15.91
10AlC	1	80	396	467.4	0.0036	597.7	18.176	56.95	4.31
11AlC	3	80	536	580.7	0.0106	557.1	18.176	53.09	12.65
12AlC	5	80	534	585.1	0.0084	624.7	18.176	59.53	10.09
13AlC	7	80	537	575.7	0.00100	548.1	18.176	52.24	11.97
14AlC	9	80	536	584.3	0.0091	602.2	18.176	57.38	10.94
15AlC	11	80	535	578.5	0.0077	618.0	18.176	58.89	9.23
16AlC	15	80	537	569.8	0.0086	557.1	18.176	53.09	10.26
17AlC	5	80	536	571.3	0.0083	570.6	18.176	54.37	9.92
18AlC	5	80	536	556.3	0.0076	530.0	18.176	50.51	9.06
19AlC	5	80	351	523.6	0.0130	746.5	18.176	71.14	15.56
20AlC	5	80	351	476.6	0.0044	694.7	18.176	66.20	5.30
21AlC	5	80	351	500.1	0.0100	683.4	18.176	65.13	11.97
22AlC	5	80	372	517.7	0.0096	710.5	18.176	67.71	11.45
23AlC	5	80	372	536.7	0.0137	739.8	18.176	70.50	16.41
24AlC	5	80	372	487.0	0.0047	687.9	18.176	65.56	5.64
25AlC	5	80	468	519.4	0.0040	672.1	18.176	64.05	4.79
26AlC	5	80	468	570.7	0.0134	638.3	18.176	60.83	16.07
27AlC	5	80	514	588.9	0.0131	599.9	18.176	57.18	15.73
28AlC	5	80	514	531.9	0.0039	647.3	18.176	61.68	4.62
29AlC	5	80	536	581.2	0.0086	604.4	18.176	57.59	10.26
30AlC	5	80	536	606.0	0.0137	604.4	18.176	57.59	16.41
31AlC	5	80	536	588.1	0.0097	604.4	18.176	57.59	11.62
32AlC	5	80	536	554.2	0.0046	654.1	18.176	62.34	5.47

TEMP (°C)	EQUATION	CORRELATION COEFFICIENT	REDUNDANT WORK TERM
250	$p = 179.2 + 111.0 \ln R$	0.992	1.61
350	$p = 122.0 + 96.1 \ln R$	0.990	1.27
450	$p = 92.7 + 89.8 \ln R$	0.986	1.03
500	$p = 61.3 + 91.3 \ln R$	0.993	0.67
540	$p = 71.8 + 82.5 \ln R$	0.988	0.87

TABLE 11

Pressure vs. lnR equations for HE9 extrusions
at different temperatures

300°C		350°C		400°C		450°C		500°C	
Twist Rate (Revs/sec)	Max Torque (NM)	Twist Rate	Max Torque	Twist Rate	Max Torque	Twist Rate	Max Torque	Twist Rate	Max Torque
0.14	10.25	0.16	7.11	0.16	5.81	0.16	4.57	0.16	3.51
0.42	12.02	0.42	7.53	0.45	6.38	0.46	5.15	0.47	4.04
2.99	12.56	2.99	10.16	3.02	8.13	3.17	6.21	3.03	5.38
7.55	13.47	7.66	10.39	6.30	8.63	7.69	7.45	7.77	5.51
				12.50	8.91				
15.09	14.03	14.81	11.12	10.87	8.75	15.38	8.38	15.38	6.81
				15.34	9.07				

TABLE 12

HE9 torsion test results

400°C		450°C		500°C		550°C	
Twist Rate (Revs/sec)	Max Torque (NM)	Twist Rate	Max Torque	Twist Rate	Max Torque	Twist Rate	Max Torque
0.43	8.82	0.16	7.58	0.16	5.48	0.16	3.07
3.03	11.31	0.43	7.58	0.46	5.84		
7.69	12.16	3.18	9.31	3.07	7.84		
14.45	12.63	7.04	10.50	7.81	7.47		
		15.06	10.81	16.00	9.48		

TABLE 13

HE30 torsion test results

Temperature (°C)	m / Shear Strain rate (sec^{-1})	0.5	2.0	10	25	50
				n values		
300	0.006	-0.148	---	-0.139	-0.227	-0.146
350	0.100	-0.124	-0.073	-0.135	-0.210	-0.273
400	0.136	-0.001	-0.170	-0.096	-0.147	-0.300
450	0.165	0.060	0.001	-0.217	-0.265	-0.252
500	0.070	0.183	0.060	-0.255	-0.233	-0.333

TABLE 14   Backofen analysis exponents for HE9

Temperature (°C)	m / Shear Strain rate (sec^{-1})	0.5	2.0	10	25	50
				n values		
400	0.124	-0.088	-0.119	-0.094	-0.048	-0.08
450	0.107	0.159	-0.016	---	-0.115	-0.123
500	0.146	0.103	-0.231	0.038	-0.116	-0.022
550	---	0.211	---	---	---	---

TABLE 15   Backofen analysis exponents for HE30

300°C		350°C		400°C		450°C		500°C	
Shear Flow Stress (MN/m^2)	Shear Strain Rate (sec^{-1})	Shear Flow Stress	Shear Strain Rate	Shear Flow Stress	Shear Strain Rate	Shear Flow Stress	Shear Strain Rate	Shear Flow Stress	Shear Strain Rate
37.3	0.49	26.94	0.49	21.19	0.49	17.49	0.49	13.46	0.49
---	---	26.25	1.32	24.09	1.40	20.76	1.43	14.95	1.46
45.9	9.39	38.35	9.38	31.47	9.78	23.35	9.96	17.38	9.52
47.7	23.71	38.23	24.07	---	---	27.51	24.17	20.12	24.40
51.1	47.42	40.02	46.54	32.75	48.18	31.08	48.18	23.73	48.38

TABLE 16

Flow stress vs. strain rate data from HE9 torsion tests

400°C		450°C		500°C		550°C	
Shear Flow Stress (MN/m^2)	Shear Strain Rate (sec^{-1})	Shear Flow Stress	Shear Strain Rate	Shear Flow Stress	Shear Strain Rate	Shear Flow Stress	Shear Strain Rate
28.79	0.49	26.28	0.49	18.86	0.49	10.39	0.49
30.38	1.36	26.05	1.36	17.89	1.45		
43.13	9.51	39.09	22.12	28.62	9.64		
45.55	24.17	35.87	47.31	27.97	24.54		
47.25	45.40			33.53	50.27		

TABLE 17

Flow stress vs. strain data from HE30 torsion tests

Temperature (°C)	β	n_2	α
300	0.212	14.311	0.015
350	0.210	10.602	0.020
400	0.185	8.126	0.023
450	0.237	8.512	0.028
500	0.276	6.400	0.043

TABLE 18

Hot working theory "constants" for HE9
at different temperatures

Temperature (°C)	β	n_2	α
400	0.082	4.016	0.020
450	0.175	9.693	0.018
500	0.157	6.600	0.024

TABLE 19

Hot working theory "constants" for HE30
at different temperatures

	HE9	HE30
A_1 (sec^{-1})	0.898×10^{11}	0.271×10^{11}
α (M /MN)	0.038	0.040
n	5.16	3.87
ΔH (J/mole)	167224	170881

TABLE 20

Hot working theory constants and activation energies produced by optimization procedure

HE9 (with pads)

Ram Speed (M/sec) \ Temp (°C)	250	350	450	500	540
0.003	C	A	B	A	A
0.008	C	C	C	A	A
0.013	A	A	A	A	A

HE9 + 5 wt.% Glass (with pads)

Ram Speed (M/s) \ Temp (°C)	250	300	350	400	450	500	550
0.003	--	--	C	B	A	A	A
0.008	--	--	C	A	A	A	A
0.013	--	--	C	A	A	A	A

(with pads) HE9 + x% Glass, ram speed = 0.004 m/sec.

Temp (°C) \ wt.% Glass	1	5	8	12	15	17
350	--	B	--	--	--	--
400	--	C	--	--	--	--
450	A	A	C	F	F	G
500	--	A	--	--	--	--
550	--	A	--	--	--	--

(with pads) HE9 + x% Glass, Ram Speed = 0.008 m/sec

Temp (°C) \ wt.% Glass	1	5	8	12	15	17
350	--	B	--	--	--	--
400	--	B	--	--	--	--
450	B	B	F	G	G	H
500	--	A	--	--	--	--
550	--	A	--	--	--	--

(with pads) HE9 + x% Glass, Ram Speed = 0.013 m/sec

Temp (°C) \ wt.% Glass	1	5	8	12	15	17
350	--	B	--	--	--	--
400	--	A	--	--	--	--
450	A	A	F	G	G	H
500	--	A	--	--	--	--
550	--	A	--	--	--	--

HE30 (with pads)

Ram Speed (M/sec) \ Temp (°C)	250	350	450	500	540
0.003	B	B	B	B	B
0.008	--	A	A	A	A
0.013	--	A	B	A	A

A1 (no pads)

Ram Speed \ Temp (°C)	250	300	350	400	450	500	550	600
0.003	--	D	D	D	D	D	D	D
0.008	--	--	--	--	D	D	--	--
0.013	--	D	D	D	D	D	D	A

A1 + 5wt.% Glass (with pads)

Ram Speed m/s \ Temp (°C)	350	375	400	425	450	475	525	550
0.003	--	D	D	D	D	D	D	D
0.008	--	D	--	D	D	--	--	C
0.013	C	C	F	--*	F	C	C	C

A1-Mg (no pads)

Ram Speed \ Temp (°C)	400	450	500	550
0.003	--	A	A	A
0.008	B	A	A	A
0.013	--	B	--	B

A1-Mg (with pads)

Ram Speed \ Temp (°C)	450	500
0.003	D	A
0.008	B	B
0.013	A	B

TABLE 21

Effect of temperature, strain rate and glass content variations on extrude surface finish

TABLE 22   Tensile test results

Extrusion No.	Room Temp. 0.2% P.S. (MN/m²)	Room Temp. U.T.S. (MN/m²)	Room Temp. % Elongation	400°C 0.2% P.S. (MN/m²)	400°C U.T.S. (MN/m²)	400°C % Elongation
(HF9)						
1	--	--	--	16.6	26.4	--
2	73.5	142.0	--	16.0	26.6	--
3	--	--	--	15.2	25.2	--
4	72.8	129.0	--	16.6	25.4	--
5	77.8	128.7	--	18.3	25.2	--
6	--	--	--	12.5	25.1	--
7	88.1	132.9	25.8	--	23.6	--
8	88.8	131.5	25.8	16.4	26.2	36.6
9	86.0	130.3	25.4	17.2	24.5	31.6
10	83.6	129.5	27.8	13.6	25.3	38.7
11	85.9	129.9	27.0	15.1	24.9	38.0
12	90.1	129.6	28.2	13.0	25.7	37.7
13	88.4	131.9	29.2	15.2	25.5	43.5
14	82.1	134.6	26.5	14.8	25.2	39.4
15	88.1	126.8	28.1	13.9	24.2	37.6
16	86.3	124.7	27.9	11.8	23.9	40.9
17	86.1	124.0	27.8	13.2	23.2	40.8
18	104.7	150.4	23.9	16.2	24.8	42.3
19	69.1	130.9	31.5	15.0	24.5	27.9
20	113.4	159.7	22.2	17.8	29.2	33.3
21	--	--	--	--	--	--
22	104.9	153.1	24.0	18.2	25.9	44.9
23	101.0	143.3	27.0	14.5	26.5	42.5
24	77.3	136.8	26.0	15.6	22.9	38.6
25	91.7	137.2	26.9	--	25.1	--
26	95.5	155.4	27.1	18.6	24.6	40.6
27	81.8	143.2	26.1	17.8	24.1	43.1
28	71.7	148.3	--	14.3	--	--
29	69.0	146.9	--	16.1	23.8	--
30	87.5	148.4	--	17.0	24.0	--
31	--	--	--	--	--	--
32	80.3	144.8	21.6	16.0	23.6	43.1
33	99.2	141.1	--	18.7	24.2	--
34	79.2	135.2	26.1	--	--	--
35	81.2	143.8	27.6	15.8	24.4	39.7
36	92.2	150.1	27.3	11.8	24.2	42.3
37	84.5	144.0	29.9	--	--	--
38	61.2	142.4	28.6	18.1	23.7	--
39	85.3	132.5	--	16.9	24.5	--
40	80.6	136.4	22.3	11.4	24.6	41.9
41	77.4	138.8	23.0	16.9	22.9	40
42	79.9	139.5	--	18.2	22.6	--
43	93.3	143.5	--	15.9	23.3	--
44	91.2	147.7	26.4	14.7	24.3	40.8
45	89.7	141.7	28.4	18.7	22.6	--
46	97.4	141.6	--	--	23.9	--
47	72.5	129.4	28.9	15.8	22.6	43.1
48	--	--	--	--	--	--
49	71.7	150.5	--	15.7	23.1	--
50	84.2	142.4	--	17.6	25.4	--
51	65.2	151.1	--	14.5	22.6	--
52	85.5	148.5	--	14.6	21.8	--
62	--	136.0	27.8	--	24.1	--
63	77.0	132.8	21.9	14.4	27.3	39.0
64	92.2	146.4	26.5	14.7	25.7	15.3
65	88.9	132.0	--	17.3	25.0	--
66	77.9	129.8	27.2	--	26.1	--
67	81.4	129.8	27.4	17.1	21.6	41.7

Table 22 continued ... 250

Extrusion No.	Room Temp. 0.2% P.S. (MN/m²)	Room Temp. U.T.S. (MN/m²)	Room Temp. % Elongation	100°C 0.2% P.S. (MN/m²)	100°C U.T.S. (MN/m²)	100°C % Elongation
(HE9)						
68	109.5	147.5	27.5	18.7	26.7	45.4
69	122.6	159.1	22.7	21.5	32.8	32.8
70	104.3	152.4	23.4	18.0	30.1	41.6
71	112.9	152.8	28.0	--	--	--
72	--	--	--	--	--	--
73	--	--	--	--	--	--
74	107.2	149.6	--	16.0	31.4	--
75	--	--	--	--	--	--
76	112.5	152.8	--	--	--	--
77	105.9	155.5	24.2	13.5	28.6	47.1
78	79.6	123.1	30.7	14.6	25.7	46.2
79	83.6	130.2	--	14.2	24.4	--
80	87.3	122.8	--	17.5	24.7	--
81	80.2	132.3	--	18.2	24.2	--
82	87.7	143.9	30.1	13.4	24.8	42.7
(HE30)						
1A	141.5	210.8	37	25.5	47.7	53
2A	124.4	181.4	--	20.0	41.5	--
3A	120.0	189.6	40.7	22.5	35.3	52.9
4A	116.7	181.7	40.2	--	47.9	--
5A	129.9	185.1	39.2	26.9	41.5	54.3
6A	--	--	--	--	--	--
7A	--	--	--	--	--	--
8A	108.3	170.3	--	24.2	39.1	--
9A	104.2	174.8	--	25.4	37.7	--
10A	116.0	175.2	46.0	--	--	--
11A	114.7	172.5	34.6	28.2	39.8	60.8
12A	123.8	177.6	41.4	--	45.6	--
13A	139.8	198.6	32.4	26.1	45.8	46.2
14A	142.0	198.1	33.5	24.2	47.7	58.7
15A	145.3	190.2	--	42.9	48.7	--
16A	140.8	192.2	31.8	27.6	46.9	53.7
17A	142.1	189.8	37.8	26.7	49.2	52.7
18A	158.3	212.6	39.6	26.2	48.4	60.1
19A	--	--	--	--	--	--
20A	--	--	--	--	--	--
21A	--	--	--	--	--	--
22A	--	--	--	--	--	--
23A	--	--	--	--	--	--
24A	149.8	200.5	38.2	20.0	51.0	57.0
25A	157.8	212.6	36.1	28.6	48.0	60.5
26A	141.1	191.8	--	26.1	46.7	--
27A	126.7	181.5	--	24.2	47.9	--
28A	144.5	208.9	36.8	25.5	46.4	56.0
29A	117.0	183.9	40.1	26.7	38.4	53.9
30A	126.7	178.7	40.1	30.6	43.4	55.2
31A	145.1	202.2	--	30.4	48.3	--
32A	--	--	--	--	--	--
33A	--	--	--	--	--	--
34A	144.0	191.2	--	27.8	46.5	--
35A	131.0	190.3	39.6	29.3	49.6	55.6
36A	127.5	179.0	--	31	43.8	--
37A	101.4	173.7	44.0	--	--	--
38A	115.6	185.8	40.7	22.0	41.4	57.6
39A	131.1	183.2	--	20.9	47.7	50.3

Table 22 continued ...

Extrusion No.	Room Temp 0.2% P.S. (MN/m²)	Room Temp U.T.S. (MN/m²)	Room Temp % Elongation	400°C 0.2% P.S. (MN/m²)	400°C U.T.S. (MN/m²)	400°C % Elongation
(Al-Mg)						
4N	176.2	305	22.1	--	--	--
5N	163.4	298.4	21.7	--	--	--
6N	155.1	285.7	21.7	--	--	--
7N	147.0	278.7	21.1	--	--	--
8N	152.0	283.2	22.1	--	--	--
9N	159.2	290.8	21.4	--	--	--
10N	167.5	299.0	21.6	--	--	--
11N	168.6	302.5	21.7	--	--	--
13N	170.5	301.5	20.3	--	--	--
14N	161.9	289.9	18.4	--	--	--
15N	155.4	282.8	19.5	--	--	--
21N	146.8	265.3	17.7	--	--	--
(Al)						
15Al	66.3	85.4	2.6	--	--	--
18Al	57.4	78.6	2.9	--	--	--
19Al	53.3	73.5	3.0	--	--	--
22Al	65.1	120.7	9.5	--	--	--
23Al	77.2	162.6	10.5	--	--	--
(HE9 + GLASS)						
39C	93.3	207.4	18.5	--	--	--
40C	89.9	149.3	27.9	--	--	--
41C	82.0	243.7	14.1	--	--	--
42C	81.0	221.9	15.7	--	--	--
45C	--	--	--	--	--	--
46C	79.0	198.0	22.3	--	--	--
48C	120.0	189.4	19.0	--	--	--
58C	82.2	223.6	21.0	--	--	--
59C	79.6	195.9	25.2	--	--	--
60C	112.9	206.4	22.1	--	--	--
61C	76.7	216.0	23.9	--	--	--
62C	71.2	212.0	23.6	--	--	--
63C	87.4	215.3	22.8	--	--	--
69C	76.5	218.9	28.7	--	--	--
70C	83.6	189.7	21.2	--	--	--
120C	85.3	204.7	22.7	--	--	--
121C	79.2	197.0	23.3	--	--	--
123C	65.9	210.8	26.0	--	--	--
125C	81.8	167.6	16.4	--	--	--
126C	75.9	180.0	13.5	--	--	--
127C	75.9	193.6	13.7	--	--	--
128C	75.4	197.6	19.9	--	--	--
129C	73.8	166.2	23.2	--	--	--
130C	78.3	204.3	27.3	--	--	--
(Al-Mg + GLASS)						
1NR	158.8	297.1	20.3	--	--	--
2NR	147.1	305.2	16.8	--	--	--
3NR	137.4	289.1	9.9	--	--	--
4NR	131.1	215.1	6.3	--	--	--
(Al + GLASS)						
11AlC	58.3	96.7	3.8	--	--	--
12AlC	59.4	94.2	3.1	--	--	--
13AlC	58.5	101.0	4.0	--	--	--
14AlC	62.6	101.4	4.1	--	--	--
15AlC	73.5	139.6	4.4	--	--	--

HE9		HE9 + GLASS		HE30		Al-Mg		Al-Mg + GLASS		Al		Al + GLASS	
Extrude No.	HV	Extrude No.	HV	Extrude No.	HV	Extrude No.	HV	Extrude No.	HV	Extrude No.	HV	Extrude No.	HV
1	36.5	11c	40.0	4A	54.1	7N	77.9	4NR	38.9	2Al	43.1	5Alc	41.3
2	41.3	12c	38.6	5A	54.1	18N	77.9	9NR	63.6	4Al	39.4	9Alc	28.8
3	37.5	13c	32.8	12A	55.4	19N	78.4	10NR	78.0	10Al	39.7	19Alc	27.0
4	37.3	14c	24.0	13A	60.0	20N	75.4	11NR	77.0	17Al	30.3	21Alc	29.9
6	35.2	15c	40.6	14A	58.8			13NR	61.3	20Al	39.3	25Alc	46.6
7	35.4	16c	18.2	25A	60.7							32Alc	49.7
8	36.2	17c	--										
9	38.2	18c	--										
10	40.4	22c	37.3										
11	34.2	31c	26.6										
12	36.8	72c	32.8										
13	39.7	79c	40.0										
14	43.1	87c	23.5										
17	42.5	90c	32.4										
18	41.4	95c	34.8										
65	42.8	113c	34.8										
75	41.3	114c	32.5										
78	42.2	130c	46.6										
103	41.0												
106	41.0												
107	46.0												

TABLE 23

Hardness tests results

HE9	
Extrude No.	Energy Absorbed (J)
10	49.7
11	41.2
12	45.9
13	44.8
14	39.9
15	41.5
16	44.8
17	44.6
18	42.4
19	47.9
20	42.0
22	49.5
25	36.8
26	52.8
33	38.1
35	39.7
36	35.0
37	38.3
42	39.6
43	41.4
45	42.0
64	28.8
65	39.1
81	46.6
82	43.7

TABLE 24

HE9 fracture toughness
results

HE30	
Extrude No.	Energy Absorbed (J)
1A	34.9
2A	42.0
3A	30.3
17A	38.8
18A	44.0
24A	42.8
25A	43.3
28A	38.1
29A	34.0
31A	38.0
38A	39.1
39A	38.8

TABLE 25

HE30 fracture toughness results

Soaking Temperature (°C)	500	520	560	580
0.2% P.S. (MN/m²)	124.9	140	144.8	142.4
U.T.S. (MN/m²)	165.7	177.7	178.6	179.5
% Elongation	19.2	18.8	13.7	16.1

(specimens soaked for 5 hours, water quenched, aged for 6 hours at 180°C)

TABLE 26

Soaking temperature variation results (HE9)

Ageing Temperature (°C)	140	160	180	200	220
0.2% P.S. (MN/m²)	96.3	151.1	144.8	124.5	101.6
U.T.S. (MN/m²)	166.6	195.3	177.5	159.5	139.7
% Elongation	19.3	13.5	13.7	15.7	21.3

(specimens soaked for 4 hours at 560°C, water quenched, aged for 6 hours)

TABLE 27

Ageing temperature variation results (HE9)

Ageing Time (hours)	1	2	4	6	20
0.2% P.S. (MN/m²)	87.7	96.6	111.3	144.8	153.1
U.T.S. (MN/m²)	147.1	146.6	155.5	178.5	185
% Elongation	20.8	19.0	17.9	13.7	10.9

(specimens saoked for 4 hours at 560°C, water quenched, aged at 180°C)

TABLE 28

Ageing time variation results (HE9)

Ageing Temperature (°C)	170	180	190	200	220	240
0.2% P.S. (MN/m²)	231	244.5	233.4	191.1	162	120
U.T.S. (MN/m²)	273.4	276.8	267.2	232	205.3	171.8
% Elongation	21.2	18.2	20.1	17.3	21.7	21.1

(specimens soaked for 5½ hours at 550°C, water quenched, aged for 6 hours)

TABLE 29

Ageing temperature variation results (HE30)

Ageing Time (hours)	1	2	7	16	24
0.2% P.S. (MN/m^2)	169.6	216.1	235.4	235.3	226.4
U.T.S. (MN/m^2)	236.6	257.5	264.2	267.1	258.6
% Elongation	22.2	21.4	18.9	17.1	16.6

(Specimens soaked for 5½ hours at 550°C, water quenched, aged at 180°C)

TABLE 30

Ageing time variation results (HE30)

0.2% P.S. (MN/m^2)	88.0	78.5	76.1	76.3	76.2	72.5
U.T.S. (MN/m^2)	143.9	125.9	126.4	126.6	126.3	124.8
Ageing Time (hours)	0	2	3	3.75	5	6

(Specimens extruded, air (press) quenched, aged at 180°C)

TABLE 31

Results of press quenching HE9 extrudes

Condition	0.2% P.S. (MN/m^2)	U.T.S. (MN/m^2)	% Elongation
TB	70	120	13
TE	110	150	7-8
TF	130-160	150-185	6-8

TABLE 32

Properties of heat treated cast and wrought alloys

Extrude	Soak	Quench	Age	Cool	U.T.S. (MN/m^2)	0.2% P.S. (MN/m^2)
HE9+10% glass	--	--	--	--	241	87
"	--	--	6 hr @ 180°C	air	239	91
"	--	--	6 hr @ 180°C	water	229	93
"	5½ hr @ 500°C	water	6 hr @ 180°C	air	236	88
"	5½ hr @ 500°C	air	6 hr @ 180°C	air	232	91

TABLE 33

Summary of results of heat treatments carried out on HE9 + 10 wt.% glass extrude

Material	Room Temperature Test	400°C Test
HE9	Cup + cone (Ductile) Transparticle	Cup + cone (Ductile Transparticle
HE9 + 5wt.% glass	● ●	● ●
HE30	● ●	● ●
Al	Brittle Interparticle	——
Al + 5wt.% glass	● ●	——
Al-3%Mg	45° shear (Ductile, some necking) Transparticle	Cup + cone (Ductile) Transparticle
Al-3%Mg + 5wt.% glass	● ●	——

TABLE 34

Type of fracture experienced by various extruded
materials

CHAPTER 6

CONCLUSIONS

1. Aluminium, Al-Mg and Al-Mg-Si alloy powders
    produced by water and air atomization techniques
    possess very fine structures which are dendritic
    in nature.

2. Al-Mg-Si powder compacts formed by cold pressing,
    obey Konopicky's relationship giving an equation :-

    $$\ln \left(\frac{1}{1-D}\right) = 0.293 \times 10^{-2} \, P + 1.349$$

    D = relative density
    P = compaction pressure

    The strength of such compacts increases rapidly
    with sintering temperature if the cold pressed
    compacts are sintered. The powder particle
    size also affects compact strength markedly,
    the strength decreasing with increasing powder
    particle size.

3. The load-ram displacement curves obtained
    during powder compact extrusion differ signific-
    antly in form from typical solid billet extrusion
    curves, particularly in the initial, upsetting
    phase.

4. Powder compacts obey a law of the form:-

    $P/\text{constant}' = \text{constant}'' + \ln R$ during extrusion
    at one temperature.
    P = extruson pressure
    R = extrusion ratio
    The equation becomes (For Al-Mg-Si at 540°C):

$$\frac{P}{constant} = 0.87 + \ln R$$

Additions of 5wt.% glass have a negligible effect
on this behaviour. The value of the constant
on the right hand side indicates the amount
of redundant work involved in extrusion. This
value is much higher for powder compact extrusion
than for solid billet extrusion. This redundant
work is probably the energy source involved
in "building" the extrude as the powder traverses
the deformation zone.

5. Powder compact extrusion load-ram displacement curves
    exhibit initial peaks, the magnitude of the peak
    increasing with strain rate and with decreasing
    temperature. This indicates that the phenomenon
    is connected with a dynamic process involving
    dislocation multiplication and annihilation.

6. As the redundant work term and the extrusion
    temperature obey an Arrhenius type of relation
    it is fairly clear that powder consolidation
    during extrusion is a thermally activated process.

7. During extrusion of Aluminium, Al-Mg-Si and
    Al-Mg powder compacts the peak extrusion
    pressure is linearly related to the extrusion
    temperature.

8. A minimized plane strain upper bound solution
    may be used to predict powder compact extrusion
    pressures if a knowledge of the strain and strain
    rate dependence of the flow stress exists.
    Torsion and tensile tests predict a relation of
    the form:-

$$K_{ij} = \frac{40}{\sqrt{3}} \dot{\varepsilon}^{0.1} \varepsilon^{0.21}$$

For HE9 at 400°C.

The predicted loads are, however, very inaccurate
and the method is unacceptable. Attempts to
modify the solution for axi-symmetric extrusion
produce answers which are commonly 50% less
than the experimentally measured values.

9. The use of a minimized axi-symmetric upper bound
    solution enables much more accurate predictions
    of powder compact loads to be made. Typically,
    for HE9 and HE30 the predicted values are never
    greater than 10% in error over the extrusion
    ratio range 5:1 to 180:1.

10. This latter theory also predicts that the
    strain required for complete consolidation
    ($\sim$2.3) is not reached until a late stage in
    the deformation zone.eg. 70 % of the deformation
    zone experiences a strain of less than 2.3 even
    at an extrusion ratio of 80:1. This agrees
    with the long held belief that, during powder
    compact extrusion, complete consolidation and
    therefore final extrude properties are not
    attained until the compact has almost traversed
    the deformation zone.

11. Extrusion strain rates predicted by this theory
    agree reasonably well with those predicted by
    Feltham's equation at high extrusion ratios.

12. Graphs of maximum torque V. ln. twist rate
    produced from torsion data for both HE9 and HE30
    are linear. Both materials also obey equations
    of the form:-

    $$\text{Flow stress} = \text{const. } \varepsilon^{n}$$

    The strain rate exponent, n , increases with
    temperature.

13. The torsion test data yields activation energies
    of 167,224 J/mole for HE9 and 170,881 J/mole for
    HE30. These values are somewhat higher than the
    value of 156,000 J/mole usually quoted for
    aluminium. This descrepancy is probably due
    to the oxide content of the powder extrudes.

14. The Zener-Holloman constants α and n have values
    of 0.038 and 5.16 respectively for HE9 and 0.04
    and 3.87 for HE30. These values agree quite well
    with those obtained by other workers for solid
    aluminium extrusion.

15. Generally, the surface finish of the extrudes is
    very dependent upon the extrusion temperature
    and strain rate. For HE9, HE30 and aluminium
    powder compact extrudes, the surface finish
    improves with increasing ram speed and temperature.
    However, the surface finish of Al-Mg extrudes
    improves with decreasing ram speed. Additions
    of up to 5 wt.% glass have little effect on the
    surface finish. Additions of glass to aluminium
    and Al-Mg extrudes have a deleterious effect on
    the strength and elongation properties.

16. Generally the strength and elongation properties
    of as-extruded HE9, HE30 and Al-Mg powders are
    very much superior to those of their "solid"
    counterparts (Often by as much as 50%). The
    strength of the extruded aluminium powder is
    also much greater than that of commercially
    extruded solid aluminium although the elongation
    value is considerably less due to the high oxide
    content.

17. The Al-Mg powder extrudes exhibit serrated yielding
    during room temperature tensile tests.

18. Additions of glass to aluminium and Al-Mg powder extrudes have a deleterious effect on the strength and elongation properties.

19. Additions of glass to HE9 powder extrudes improve the as-extruded U.T.S., value by 40% (for 8 wt.% glass). Generally, the proof stress and elongation values are not greatly affected.

20. The elastic modulus of HE9 is reduced by approximately 10-12% by the addition of 5 wt.% glass.

21. The toughness of reinforced HE9 decreases rapidly with increasing glass content.

22. The mechanical properties of the powder extrudes are very dependent upon the extrusion temperature. Generally the strength of the unreinforced extrudes decreases with increasing temperature (except for aluminium powder) and the elongation improves. Reinforced HE9 exhibits an increase in strength and elongation with increasing temperature.

23. The decrease in strength, with increasing test temperature, shown by HE9 powder extrude is in agreement with the predictions made by Seeger's analysis.

24. Tensile tests performed at different temperatures show that the strain rate sensitivity of HE9 and HE30 powder extrudes increases with temperature. (At room temperature both sensitivities are slightly negative).

25. The tensile strength of powder extrudes decreases rapidly with increasing initial powder particle size.

26. The strength of HE9 and Al—Mg powder extrudes increases with glass content to a maximum and then falls off rapidly. The deterioration is caused by matrix cracking due to elastic expansion of the glass. The optimum content for HE9 is 8 wt.% for Al—Mg, approximately 2 wt.%.

27. The strength and elongation properties of reinforced HE9 decrease rapidly with increasing glass particle size.

28. Generally the hardness of reinforced powder extrudes decreases with increasing glass content.

29. Both HE9 and HE30 powder extrudes respond well to a TF type, three stage heat treatment. Reinforced HE9 extrudes are not responsive to such treatment. Press quenching is also completely ineffective.

30. HE9, HE30, Al and Al—Mg powder extrudes reveal fibrous, cold worked microstructures under the optical microscope. The structure is elongated in the extrusion direction and "equi-axed" in the transverse direction.

31. Optical microscopy reveals the imperfection of the fibres. A variation in fibre morphology across the extrude section manifests the variation in strain encountered.

32. Electron microscopy of HE9, HE30 and Al—Mg powder extrudes reveals a total lack of recrystallisation under any of the extrusion conditions investigated. This is due to the presence of the oxide particles. In all of the extrudes subgrains elongated in the extrusion direction and produced by dynamic recovery,

are present. Increasing the extrusion temperature produces subgrains which are more "equi-axed" in nature. The subgrain size also increases markedly with extrusion temperature.

33. Unreinforced HE9 and HE30 extrudes exhibit cup and cone ductile fracture during tensile tests. Unreinforced aluminium extrudes exhibit brittle interparticle fracture. Additions of up to 5. wt.% glass cause embrittlement.

34. During extrusion the reinforcing glass chemically reacts with the metal matrix. A spinel, $Mg\,Al_2O_4$, is produced at the interface (in the case of He9 and HE30). This reaction of the matrix magnesium in the formation of this spinel is one of the main reasons for the lack of response shown by reinforced extrudes to heat treatments.

```
00100   PROGRAM UPPERE(INPUT,OUTPUT)
00200 1 PRINT 4
00300 4 FORMAT(*READ IN RADIUS D,ER,OM,PHI*)
00400   READ*,D,ER,OM,PHI
00500   A=D-(D/ER)
00600   B=D-A
00700   N=1
00800C CONVERT OMEGA AND PHI TO RADIANS
00900C
01000   R1OM=OM/57.29578
01100   R1PHI=PHI/57.29578
01200C
01300C   TO CALCULATE THE DEPTH OF WORKING
01400 100 A1=(A**2)/((1.+(A/B))*(SIN(R1OM)**2))
01500   B1=(A*B)/((1.+(A/B))*(SIN(R1PHI)**2))
01600   X=SQRT(A1+B1)
01700   N=1
01800C
01900C TO CALCULATE AND WRITE OUT NEW ANGLES
02000   EOM=(4.*A)/(3.*X)
02100   EPHI=(4.*B)/(3.*X)
02200   R2OM=ATAN(EOM)
02300   R2PHI=ATAN(EPHI)
02400   DIF1=SQRT((57.29578*(R1OM-R2OM))**2)
02500   DIF2=SQRT((57.29578*(R1PHI-R2PHI))**2)
02600   N=N+1
02700   IF (DIF1.LT.0.01.AND.DIF2.LT.(.01)GO TO 9
02800   IF (N.EQ.50)GO TO 101
02900   R1OM=R2OM
03000   R1PHI=R2PHI
03100   GO TO 100
03200C CALCULATE LOAD USING VALUES OF X,OM,PHI
03300 9 C1=(2.*(A**2))/(X*(SIN(R2OM))**2)
03400   C2=(2.*A*B)/(X*(SIN(R2PHI))**2)
03500   C3=(3.*A)/TAN(R2OM)
03600   C4=(3.*A)/TAN(R2PHI)
03700   PRINT 15,C1,C2,C3,C4
03800 15 FORMAT(3HC1=,F10.4,2X,3HC2=,F10.4,2X,3HC3=,F10.4,2X,3HC=,F10.4)
03900   ALOAD=(2.*X)+(2.*X*A)/B+C1+C2-C3-C4
04000   PRESS=ALOAD/D
04100   OM=R2OM*57.29578
04200   PHI=R2PHI*57.29578
04300   PRINT 10,A,B,D,ER,X,OM,PHI,ALOAD,PRESS
04400 10 FORMAT(2HA=,F10.4,2X,2HB=,F10.4,2X,2HD=,F10.4//
04500+16HEXTRUSION RATIO=,F10.4/2HX=,F10.4,2X,3HOM=,F10.4,
04600+2X,4HPHI=,F10.4//10HALOAD/2K=,F10.4//13HPRESSURE/K=  ,F10.4)
04700C
04800C
04900   PRINT*,'ANY MORE INPUT'
05000   READ 106,NSWER
05100   IF(NSWER.EQ.1HY)GO TO 1
05200 106 FORMAT(A1)
05300   STOP 1
05400 101 PRINT 102
05500 102 FORMAT(*N=50*)
05600 105 STOP
05700   END
```

APPENDIX 2

```
00100 PROGRAM UPBOUND(INPUT,OUTPUT,TAPE 5=INPUT,TAPE 6=OUTPUT)
00200 COMMON/1/ ER,ALP,BET,PI,EM,SUM,RB,RE,V1,V3
00300 COMMON/2/ X(2),ED12,ED23,ED24,ED2,AA,EE,EPSEF,THET
00400C************************VERSION 1********************
00500C RB=FILLET RADIUS
00600C RE= EXTRUDE RADIUS
00700CER=EXTRUSION RATIO
00800C ALP=ANGLE ALPHA=ANGLE BETWEEN BILLET WALL AND DEAD METAL ZONE
00900C BET=ANGLE BETA =ANGLE BETWEEN V23 AND VERTICAL
01000C EM=ANGLE M=ANGLE BETWEEN V12 AND VERTICAL
01100C V1=RAM VELOCITY
01200C V3=EXTRUDE VELOCITY
01300C ED23= ENERGY DISIPATED ALONG E23/K
01400C ED24=ENERGY DISIPATED ALONG E24/K
01500C ED2= ENERGY DISIPATED WITHIN TRIANGLE 2/SQRT3 K
01600C THIS PROGRAM CALCULATES VALUES OF P/K USING A SINGLETRIANGLE UPPER
01700C BOUND SOLUTION, INVOLVING INTEGRATION BY SIMPSONS RULE
01800CIT CALLS UPON THE LIBRARY ROUTINE EO4CBF TO MINIMISE THE VALUE OF
01900CP/K BY VARYING THE ANGLES ALPHA AND BETA. IT ASSUMES THAT THE SHEAR
02000CSTRESS,K, TAKES A CONSTANT VALUE THROUGHOUT THE DEFORMATION ZONE
02100 PRINT 199
02200 199 FORMAT(*XXXXXXXXXXXXXX XXXXXXXXXXXXXXXXXXXXXXXXX*,/
02300+26X,*X ALPHA   Y*,/
02400+27X,*X          X*,/
02500+28X,*X         X*,/
02600+29X,*X       Y*,/
02700+30X,*X     X*,/
02800+10X,*BILLET*,15X,*X   X*,/
02900+32X,*X   X*,/
03000+33X,*X X*,/
03100+34X,*XX*,/
03200+35X,*XXXYXXXXXXXYXXXX*,/
03300+34X,*X.*,/
03400+33X,*X-.--BETA*,/
03500+32X,*X   .*,/
03600+31X,*X   .  EXTRUDE*,/
03700+30X,*X    .*,/
03800+29X,*X     .*,/
03900+*-------------------------------------------------*,/////
04000+9X,*POSITIONS OF ANGLES ALPHA AND BETA*)
04100C
04200C
04300 CALL TYPIN
04400 CALL UNITS
04500 X(1)=ALP
04600 Y(2)=BET
04700 PI=3.14159
04800 V3=V1*RB*RB/(RE*RE)
04900C
05000 CALL MINIMIZ
05100 STOP
05200 END
05300C
05400 SUBROUTINE TYPIN
05500 COMMON/1/ ER,ALP,BET,PI,EM,SUM,RB,RE,V1,V3
05600 303 PRINT 301
05700 301 FORMAT(*PROGRAM REQUIRES EXTRUSION RATIO OR EXTRUDE RADIUS. *,/
05800+*IF ENTERING EXTRUSION RATIO TYPE 'A', IF ENTERING EXTRUDE RADIUS*,/
05900+*TYPE 'B'.*)
06000 READ 302,NSWER
06100 302 FORMAT(A1)
06200 IF(NSWER.EQ.1HA)GO TO 304
06300 IF(NSWER.EQ.1HB)GO TO 306
06400 PRINT*,' IDIOT, CANT YOU READ? '
06500 GO TO 303
06600 304 PRINT 305
06700 305 FORMAT(*ENTER BILLET RADIUS IN MMS, EXTRUSION RATIO, AN ESTIMATE*
06800+/*OF ANGLES ALPHA AND BETA IN DEGREES AND RAM VELOCITY IN MM/S-C *)
06900 READ(5,*)RB,ER,ALP,BET,V1
07000 RE=RB/SQRT(ER)
07100 GO TO 308
07200 306 PRINT 307
07300 307 FORMAT(* ENTER BILLET RADIUS,EXTRUDE RADIUS IN MMS, AN ESTIMATE
07400+OF ANGLES ALPHA AND BETA IN DEGREES AND RAM VELOCITY IN MM/SEC.*)
07500 READ(5,*)RB,RE,ALP,BET,V1
07600 ER=RB*RB/(RE*RE)
07700 308 RETURN
07800 END
07900C
08000C
08100 SUBROUTINE UPB(N,X,ALOAD)
08200 COMMON/1/ ER,ALP,BET,PI,EM,SUM,RB,RE,V1,V3
08300C THE FOLLOWING RELATES ALPHA AND BETA TO M
08400C
08500 DIMENSION X(2)
08600 ALP = X(1)
```

```
08700    BET = X(2)
08800    CALL GEOM(ALP,PI)
08900    CALL GEOM(BET,PI)
09000    TEM=((RB-RE)/TAN(ALP)-RE*TAN(BET))/RB
09100    EM=ATAN(TEM)
09200 C
09300 CPRINT 10,ALP,BET
09400 C10 FORMAT(*UPB,,ALP,BET= *,2E12.5)
09500    CALL SUMEM
09600 C
09700    ALOAD=SUM/(PI*RB*RB*V1)
09800 C
09900 C  ALOAD=P/K
10000 C
10100 C
10200    RETURN
10300    END
10400 C
10500    SUBROUTINE GEOM(ANGLE,PI)
10600 CTHIS ROUTINE LIMITS THE VALUES OF ALPHA AND BETA TO LESS THAN 90
10700 CAND GREATER THAN 0 DEGREES.
10800    IF(ANGLE)30,20,10
10900    10 IF(ANGLE.LT.PI/2.)RETURN
11000    ANGLE=ANGLE-PI/2
11100    GO TO 10
11200    20 PRINT*,'THERE IS AN ERROR   ALPHA OR BETA = 0 DEGREES.'
11300    30 IF(ANGLE.GT.0.0)RETURN
11400    ANGLE=ANGLE+PI/2.
11500    GO TO 30
11600    END
11700    SUBROUTINE UNITS
11800    COMMON/1/ ER,ALP,BET,PI,EM,SUM,RB,RE,V1,V3
11900    COMMON/2/ X(2),ED12,ED23,ED24,ED2,AA,BB,EPSBR,THET
12000 C
12100 C THIS ROUTINE PITS RB AND RE IN METRES, ANGLES IN RADIANS AND V1
12200 C IN METRES PER SECOND
12300 C
12400    RB=RB/1000.
12500    RE=RE/1000.
12600    ALP=ALP/57.2958
12700    BET=BET/57.2958
12800    V1=V1/1000.
12900    RETURN
13000    END
13100 C
13200    SUBROUTINE  SUMEM
13300    COMMON/1/ ER,ALP,BET,PI,EM,SUM,RB,RE,V1,V3
13400    COMMON/2/ X(2),ED12,ED23,ED24,ED2,AA,BB,EPSBR,THET
13500 C
13600 C THIS ROUTINE CALLS TWO OTHER ROUTINES THAT PRODUCE THE VALUES OF
13700 C ENERGY DISSIPATION AT VELOCITY DISCONTINUITIES AND WITHIN THE SINGLE
13800 C TRIANGLE, AND SUMS THEM.
13900 C
14000    CALL E1E2E3
14100 C
14200    CALL F2CALC
14300 C
14400    SUM =ED12+ED23+ED24+ED2
14500    RETURN
14600    END
14700 C
14800 C
14900    SUBROUTINE E1E2E3
15000    COMMON/1/ ER,ALP,BET,PI,EM,SUM,RB,RE,V1,V3
15100    COMMON/2/ X(2),ED12,ED23,ED24,ED2,AA,BB,EPSBR,THET
15200 C
15300 C THIS ROUTINE PRODUCES THE THREE VALUES OF ENERGY
15400 C DISIPATION AT VELOCITY DISCONTINUITIES V12,V24,V23
15500 C
15600    RB2=RB*RB
15700    A=V1*SIN(ALP)/COS(ALP+EM)
15800    B=PI*RB2/COS(EM)
15900    ED12=A*B
16000 C
16100    RE2=RE*RE
16200    C=V3*SIN(ALP)/COS(ALP-BET)
16300    D=PI*RE2/COS(BET)
16400    ED23=C*D
16500 C
16600    E=2.*PI*RB2*V1/COS(ALP)
16700    F=TAN(PI/4.+BET/2.-ALP/2.)
16800    G=TAN(PI/4.-EM/2.-ALP/2.)
16900 CPRINT 101,E,F,G
17000 C101 FORMAT(*E,F,G= *,3E12.5)
17100    ED24=E*ALOG(F/G)
17200    RETURN
```

```
17300 END
17400 SUBROUTINE F2CALC
17500C
17600 COMMON/1/ FF,ALP,BET,PI,EM,SUM,PE,RE,V1,V3
17700 COMMON/2/ Y(2),FD12,FD23,FD24,FD2,AA,BE,FPSBF,THET
17800C THIS ROUTINE CALCULATES THE ENERGY DISIPATION WITHIN TRIANGLE 2
17900C AND CALLS UPON A SIMPSONS RULE ROUTINE
18000C
18100 DIMENSION F(200)
18200C
18300 NSTEP =100
18400 THETMIN=PI/2.0-EM
18500 THETMAX=PI/2.0+BET
18600 THETSTP=(THETMAX-THETMIN)/100.
18700 THET=(THETMIN-THETSTP)
18800C
18900 DO 200 I=1,NSTEP+1
19000 THET=THET+THETSTP
19100C
19200 CALL FOTHET
19300C
19400 F(I)=(PSBP*SIN(THET)/(BB*BB)
19500 200 F(I)=F(I)*BB*BB/AA
19600C
19700 CALL SIMPV(F,NSTEP,THETSTP,SINT)
19800C
19900 FD2=PI*SQRT(2.)*SINT
20000 RETURN
20100 END
20200C
20300C
20400 SUBROUTINE FOTHET
20500 COMMON/1/ FF,ALP,BET,PI,EM,SUM,FR,RE,V1,V3
20600 COMMON/2/ X(2),FD12,FD23,FD24,FD2,AA,BE,FPSBP,THET
20700C
20800C THIS ROUTINE CALCULATES STRAIN RATES IN POLAR COORDINATES
20900C
21000 AA=COS(EM)*COS(EM)/(COS(EM+ALP)*COS(EM+ALP))
21100 BB=SIN(THET-ALP)
21200 CC=COS(THET-ALP)
21300 DD=V1*AA*BB/SIN(THET)
21400 DF=1.+(COS(THET)*COS(THET)/(SIN(THET)*SIN(THET)))
21500 EE=BE*V1*AA*SIN(ALP)*DF
21600 FF=DD*2.*CC
21700C
21800 EPSL1=FF+EE
21900C
22000 GG=BB/TAN(THET)
22100C
22200 EPSL2=DD*(CC+GG)
22300C
22400 HH=-DD*BB*2.
22500 PP=V1*AA*SIN(ALP)
22600 QQ=CC*PP*DF
22700C
22800 EPSL3=HH+QQ
22900C
23000 EPSL1S=EPSL1*EPSL1
23100 EPSL2S=EPSL2*EPSL2
23200 EPSL3S=EPSL3*EPSL3
23300C
23400 EPSBRI=SQRT((EPSL1S+EPSL2S+EPSL3S/2.)*2./3.)
23500C
23600 EPSBP=EPSBRI/SQRT(2./3.)
23700 RETURN
23800 END
23900C
24000 SUBROUTINE SIMPV(F,NSTEP,H,SINT)
24100C
24200C THIS ROUTINE PERFORMS AN INTEGRATION BY SIMPSONS RULE
24300C THE FIRST PART CHECKS THAT NSTEP IS AN EVEN NUMBER
24400C
24500 DIMENSION F(200),X(2)
24600 IF (MOD(NSTEP,2).EQ.0) GO TO 1
24700 WRITE (6,61)NSTEP
24800 61 FORMAT (*EXECUTION TERMINATED IN SIMPV BY ODD NSTEP = *,I6)
24900 STOP
25000 1 SINT=0
25100 DO 2 J=2,NSTEP,2
25200 2 SINT =SINT+F(J-1)+4.*F(J)+F(J+1)
25300 SINT=SINT*H/3.
25400 RETURN
25500 END
25600 SUBROUTINE MINIMIZ
25700 COMMON/1/ FF,ALP,BET,PI,EM,SUM,PE,RE,V1,V3
25800 COMMON/2/ X(2),FD12,FD23,FD24,FD2,AA,BE,FPSBP,THET
```

```
25900    EXTERNAL UPB,WRITOUT
26000    DIMENSION EPS(2),GRAD(2),DFIRST(2),W(17)
26100    N=2
26200    IW=7*N+N*(N+1)/2
26300    ITERAT=200
26400    DO 1 I=1,N
26500    EPS(I)=1.0E-4
26600  1 DFIRST(I)=0.001
26700    ACC=1.0E-10
26800    ESTIM=7.0
26900    EF=1.0E-9
27000    IERR=0
27100 C
27200    CALL E04CBF(N,X,ALOAD,GRAD,EPS,ESTIM,ACC,W,IW,DFIRST,EF,UPB,WRITOUT
27300   +,ITERAT,IERR)
27400    IF (IERR.NE.0) GO TO 10
27500    ALP=ALP*57.2958
27600    BET=BET*57.2958
27700    RB=RB*1000.
27800    PRINT*,'XXXXXXXXXXXXXXXXXXXXXXXXXXXXXXXXXXXXXXXXXXXXXXXXXXXXXXXXXXXX'
27900    PRINT 16,ER,RB
28000 16 FORMAT(//////,7X,*EXTRUSION RATIO = *,F8 4,3X,*BILLET RADIUS = *,F8.4)
28100    WRITE (6,150)ALP,BET,ALOAD
28200 150 FORMAT(* MINIMUM IS AT:    ALPHA = *,F10 6,* DEGREES */
28300   +17X,* BETA = *,F10.6,* DEGREES */18X,* P/K = *,F10.6,* METRES SQUARED*)
28400    PRINT*,'              THIS IS A SINGLE TRIANGLE SOLUTION.'
28500    PRINT 17
28600 17 FORMAT(//////,10X,*XXXXXXXXXXXXXXXXXXXXXXXXXXXXXXXXXXXXXXXX*,15X)
28700    STOP
28800 10 WRITE(6,120)IERR,X,ALOAD
28900 120 FORMAT(* FAIL*,I2/* AT */2F12.8/* P/K = *,E16.8)
29000    STOP
29100    END
29200 C
29300    SUBROUTINE WRITOUT (N,X,ALOAD,GRAD,ITERAT)
29400    COMMON/1/ ALP,BET,PI,EM,SUM,RB,RE,V1,V3
29500    DIMENSION X(2),GRAD(2)
29600    WRITE(6,1)ITERAT
29700  1 FORMAT(* ITERATION = *,I4)
29800    RETURN
29900    END
```

```
00100 PROGRAM QUICK(INPUT,OUTPUT,TAPE5=INPUT,TAPE6=OUTPUT,TAPE7)
00200C
00300C
00400C      VERSION 1************H.MCSHANE AND M.TUTCHER.***************5-4-77.
00500C
00600C
00700C  THIS PROGRAM GIVES A MINIMISED UPPER BOUND SOLUTION FOR AXISYMMETRIC
00800C  EXTRUSION USING A SINGLE TRIANGLE DEFORMATION FIELD. THIS SINGLE TRIANGLE
00900C  IS DIVIDED INTO A GRID OF 50 ELEMENTS DEFINED BY TEN UNITS DOWN THE
01000C  D.M.Z. INTERFACE AND FIVE UNITS DOWN THE RADIUS. THE TEN UNITS ARE
01100C  FORMULATED SUCH THAT THE INTERNAL ANGLE OF THE TRIANGLE IS SPLIT INTO
01200C  TEN EQUAL ANGLES AND THE FIVE ARE FORMULATED SUCH THAT THE RADIUS IS
01300C  SPLIT INTO FIVE EQUAL LENGTHS.
01400C  THE GEOMETRY IS DEFINED SUCH THAT: ALFHA = D.M.Z. ANGLE; PHI= ANGLE
01500C  BETWEEN VERTICAL AND THE FINAL VELOCITY DISCONTINUITY; RB = BILLET
01600C  RADIUS; RE = EXTRUDE RADIUS; V1 = RAM APPROACH VELOCITY.
01700C
01800C
01900      COMMON/1/ R1,Y,Z,DELTAR,ALAMDAT,ALAMDAC,RR,RRC
02000      COMMON/2/ RE,RC,V1,V3,PI
02100      COMMON/3/ SNALPHA,SNBETA,SNGAM,CSGPA,CSALPHA,CSBETA,SNDTB2,CSDTB2,
02200     +Q,QQ,CONSTAN,SNEND,CSAMP,SNF,CSP,SNTHETA,CSTHETA,CSGAM
02300      COMMON/ANGLE/ ALPHA,GAMMA,PHI,THETA,ETHETA,BETA
02400      COMMON/ENER/ E2,E24,E23,E12,E12T,E23T,E24T,E2T
02500 LOGICAL LINE,LOGW
02600 DIMENSION IXTYP(2),IGTYP(5),LINE(5),LOGW(15),W(65),X(2)
02700      COMMON/HAF/ MET,IPRIN,IT
02800      COMMON/STN/ TEMP,STRAIN2(5),STRN(10,5),ST(10),STRAIN(5)
02900 EXTERNAL GRID,DGRID,DDGRID,MON,MONE
03000 DATA N,INF,IST,MAX1,IFAIL/2,0,1,500,0/
03100 DATA PMX,AAX/1.0E-3,1.0E-3/
03200 RB=0.0375
03300C
03400C PRINT*,' DO YOU REQUIRE HELP WITH THIS PROGRAM OR A FULLER DESCRIPTION
03500+ ANSWER Y FOR YES OR 0 FOR NO.'
03600 READ(5,302) NANSWER
03700 302 FORMAT(A1)
03800 IF(NANSWER.EQ.1H0) GO TO 5555
03900 IF(NANSWER.EQ.1HY) GO TO 5556
04000 5556 PRINT*,'***************************INFORMATION******************
04100+        THIS PROGRAM GIVES A MINIMISED UPPER BOUND SOLUTION FOR AXI-
04200+SYMMETRIC EXTRUSION USING A SINGLE TRIANGLE DEFORMATION ZONE. GREATER
04300+DETAILS CAN BE FOUND IN ADIES PH.D THESIS ON THE SAME SUBJECT. THE
04400+GEOMETRY IS SET UP SUCH THAT: RB IS THE BILLET RADIUS; RE IS THE EXTRUDE
04500+RADIUS; V1 IS THE RAM VELOCITY AND V3 IS THE EXTRUDE VELOCITY:. A
04600+FULLER DESCRIPTION IS GIVEN IN THE DIAGRAM FOLLOWING. THE PROGRAM USES
04700+AN ELEMENTAL TECHNIQUE. THE MESH IS CONSTRUCTED SUCH THAT THE TRIANGLE
04800+ ABC IS DIVIDED IN TO 50 SECTORS:- TEN UNITS DOWN AB AND FIVE DOWN BC.
04900+THIS MEANS THAT ANGLE ACB IS DIVIDED INTO TEN EQUAL ANGLES WHILE AC IS
05000+DIVIDED INTO FIVE EQUAL LENGTHS. THE ANGLE GAMMA IS DEFINED AS THE
05100+ANGLE BETWEEN AC AND THE PERPENDICULAR NO MATTER WHICH SIDE OF IT,
05200+IT APPEARS. THE DEFORMATION REGION IS SPLIT INTO FOUR REGIONS AS SHOWN
05300+IN THE DIAGRAM.
05400+ SHOULD ANY OTHER HELP BE REQUIRED PLEASE CONTACT THE AUTHORS -
05500+H. MCSHANE OR M.TUTCHER IN ROOM LG.05.'
05600 WRITE(6,8888)
05700 8888 FORMAT(16X,*A*,/3X*--------------------*/13X,*I    *ALPHAI*/
05800+13X,*I    *   A I*/13X,*I    *    I*/13X,*I    *  I*
05900+/*   BILLET   RB   2 * I*/13X*I      *IB----*/13X*I I    *
06000+*/.   I*/13X,*I    /-I-PHI I*/13X,*I    / RI   RE*/
06100+13X,*I   /   I   I*/13X,*I   /C  I   I*/3X*. . . . . . . .*
06200+*. . . . .*)
06300 5555 PRINT*,' ENTER THE VALUE OF THE RAM SPEED IN MMS/SECOND.'
06400 READ(5,*) V1
06500C
06600 V1=V1/1000.
06700 PI=3.14159
06800C
06900 PRINT*,'ENTER THE VALUES OF EXTRUSION RATIO AND GUESS OF ALPHA AND PHI'
07000 READ(5,*) ER,X(1),X(2)
07100 PRINT*,'ENTER THE ESTIMATE OF THE VALUE OF PRESSURE IN MN/M SQUARED.'
07200 PRINT*,'SHOULD THE ESTIMATE OF PRESSURE BE GREATER THAN A VALUE FOUND IN T
07300+HE   MINIMISATION PROCESS, THE ROUTINE WILL FAIL WITH ERROR LEVEL 5 AS
07400+ FOUND IN THE DAYFILE.'
07500 READ(5,*) EST
07600 PRINT*,'ENTER THE VALUES OF THE CONSTANT AND Q IN THE EQUATION........'
07700 PRINT*,'..........K=CONSTANT.(STRAIN RATE) TO THE POWER Q.'
07800 READ(5,*) CONSTAN,Q
07900 PRINT*,' ENTER THE VALUE OF THE STRAIN HARDENING EXPONENT.'
08000 READ(5,*) QQ
08100C
08200C
08300 RE=RB/SQRT(ER)
08400 V3=V1*RB*RB/(RE*RE)
08500 M=4
08600 MET=0
```

```
06700C
06600C
08900 PRINT*,'ENTER THE FREQUENCY WITH WHICH THE MONITORING SUBROUTINE IS TO
09000+BE CALLED. ZERO WILL GIVE NO CALLS WHILE 1 WILL CALL IT EVERY CYCLE.
09100+IT SHOULD BE NOTED THAT THIS PROGRAM EMPLOYS AN ITERATIVE METHOD FOR
09200+SOLUTION AND MAY THEREFORE TAKE SOME TIME BEFORE GIVING AN ANSWER.'
09300 READ(5,*) IPRIN
09400C
09500C
09600 IT=0
09700C
09800C
09900 IXTYP(1)=90
10000 IXTYP(2)=90
10100 IGTYP(1)=2
10200 IGTYP(2)=2
10300 IGTYP(3)=2
10400 IGTYP(M)=1
10500C
10600 LINE(1)=.TRUE.
10700 LINE(2)=.TRUE.
10800 LINE(3)=.TRUE.
10900 LINE(M)=.FALSE.
11000C
11100 M2N=M+2*N
11200 IW=5*N+4*M+M*N+2*N*N
11300C
11400C
11500C SUBROUTINE EO4HAF IS THE LIBRARY MINIMISING ROUTINE
11600C
11700 CALL EO4HAF(N,M,X,EST,EAX,AAX,IST,INF,MET,LOSW,M2N,W,IW,IXTYP,IGTYP
11800+,LINE,GRID,DGRID,DDGRID,MON,MONE,IPRIN,MAXI,IFAIL)
11900C
12000 V1=V1*1000.
12100C
12200 WRITE(6,951)
12300 WRITE(6,961)IFAIL
12400 WRITE(6,902)EST, (X(I),I=1,N)
12500 WRITE(6,966) ER,V1,C,CONSTAN,QQ
12600 WRITE(6,901) IPRIN,MAXI
12700C
12800 STOP
12900C
13000 951 FORMAT(75(1HX),///)
13100 901 FORMAT(/,17X,I5,* ITERATIONS *,I5,*  PENALTY EVALUATIONS*,///75(1HX))
13200 902 FORMAT(20X,*PRESSURE IS *,E12.5,4X,*AT */17X,*ALPHA = *,F10.6,7X
13300+* PHI = *,F10.6)
13400 961 FORMAT(32X,*IFAIL =*,I2,//)
13500 966 FORMAT(4X,*EXTRUSION RATIO IS *,F6.2,* : 1 AT A RAM SPEED OF *,
13600+F10.4,*INS/SEC.*,//,1X,*O = *,F6.4,5X,*CONSTANT = *,F6.4,4X,
13700+*STRAIN HARDENING EXPONENT = *,F5.4)
13800C
13900C
14000C
14100 END
14200C
14300C
14400 SUBROUTINE MONE(N,M,URMIN,XMIN,GMIN,UMIN,IORD)
14500C
14600C
14700C THIS ROUTINE GIVES A MONITOR OF THE DUAL AND EXTRAPOLATED SOLUTIONS
14800C AT THE END OF EACH CYCLE.
14900C
15000 DIMENSION URMIN(5),XMIN(2),GMIN(5),UMIN(5)
15100C
15200 COMMON/HAF/ MET,IPRIN,IT
15300C
15400 WRITE(6,1007)
15500 WRITE(6,1005) (I,URMIN(I),I=1,M)
15600 WRITE(6,1000) IORD
15700 WRITE(6,1001)
15800 WRITE(6,1002) (I,XMIN(I),I=1,N)
15900 WRITE(6,1003)
16000 WRITE(6,1004) (I,GMIN(I),I=1,M)
16100 WRITE(6,1005)
16200 WRITE(6,1006) (I,UMIN(I),I=1,N)
16300C
16400C
16500 1000 FORMAT(/,*EXTRAPOLATION SOLUTION ORDER= *,I5)
16600 1001 FORMAT(/,*SOLUTION VECTOR*)
16700 1002 FORMAT(1C(4(1X,1HX,I3,E12.5)/))
16800 1003 FORMAT(*CONSTRAINTS AND OBJECTIVE FNS*)
16900 1004 FORMAT(1C(4(2X,3HCON,I3,E12.5)/))
17000 1005 FORMAT(*DUAL SOLUTION OF EXTRAPOLATED SOLUTIONS*)
17100 1006 FORMAT(1C(4(1X,4HDUAL,I3,E12.5)/))
17200 1007 FORMAT(//*DUAL SOLUTION AT END POINT OF CYCLE*)
```

```
17300C
17400C
17500 RETURN
17600 END
17700C
17800C
17900 SUBROUTINE MON(N,M,XR,PRXR,PG,PUPONK,R,ITCH,NEWCYC,NP,NG,NH,NRF)
18000C
18100C
18200CC THIS ROUTINE MONITORS THE CHANGE OF ANGLES ALPHA AND PHI AND THE
18300CC RESULTING CHANGE IN THE PRESSURE.
18400CC
18500 LOGICAL NEWCYC
18600    COMMON/HAF/ MET,IPRIN,IT
18700C DIMENSION XR(2),PG(2),PUPONK(5)
18800C
18900 IT=IT+IPRIN
19000 IF(.NOT.NEWCYC) GO TO 101
19100 IT=C
19200C
19300 WRITE(6,1000) R
19400C
19500 101 WRITE(6,1001) IT,PRXR
19600C
19700CC
19800 IF(ITCH.LE.0) WRITE(6,1006)
19900 IF(ITCH.EQ.3.OR.ITCH.EQ.-3) WRITE(6,1007)
20000 IF(ITCH.EQ.2.OR.ITCH.EQ.-2) WRITE(6,1008)
20100CC
20200CC
20300 WRITE(6,1009)
20400 WRITE(6,1010) (J,XR(J),J=1,N)
20500C
20600C IF(MET.LT.1) GO TO 106
20700CC
20800 WRITE(6,1002)
20900 WRITE(6,1003) (I,PG(I),I=1,N)
21000C
21100 106 WRITE(6,1011)
21200 WRITE(6,1012) (I,PUPONK(I),I=1,M)
21300CC
21400CC
21500 1000 FORMAT(/*BEGINING OF CYCLE FOR R= *,E15.6)
21600C 1001 FORMAT(/*ITERATION NO *,I3,*  PENALTY FUNCTION VALUE *,E15.6)
21700 1002 FORMAT(*PENALTY GRADIENT*)
21800 1003 FORMAT(10(4(3X,1HG,I3,E12.5)/))
21900C 1006 FORMAT(/*LINE SEARCH TROUBLES*)
22000 1007 FORMAT(* H NOT FAC*)
22100 1008 FORMAT(* H INDEF*)
22200C 1009 FORMAT(/*SOLUTION VECTOR*)
22300C 1010 FORMAT(10(4(3X,1HX,I3,E12.5)/))
22400C 1011 FORMAT(*CONSTRAINTS AND OBJECTIVE FNS*)
22500C 1012 FORMAT(10(4(2X,3HCON,I3,E12.5)/))
22600CC
22700CC
22800 RETURN
22900 END
23000C
23100C
23200C
23300 SUBROUTINE GRID(N,X,I,PUPONK)
23400C
23500C
23600CC THIS IS THE MAIN CALCULATION ROUTINE CALLED BY THE MINIMISATION
23700CC ROUTINE AND ITSELF CALLING THE REMAINING ROUTINES TO CALCULATE THE
23800CC PRESSURE.
23900C
24000CC
24100    COMMON/1/ R1,Y,Z,DELTAR,ALAMOAT,ALAMOAC,RR,RRC
24200    COMMON/2/ RB,RE,V1,V3,PI
24300    COMMON/3/ SNALPHA,SNBETA,SNGAM,CSGPA,CSALPHA,CSBETA,SNDTB2,CSCTB2,
24400+Q,QC,CONSTAN,SNBND,CSAMP,SNP,CSP,SNTHETA,CSTHETA,CSGAM
24500    COMMON/ANGLE/ ALPHA,GAMMA,PHI,THETA,DTHETA,BETA
24600    COMMON/ENER/ E2,E24,E23,E12,E12T,E23J,E2-T,E2T
24700    COMMON/STN/ TEMP4,STRAIN2(5),STRN(10,5),ST(10),STRAIN(5)
24800C
24900C
25000 DIMENSION X(2)
25100 ALPHA=X(1)/57.2958
25200 PHI=X(2)/57.2958
25300C
25400C
25500 IF(I.EQ.1) GO TO 889
25600 IF(I.EQ.2) GO TO 999
25700C
25800 TGAMMA=ABS((((RB-RE)/TAN(ALPHA))-(RE*TAN(PHI)))/RB)
```

```
25900    GAMMA=ATAN(TGAMMA)
26000    IF(I.EQ.3) GO TO 699
26100    A1=RE*TAN(PHI)
26200    A2=(RS-RE)/TAN(ALPHA)
26300 C
26400    E24T=0
26500    E12T=0
26600    E23T=0
26700    E2T=C
26800 C
26900 C
27000    JJ=10
27100    K=5
27200 C
27300    IF(A1.GT.A2) GO TO 799
27400    DTHETA=(GAMMA+PHI)/10.
27500    THETA=((PI/2.)-GAMMA)-(DTHETA/2.)
27600    GO TO 599
27700    799 DTHETA=(PHI-GAMMA)/10.
27800    THETA=((PI/2.)+GAMMA)-(DTHETA/2.)
27900    599 Z=1
28000 C
28100 C  THE FOLLOWING DO-LOOPS DO THE CALCULATIONS DOWN EACH SET OF ELEMENTS
28200 C  AND AROUND THE ELEMENTS RADIALLY.
28300 C
28400    DO 100 L=1,JJ,1
28500 C
28600    THETA=THETA+DTHETA
28700    Y=1
28800 C
28900    DO 200 MM=1,K,1
29000 C
29100    BETA=THETA-ALPHA
29200    SNALPHA=SIN(ALPHA)
29300    SNBETA=SIN(THETA-ALPHA)
29400    SNGAM=SIN(GAMMA)
29500    CSGAM=COS(GAMMA)
29600 C
29700 C
29800    IF(A1.GT.A2) GO TO 4001
29900 C
30000 C
30100    CSGPA=COS(GAMMA+ALPHA)
30200 C
30300 C
30400    GO TO 4002
30500    4001 CSGPA=COS(ALPHA-GAMMA)
30600    4002 CSALPHA=COS(ALPHA)
30700 C
30800 C
30900    CSBETA=COS(THETA-ALPHA)
31000    SNDTE2=SIN(DTHETA/2.)
31100    CSDTE2=COS(DTHETA/2.)
31200    SNBMD=SIN(BETA-(DTHETA/2.))
31300    CSAMP=COS(ALPHA-PHI)
31400    SNP=SIN(PHI)
31500    CSP=COS(PHI)
31600    SNTHETA=SIN(THETA)
31700    CSTHETA=COS(THETA)
31800 C
31900 C
32000    R1=RS/CSGAM
32100 C
32200 C
32300 C
32400    CALL CENTRE C(MM,L)
32500    IF(L.EQ.1) CALL E12CALC(MM,L)
32600    IF(MM.EQ.1) CALL E24CALC(MM,L)
32700    IF(MM.EQ.5) CALL TRIANGL(MM,L)
32800    IF(MM.EQ.5) GO TO 300
32900    CALL ENERGYC(MM,L)
33000    300 IF(L.EQ.10) CALL E23 CALC(MM,L)
33100 C
33200 C
33300 C
33400 C
33500    E2T=E2T+E2
33600 C
33700 C
33800    Y=Y+2.
33900 C
34000 C
34100    200 CONTINUE
34200 C
34300    Z=Z+2.
34400 C
```

```
34500 100 CONTINUE
34600C
34700C
34800C
34900CC
35000CC
35100C  THE SEPERATE ENERGIES ARE SUMMED
35200C
35300  P=E12T+E23T+E24T+E2T
35400CC
35500CC
35600C  THE TOTAL ENERGY IS THEN EQUATED TO THE PRESSURE.AREA.RAM VELOCITY.
35700CC
35800  PUPCNK=P/(PI*R-*RB*V1)
35900CC
36000CC
36100CC
36200CC  THE FOLLOWING ARE THE CONSTRAINTS USED IN THE MINIMISATION. THEY ALL
36300CC  PASS THROUGH AS THE REQUIRED RESULT. I.E. IN PUPONK. THE CONSTRAINTS
36400CC  EMPLOYED ARE THAT: NEITHER ALPHA OR BETA CAN EXCEED 90 DEGREES.
36500CC  THAT ANGLE ALPHA MUST ALWAYS BE GREATER THAN ANGLE GAMMA.
36600CC
36700CC
36800  GO TO 1099
36900  889 PUPCNK=(PI/2.)-ALPHA
37000  GO TO 1099
37100  999 PUPCNK=(PI/2.)-PHI
37200  GO TO 1099
37300  699 PUPCNK=ALPHA-GAMMA
37400  1099 RETURN
37500C
37600C
37700 END
37800C
37900CC
38000  SUBROUTINE CENTREC(MM,L)
38100C
38200CC
38300CC  ROUTINE TO CALCULATE THE BASIC GEOMETRICAL TERMS REQUIRED BY EACH
38400CC  ELEMENT. RR IS THE RADIUS FROM THE CENTRE TO THE EDGE OF THE ELEMENT
38500CC  RPC IS THE DISTANCE FROM THE CENTRE TO THE CENTRE OF GRAVITY.
38600CC  DELTAR IS THE ELEMENT HEIGHT. ALAMDAT IS THE TOP EDGE DIAMETER.
38700CC  ALAMDAC IS THE CENTRE OF GRAVITY DIAMETER.
38800C
38900CC
39000  COMMON/1/ R1,Y,Z,DELTAR,ALAMDAT,ALAMDAC,RR,RRC
39100  COMMON /2/RB,RB,V1,V3,PI
39200  COMMON /3/SNALPHA,SNBETA,SNGAM,CSGPA,CSALPHA,CSBETA,SNDTB2,CSDTB2,
39300+Q,QC,CONSTAN,SNBMD,CSAMP,SNP,CSP,SNTHETA,CSTHETA,CSGAM
39400  COMMON /ANGLE/ALPHA,GAMMA,PHI,THETA,DTHETA,BETA
39500  COMMON/STN/ TEMP4,STRAIN2(5),STRN(10,5),ST(10),STRAIN(5)
39600CC
39700CC
39800  RR=(R1*SIN(BETA-(Z*(DTHETA/2.))))/SNBETA
39900CC
40000  DELTAR=RR/5.
40100  RRC=RR-Y*(DELTAR/2.)
40200CC
40300  ALAMDAT=(2.*(RRC+(DELTAR/2.))*SNDTB2)/SNBMD
40400  ALAMDAC=(2.*RRC*SNDTB2)/SNBMD
40500CC
40600  RETURN
40700  END
40800C
40900CC
41000  SUBROUTINE E12 CALC(MM,L)
41100C
41200CC
41300CC ROUTINE TO CALCULATE THE ENERGY REQUIRED IN CROSSING THE DISCONTINUITY
41400CC  V12.
41500CC
41600  COMMON/1/ R1,Y,Z,DELTAR,ALAMDAT,ALAMDAC,RR,RRC
41700  COMMON/2/RB,RB,V1,V3,PI
41800  COMMON/3/ SNALPHA,SNBETA,SNGAM,CSGPA,CSALPHA,CSBETA,SNDTB2,CSDTB2,
41900+Q,QC,CONSTAN,SNBMD,CSAMP,SNP,CSP,SNTHETA,CSTHETA,CSGAM
42000  COMMON/ENER/E2,E24,E23,E12,E12T,E23T,E24T,E2T
42100  COMMON/ANGLE/ALPHA,GAMMA,PHI,THETA,DTHETA,BETA
42200  COMMON/STN/ TEMP4,STRAIN2(5),STRN(10,5),ST(10),STRAIN(5)
42300CC
42400CC
42500  V12=(V1*SNALPHA)/CSGPA
42600  DV12=0.
42700  ELEMENL=(RB/CSGAM)/5.
42800  ELEMENR=(RB/CSGAM)*((10.-Y)/10.)
42900  AREA12=ELEMENL*ELEMENR*2.*PI*CSGAM
43000C
```

```
43100 CALL SRATE(V12,DV12,AK12,ELEMENR,STRATE)
432CC CALL STRAN12(MM,L,V12,BK12)
4330CC
4340CJ E12=V12*AREA12*AK12*BK12
4350CCC
4360CCC
437CCC THE ENERGY FOR THE PRESENTELEMENT IS THEN ADDED TO THAT FOR PREVIOUS
438CCC SIMILLAR ELEMENTS.
43900C
44300J E12T=E12T+F12
44100C
44200C
44300C RETURN
44400C END
44500C
44600C
44700C SUBROUTINE E24 CALC(HM,L)
44800C
44900CC
45000CC ROUTINE CALCULATES THE ENERGY REQUIRED TO ACCELERATE THE MATERIAL
45100CC DOWN THE O.M.Z BOUNDARY.
45200C
45300C     COMMON/1/ R1,Y,Z,DELTAR,ALAMDAT,ALAMDAC,RR,RRC
45400C     COMMON/2/ RB,RE,V1,V3,PI
45500C     COMMON/3/ SNALPHA,SNBETA,SNGAM,CSGPA,CSALPHA,CSBETA,SNDTB2,CSDTB2,
45600CC
45700+Q,QQ,CONSTAN,SNBMD,CSAMP,SNF,CSP,SNTHETA,CSTHETA,CSGAM
45800C     COMMON/ENER/E2,E24,E23,E12,E12T,E23T,E24T,E2T
45900C     COMMON/ANGLE/ALPHA,GAMMA,PHI,THETA,DTHETA,BETA
46000C     COMMON/STN/ TEMP4,STRAIN2(5),STRN(10,5),ST(10),STRAIN(5)
46100C
46200CC
4630C     V24=(V1*CSGAM*CSGAM*SNBETA)/(SNTHETA*CSGPA*CSGPA)
46400J     DV24=((V1*CSGAM*CSGAM)/(CSGPA*CSGPA))*((SNTHETA*COS(ALPHA-
46500+THETA)-SNBETA*CSTHETA)/(SNTHETA*SNTHETA))
46600J     AREA24=ALAMDAT*2.*PI*RR*COS(GAMMA-(Z*DTHETA/2.))
4670CCC
46300J CALL SRATE(V24,DV24,AK24,RR,STRATE2)
46900C PRINT*,'POS 2', MM,L,RR,DELTA-,V24,STRATE2,BK24
47000C CALL STRAN24(MM,L,ALAMDAT,V24,STRATE2,BK24)
47100C PRINT*,'POS 1', MM,L,RR,DELTAR,V24,STRATE2,BK24
47200C
47300C
47400C E24=V24*AREA24*AK24*BK24
47500C
47600C
47700C E24T=E24T+E24
47800C RETURN
47900C END
48000C
48100C
48200C SUBROUTINE E23 CALC(HM,L)
48300CC
48400CC
48500CC ROUTINE CALCULATES THE ENERGY INVOLVED IN CROSSING THE BOUNDARY 23.
48600C
48700C     COMMON/1/ R1,Y,Z,DELTAR,ALAMDAT,ALAMDAC,RR,RRC
48800C     COMMON/2/ RB,RE,V1,V3,PI
48900C     COMMON/3/ SNALPHA,SNBETA,SNGAM,CSGPA,CSALPHA,CSBETA,SNDTB2,CSDTB2,
49000C+Q,QQ,CONSTAN,SNBMD,CSAMP,SNF,CSP,SNTHETA,CSTHETA,CSGAM
49100C     COMMON/ENER/ E2,E24,E23,E12,E12T,E23T,E24T,E2T
49200C     COMMON/STN/ TEMP4,STRAIN2(5),STRN(10,5),ST(10),STRAIN(5)
493CCC
49400J V23=(V3*SNALPHA)/CSAMP
49500C DV23=0.
49600J ELEMENL=(RE/CSP)/5.
49700C ELEMENR=(RE/CSP)*((10.-Y)/10.)
498CCC
49900C AREA23=ELEMENL*ELEMENR*2.*PI*CSP
50000C
50100C CALL SRATE(V23,DV23,AK23,ELEMENR,STRATE)
50200J CALL STRAN23(MM,L,BK23)
50300CC
50400C E23=AREA23*V23*AK23*BK23
50500CC
50600J E23T=E23T+E23
50700C RETURN
50800C END
50900C
51000CC
51100 SUBROUTINE ENERGYC(MM,L)
51200CC
51300CC
51400CC ROUTINE CALCULATES THE ENERGY DISSIPATED WITHIN EACH RECTANGULAR
51500CC ELEMENT.
51600C
```

```
51700      COMMON/1/ R1,Y,Z,DELTAR,ALAMDAT,ALAMDAC,RR,RRC
51800      COMMON/2/ RD,RE,V1,V3,PI
51900      COMMON/3/ SNALPHA,SNBETA,SNGAM,CSGPA,CSALPHA,CSBETA,SNDTB2,CSDTB2,
52000     +Q,QC,CONSTAN,SNBND,CSAMP,SNF,CSP,SNTHETA,CSTHETA,CSGAM
52100      COMMON/ENER/E2,E24,E23,E12,E12T,E23T,E24T,E2T
52200      COMMON/ANGLE/ALPHA,GAMMA,PHI,THETA,DTHETA,BETA
52300      COMMON/STN/ TEMP4,STRAIN2(5),STRN(10,5),ST(10),STRAIN(5)
52400 C
52500 C
52600 C C  THIS ROUTINE USES A METHOD INVOLVING STRAIN RATE WHICH IS CALCULATED
52700 C C  USING THE METHOD EMPLOYED BY ADIE AND ALEXANDER IN ADIES PH.D THESIS.
52800 C C
52900 C C
53000      ELEMENV=ALAMDAC*DELTAR*2.*PI*RRC*SNTHETA
53100      VELOC=(V1*CSGAM*CSGAM*SNBETA)/(SNTHETA*CSGPA*CSGPA)
53200 C
53300      DVELOC=((V1*CSGAM*CSGAM)/(CSGPA*CSGPA))*((SNTHETA*COS(ALPHA-THETA)
53400     +-SNBETA*CSTHETA)/(SNTHETA*SNTHETA))
53500 C
53600      ETHET=((VELOC*CSBETA*2.)+(SNBETA*DVELOC))/-RRC
53700      EPHI=(VELOC/RRC)*(CSBETA+(1./TAN(THETA))*SNBETA)
53800 C
53900      ERTHET=((-VELOC*SNBETA*2.)+(CSBETA*DVELOC))/RRC
54000      EBARDOT=SQRT((2./3.)*((ETHET*ETHET)+(EPHI*EPHI)+(0.5*(ERTHET*ERTHET))))
54100 C
54200      CALL SRATE(VELOC,DVELOC,AK2,RRC,STRATE3)
54250      WRITE(7,1004)MM,L,STRATE 3
54260 1004 FORMAT(*ELEMENTS*,/,I2,2X,I2,E12.5)
54300      CALL CNTSTRN(MM,L,ALAMDAC,VELOC,
54400     +STRATE3,BK2)
54500      E2=EBARDOT*ELEMENV*AK2*BK2*SQRT(3.0)
54600 C
54700      RETURN
54800      END
54900 C
55000 C
55100      SUBROUTINE TRIANGL(MM,L)
55200 C
55300 C
55400 C  ROUTINE CALCULATES THE ENERGY DISSIPATED WITHIN THE 5 TRIANGULAR
55500 C C ELEMENTS AT THE CENTRE OF THE MESH.
55600 C C C
55700 C
55800      COMMON/1/ R1,Y,Z,DELTAR,ALAMDAT,ALAMDAC,RR,RRC
55900      COMMON/2/ RE,RE,V1,V3,PI
56000      COMMON/3/ SNALPHA,SNBETA,SNGAM,CSGPA,CSALPHA,CSBETA,SNDTB2,CSDTB2,
56100     +Q,QC,CONSTAN,SNBND,CSAMP,SNF,CCP,SNTHETA,CSTHETA,CSGAM
56200      COMMON/ANGLE/ ALPHA,GAMMA,PHI,THETA,DTHETA,BETA
56300      COMMON/ENER/ E2,E24,E23,E12,E12T,E23T,E24T,E2T
56400      COMMON/STN/ TEMP4,STRAIN2(5),STRN(10,5),ST(10),STRAIN(5)
56500 C C
56600 C C
56700      XR1=((ALAMDAT/2.)*SNBETA)/SNDTB2
56800      TRIRAD=(2./3.)*(RR/5.)
56810      TRIC=(2.*TRIRAD*SNDTB2)/SNBND
56900      TRIAREA=0.5*ALAMDAT*XR1*SIN(BETA-(DTHETA/2.))
57000      TRIVOL=TRIAREA*2.*PI*TRIRAD*COS(GAMMA-(Z*(DTHETA/2.)))
57100      VT=(V1*CSGAM*CSGAM*SNBETA)/(SNTHETA*CSGPA*CSGPA)
57200      DVT=((V1*CSGAM*CSGAM)/(CSGPA*CSGPA))*((SNTHETA*COS(ALPHA-
57300     +THETA)-SNBETA*CSTHETA)/(SNTHETA*SNTHETA))
57400 C
57500      CALL SRATE(VT,DVT,AKT,TRIRAD,STRATE4)
57550      WRITE(7,1005)MM,L,STRATE4
57560 1005 FORMAT(*TRIANGLES*,/,I2,2X,I2,E12.5)
57600      CALL CNTSTRN(MM,L,TRIC,VT,
57700 C
57800     +STRATE4,BKT)
57900      E2=TRIVOL*VT*AKT*BKT*SQRT(3.0)
58000 C
58100      RETURN
58200      END
58300 C
58400 C
58500      SUBROUTINE DGRID(N,X,I,G)
58600 C
58700 C
58800 C  ROUTINE INCLUDED SINCE A DECLARATION IS REQUIRED BY THE LIBRARY ROUTINE.
58900 C  IT HAS NO USE IN THE CALCULATION.
59000 C C
59100      DIMENSION G(4),X(2)
59200      RETURN
59300      END
59400 C
59500 C C
59600      SUBROUTINE DDGRID(N,X,I,DG)
59700 C
```

```
59900C
5990CC ROUTINE INCLUDED FOR THE SAME REASON AS OGRID
60000C
60100 DIMENSION DG(4,4),X(2)
60200 RETURN
60300 END
60400C
60500C
60600 SUBROUTINE SRATE(V,DV,AK,RADIUS,STRATE)
60700C
60800C
60900CC THIS ROUTINE CALCULATES THE VALUE OF THE STRAIN RATE FOR EACH ELEMENT
61000CC AND RAISES IT TO THE POWER G DETERMINED ON ENTRY BY THE USER.
61100C
61200    COMMON/3/ SNALPHA,SNBETA,SNGAM,CSGPA,CSALPHA,CSBETA,SNDTB2,
61300+CSDTB2,Q,QQ,CONSTAN,SNSMD,CSAMP,SNP,CSP,SNTHETA,CSTHETA,CSGAM
61400    COMMON/ANGLE/ ALPHA,GAMMA,PHI,THETA,DTHETA,BETA
61500C
61600C
61700 STRAINT=(V*CSBETA*2.+(SNBETA*DV))/RADIUS
61800 STRAINP=(V/RADIUS)*(CSBETA+(1./TAN(THETA))*SNBETA)
61900 STRAINR=((-V*SNBETA*2.)+(CSBETA*DV))/RADIUS
62000 STRATE=SQRT((2./3.)*((STRAINT*STRAINT)+(STRAINP*STRAINP)
62100+*(0.5*(STRAINR*STRAINR))))
62200C
62300C
62400 AK=CONSTAN*(STRATE**Q)
62500C
62600 RETURN
62700 END
62800C
62900C
63000 SUBROUTINE STRAN12(MM,L,V12,BK12)
63100C
63200C
63300CC THIS ROUTINE CALCULATES THE STRAIN AT A DISCONTINUITY 12 AND RAISES
63400CC TO THE POWER QQ AS DETERMINED BY THE USER.
63500C
63600    COMMON/2/ RB,RE,V1,V3,PI
63700    COMMON/3/ SNALPHA,SNBETA,SNGAM,CSGPA,CSALPHA,CSBETA,SNDTB2,CSDTB2,
63800+Q,QQ,CONSTAN,SNSMD,CSAMP,SNP,CSP,SNTHETA,CSTHETA,CSGAM
63900    COMMON/STN/ TEMP4,STRAIN2(5),STRN(10,5),ST(10),STRAIN(5)
64000C
64100C
64200 STRAIN(MM)=V12/(SQRT(3.)*V1*SNTHETA)
64300 IF(STRAIN(MM).LT.2.3) GO TO 1
64330 CALL FIRSTST(BK12)
64350 TEMP1=BK12
64370 RETURN
64400 1 EXPO1=(STRAIN(MM)**(QQ+1.))
64500C
64600 BK12=(EXPO1/STRAIN(MM))/(SQRT(3.)*(QQ+1.))
64700 TEMP1=BK12
64800 GO TO 3002
64900 3001 BK12=TEMP1
65000C
65100 3002 RETURN
65200 END
65300C
65400C
65500 SUBROUTINE CNTSTRN(MM,L,ALENGTH,VEL,STRATE,BK2)
65600C
65700C
65800C THIS ROUTINE CALCULATES THE STRAIN FO EACH ELEMENT EXCLUDING THE
65900C BOUNDARY.
66000C
66100    COMMON/3/ SNALPHA,SNBETA,SNGAM,CSGPA,CSALPHA,CSBETA,SNDTB2,CSDTB2,
66200+Q,QQ,CONSTAN,SNSMD,CSAMP,SNP,CSP,SNTHETA,CSTHETA,CSGAM
66300    COMMON/ANGLE/ ALPAH,GAMMA,PHI,THETA,DTHETA,BETA
66400    COMMON/STN/ TEMP4,STRAIN2(5),STRN(10,5),ST(10),STRAIN(5)
66500C
66600C
66700 DT=ALENGTH/VEL
66800 IF(L.GT.1) GO TO 777
66900 STRN(L,MM)=(STRATE*DT)+STRAIN(MM)
67000 IF(STRN(L,MM).LT.2.3) GO TO 1
67030 CALL FIRSTST(BK2)
67050 TEMP2=BK2
67070 RETURN
67100 1 P1=STRAIN(MM)**(QQ+1.)
67200 P2=STRN(L,MM)**(QQ+1.)
67300 BK2=((P2-P1)/(STRN(L,MM)-STRAIN(MM)))/(SQRT(3.)*(QQ+1.))
67400 TEMP2=BK2
67500 GO TO 778
67600 777 STRN(L,MM)=(STRATE*DT)+STRN(L-1,MM)
67650C
```

```
67700 IF(STRN(L,MY).GE.2.3) GO TO 4001
67810 POWER2=(STF((L,MM)**(QQ+1.))
67900 POWER1=(STRN(L-1,MM)**(QQ+1.))
68000C
68100 SK2=((POWER2-POWER1)/(STRN(L,MM)-STRN(L-1,MM)))/(SQRT(3.)*(QQ+1.))
68200 TEMP2=SK2
68300 GO TO 778
68400 4001 SK2=TEMP2
68500C
68600 778 RETURN
68700 END
68800C
68900C
69000 SUBROUTINE STRAN23(MM,L,SK23)
69100C
69200CC
69300C ROUTINE CALCULATES THE STRAIN AT THE BOUNDARY 23.
69400C
69500    COMMON/2/ RB,RE,V1,V3,PI
69600    COMMON/3/ SNALPHA,SNBETA,SNGAM,CSGPA,CSALPHA,CSBETA,SNCTB2,CSCTB2,
69700   +Q,QQ,CONSTAN,SNBRD,CSAMP,SNP,CSP,SNTHETA,CSTHETA,CSGAM
69800    COMMON/STN/ TEMP4,STRAIN2(5),STRN(10,5),ST(10),STRAIN(5)
69900CC
70000C
70100 V2O3=V3*CSP/CSAMP
70200 V23=V3*SNALPHA/CSAMP
70300 STRAIN2(MM)=V23/(SQRT(3.)*V2O3*SNTHETA)+STRN(L,MM)
70330 CALL FIRSTST(SK23)
70350 TEMP3=SK23
70370 RETURN
70400 IF(STRAIN2(MM).LT.2.3) GO TO 1
70500 1 EXPON1=(STRN(L,MM)**(QQ+1.))
70600 EXPON2=(STRAIN(MM)**(QQ+1.))
70700CC
70800 SK23=(EXPON2-EXPON1)/(STRAIN2(MM)-STRN(L,MM))/(SQRT(3.)*(QQ+1.))
70900 TEMP3=SK23
71000 GO TO 5002
71100 5001 SK23=TEMP3
71200C
71300 5002 RETURN
71400 END
71500C
71600CC
71700C SUBROUTINE STRAN24(MM,L,ALAMDAT,VELO,STR,SK24)
71800CC
71900CC
72000CC
72100CC THIS ROUTINE CALCULATES THE STRAIN AT THE BOUNDARY 24
72200C
72300    COMMON/3/ SNALPHA,SNBETA,SNGAM,CSGPA,CSALPHA,CSBETA,SNCTB2,CSCTB2,
72400   +Q,QC,CONSTAN,SNBRD,CSAMP,SNP,CSP,SNTHETA,CSTHETA,CSGAM
72500    COMMON/ANGLE/ ALPHA,GAMMA,PHI,THETA,ETHETA,BETA
72600    COMMON/STN/ TEMP4,STRAIN2(5),STRN(10,5),ST(10),STRAIN(5)
72700C
72800C
72900 DT=ALAMDAT/VELO
73000 IF(L.GT.1) GO TO 7799
73100 ST(L)=(STR*DT)+STRAIN(MM)
73200CPRINT*,'LINE 73200STL AND STRAINMM.',ST(L),STRAIN(MM)
73300 IF(ST(L).LT.2.3) GO TO 1
73400 CALL FIRSTST(SK24)
73500 TEMP4=SK24
73600CPRINT*,'AT LINE 71155',TEMP4
73700 RETURN
73800 1 P3=ST(L)**(QQ+1.)
73900 P4=STRAIN(MM)**(QQ+1.)
74000CPRINT*,'P3 AND P4', P3,P4
74100 SK24=((P3-P4)/(ST(L)-STRAIN(MM)))/(SQRT(3.)*(QQ+1.))
74200 TEMP4=SK24
74300CPRINT*,'AT LINE 71211', TEMP4
74400CCPRINT*,SK24
74500 GO TO 7798
74600 7799 ST(L)=(STR*DT)+ST(L-1)
74700 IF(ST(L).GE.2.3) GO TO 6001
74800 POW2=(ST(L)**(QQ+1.))
74900 POW1=(ST(L-1)**(QQ+1.))
75000CPRINT*,'POW2 AND POW1',POW2,POW1
75100 SK24=((POW2-POW1)/(ST(L)-ST(L-1)))/(SQRT(3.)*(QQ+1.))
75200 TEMP4=SK24
75300 GO TO 7798
75400 6001 SK24=TEMP4
75500 7798 RETURN
75600 END
75700 SUBROUTINE FIRSTST(SK)
75800 COMMON/3/ SNALPHA,SNBETA,SNGAM,CSGPA,CSALPHA,CSBETA,SNCTB2,CSCTB2,
75900 +Q,QQ,CONSTAN,SNBRD,CSAMP,SNP,CSP,SNTHETA,CSTHETA,CSGAM
```

```
76000 BK=((2.3**(QQ+1.))/(2.3))/(SQRT(3.)*(QC+1.))
76100 PRINT*,'IN FIRSTST' ,BK
76200 RETURN
76300 END
```

APPENDIX 4

```
00100 PROGRAM EXTRUDE(INPUT,OUTPUT,TAPE5=INPUT,TAPE6=OUTPUT)
00110C
00120C
00130C
00140C
00150C
00160C          THE MATHS. IS IN THE S.I. SYSTEM.
00170C
00180C          THE FOLLOWING HAVE BEEN ASSUMED TO BE CONSTANT:-
00190C            BILLET DIAMETER,DB:
00200C            BILLET LENGTH,BL:
00210C            CONTAINER TEMPERATURE,TEMPCON:
00220C            ACTIVATION ENERGY,Q:
00230C            GAS CONSTANT,R:
00240C            LAND LENGTH,ALL:
00250C            DENSITIES OF ALUMINIUM ALLOY AND STEEL,RHOAL,RHOST:
00260C            HEAT CAPACITIES OF ALUMINIUM ALLOY AND STEEL,CAL,CST:
00270C            THERMAL CONDUCTIVITIES OF ALUMINIUM ALLOY AND STEEL,AKAL,AKST:
00280C
00290C
00300   DIMENSION V(50),ALOAD(50),TEMPT(50),TB(50),AK6(50),AK8(50),AK10(50),
00310  +TIME(50),CTOT1(50),CTOT2(50),CTOT3(50),DELTAT(50),TEMPD(50),STATE(50),
00320  +FLOG7(50),SIGMA(50),ALPHAS(50),SINH(50),PLOG(50),V1(50),ALOAD1(50)
00330 1 PRINT 60
00340 60 FORMAT('READ IN THE EXTRUSION RATIO,ALPHA,THEN THE NUMBER OF RESULTS'
00350  +/'(UP TO 50) FOLLOWED BY THE RAM SPEED(MM/S),THE LOAD(MN/MSQED.)'
00360  +/'AND THE INITIAL BILLET TEMP. (DEG.C.) FOR EACH POINT.')
00370   READ(5,55,=1,5,*),55,ALPHA,N,(V1(I),ALOAD1(I),TB(I),I=1,N)
00380 52 PRINT*,'IS THE INFORMATION CORRECT?'
00390   READ 50,NNSWER
00400 50 FORMAT (A1)
00410   IF (NNSWER.EQ.1HY) GO TO 51
00420   IF (NNSWER.EQ.1HN) GO TO 1
00430   GO TO 52
00480C
00490C
00500 51 DB = 0.075
00510   BL = 0.090
00520   TEMPCON = 573.00
00530   Q = 151000.0
00540   R = 8.317
00550   ALL = 0.00508
00560   RHOAL = 2795.9
00570   RHOST = 7860.0
00580   CAL = 1167.9
00590   CST = 489.762
00600   AKAL = 201.0
00610   AKST = 32.6508
00620C
00630C
00640C          VALUES OF THE WORK CONSTANT AND THE ANGLE OF
00650C                THE DEFORMATION ZONE.
00660C
00670C
00680   IR = IFIX(55)
00690   IF (IR.NE.40) GO TO 2
00700   ROM =53.53
00710   C=14.996
00720   GO TO 9
00730 2 IF (IR.NE.80) GO TO 3
00740   ROM=54.91
00750   C=18.176
00760   GO TO 9
00770 3 IF (IR.NE.60) GO TO 93
00780   ROM=54.39
00790   C=16.82
00800 93 CONTINUE
00810C
00820C          EVALUATION OF THE CONSTANTS USED IN THE PROGRAM
00830C
00840C
00850 9 ANGLE = 90.0-ROM
00860   RANGLE = ANGLE/57.29573
00870   RADROM = ROM/57.29573
00880   TANANG = SIN(RANGLE)/COS(RANGLE)
00890   TANROM = SIN(RADROM)/COS(RADROM)
00900   DE = SQRT(DB*DB/55)
00910   ALO = (DB-DE)/2.0*(1.0-TANANG)
00920   ALT = BL-ALO-((DB-DE)/2.0*TANANG)
00930   ALFAST = AKST/(CST*RHOST)
00940   ALFAAL = AKAL/(CAL*RHOAL)
00950   ALFA = SQRT(ALFAST/ALFAAL)
00960C
00970C
00980C          CALCULATION OF CONSTANTS IN THE HEAT BALANCE EQUATION
00990C
```

```
01000C
01010  AK1 = (3.142*((DE*DE)-(DE*DE))/COS(FANGLE))*SQRT(AKST*CST*RHOST/12.0)
01020  AK2 = 3.142 *ALD/6.0*(18.0*AKST*DE*SQRT(RHOST*CST))**(2.0/3.0)
01030  AK3 = 3.142 *ALD/6.0*DE*(18.0*AKST*DE*((RHOST*CST)**2))**(1.0/3.0)
01040  AK4 = 3.142*ALL/6.0*(18.0*AKST*DE*SQRT(RHOST*CST))**(2.0/3.0)
01050  AK5 = 3.142*ALL/6.0*DE*(18.0*AKST*DE*((RHOST*CST)**2))**(1.0/3.0)
01060  AK7 = 3.142/6.0*ALT*(18.0*AKST*DE*SQRT(CST*RHOST))**(2.0/3.0)
01070  AK9 = 3.142/6.0*(18.0*AKST*(DE**4)*(ALT**3)*(RHOST*CST)**2)**(1.0/3.0)
01080  AK11 = 3.142 *DE*DE*SQRT(RHOST*AKST*CST/12.0)
01090C
01100C
01110C          EVALUATION OF THE TEMPERATURE RISE
01120C
01130C
01140  DO 10 I=1,N
01150  ALOAD(I) = ALOAD1(I)*1.03305E0.0
01160  V(I) = V1(I)/1000.0
01170  AK6(I) = 3.142*DE*DE/4.0*RHOAL*CAL*EP*V(I)
01180  AK8(I) = -AK7*3.0*V(I)/(5.0*ALT)
01190  AK10(I) = -AK9*3.0*V(I)/(4.0*ALT)
01200  TIME(I) = ALT/V(I)
01210  CTOT2(I) = (AK1*SQRT(TIME(I)))+((AK2+AK4)*TIME(I)**(2.0/3.0))+((AK3+
01220 +AK5)*TIME(I)**(1.0/3.0))
01230  CTOT1(I) = (AK6(I)*TIME(I))+CTOT2(I)
01240  CTOT3(I) = CTOT2(I)+(AK7*TIME(I)**(2.0/3.0))+(AK8(I)*TIME(I)**(5.0/3.0))
01250 ++(AK9*TIME(I)**(1.0/3.0))+(AK10(I)*TIME(I)**(4.0/3.0))
01260 ++(AK11*SQRT(TIME(I)))
01265  T3(I)=T3(I)+273.
01267  ALOAD(I)=ALOAD(I)*3.142*0.075*0.075/4.
01270  TEMPT(I) = (T3(I)+(ALFA*TEMPCON))/(1.0+ALFA)
01280  DELTAT(I) = (ALOAD(I)*ALT-(TEMPI(I)-TEMPCON)*CTOT3(I))/CTOT1(I)
01290  TEMPD(I) = T3(I)+DELTAT(I)
01300C
01310  WRITE(6,600) TEMPD(I)
01320 600 FORMAT(F20.6)
01325 10 CONTINUE
01330  STOP
01340  END
```
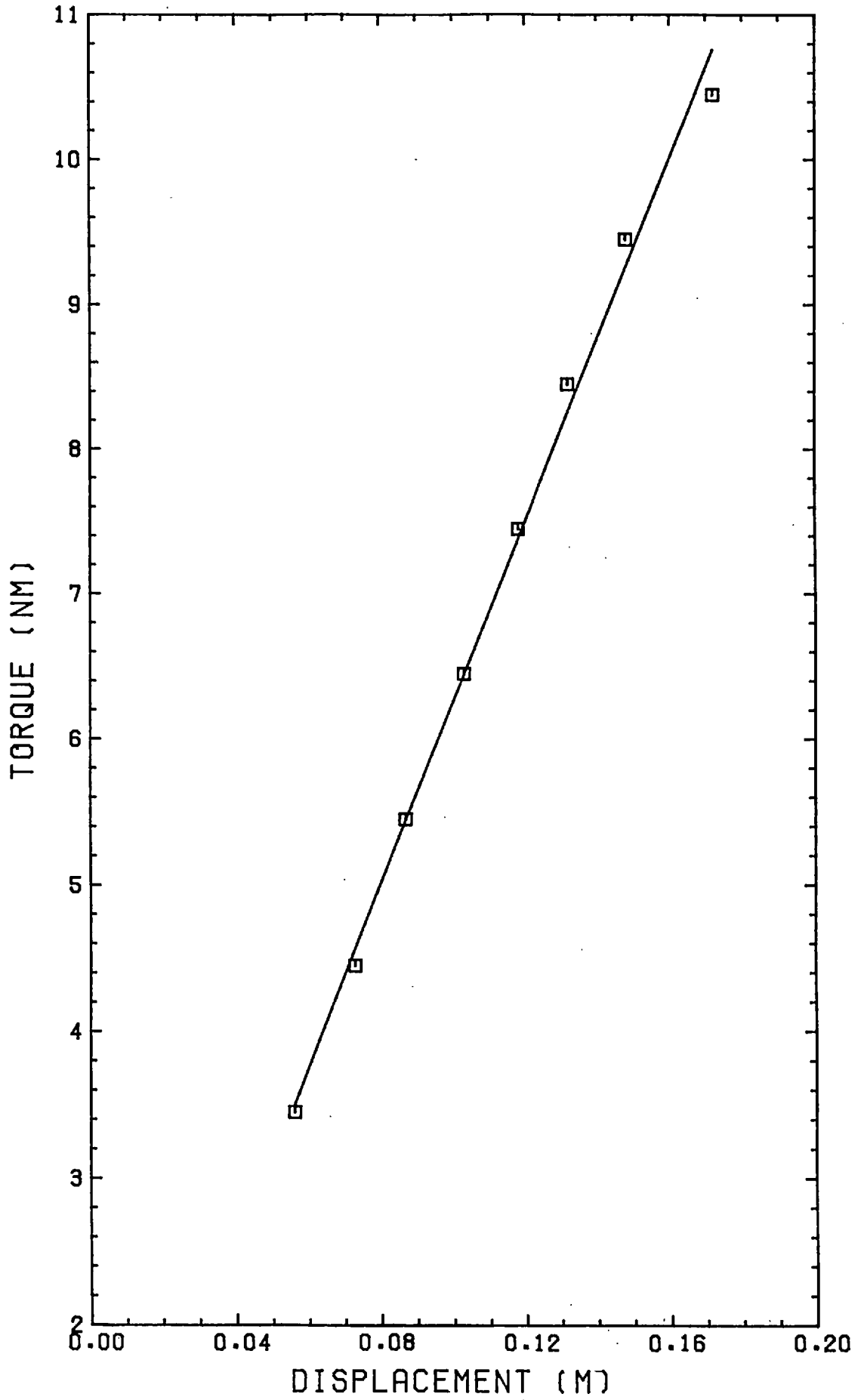
APPENDIX 5
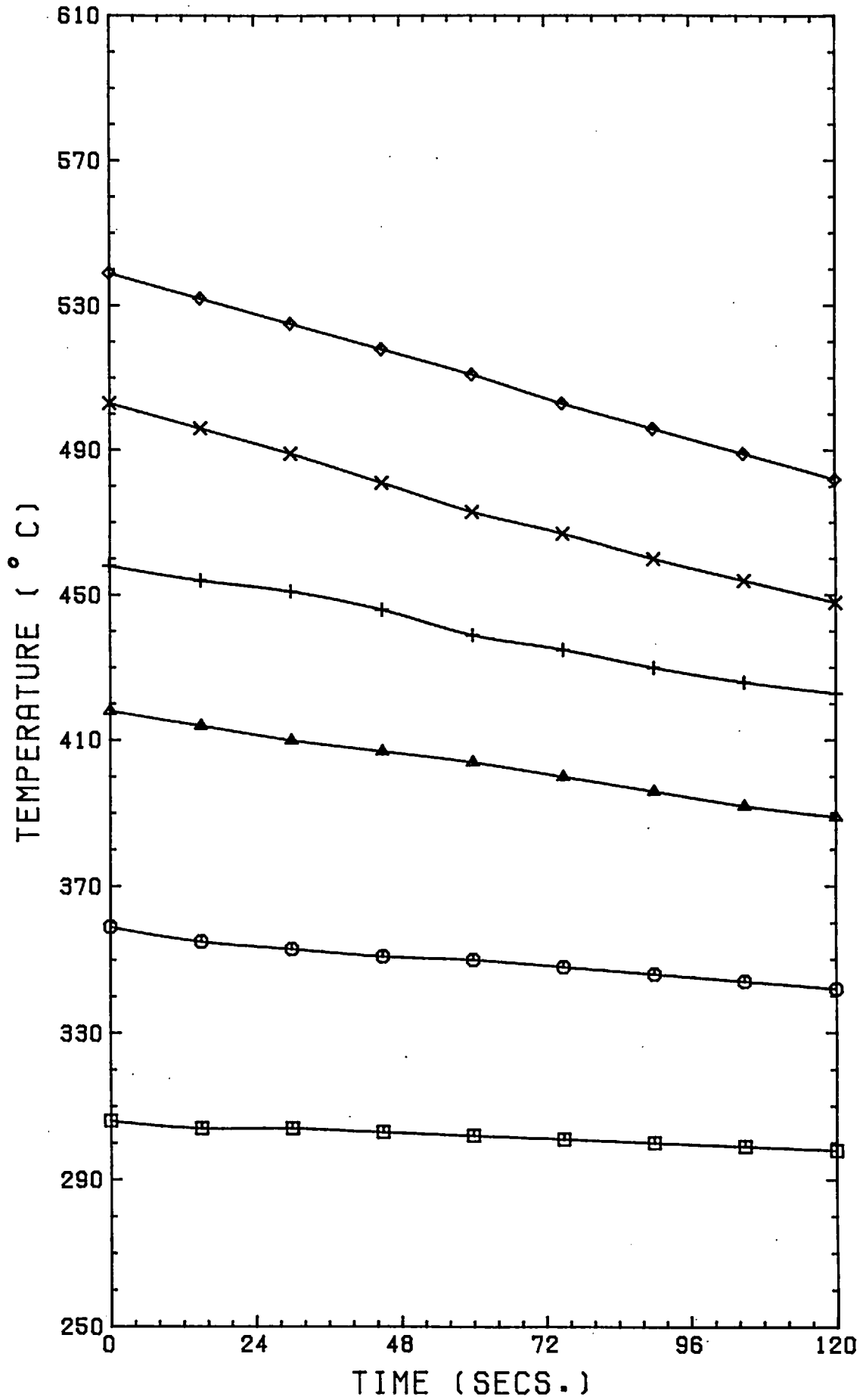
Billet cooling curves

Torsion machining calibration curve

APPENDIX 7

ERRORS

In the present investigation, during each series
of tests, certain runs were duplicated to discover the
reproducibility of the results. Listed in the table
below are the percentage reproducibility errors for
the parameters of major importance. (Each figure is
the result of at least five pairs of duplicated runs).

% Reproducibility Error	Parameter
8%	Extrusion load
4%	Extrusion ram speed
4%	Tensile strength (R.T.)
7%	Tensile strength (400°C)
8%	Elongation (R.T.)
10%	Elongation (400°C)

The accuracy of the integral profile technique used
to predict the deformation zone temperature during
extrusion is rather uncertain. Experimental verification
of the predictions presents tremendous difficulties.
Extrusion of compacted powder billets containing thermo-
couples is almost impossible. Raybould and Sheppard
who developed the integral profile technique for extrusion,
carried out some aluminium extrusions using thermocouples
to monitor the die surface and dead metal zone temperatures.
They found that the disagreement between experimentally
measured temperatures and theoretically predicted tem-
peratures was usually less than 10°C (for R = 30:1 and
50:1 and ram speeds varying from 0.0005 m/s to 0.1 m/s).
The maximum variation was 20°C obtained using medium ram
speeds at R = 30:1. Raybould and Sheppard   also
compared experimental results obtained by Singer and

Al-Samarrai for R = 12:1 with integral profile pre-
dictions. Once again the error was usually of the
order of 10-15°C. It should be remembered that these
experiments involved extrusions in which the initial
billet temperature and the container temperature were
the same. In the present series of experiments this
was usually not the case. However, the theory was
modified to allow for this initial temperature difference.
In general the disagreement between the theoretically
predicted temperature and the actual temperature should
certainly not exceed 20°C which represents a 5% error
in a 450°C extrusion.

APPENDIX 8

RECOMMENDATIONS FOR FURTHER WORK

The present investigation has dealt with the extrusion of aluminium, Al–Mg and Al–Mg–Si atomized powders containing various amounts of B_2O_3 – 10% SiO_2 glass. Although these systems have been dealt with in some detail in the present series of experiments several major research topics, touched on by this project, have still to be investigated in a completely satisfactory manner. These include:-

1) The temperature rise during extrusion

2) The operating mechanism which produces the peak in the extrusion load–ram displacement curve.

3) A detailed, scientific investigation of extrusion defects and their causes.

4) Other types of glasses which might be used to fibre–reinforce metal matrices.

5) The use of other materials, such as metal wires, in the reinforcement of metal matrices.

1)   The importance of knowing the deformation temperature accurately is obvious as this parameter controls, to a large extent, the product structure and properties. A more satisfactory model for predicting temperature rise during extrusion might be produced by using a finite element technique or by modifying the minimised axisymmetric upper bound solution used in this project. These methods are feasible only if excellent computing facilities are available.

2)   The magnitude of the peak in the extrusion load curve determines the press capacity required for a particular process. Thus the smaller the peak, the more efficient the process. In order to minimise this peak a thorough

knowledge of the factors believed to cause it (i.e. die-quenching friction effects, dislocation dynamics) must be obtained.

3) In the past, the production of an extrude possessing a good surface finish has usually been more of an art than a science. The exact effect on surface finish of varying parameters such as billet temperature, container temperature, ram speed and lubrication conditions must be investigated. The exact operating mechanisms which produce hot and cold shortness, surface checking etc. must be understood.

4) One of the main reasons for choosing the B_2O_3 - 10% SiO_2 glass for this project was the low softening temperature of this glass (< 300°C). The glass requirements i.e. acceptable chemical and mechanical properties and low softening temperature, limit the choice to some B_2O_3 based glass. If the SiO_2 content were increased the strength of the glass would increase and although the softening temperature would also increase, extrusion in aluminium should still be possible. Therefore further work involving B_2O_3-SiO_2 glasses containing more than 10% SiO_2 might be useful.

It might also prove possible to incorporate other strong, chemically stable glasses with higher softening temperatures in metals with higher melting points than aluminium. For example silica softens in the temperature range 1500-1600 $^\circ$C. Additions of boric acid would reduce this softening point to a temperature suitable for the extrusion of iron powder. The properties of silica reinforced iron might prove very interesting.

5) In the past a considerable amount of research involving the use of metal wires to reinforce metal matrices has been carried out. Very often this work has involved steel wires in aluminium. The wires have

usually been aligned individually and then incorporated in a metal powder compact or alternatively vacuum infiltrated with molten matrix metal. Extrusion at fairly low ratios has sometimes been used to consolidate the product and improve the fibre alignment. However, the present research project has demonstrated that powder extrusion at high ratios in fact serves three purposes, namely:-

1) Consolidation of product
2) Fibre formation
3) Fibre alignment

This powder extrusion process also has the advantages of speed and simplicity. Therefore, it might be worth re-examining some metal-metal systems composites of which were originally produced by the tedious methods mentioned in the previous paragraph. Ideally, a strong, stiff metal in powder form would be mixed with a weaker ductile, (hopefully cheaper) metal powder, the two metals having a similar range of hot working temperatures. The table below shows the relevant properties of some of the more likely metals.

Four systems which look promising in view of the tabulated data are:

1) Copper reinforced with Beryllium to increase the tensile strength and "stiffness" and to decrease the specific gravity.

2) Copper reinforced with Nickel to increase the tensile strength and "stiffness".

3) Stainless steel reinforced with Beryllium, once again to increase the tensile strength and stiffness and to decrease the specific gravity.

4) Titanium reinforced with Nickel solely to
increase the "stiffness".

Material	U.T.S. (MN/M^2) $(x10^6)$	E (MN/M^2) (10^6)	Melting Point (^{O}C)	Specific Gravity
Austenitic Stainless steel (22%Cr, 22%Ni)	0.725	0.207	(1147)	7.8
β-Titanium	2.21	0.117	1677	4.6
Nickel	0.60	0.207	1453	8.9
Aluminium (99.9% pure)	0.06	0.069	660	2.8
Copper	0.41	0.124	1083	8.9
Molybendum	2.07	0.365	2610	10.3
Tungsten	2.90	0.345	3380	19.3
Beryllium	1.10	0.310	1284	1.8

NOMENCLATURE

A	Area
	Constant in flow stress equation
	Extrusion constant
A_B	Cross sectional area of ram
A_1, A_2, A_3	Constants in hot working theory
a	Radius of billet - radius of extrude
	Compaction constant
	Notch depth
B	Extrusion constant
B_i	Mobility of species i
b	Burgers vector
C	Compaction constant
	Heat capacity
C_s, C_{AL}	Heat capacities of steel and aluminium
C*	Degree of volume reduction
dC_i/dX	Concentration gradient
D	Deformation zone diameter
	Distance apart of obstacles
	Compact relative density
	Grain diameter
D_E	Extrude diameter
D_B	Billet diameter
d	Radius of extrude
	Width of obstacle
E_F	Elastic modulus of fibre
E_M	Elastic modulus of matrix
E_C	Elastic modulus of composite
$\dot{E}$	Rate of energy dissipation
G	Shear modulus
ΔH	Activation energy
J_i	Rate of self diffusion of species i
K	Shear flow stress
	Boltzman's constant

K_s	Shear flow stress
K_A	Athermal component of shear flow stress
K'	Compaction constant
K_{ij}	Shear flow stress at discontinuity ij
L	Extrusion load
L_{crit}	Critical fibre length
l_D	Height of control volume 1
l_T	Height of control volume 2
l_1	Length of die land
l	Dislocation length
M	Torque
m	Strain exponent
n	Strain rate exponent Constant in hot working theory
n_2	Constant in hot working theory
P	Extrusion pressure Compaction pressure Tensile load on fibre
Q	Heat flow
R	Extrusion ratio Universal gas constant Freezing rate
R_B	Billet radius
$r_{(\theta)}$	Radial distance from O_2
r	Fibre radius
S	Area of velocity discontinuity Distance from heat source
T	Temperature
T_M	Melting point temperature
T_B	Billet temperature
T_I	Billet-container interface temperature
T_S	Container temperature

ΔT	Temperature rise in deformation zone
ΔT_D	$T_I - T_s$
T'	Line tension
t	Time
U, U_O	Energy barriers (To dislocation motion)
u	Velocity
$u_{\overline{ij}}$	Velocity perpendicular to discontinuity ij
V	Ram speed Actual compact volume under pressure Activation volume
V_O	Initial apparent compact colume
V_F	Volume fraction of fibres
v	Velocity
$v_{\overline{ij}}$	Velocity discontinuity ij
v_M	Volume fraction of matrix
v_W	Volume fraction of whiskers
dw/dt	Rate of working
x	Depth of deformation zone
α	Angle in axisymmetric velocity field Constant in hot working theory
β	Angle between stream-line and radial line from O_2 Constant in hot working theory
γ	Angle in axisymmetric velocity field Surface energy per unit area
$\dot{\gamma}$	Shear strain rate
δ	Angle in axisymmetric velocity field
ε	Natural strain
ε_{ij}	Strain due to discontinuity ij
$\dot{\varepsilon}$	Natural strain rate
$\overline{\dot{\varepsilon}}$	Mean strain rate
$\dot{\varepsilon}_x$	Natural strain rate in x direction

ϕ	Angle in plane strain velocity field
	Inclination of fibres to stress axis
ρ	Density
	Radius of curvature of notch
$\theta*$	Averaging term
θ	Angle in axisymmetric velocity field
	Torsional twist
λ	Interfibre distance
	Interparticle spacing
ν_o	Frequency of jumps
σ	Flow stress
σ_c	U.T.S. of composite
σ_u	U.T.S. of matrix
σ_w	U.T.S. of whiskers
σ_F	U.T.S. of fibres
σ_m'	Tensile strength of matrix at fibre fracture strain
σ_A	Bulk applied stress
σ_Y	Local tensile stress perpendicular to notch
τ_s	Shear yield stress
τ_m	Shear stress in matrix
τ_i	Lattice friction stress
ω	Deformation zone semi-angle

N.B. on graphs only

C	Correlation coefficient
S	Standard error of estimate

REFERENCES

1) R.L. HEWITT et al.   Powder Met. (1974), 17, No. 33, 1

2) N.F. KUNIN and B.D. YURCHENKO,   Porosch Kovaya Met. (1963), 18, 3

3) K.E. EASTERLING and A.R. ROLEN,   Powder Met. (1973), 16, No. 31, 112

4) I. SHAPIRO and I.M. KOLTHOFF,   J. Phys. Colloid Chem. (1947), 51, 483

5) K. KONOPICKY,   Radex Rundschau (1948), 3, 141

6) R.L. HEWITT et al   Powder Met. (1973), 16, No. 31, 88

7) R.W. HECKEL,   Trans. Met. Soc. AIME, (1961), 221, 1001

8) K. KAWAKITA,   J. Japan Soc. Powder Met. (1963), 10, 236

9) M. STROMGREN et al   Powder Met. (1973), 16, No. 32, 155

10) F. WATKINS et al   Proc. Nat. Conf. Tech. Eng. Manufacture, Inst. Mech. Eng. (1958)

11) W. JOHNSON and A.G. MAMALIS,   17th M.T.D.R., McMillan and Co., London (1976) 539

12) C.R. SHAKESPEARE and D.A. OLIVER,   Powder Met. (1964), 7, 203

13) A.R. CASTLE and T. SHEPPARD,   Metals Tech. 1976

14) J. SEJOURNET   Rev. Met., (1956) 53, 897

15) W. ZIEGLER and K. SIEGERT,   Z. Metallkunde (1973), 63, 224

16) N.A. AEDUL   17th M.T.D.R., McMillan and Co., London (1976)

17) J.M. ALEXANDER and B. LENGYEL   Proc. Inst. Mech. Eng. (1965-66)

18) D. GREEN   J.I.M. (1972), 100, 295

19) P.J.M. CHARE   Ph.D. Thesis (1972), London University

20) J.M. LEES   Private Communication

21) T.T. VOLMER and M.G. JONES   Powder Met. (1977), 20 (no. 2) 78

22) J.J. DUNKELY and R.J. CAUSTON   Powder Met. Conference, Brighton, 1976

23) P.J.M. CHARE and T. SHEPPARD,   Powder Met. (1973), 16, 437

24) F.J. GURNEY et al   Powder Met. (1974), 17, No. 13, 46

25) W. JOHNSON and H. KUDO,   The Mechanics of Metal Extrusion (1962) Manchester University Press.

26) R. HILL,   J.I.S.I. (1948) 158, 177

27) W. JOHNSON,   J. Mech. Phys. Solids (1955), 3, 218

28) R. SOWERBY et al   Int. J. Mech Sci. (1968), 10, 231

29) L.C. DODEJA and W. JOHNSON,   J. Mech. Phys. Solids (1957), 5, 267

30) L.E. FARMER and P.L.B. OXLEY   J. Mech. Phys. Solids (1971), 19, 369

31) W. JOHNSON   Proc. Inst. Mech. Eng. (1959), 173, 61

32) T. SHEPPARD and D. RAYBOULD   J.I.M. (1973), 101, 73

33) E.G. THOMSEN et al   Plastic Deformation in Metal Processing (1965) McMillan and Co.

34) T. SHEPPARD and D. RAYBOULD   J.I.M. (1973), 101, 33

35) S. KOBAYASHI   Trans. Am. Soc. Mech. Engrs. (1964), 86B, 122

36) J. HALLING and L.A. MITCHELL   Int. J. Mech. Sci. (1965), 7, 277

37) J.F. ADIE and J.M. ALEXANDER   Int. J. Mech. Sci. (1967), 19, 349

38) P. FELTHAM,   Metal Treatment (1956), 23, 440

39) J.M. ALEXANDER   J.I.M., (1961-62), 90, 361

40) R.J. WILCOX and P.W. WHITTON   J.I.M. (1958-59), 87, 289.

41) T. CHANDRA and J.J. JONAS   Met. Trans. (1970), 1, 2079

42) T. CHANDRA and J.J. JONAS   Met. Trans. (1971), 2, 877

43) J.J. JONAS and T. CHANDRA   Metal Forming: Interrelation between theory and practice, Plenus press (New York)

44) R.J. TANNER and W. JOHNSON   Int. J. Mech. Sci. (1960), 1, 28

45) W. JOHNSON and H.KUDO   Int. J. Mech. Sci. (1960), 1, 175

46) A.R.E. SINGER and S.W.K. AL-SAMARRAI   J.I.M. (1960), 89, 225

47) R. AKERET   J.I.M. (1967), 95, 204

48) P. REYNOLDS,   J.I.M., (1966), 94, 379.

49) J.J. JONAS et al   I.S.I. Publication 108 (1968), 49

50) P.R. SWANN   Electron Microscopy and Strength of Crystals (1963), Interscience

51) H.P. STUWE   I.S.I. Publication 108 (1968), 1

52) A.F. CASTLE   Ph.D. Thesis (1974), London University

53) J.C. LI   Acta Met. (1963), 11, 563

54) H. HU   Trans. AIME (1962), 224, 131

55) J.J. JONAS et al   Met. Review (1969), 12, 130

56) D. NOBILI and R. DE MARIA,   J. Nucl. Mat. (1965), 1, 75

57) D. NOBILI et al   J. Mat. Sci. (1968), 3, 382

58) A. PLUMTREE and G. DEEP   Metals Tech. (1977), 4, (No. 1), 1

59) C.R. BARRET and W.D. NIX   Acta Met. (1965), 13, 1247

60) J. WEERTMAN   J.A.P. (1955), 26, 1213

61) J. WEERTMAN   J.A.P. (1957), 28. 362

62) D. MCLEAN   Rep. Prog. Phys. (1966), 29, 1

63) D. MCLEAN   Met. Rev. (1962), 7, 481

64) H.P. STUWE and B. ORTNER   Metal Science (1974), 8, 161

65) C. ZENER and J.H. HOLLOMAN   Trans. A.S.M. (1944), 33, 163

66) F. GAROFALO and J.H. HOLLOMAN   Trans. A.S.M. (1944), 33, 163

67) C. SELLARS and W.J. MCG.TEGART   Mem Sci. Rev. Met. (1963), 63, 731

68) W. WONG and J.J. JONAS   Trans. A.S.M.E. (1968), 242, 2271

69) J.W. MARTIN   Precipitation Hardening (1968), Pergamon Press

70) J.D. EMBURY and R.B. NICHOLSON   Acta Met. (1965), 13, 403

71) A. GUINIER and H. LAMBOT   Compt. Rend. (1948), 227, 74

72) G. THOMAS   J.I.M. (1961-62) 90, 57.

73) D.W. PASHLEY et al   J.I.M. (1966), 94, 41

74) J.C. BLADE et al   Metals Tech. (1967) 3

75) T.R.G. WILLIAMS   M.Sc. Thesis (1954), Cardiff University

76) I. KOVACS et al   Acta Met. (1972), 20, 975

77) M.H. JACOBS   Phil. Mag. (1972), 26, 1

78) J.P. LYLE   Metal Progress (1952), 62, (No. 6), 97

79) R.J. TOWNER   Metal Progress (1958), 73, (No. 5), 70

80) E. OROWAN   Symposium on Internal Stresses in Metals and Alloys (1948), Inst. Metals (London), 451

81) A. KELLY and R.B. NICHOLSON   Prog. Mat. Sci. (1963), 10, 149

82) G.S. ANSELL and F.V. LENEL   Acta Met. (1960), 8, 612

83) J.C. FISHER et al   Acta. Met. (1953), 1, 336

84) N. HANSEN   Acta Met. (1939), 17, 637

85) A.A. BAKER and D. CRATCHLEY   Applied Mat. Research, (1966), 5, 92

86) J.G. MORLEY   Int. Metals Review (1976), 21, 153

87) A. KELLY and G.J. DAVIES   Met. Review (1965), 10, 1

88) W.H. SUTTON and J. CHORNE   Met. Eng. Q (1963), 3, (1), 44

89) R.L. MEHAN and E. FEINGOLD   J. Materials (1967), 2, (2), 239

90) S.S. BRENNER   J.A.P. (1962) 33, 33

91) D. CRATCHLEY   Met. Rev. (1965), 10, 79

92) A.A. BAKER and D. CRATCHLEY   Applied Mat. Research, (1964), 3, 215

93) D. CRATCHLEY and A.A. BAKER   Metallurgia (1964), 69-70, 153

94) A.A. BAKER   J. Mat. Sci. (1968), 3, 412

95) J.G. MORLEY   Kirk-Othmer Encyclopedia of Chemical Technology (1971)
John Wiley and Sons (New York)

96) P.W. JACKSON and J.R. MARJORAM   J. Mat. Sci. (1970), 5, 9

97) A.A. BAKER   Mat. Sci. Eng. (1975), 17, 177

98) P.W. JACKSON et al   Fibre Sci. Tech. (1972), 5, 219

99) D.L. MCDANIELS et al   Metals Progress (1960), 78, (6), 118

100) D. CRATCHELY   Powder Met. (1963), 11, 59

101) A.A. BAKER   Applied Mat. Research (1966), 5, 143

102) J.D. HUNT and K.A. JACKSON   Trans. AIME (1966), 236, 843

103) E.R. THOMPSON and F.D. LEMKEY   Composite Materials (1974), Academic
Press (New York and London)

104) H.L. COX   Brit. J. App. Phy. (1952), 3, 72

105) A. NADAI ·   Theory of Flow and Fracture of Solids (1950)
McGraw-Hill Book Co Inc. (New York), p349

106) D.S. FIELDS Jr. and W.A. BACKOFEN   Proc. ASTM (1957), 57, 1259

107) J.J. JONAS and W.A. WONG   Trans. AIME (1968), 242, 2271

108) L.S. DARKEN   Trans. AIME (1948), 175, 184

109) A. SEEGER   Z. Metallkunde (1953), 44, 247

110) R. D'ANTONIO et al   Trans. AIME (1968), 242, 2295

111) J.D. LUBAHN and R.P. FELGAR   Plasticity and Creep of Metals (1961) Wiley

112) K. ASHCROFT and G.S. LAWSON   J.I.M. (1960-61), 89, 369

113) M. NEGM and R. DAVIES   Proc. 15th M.T.D.R. (1975), p637,
McMillan (London)

114) W.R.D. WILSON   Int. J. Mech. Sci. (1971), 13, 17

115) J.J. JONAS et al   Met. Review, (1969), 14, 1

116) C.E. PEARSON   The Extrusion of Metals (1944), Chapman and Hall (London)

117) J.M. ALEXANDER   Proc. I. Mech. Eng. (1959), 173, 85

118) W.A. WONG et al   J.I.M. (1967), 95, 129

119) J.C. BLADE et al   Metals Tech. (1976) 3

120) R. DAVIES and R.H.T. DIXON   Powder Met. (1971), 14, 207

121) O.C. ZIENKIEWICZ and P.N. GODBOLE   Int. J. Num. Methods Eng. (1974), 8, 3

122)   S. ELWAK. and A.S. EL-SABBAGH   Proc. 18th Int. M.T.D R. (1971)
                                         McMillan (London)

123)   T. SHEPPARD   Proc. 15th Int. M.T.D.R. (1974), McMillan (London)

124)   D.J. MARSH   Proc. 18th Int. M.T.D.R. (1977) McMillan (London)

125)   W. JOHNSON and P.B. MELLOR   Engineering Plasticity (1973),
                                      Van Nostrand Reinhold (London)

126)   P.E. GILL and W. MURRAY   Quasi-Newton Methods for Unconstrained Optimization
                                         (1972), J.I.M.A., 9, 91

127)   F.A. LOOTSHA   Numerical Methods for Non-Linear Optimization, (1972)
                         Academic Press (London)

128)   E.P. WOOD and T. SHEPPARD   Proc. 17th Int. M.T.D.R. (1967), McMillan
                                                              (London)

129)   B.S. 1976, (1952)

130)   R. HILL   J. Mech. and Phys. Solids (1963), 11, 357

131)   M. SELLARS and W.J. MCG.TEGART   Int. Met. Review (1972), 17, 1

132)   R.J. WILCOX and P.W. WHITTON   J.I.M. (1959-60), 88, 145
†
134)   J.F. ALDER and K.A. PHILLIPS   J.I.M. (1954), 83, 80

135)   P.J. CHARE and T. SHEPPARD   Powder Met. (1975), 18, 1

136)   T.H. CHILDS   Metals Tech. (1974), 1, 305

137)   G.S. ANSELL and H.S. KIM   Powder Met. (1962), 10, 61

138)   R. THOMPSON et al   Powder Met. (1976), 19, 181

139)   H. ORMEROD and W.J. MCG.TEGART   J.I.M., (1960-61), 89, 94

140)   F.J. HUMPHREYS   ACTA Met. (1977), 25, (No 11), 1323

141)   A.J. BRYANT   J.I.M. (1972), 100, 192

† 133) B. PARSONS, D.B. LAYCOCK and B.N. COLE   Proc. 8th Int. M.T.D.R. (1967)
                                                    Manchester 1003.

probably the inaccuracies arise because of insufficient experimental data in determining the stress/strain and stress/strain-rate relationships. The tests were all conducted at 400°C and other temperatures should be investigated using compression as well as torsion and tensile data to determine the relevant flow and shear stresses. Nevertheless the upper-bound based upon an actual deformation (or physical field) shows very good agreement with experimental observation.

CONCLUSIONS

1. The plane-strain analogue approach is not suitable for predicting powder compact pressure.

2. The minimized axisymmetric upper-bound theory predicts pressures with acceptable accuracy, provided the extrusion ratio is < 100.

3. The upper-bound solution based upon an observed physical field gives very good agreement with observed pressures.

4. The variation between theoretical and experimental curve slopes requires further experimental investigation.

REFERENCES

1. T. SHEPPARD and P. J. M. CHARE: *Powder Met.*, 1972, **15**, 17.
2. P. J. M. CHARE and T. SHEPPARD: *ibid.*, 1973, **16**, 437.
3. P. J. M. CHARE and T. SHEPPARD: *Int. J. Powder Met. & Powder Tech.*, 1974, **10**, 203.
4. T. SHEPPARD: Proc. 15th Int. MTDR, p. 659. 1975: London (Macmillan).
5. T. SHEPPARD: *Powder Technol.*, 1974, **10**, 257.
6. A. GREASLEY and T. SHEPPARD: Proc. 2nd Int. Conf. on Consolidation of Particulate Matter, Brighton, August 1975.
7. W. JOHNSON: *J. Mechanics and Physics Solids*, 1956, **4**, 269.
8. T. SHEPPARD and D. RAYBOULD: *J. Inst. Metals*, 1973, **101**, 33.
9. T SHEPPARD and H. McSHANE: *Powder Met.*, this issue, p. 126.
10. E. G. THOMSEN and T. JORDAN: Ref. 7, p. 184.

IRON AND STEEL ABSTRACT CARD AND PROFILE SHEET SERVICES OF THE METALS SOCIETY

Full abstracts of articles drawn from the world's iron and steel literature are available in the following forms:

ABTICS (Abstract and Book Title Index Card Service)

A weekly service for a year (January–December) in which cards are sent to subscribers containing full abstracts and book titles classified under the Universal Decimal Classification (UDC). Such cards form a simply operated filing system for which various aids are provided.

ISIP (Iron and Steel Industry Profiles)

A weekly service for a year (beginning any time, covering any subject, and charged *pro rata*) in which sheets are sent to subscribers arranged according to declared fields of subject interest and containing full abstracts, book titles, and translation references. Such profiles forming a current awareness service can be mailed (by air, when appropriate) direct to subscribers or in a batch to a company. An order form sent with the weekly profiles enables orders for loans, photocopies, and translations to be handled promptly.

Prices

Details of subscription rates and further information will be sent on request by Mr M. L. Pearl, The Metals Society, 1 Carlton House Terrace, London SW1Y 5DB.

Production of an aluminium-rich magnesium silicide alloy from atomized powder

T. Sheppard and H. McShane

The production of an aluminium-rich magnesium silicide alloy by extrusion from the powder phase is described. The pressure requirements of such a process are investigated and it is shown that the operation may be described as thermally activated. The strain-rate sensitivity is shown to be less than the equivalent cast and extruded material. The mechanical properties of the as-extruded product are far superior to those of the conventional alloy and the powder material is heat-treatable.

Until the advent of modern atomizing techniques the production of components from aluminium parts was hindered to a large extent by the cost of powders. Atomization has overcome this main obstacle, although in general the dispersion-hardening effect is not so pronounced because the Al_2O_3 content is reduced compared with the original SAP-type alloys. An additional obstacle to widespread use of these light alloys is that the oxide dispersion acts as a vacancy barrier during the sintering process, prolonging that operation. A convenient process which ensures that the powder compact forms a homogeneous 100% dense product is extrusion, which can be carried out at high or low temperature with large strains. It has been shown[1,2] that such a process eliminates the sintering operation and it is suggested that energy which is termed 'redundant' in the extrusion of cast ingots is utilized to assemble the powders into solid form. Powder compacts also have an advantage over the normal ingot because less pressure is required[3] to effect extrusion. This is due to the differing rheological nature of the quasi-static deformation zone.

The atomizing process has other advantages in addition to the dispersion-hardening effect of the oxide film which almost invariably develops as an envelope surrounding each particle. The particles are usually cooled at a rate far in excess of those found in the normal continuous casting of aluminium alloys. This rapid cooling gives a fine eutectic, due to nucleation at lower temperatures, and the size and nature of precipitates can be expected to differ. In a heat-treatable alloy the oxide film and the differing nature of the

precipitates may together be expected to alter the heat-treatment reaction. There appears to be no reported literature on this subject.

The Al–Mg–Si system, when aluminium-rich, is among the most widely used aluminium alloys, having architectural and structural applications. The object of the present work was to examine the rate-controlling deformation mechanism, the nature of product densification, the alloy structure, and the effect of oxide dispersions on the ageing process.

EXPERIMENTAL
Material
The air-atomized Al–Mg–Si (HE9) alloy powder, supplied by Borax Consolidated Limited, nominally contained 0·5 wt.-%Mg, 0·5 wt.-%Si, balance Al. Initially the powder particle size distribution was obtained using standard 200 mm BS sieves stacked on an Endrock mechanical shaker to sieve a standard weight of powder (175 g) for a specified time (1 h). The results are shown in Table I.

Samples of the powder were analysed by the Imperial College Analytical Services Laboratory. The chemical composition is given in Table II.
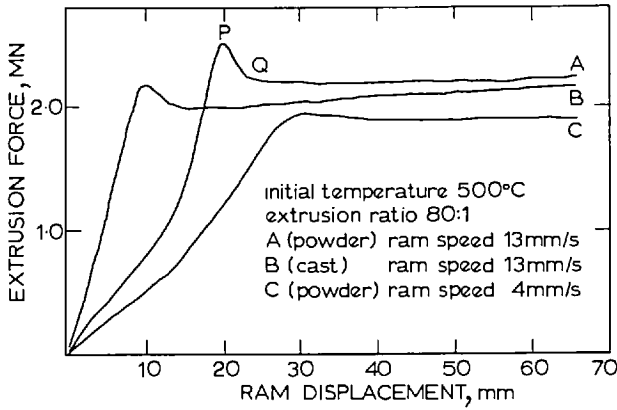
Preparation for extrusion
To facilitate handling at the press, the powder was compacted into billets using a 150 ton Tangye hydraulic press. To ensure easy removal of the billets from the die the tool surfaces were cleaned and painted with a stearic acid–chloroform lubricant before each compaction.

Table I   Size distribution of Al–Mg–Si alloy powder

Particle size, μm	Weight percent
+355	2·14
−355+180	30·77
−180+106	25·73
−106+90	5·39
−90+75	5·20
−75+63	5·65
−63+53	5·15
−53	19·72

Table II   Chemical analysis of powder (remainder Al) (wt.-%)

O	Mg	Si	Cr	Cu	Fe	Mn	Ti	Zn	Ni
0·062	0·33	0·12	0·01	0·014	0·15	0·10	0·014	0·025	0·004

1 Load displacement diagrams.

Extrusion

Extrusion was performed on an Enefco 5 MN hydraulic extrusion press having a container bore of 76 mm nom. dia. The container was maintained at 300°C for all extrusions. Details of the equipment and instrumentation have been previously reported.[1] Square-edged dies with reduction ratios of 5, 10, 30, 40, 60, 80, and 180 were used. To ensure an adequate surface finish a 10 mm thick pad of solid HE9 material was placed in front of each billet before extrusion. The billets were heated in an air circulating furnace situated adjacent to the extrusion press. The preheat temperature varied between 250 and 540°C. The billet transfer time between furnace and container varied from 10 to 15 s. This necessitated a correction of the temperature at the beginning of extrusion from predetermined cooling curves.

Preparation of specimens for mechanical testing and microscopy

The specimens were cut from the same region in each extrusion to allow for the variation in structure and properties along the extrusion length.

The electron microscope foils were prepared by grinding on water-lubricated silicon carbide paper to a thickness of ~0·15 mm, followed by thinning using a standard window technique. The electropolishing was carried out in a solution of 30% nitric acid in methanol under a potential difference of 15 V and at a temperature of −30°C. The transmission microscopy was carried out on an AEI EM6G 100 kV electron microscope.

Standard Hounsfield No. 12 specimens were machined for tensile tests performed at room temperature and at various temperatures up to 400°C. The tensile tests were performed on an Instron tensile testing machine fitted with a split furnace for the higher temperature tests.

Impact tests on notched specimens were carried out using a Hounsfield balanced impact machine. The notch cross-section, method of supporting the specimen, and direction of delivery of the blow were the same as in the standard Izod impact test, but specimen size and shape were different (8 mm dia. bar 44·5 mm long, compared with 10 mm square bar 75 mm long for an Izod specimen). The energy reading given by this machine was multiplied by a factor of 2·4 in order to obtain the corresponding Izod value.

RESULTS AND DISCUSSION

Extrusion

The load-displacement curves for two powder billets and a solid billet of the same alloy composition (excluding Al₂O₃) are shown in Fig. 1. The curves differ significantly in the
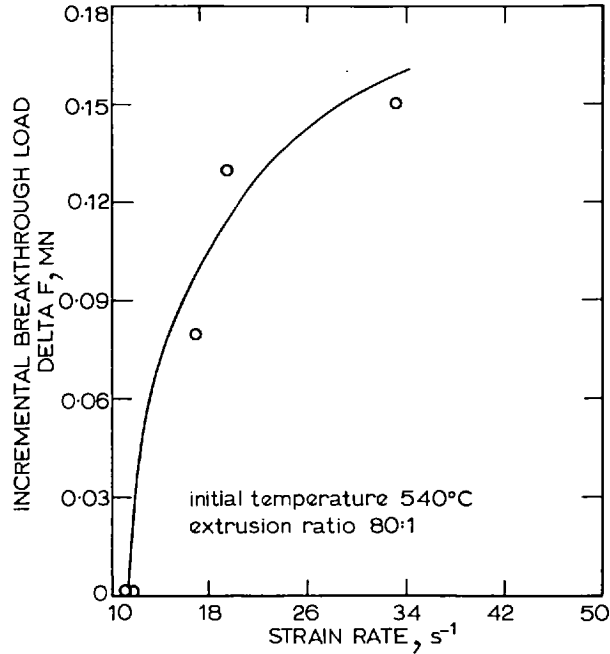
2 Incremental breakthrough load as function of strain rate.

initial stages of the process (i.e., while the quasi-static deformation zone is being established). The cast billet depicts the normal linear upset forging zone before the peak load is reached, whereas the powder billet shows a non-linear compaction zone which has been shown[1] to correspond to the compact obtaining 100% density. It should be clearly understood that the attainment of theoretical density does not coincide with attainment of optimum properties. In fact, at this stage, the billet is brittle and has practically no resistance to shear. The massive literature on the forging of metal powders[4] supports the thesis[1] that, since deviatoric deformation is a prerequisite for the achievement of acceptable properties, the extruding compact cannot obtain optimum properties until it has completely traversed the deformation zone.

The existence of a peak (denoted by PQ in Fig. 1) in one of the powder billets is contrary to evidence reported on the extrusion of nickel-rich alloys.[5] This breakthrough pressure
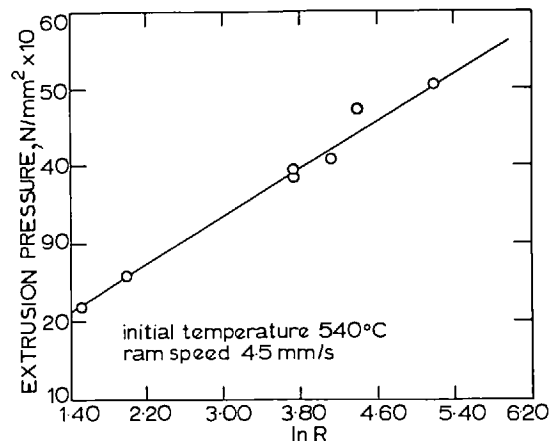
3 Extrusion pressure as function of extrusion ratio.

Nomenclature

A	hot working constant
A_1, A_2	constants in extrusion equation
A_3, A_4	constants in stress/strain-rate equations
C	load constant for cast billet
C_3	load constant for powder billet
$C_1(t), C_2(t)$	time-dependent constants in temperature calculation
D_B	diameter of billet
D_E	diameter of extrudate
G	gas constant
ΔH	activation energy for deformation process
L_E	load
n, n_1	stress/strain-rate exponents
p	extrusion pressure
R	extrusion ratio
T	temperature
t	time
ΔT_D	temperature differential between product and tools
U_o	energy barrier
V	ram speed
V_1	activation volume
Z	Zener–Holloman parameter
α, β	constants in stress/strain relationship
$\dot{\epsilon}$	strain rate
$\dot{\epsilon}_o$	constant in Seeger analysis
σ_A	thermal component of flow stress
σ	flow stress
ω	90° dead metal zone angle

can clearly be seen to be more than that necessary to overcome friction between the compact and the extrusion container and has been attributed to temperature quenching at the die/billet interface.[6] In the present series of experiments billets extruded at the same temperature as the tools exhibited such peaks, so that this explanation is also quite clearly in error. Castle and Sheppard[7] have presented an explanation based on dislocation dynamics but for cast billets their experimental evidence is that the strain-rate has no effect. Fig. 1 suggests that this is not so for the compacts extruded, since the billet extruded at a lower strain-rate shows no peak to occur. However, the maximum load is also lower in this experiment and existing evidence does suggest that there is a threshold load value below which these pressure peaks either do not occur or cannot be detected.

The evidence, then, would support the view that this phenomenon is connected with a dynamic process. At high strain rates an excess of dislocations is generated immediately after the compaction phase and before dynamic softening processes (e.g. recovery) commence to operate; while at lower strain rates the rate of dislocation production is never large enough to overcome the dynamic softening process. The same argument could be applied to those extrusions in which the maximum pressure is low. Fig. 2 shows supporting evidence that the difference between this peak pressure and the steady-state pressure increases with increasing strain rate (calculated using the Feltham equation as shown below). It should be recalled, however, that increasing the strain rate will increase the temperature rise obtaining as well as increasing the flow stress in the absence of temperature rise. Hence the pressure required may be greater or lower depending upon the balance of these variables.

Fig. 3 shows that the usual relationship is found between the steady-state pressure required for extrusion and the logarithm of the extrusion ratio. For this alloy at 540°C the relationship may be written:

$$p = 103\cdot4 + 76\cdot2 \ln R \quad\ldots\ldots\ldots\ldots\ldots (1)$$

whereas for cast billets the usual form of this equation[8] is

$$\frac{p}{\sigma} = 0\cdot52 + 1\cdot32 \ln R \quad\ldots\ldots\ldots\ldots\ldots (2)$$

For comparative purposes it is convenient to write eqns. (1) and (2) in the form:

$$\frac{p}{A_1\sigma} = 1\cdot357 + \ln R \qquad \text{for a powder compact} \quad\ldots (3)$$

and

$$\frac{p}{A_2\sigma} = 0\cdot393 + \ln R \qquad \text{for a cast billet.}\quad\ldots\ldots (4)$$

The significant feature here is the relative magnitude of the constant on the right-hand side of these equations since this is generally recognized to be a measure of the so-called 'redundant' work (i.e., work not directly contributing to a shape change). It has been shown[9] that theoretically the energy required for homogeneous deformation will be lower for a powder compact and these equations tend to substantiate this. They also indicate that the redundant portion of the total energy is very large, being 27% at an extrusion ratio of 40:1 compared with only 10% for a cast billet. This is again consistent with the concept of 'building' the alloy as it traverses the deformation zone; weld necks being continuously broken and rewelded until the compact as a whole can withstand the applied deviatoric stresses. Thus the actual construction of the alloy (normally achieved by sintering) is performed by the portion of the extrusion pressure normally termed redundant—clearly a misnomer for powder extrusion processes.

The steady-state extrusion pressure is shown plotted against temperature in Fig. 4. The graph, for an extrusion ratio of 40:1, is linear and suggests that the effective flow stress is directly related to the extrusion temperature. Calculation of the extrusion pressure and comparison of experimental and theoretical results are dealt with in a companion paper.[9]
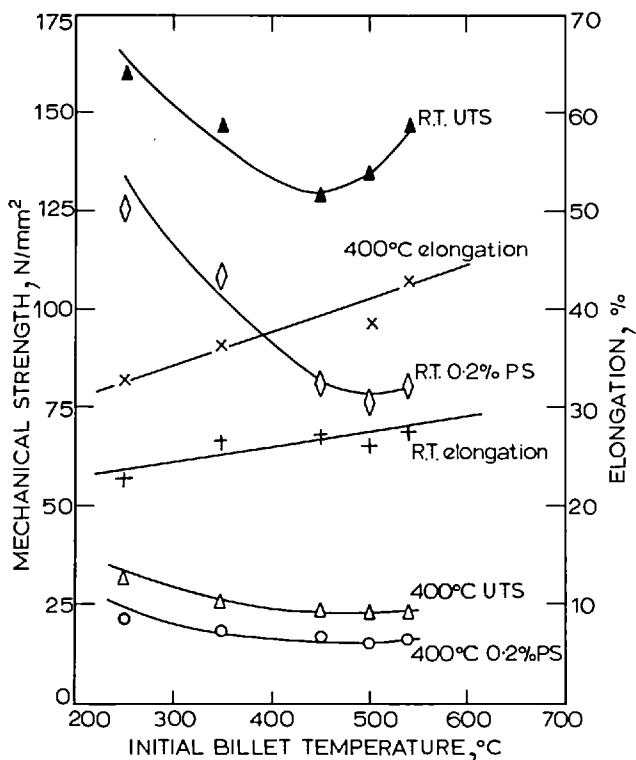
Mechanical properties of the extrudate

The variation of mechanical properties with initial billet temperature is shown in Fig. 5. The room-temperature proof and ultimate stresses show the expected decrease in value with increasing initial billet temperature (in the range 250–480°C) which is clearly due to softening, probably by dynamic recovery. However, from 480 to 540°C the trend is reversed: the material becomes stronger and elongations continue to improve. This is probably because, at the higher temperatures, a limited amount of magnesium silicide (Mg₂Si) will be taken into solution and on subsequent air cooling after extrusion a supersaturated solution with a non-equilibrium vacancy concentration will result. It could also be caused by a natural ageing process which occurs at room temperature[10] over a period of weeks and in the cast alloy is due to a fine precipitate of Mg₂Si. Further study on the transmission electron microscope would be required to verify this point. The room-temperature proof stress varies from 125–75 N/mm² over the temperature range investigated, which compares with an as-extruded strength of 50–55 N/mm² for the normal cast alloy. In fact this strength
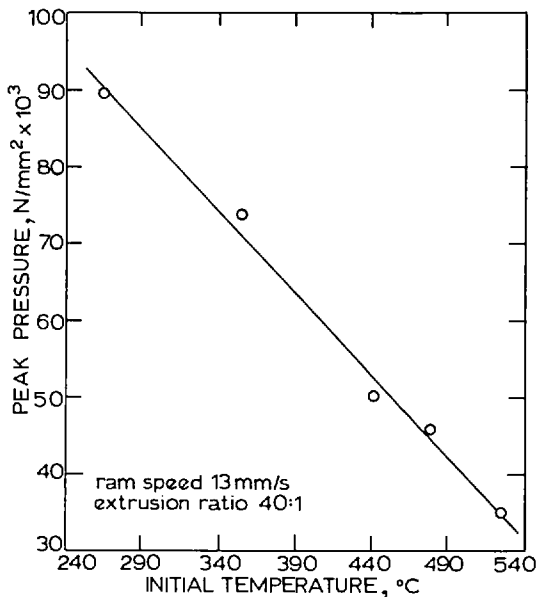
4 Extrusion pressure as function of initial billet temperature.

compares well with the strength of the heat-treated alloy, quoted as 130–160 N/mm^2. The elongation varies from 20 to 25%, which is remarkable since the normal as-extruded product is assigned a value of 12% for this property as-extruded and only 7% in the heat-treated condition.

The 400°C properties, determined primarily to estimate the product flow stress for insertion into the load model, show a small decrease with increasing billet temperature.

5 Variation of mechanical properties with initial billet temperature.
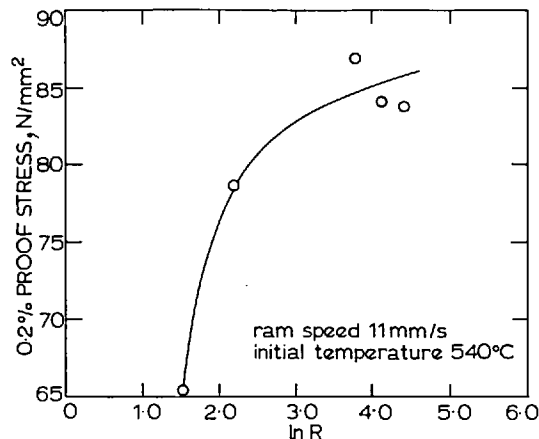
6 Variation of proof stress with extrusion ratio.

This indicates that at the higher test temperature the form and distribution of precipitate have little effect on resistance to deformation. The alloy is clearly not suitable for high-temperature application, its properties being greatly inferior to those reported previously for commercially pure atomized powders.[1]

Fig. 6 shows the relationship between mechanical properties and extrusion ratio at an initial extrusion temperature of 540°C. This figure does not show optimum values since these are obtained according to Fig. 5 at ~250°C. Nevertheless, the extrusion ratio does affect mechanical properties and the maximum proof stress (86 N/mm^2) is considerably higher than that for the normal alloy.

The significant effect of the temperature on the proof stress values is shown in Fig. 7 which is of the same form as that predicted by Seeger's[11] analysis. Thus the governing equation may be written:

$$\sigma = \sigma_A + \frac{[U_0 - GT \ln(\dot{\epsilon}_0/\dot{\epsilon})]}{V_1} \qquad \ldots \ldots \ldots (5)$$

which can be regarded as consisting of: a thermally activated component (the second term) due to short-range obstacles such as forest dislocations, solute atoms, and lattice friction effects; and an athermal component, σ_A, due to long-range
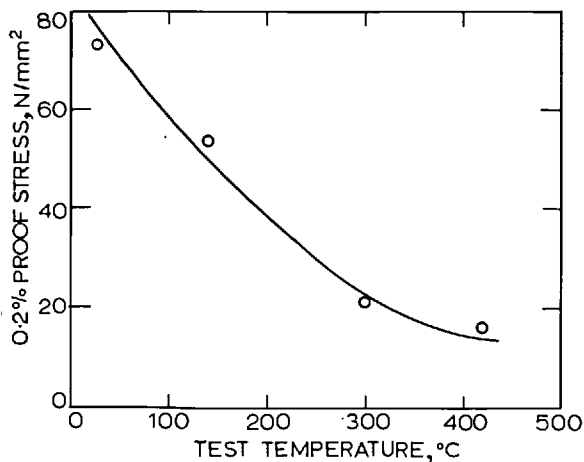
7 Flow stress as function of temperature.

billet temperature 450°C
extrusion ratio 80:1
ram speed 12·5mm/s
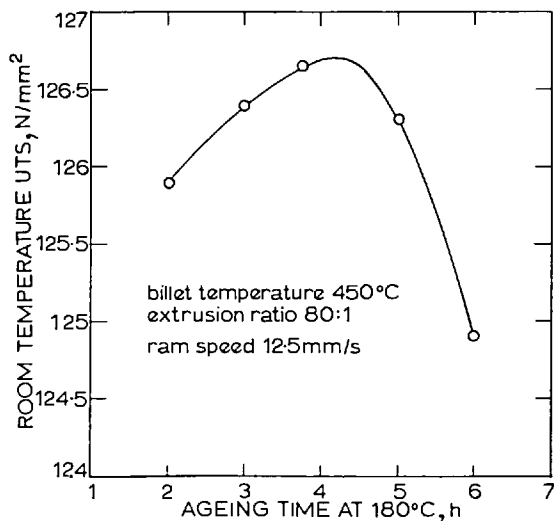
8 Effect of ageing time on strength of press-quenched extrudate.

obstacles such as large precipitates, oxide dispersions, etc. Thus for powder material we would expect σ_A to be larger, and Fig. 7 gives a value of 15 compared with 7–8 N/mm² for the normal alloy.

The material exhibited no correlation between extrusion process parameters and notch ductility (Izod) values. However, the results from some 20 tests showed little scatter and gave an impact value of 42·17 N m (31·13 lbf ft) which is almost identical to that reported for cast and wrought material (31 lbf ft nominal).

Heat-treatment studies

The alloy investigated is the most widely used precipitation-hardening alloy and is usually subjected to one of three differing heat-treatments designated—

TB: solution heat-treated only, involving soaking at 500–560°C, and quenched.

TE: solution heat-treated, quenched, cold-worked, and naturally aged.

TF: solution heat-treated, quenched, and subsequently precipitation-treated for several hours (depending on geometry) at ∼180–200°C.

A transformation of the type: *needle-shaped zones → rods → platelets of equilibrium Mg₂Si* occurs with increasing ageing time.

Typical properties for the cast and wrought alloy for the differing heat treatments are given in Table III.

The most common treatment in industrial usage is in fact a compromise. The product is press-quenched (i.e., the heating and extrusion of the billet replaces the solution treatment) and subsequently aged. A homogenization treatment before extrusion serves to organize the precipitate

so that it is taken into solution during the extrusion cycle and this also ensures that minimum die pick-up occurs during the process. When this procedure was applied to the extruded powder material a weakening of the product occurred (see Fig. 8). This is almost certainly due to the omission of the usual homogenization treatment before extrusion, preventing dissolution of the silicide precipitate. The Al_2O_3 layer surrounding each particle will of course also hinder this dissolution. Thus only a small volume fraction of Mg₂Si precipitate is available for strengthening and Fig. 8 indicates that this grows to optimum size during the initial four hours of treatment. Longer treatment involves further precipitate growth and the total variation in strength is an indication of the low level of activity during the process. The weakening effect occurs because the overall precipitate strengthening is less than the softening effect due to static recovery. It may be possible to overcome this effect by compacting to higher densities (thus, it is hoped, breaking up the Al_2O_3 layer) and carrying out a pre-extrusion solution soak, but it is doubtful whether sufficient disintegration of the oxide layer would occur. Even if such action succeeded it would still be difficult to prevent reoxidation during heat-treatment. Nevertheless this line of approach is at present being pursued.

The product was also subjected to a TF-type heat-treatment involving solution soak, quench, and age. Fig. 9 indicates that substantial strengthening occurs, the properties roughly corresponding to the normal alloy TE treatment but with much better elongation properties (from 15 to 20%). Clearly the oxide barriers have been completely broken by the massive shearing in the deformation zone during extrusion and dissolution of the silicide can now occur during the solution treatment. On subsequent ageing there is sufficient volume of precipitate to cause a substantial increase in strength. The magnitude of the elongation figures suggests that optimum properties have not yet been attained and work continues on varying soaking and ageing times.

Table III Properties of Alloy 50S

Condition	Proof stress, N/mm²	Ultimate stress, N/mm²	Elongation, %
TB	70	120	13
TE	110	150	7–8
TF	130–160	150–185	6–8
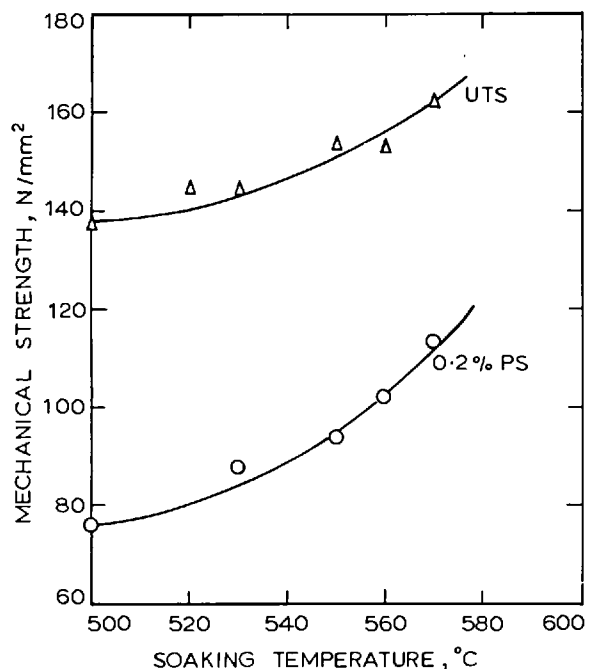
9 Effect of soaking temperature on strength of 3-stage heat-treated extrudate.
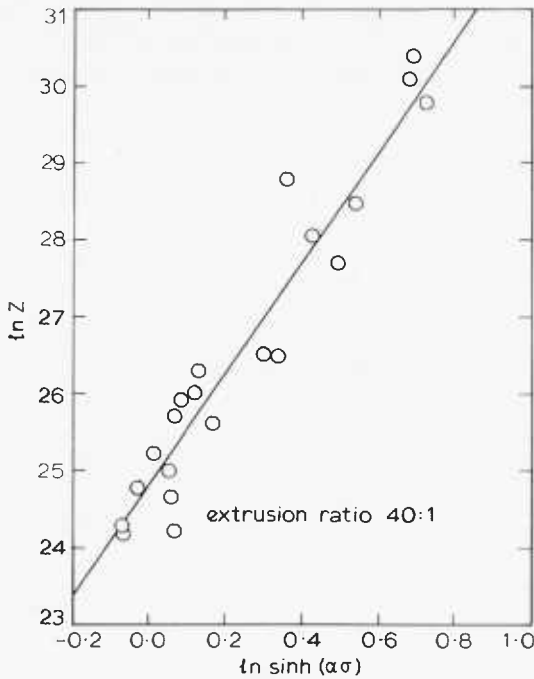
10 Variation of ln Z with **ln sinh** $(\alpha\sigma)$.

Thermal activation

It has been shown previously[12] that the extrusion of light-alloy metal powders is a thermally activated process governed by the general Zener–Holloman equation:

$$Z = \dot{\epsilon} \exp \frac{\Delta H}{GT} = A (\sinh \alpha\sigma)^n \quad \ldots \ldots \ldots (6)$$

It is generally recognized that the applicability of this equation signifies the mechanism by which metals deform and thus it was of interest to examine the behaviour of the alloy according to this thesis.

Since flow stress, strain rate, and temperature are interconnected in a complex manner it is difficult to evaluate the parameters in the above Zener–Holloman equation. The Z value obviously is not constant in the deformation zone since the strain rate, temperature rise, and flow stress all vary incrementally. Since it is difficult to simplify the problem it is general practice to insert average values into the equation. It is remarkable that excellent results can usually be achieved in this way. Thus the strain rate was calculated using a modified version of Feltham's formula:

$$\dot{\epsilon} = \frac{6CV(\tan \omega)D_B^2}{D_B^3 - D_E^3} \quad \ldots \ldots \ldots (7)$$

and the temperature at the end of extrusion by the integral profile method[8] as modified by Sheppard and Wood,[13] giving:

$$\Delta T = \frac{0.9 L_E V t - T_D C_1(t)}{C_2(t)} \quad \ldots \ldots \ldots (8)$$

The average flow stress was calculated using the minimized upper bound method described in the companion paper[9] but assuming a linear flow-stress variation throughout the quasi-static deformation zone such that it is possible to write:

$$p = C_3 \sigma_{\text{exit}} \quad \ldots \ldots \ldots (9)$$

The flow stress, σ, may then be calculated by noting the relationship between C and C_3.

The constant, α, then becomes the remaining unknown. This may be found approximately by noting that at constant temperature and low stresses the relationship between strain rate and stress may be written $\dot{\epsilon} = A_3 \sigma^{n_1}$ and at high stress $\dot{\epsilon} = A_4 \exp \beta\sigma$ in which A_3 and A_4 are temperature-dependent. The value of α is then given by the magnitude of β/n_1. From data plotted in such a manner the value of α was found to be ~ 0.02. Regression analysis to give a best fit when investigating α between 0.015 and 0.025 gave an α value of 0.022. The value of ΔH is extremely difficult to calculate since it requires extrusion data at constant strain-rate and constant temperature. The interdependence of these two variables has already been noted. However, previous work has indicated a value of 150 000 J/mol which is in agreement with most published literature. This value was adopted since if it were radically in error good correlation with eqn. (6) could not be expected. Fig. 10 shows the result of this exercise giving a slope $n = 7.2849$ and constant $A = 5.988 \times 10^{10}$ and hence eqn. (6) becomes

$$Z = 5.988 \times 10^{10} (\sinh 0.022 \alpha\sigma)^{7.2849} \quad \ldots \ldots (10)$$

The nominal stress-exponent value found for cast and extruded material varies between 4 and 5 and hence it is clear that the powder material is much less strain-rate sensitive. This observation may be explained by the model proposed[1] for the deformation mode during extrusion, in
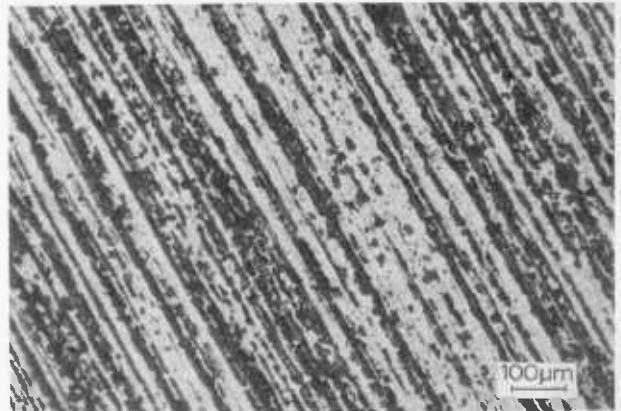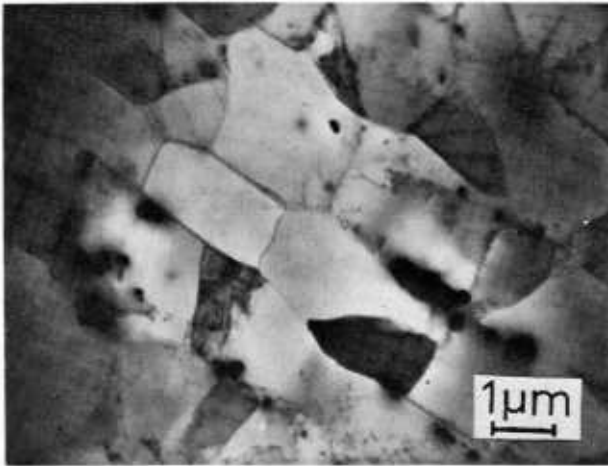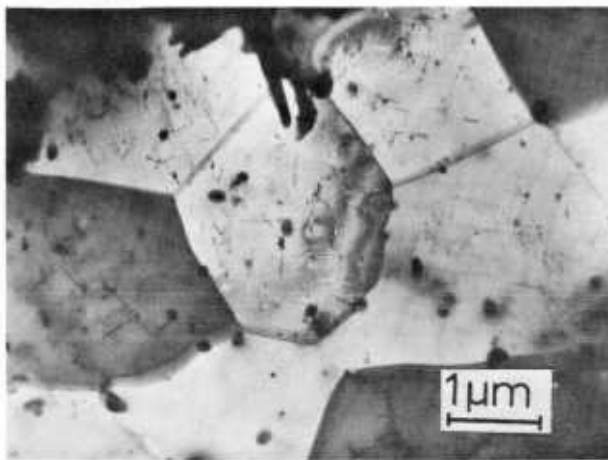

11(a)
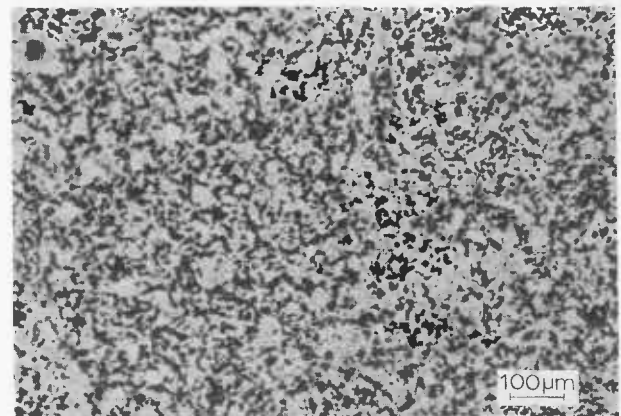
11(b)

Extrusion ratio = 80:1   Initial temperature = 450°C   Ram speed = 3.5 mm/s.
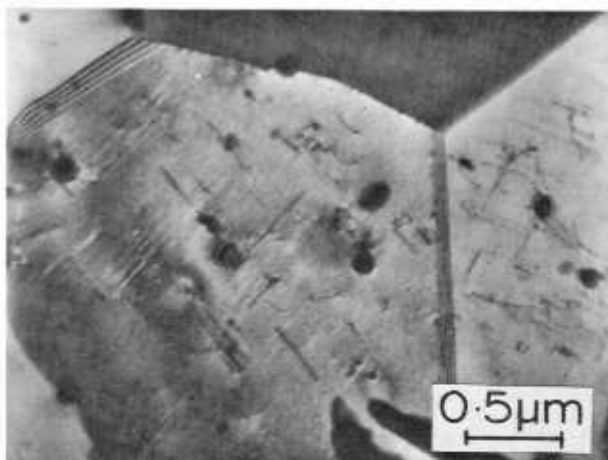
11 Optical micrographs of extruded product: (a) longitudinal; (b) transverse.

12(a)

12(b)

12(c)

Extrusion ratio = 40 : 1   Initial temperature = 250°C   Ram
speed = 4·5 mm/s.

12 Transmission electron micrographs of extruded product:
(a) longitudinal; (b) and (c) transverse.

which the material is gradually built by a welding and shearing mechanism, achieving final properties as it passes the final exit discontinuity. It also implies that, provided satisfactory surface finishes can be achieved, it should be possible to obtain higher productivity using powder material than when utilizing conventionally cast billets. The strain-rate sensitivity is, however, higher than that reported previously for powder material and this would almost certainly be due to the more refined temperature calculations used in this work. The value of A, which is termed an alloy factor, is almost identical to that reported[13] for super-purity aluminium $(5 \cdot 62 \times 10^{10})$. This is somewhat surprising because evidence[7] suggests that alloy additions should decrease the value of A. Thus the oxide content would be expected to reduce considerably the value of this constant. Nevertheless the order of magnitude is quite clearly correct.

Extrudate structure
Examined under the optical microscope, the product exhibited a fibrous cold-worked structure as shown in Fig. 11(a). The original powder particles can be seen to have been elongated in the direction of extrusion and measurements revealed that the elongation was approximately proportional to the extrusion ratio. This cold-worked microstructure was produced in extrusion performed above the recrystallization temperature of the alloy and the transverse microstructure (Fig. 11(b)) confirms the equiaxed nature of the structure. It was not possible to detect any deviation from this type of structure over the whole range of extrusions investigated, confirming that a substructure must be present and supporting the thermal activation evidence that dynamic recovery is the prevailing deformation mechanism.

Fig. 12 shows typical microstructures observed under the transmission electron microscope. The discontinuous nature of the original oxide film is evident in Fig. 12(a) and original particle boundaries may still be detected and identified by the drawn-out debris of this original oxide. The apparent presence of oxide in the centre of grains is attributed to the orientation selected during the thinning operation, such oxide being the remains of that surrounding a neighbouring grain. The sub-grains are quite clearly elongated, indicating their formation in the deformation zone before exit from the die. This is conclusive proof of dynamic recovery. The sub-grain (or cell) walls are almost perfect although one or two pinned dislocations can be identified. Figs. 12(b) and (c) are transverse sections clearly illustrating the equiaxed sub-grains. Dislocation pinning at precipitate and oxide particles is more easily distinguishable in these sections. Since the precipitates are apparently aligned in the extrusion direction this is direct evidence that pinning occurred during extrusion rather than on subsequent air cooling. It was noticeable that under the electron microscope high-angle boundaries were all sharply defined and even at the highest temperatures there was no evidence of any incipient melting. This clearly indicates that local temperatures due to pressure welding are not excessive and true 'cold' welding must be the dominant cohesion mechanism.

CONCLUSIONS
1. Additional 'breakthrough' pressure is required for the extrusion of this heat-treatable alloy. This pressure appears to be strain-rate sensitive for powder materials.

2. The greater useful-work/redundant-work ratio is consistent with the premise that 'deformation energy' is a substitute for sintering energy.

3. As-extruded properties are far superior to those of a conventionally produced alloy.

4. The powder material is heat-treatable. More work is required to optimize this process.

5. The powder process is a thermally activated process, the dominant mechanism being dynamic recovery.

REFERENCES
1. T. SHEPPARD and P. J. M. CHARE: *Powder Met.,* 1972, 15, 17.
2. P. J. M. CHARE and T. SHEPPARD: *ibid.,* 1973, 16, 437.
3. T. SHEPPARD: Proc. 15th Int. MTDR, p. 659. 1975: London (Macmillan).
4. R. DAVIES and R. H. T. DIXON: *Powder Met.,* 1971, 14, 207.
5. M. NEGM and R. DAVIES: Ref. 3, p. 637.
6. W. R. D. WILSON: *Int. J. Mech. Sci.,* 1971, 13, 17.
7. T. SHEPPARD and A. F. CASTLE: *Metals Technology,* 1976 (in press).
8. T. SHEPPARD and D. RAYBOULD: *J. Inst. Metals,* 1973, 101, 33.
9. T. SHEPPARD and H. McSHANE: *Powder Met.,* 1976, this issue, p. 121.
10. D. W. PASHLEY, J. W. RHODES, and A. SENDOREK: *J. Inst. Metals,* 1966, 94, 41.
11. A. SEEGER: *Z. Metallkunde,* 1953, 44, 247.
12. T. SHEPPARD and P. J. M. CHARE: *Powder Met.,* 1975, 18, 1.
13. T. SHEPPARD and E. P. WOOD: Proc. 17th MTDR, Birmingham, 1976.

Translations Service of The Metals Society

In 1957, The Iron and Steel Institute began a translations service (BISITS) on behalf of the iron and steel industry, which has subsequently become one of the major sources of translations in its field. The translations, cooperatively produced to serve science and industry on a non-commercial basis, are made by subject specialists and relate to both research and production.

Since 1 January 1974, consequent upon the merger of The Iron and Steel Institute and The Institute of Metals to form The Metals Society, BISITS has been expanded and material of a non-ferrous and general metallurgical nature has been included. Separate lists of translations are available with subject headings to facilitate selection, together with lists of translations in preparation.

If you wish your name to be added to our free mailing list please write to:
BISITS, The Metals Society, 1 Carlton House Terrace, London SW1Y 5DB

See also List of BISITS Translations on inside back cover

Hot re-pressing of powder made from mild steel machining swarf

B. Lengyel, C. L. Tan, and G. G. Teh

Since economic studies indicate that powder produced from mild steel machining swarf in a cryogenic hammer mill is significantly cheaper than that made by any other method, it was decided to investigate whether powder-metallurgy products of acceptable properties could be obtained from such powder by a number of alternative methods. The powder was first isostatically compacted, either with or without prior heat-treatment, at room temperature at pressures of up to 1·38 GN/m² (200 000 lbf/in²). The cylindrical preforms were then used to produce specimens by the alternative routes of sintering, or hot forging, or sintering followed by hot forging at small strains. The density and tensile properties of the swarf powder metal were determined as a function of the process variables. By using certain processing routes the density closely approached that of the parent metal while elongation and ultimate tensile strength remained relatively lower, partly because the limited capacity of the forging machine restricted the plastic strain and hence bonding of the particles, partly owing to contamination of the swarf powder. The presence of non-metallic inclusions caused considerable scatter in the results.

The reclamation of machining swarf by comminution and subsequent powder compaction is attracting considerable industrial interest. While very few details of such work have so far been published, it is known that both steel and cast iron swarf powder metals are used in industry and the utilization of non-ferrous metal swarf via a similar route is being considered.[1,2]

A recent economic study showed that low-cost swarf powder can be obtained by pulverizing mild steel swarf in a cryogenic hammer mill.[3] More recently this method was compared with the water atomization of steel swarf,[4] by considering the main processing stages shown in Chart I.

A modified present-worth method of calculation was used, similar to that developed earlier,[5] with costs estimated from data obtained from industrial sources. Assuming 30% return on investment, the calculations give the following costs per tonne of mild steel swarf powder:

Cryogenic pulverization without reclamation of cutting oil	£73.42
Water atomization without reclamation of cutting oil	£112.72
Cryogenic pulverization with reclamation of cutting oil	£53.00
Water atomization with reclamation of cutting oil	£92.20

It is obvious that cryogenic pulverization is the cheaper of the two methods. However, mild steel swarf powder produced by cryogenic comminution is rather coarse (medium particle size $\sim 450\,\mu$m) compared with the medium particle size of iron powder of $\sim 70\,\mu$m produced by water atomization. The cost difference is due to the higher production costs and relatively large capital cost of the water atomization plant. The energy cost of atomization is particularly high, which is not surprising since the process of melting metals is energy-intensive. Indeed, more direct methods of swarf recycling are sought, mainly because the present practice of remelting it as light scrap in steel making consumes a great deal of energy, so it would be difficult to justify the replacement of one energy-intensive process with another.

The relative importance of the various cost factors is shown in Fig. 1. The slope (sensitivity) of the initial capital cost line of the water atomization process is much steeper than that for cryogenic pulverization. This is also true of the annual production cost lines. The cost of swarf affects both processes equally, as indicated by the identical slope of the swarf cost lines.

Thus the results of two economic studies prove conclusively that the relatively coarse mild steel swarf powder produced in a cryogenic hammer mill is a cheap basic material, and therefore this route of recycling would be economically attractive if simple and reliable ways could be found to convert it into a swarf powder metal of acceptable quality. To find such process routes was the aim of the present investigations.[4,6]

EXPERIMENTAL METHOD

The swarf powder, either with or without prior heat-treatment, was isostatically compacted at room temperature into cylindrical billets of ~ 18 mm dia. $\times 60$ mm long. The heat-treatment was carried out in a vacuum furnace using oxygen-free nitrogen atmosphere at 850°C for 60 min. The preforms so obtained were then forged at elevated temperatures either with or without prior sintering. Sintering was at 1150°C for 30 min in vacuo.

Two forging temperatures were used. Each preform was coated with Dag glass lubricant and heated for 15 min to 1000 or 1150°C in an oxygen-free nitrogen atmosphere before being transferred from the furnace to the forging machine. About 30 s elapsed as the preform was taken out from the furnace until forging began. This time interval was

Analyses of pressure requirements for powder compact extrusions

T. Sheppard and H. McShane

Three possible theories predicting pressures for powder extrusion are developed, based upon upper-bound analysis. It is shown that a plane-strain analogue does not predict acceptable pressures, but theories based upon an observed physical field or alternatively a minimized axisymmetric approach agree with pressures observed during extrusion. The more complex observed field gives the most accurate assessment. All theories predict curves of differing slope to that observed and it is suggested that the stress/strain/strain-rate relationships require more careful experimental appraisal.

The production of 100% dense material by extrusion of atomized powders has been described[1–5] for copper, nickel, and aluminium alloys. Sheppard and Chare[1–3] have shown qualitatively that the pressure requirements for such a process should be lower than those for a similar process utilizing cast billets, and Sheppard[4,5] has shown experimentally that for Ni and Al alloys this thesis may be proven. However, it should be noted[6] that for low stacking fault energy alloys in which dynamic recovery is unlikely to occur the pressure reduction may not be very great.

There is no reported literature analysing the process, although techniques exist which can be applied to the problem. The difficulty arises because of the variation in physical properties throughout the quasi-static deformation zone. Thus upper-bound techniques, which assume that all deformation is effected at velocity discontinuities throughout the zone, offers an attractive method of dealing with the analysis. This technique was first proposed by Johnson[7] who assumed a homogeneous material and developed the theory for low extrusion ratios (i.e. 4). Later Sheppard and Raybould[8] extended the analysis to higher ratios and presented minimized solutions showing good agreement with experimental work.

The work reported here is part of a programme investigating composite materials and the experimental work is reported in a companion paper.[9] The matrix material selected for primary investigation was an aluminium-rich magnesium silicide alloy. Three differing methods of calculation are presented (each based upon an upper-bound analysis) and are compared with experimental results.

THEORY
Extrusion pressures
The most widely used formulae to predict extrusion loads are those developed by Johnson[7] and are of the form

$$\frac{p}{\sigma} = a + b \ln R \dots \dots \dots \dots \dots \dots (1)$$

It has been shown[2] that this form of equation may also be applied to powder extrusion but the magnitude of the flow stress, σ, is difficult to assess and the constants a and b are dissimilar to those observed for as-cast billet extrusion. There is a very clear assumption that the extrusion pressure is dependent only upon reduction and does not vary with differing flow patterns and die shapes associated with various types of material.

An alternative approach based on the flow of metal through the die is possible using slip-line field or load-bounding techniques which are strictly applicable only to processes in which plane-strain conditions obtain. It is possible, however, to apply these methods to the axisymmetric case[8] and the upper-bound approach is more flexible because there is not the requirement of stress equilibrium. The solution must commence with a proposed deformation field which may be derived from practical observations or perhaps suggested by a slip-line field solution. Subsequently the problem becomes one of deriving a rigid triangle hodograph such that the boundary-velocity conditions are satisfied. Since the load calculated will then be higher than that observed it is necessary either to investigate other flow fields, and hence select a minimum load, or to minimize the load by presenting the result in a manner which will enable mathematical techniques to be utilized.

Fig. 1 shows a simple deformation field completely defined by the angles ω and ϕ and by the depth of the deformation zone x. Also shown is the hodograph (or velocity field) which must satisfy the deformation conditions. We may assume that the ram is advancing with unit velocity and that material to the rear of ABC has been compacted to 100% density but has received no shear deformation. Thus material to the rear of ABC will have little or zero shear strength. On encountering the velocity discontinuity AB which, from the hodograph, is of magnitude $\overline{23}$, the powder material is subjected to substantial shear deformation and is confined to flow parallel to AO with velocity $\overline{13}$. Thus all metal in triangle ABO is assumed to attain this velocity and direction. This shear deformation is theoretically assumed to occur instantaneously in zero distance which clearly is impossible. It is assumed that the effective shear strength of the material may be related to the deformation before AB (i.e. = 0) and that after AB. The material next encounters discontinuity BO of magnitude $\overline{34}$, effecting a velocity in direction $\overline{14}$, and finally velocity discontinuity OC ensures that metal leaves the die such that $\overline{15}$ is equal to the plane-strain extrusion ratio. It is important to note that axisymmetric calculations

Nomenclature

A_{ij}	area of discontinuity ij
a	constant in typical extrusion-pressure formulae
AB etc.	length of discontinuity boundary
$\overline{23}$ etc.	corresponding value of velocity discontinuity (or velocity 'jump')
k	shear yield stress
k_{ij}	shear yield stress at discontinuity ij
p	extrusion pressure
R	extrusion ratio
s	length of velocity discontinuity boundary
U_{ij}	velocity perpendicular to velocity discontinuity ij
V_{ij}	magnitude of velocity discontinuity ij
dw/dt	rate of energy dissipation
x	parameter specifying physical field
$\dot{\epsilon}$	strain rate
ϵ_{ij}	strain at discontinuity ij
$\bar{\epsilon}_{ij}$	total equivalent strain at discontinuity ij
γ_{ij}	shear strain at discontinuity ij
ϕ, ω	angles specifying physical field
σ	flow stress
σ_0	strain-rate-dependent stress

are based upon the similarity between the material flow obtaining in that and plane-strain processes. Hence the ratio $(a + d)/d$ must be made equal to $\sqrt{R}$.

The rate of energy dissipation at each discontinuity is given by the product of the length (or area) of the discontinuity, the magnitude of the discontinuity, and the shear yield strength of the metal. Thus for linear discontinuities we may write

$$\frac{dw}{dt} = \Sigma k . v . s \quad \dots \dots \dots \dots \dots (2)$$

The plane-strain solution may then be written (considering unit depth) pressure × area × velocity $= \Sigma k.v.s.$

$$p \times (a + d)(1) \times 1 = \Sigma k . v . s$$

$$p(a + d) = [k_{AB} AB \, \overline{23} + k_{BC} BC \, \overline{24} + k_{BO} BO \, \overline{34} + \\ + k_{OC} OC \, \overline{45} + k_{AO} AO \, \overline{13}] \quad \dots \dots (3)$$

The lengths and velocities may be specified in terms of ω, x, and ϕ:

$$AO = \frac{a}{\sin \omega}, \qquad \overline{13} = \frac{a}{x \sin \omega}$$

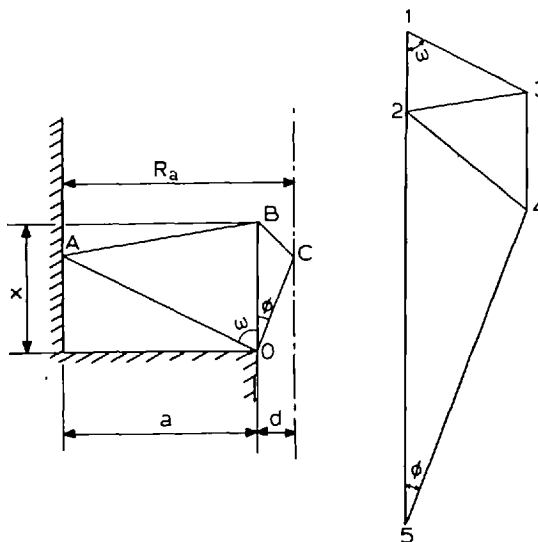$$OC = \frac{d}{\sin \phi}, \qquad \overline{45} = \frac{a}{x \sin \phi}$$

$$BO = x, \qquad \overline{34} = \left[1 + \frac{a}{d} - \frac{a}{x} \cot \omega - \frac{a}{x} \cot \phi \right]$$

$$AB = \left[\frac{a^2}{\sin^2 \omega} + x^2 - 2ax \cot \omega \right]^{\frac{1}{2}},$$

$$\overline{23} = \frac{1}{x} \left[\frac{a^2}{\sin^2 \omega} + x^2 - 2ax \cot \omega \right]^{\frac{1}{2}}$$

$$BC = \left[\frac{a^2}{\sin^2 \phi} + x^2 - 2dx \cot \phi \right]^{\frac{1}{2}},$$

$$\overline{24} = \frac{a}{xd} \left[\frac{d^2}{\sin^2 \phi} + x^2 - 2dx \cot \phi \right]^{\frac{1}{2}}$$

Differentiation of eqn. (3) is complicated for powder materials by the inclusion of shear-stress values varying at each discontinuity. It may, however, be assumed that the values of ω, ϕ, and x giving minimum pressure for constant shear-stress conditions will also yield the minimum pressure for powder compact extrusion. Thus eqn. (3) could be written

$$\text{Load} = Ak \left[2x + \frac{2ax}{d} + \frac{2a^2}{x \sin^2 \omega} + \frac{2ad}{x \sin^2 \phi} - \\ - 3a \cot \omega - 3a \cot \phi \right]$$

Differentiation with respect to x and equating to zero yields

$$x^2 = \frac{a^2}{(1 + a/d) \sin^2 \omega} + \frac{ad}{(1 + a/d) \sin^2 \phi}$$

Differentiation with respect to ω yields

$$\cot \omega = 3x/4a$$

and with respect to ϕ yields

$$\cot \phi = \frac{3x}{4d}$$

Obviously ω and ϕ are not independent of x in this way and iteration is required to ensure accurate minimization of these parameters.

Analyses such as that presented above may be used to obtain the pressure requirements for axisymmetric extrusion because Thomsen[10] has shown that (a) the material flow is similar for identical geometrical configurations, and (b) the magnitude of the velocity during axisymmetric extrusion is the square of the velocity during plane-strain extrusion. There is much experimental evidence to support this second conclusion and it quite clearly satisfies the velocity boundary conditions.

Hence for axisymmetric extrusion the surface area of the discontinuities must be considered, and the magnitude of the velocities must be squared. Hence a revised eqn. (3) will be

$$p \times \pi(a + d)^2 \times 1 = [k_{AB} A_{AB} (\overline{23})^2 + k_{BC} A_{BC} (\overline{24})^2 + \\ + k_{BO} A_{BO} (\overline{34})^2 + k_{OC} A_{OC} (\overline{45})^2 + \\ + k_{AO} A_{AO} (\overline{13})^2] \quad \dots \dots (4)$$

1 **Upper-bound solution based upon simple physical field. Extrusion ratio 40 : 1.**
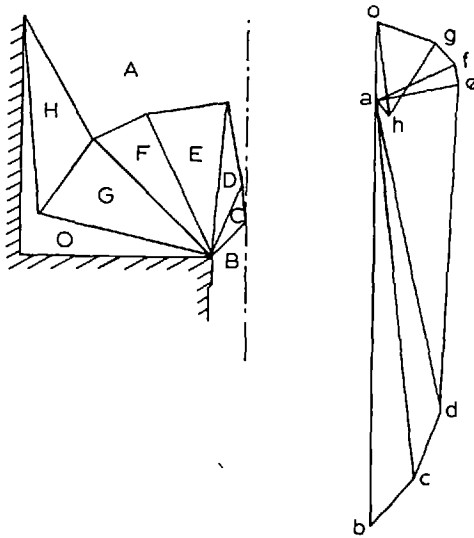
2 Upper-bound solution based upon observed physical field. Extrusion ratio 40:1.

The velocities $\overline{13}$ etc are identical to the plane-strain analysis and the surface areas by simple geometry become

$$A_{OC} = \frac{\pi d^2}{\sin \phi}, \qquad AC = \frac{\pi a(a + 2d)}{\sin \omega}, \qquad BO = 2\pi xd$$

$$AB = \pi(a + 2d)\left[\frac{a^2}{\sin^2 \omega} + x^2 - 2dx \cot \omega\right]^{\frac{1}{2}}$$

$$BC = \pi d\left[\frac{d^2}{\sin^2 \phi} + x^2 - 2dx \cot \phi\right]^{\frac{1}{2}}$$

Since metal flows for plane-strain and axisymmetric geometries are similar, the minimized values of the geometric variables will also be identical. Hence the values of x, ω, and ϕ obtained in the plane-strain analysis may be used in the axisymmetric case.

Both of the methods developed above suffer from the drawback of a limited discontinuity pattern. Thus deformation occurs in three large steps. An alternative approach is to use an observed flow pattern and to build coherent discontinuities about this pattern. This will have the advantage of many discontinuities which for powder material, where the shear yield stress is strongly dependent upon deformation, may be important. Such a physical field with its accompanying hodograph is shown for a reduction ratio of 40:1 in Fig. 2. The extrusion pressure is then given by

$$p \times \frac{\pi(a + d)^2}{4} \times 1 = [k_{AH}A_{AH}(ah)^2 + \ldots +$$

$$+ k_{BC}A_{BC}(bc)^2] \quad \ldots \ldots \ldots (5)$$

Shear yield stress

Equations (3), (4), and (5) each require that the shear stress of the compact be predicted within each rigid zone and thus at each discontinuity. The relative shear deformation at each jump is given by the magnitude of the velocity 'jump' divided by the velocity perpendicular to that jump. The material is also elongated in the direction of its deflected flow and in the three-dimensional case there will be deformations of small magnitude in directions at right-angles to this.

Fig. 3 is identical to Fig. 1 but depicts the relevant parameters. Thus for example the shear deformation at AB

is of magnitude $\ln (V_{AB}/U_{AB})^2 = \ln (\overline{23}/12')^2 = \gamma_{AB}$ and the deformation on the flow direction $= \ln (\overline{13})^2 = \epsilon_{AB}$. At BC the deformations are $\ln (\overline{24}/\overline{14'})^2 = \gamma_{BC}$ and $\ln (\overline{14})^2 = \epsilon_{BC}$.

The strains in directions perpendicular to these will be an order of magnitude less so that the total equivalent strain may be written

$$\bar{\epsilon}_{AB} = \sqrt{\frac{2}{3}} (|\epsilon_{AB}|^2 + \tfrac{1}{2}|\gamma_{AB}|^2)^{\frac{1}{2}} \text{ etc.}$$

It should be noted that the use of the velocity-squared relationship is also necessary to determine the shear yield stress to be used in the plane-strain analogue; otherwise the total strain will not correlate with that actually obtaining in the extrusion process. Since the measurement is expressed in terms of natural strain it is also necessary to take the natural logarithm of change in zero time and hence the material must have properties related to those at each side of the discontinuity. This value may best be estimated by taking the mean equivalent strain such that the deformation at each discontinuity is given by

$\tfrac{1}{2}\bar{\epsilon}_{AB}$ at   AB

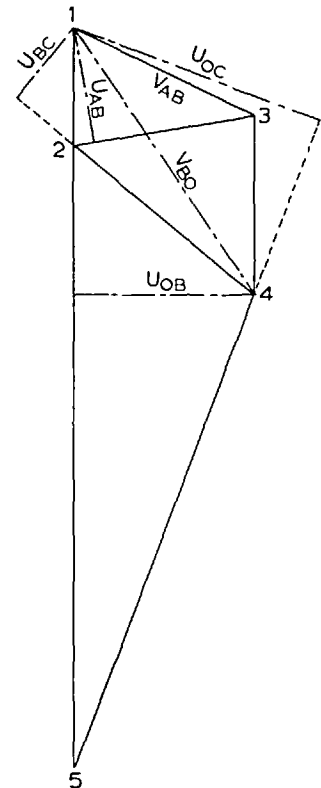$\tfrac{1}{2}\bar{\epsilon}_{BC}$ at   BC

$\bar{\epsilon}_{AB}$ at   AO

$\bar{\epsilon}_{AB} + \tfrac{1}{2}[\bar{\epsilon}_{AB} + \bar{\epsilon}_{BO}]$ at   BO

$\bar{\epsilon}_{AB} + \bar{\epsilon}_{BO} + \tfrac{1}{2}[\bar{\epsilon}_{BO} + \bar{\epsilon}_{OC}]$ at   OC
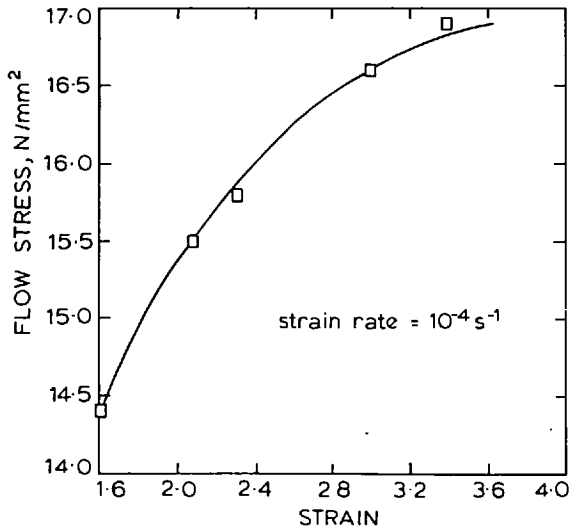
The results of tensile tests, shown for a strain-rate of 10^{-4} s^{-1} in Fig. 4, indicate a stress/strain relationship for magnesium silicide powder compacts:

$$\sigma = \sigma_0 \epsilon^{0.21}$$

where σ_0 is a strain-rate-sensitive constant.

3 Hodograph of simple field showing strain parameters.

4 Stress/strain relationship at 400°C.

A combination of tensile and torsion tests suggested a relationship between stress and strain rate:

$$\sigma_0 = 75 \; \dot{\epsilon}^{0.19}$$

The results of the strain-rate tests giving this best-fit curve are shown in Fig. 5.

Using the Von Mises yield criterion, the shear yield stress at a discontinuity is thus given by

$$k_{ij} = \frac{75}{\sqrt{3}} \; \dot{\epsilon}^{0.19} \; \bar{\epsilon}_{ij}^{0.21}$$

COMPARISON OF THEORIES WITH EXPERIMENTAL RESULTS

The plane-strain and axisymmetric extrusion pressure calculated according to eqns. (3) and (4) were programmed for computer and the results are shown in Fig. 6. A program allowing the hodograph shown in Fig. 2 to be drawn automatically is being developed, but for this work the physical fields and hodograph were drawn manually. A sample calculation for an extrusion ratio of 40:1 is given in Table I and the relevant curve has been constructed in Fig. 6.
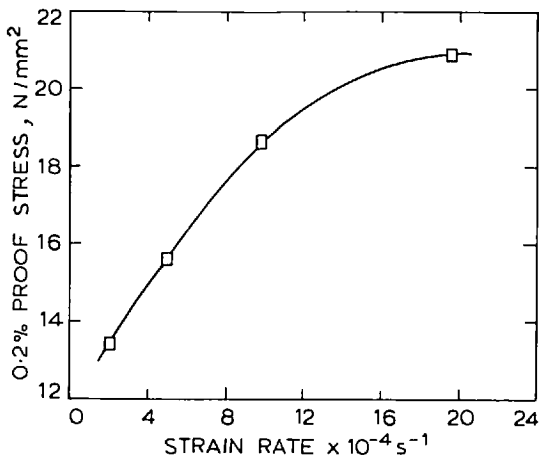
5 Stress/strain-rate relationship at 400°C.
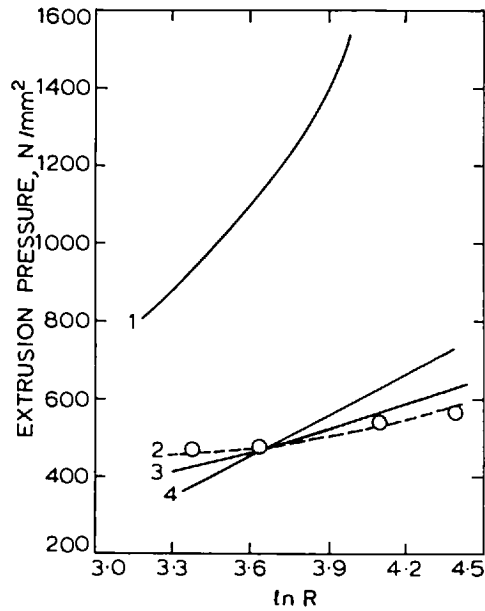
6 Comparison of experimental and theoretical results: 1 = minimized plane strain; 2 = experimental; 3 = observed physical field; 4 = minimized axisymmetric.

The most significant feature in Fig. 6 is the enormous discrepancy between the pressures predicted by the plane-strain analogue approach and those observed in practice. When extruding cast billets this method usually predicts pressures which are ~20% above those actually obtaining. Clearly, for powder compact extrusions the method is not sufficiently accurate.

The minimized axisymmetric solution gives a reasonable correlation with experiment but the predicted slope of this curve is manifestly incorrect and for high extrusion ratios (i.e. > 100) the theory would again be unacceptable.

The best curve is obtained using the approach based upon an observed physical field, although this theory also predicts a curve differing in slope to that observed. It is not clear why this should be so. Certainly for cast materials all three theories would give curves having similar slopes. Most

Table I Specimen calculation using observed physical field at extrusion ratio 40:1

Boundary	A_{ij}, mm²	V_{ij}, mm/s	$\bar{\epsilon}_{ij}$	k_{ij}, N/mm²	$k_{ij}A_{ij}(V_{ij})^2$
OH	7355	1·22	0·297	56	502 641
OG	6848	0·539	0·359	58·19	214 768
AH	4548	0·033	0·148	48·73	7 314
AF	1156	1·02	0·076	42·64	50 286
AE	376	0·986	0·063	41·08	15 231
AD	238	14·17	1·330	75·60	254 972
AC	18	20·23	1·442	76·83	27 977
HG	2291	1·17	0·508	62·36	167 170
GF	2082	0·118	0·437	60·52	14 868
FE	1291	0·042	0·292	55·45	3 039
ED	736	13·89	1·380	76·16	778 615
DC	2716	0·514	2·776	87·58	122 272
CB	131	0·649	2·964	88·74	7 545

$$k_{ij}A_{ij}(V_{ij})^2 = 2\,166\,700$$

Extrusion pressure $= \dfrac{2\,166\,700 \times 4}{\pi \times 75^2} = 490 \; N/mm^2.$

probably the inaccuracies arise because of insufficient experimental data in determining the stress/strain and stress/strain-rate relationships. The tests were all conducted at 400°C and other temperatures should be investigated using compression as well as torsion and tensile data to determine the relevant flow and shear stresses. Nevertheless the upper-bound based upon an actual deformation (or physical field) shows very good agreement with experimental observation.

CONCLUSIONS

1. The plane-strain analogue approach is not suitable for predicting powder compact pressure.

2. The minimized axisymmetric upper-bound theory predicts pressures with acceptable accuracy, provided the extrusion ratio is < 100.

3. The upper-bound solution based upon an observed physical field gives very good agreement with observed pressures.

4. The variation between theoretical and experimental curve slopes requires further experimental investigation.

REFERENCES

1. T. SHEPPARD and P. J. M. CHARE: *Powder Met.,* 1972, **15**, 17.
2. P. J. M. CHARE and T. SHEPPARD: *ibid.,* 1973, **16**, 437.
3. P. J. M. CHARE and T. SHEPPARD: *Int. J. Powder Met. & Powder Tech.,* 1974, **10**, 203.
4. T. SHEPPARD: Proc. 15th Int. MTDR, p. 659. **1975:** London (Macmillan).
5. T. SHEPPARD: *Powder Technol.,* 1974, **10**, 257.
6. A. GREASLEY and T. SHEPPARD: Proc. 2nd Int. Conf. on Consolidation of Particulate Matter, Brighton, August 1975.
7. W. JOHNSON: *J. Mechanics and Physics Solids,* 1956, **4**, 269.
8. T. SHEPPARD and D. RAYBOULD: *J. Inst. Metals,* 1973, **101**, 33.
9. T SHEPPARD and H. McSHANE: *Powder Met.,* this issue, p. 126.
10. E. G. THOMSEN and T. JORDAN: Ref. 7, p. 184.

IRON AND STEEL ABSTRACT CARD AND PROFILE SHEET SERVICES OF THE METALS SOCIETY

Full abstracts of articles drawn from the world's iron and steel literature are available in the following forms:

ABTICS (Abstract and Book Title Index Card Service)

A weekly service for a year (January–December) in which cards are sent to subscribers containing full abstracts and book titles classified under the Universal Decimal Classification (UDC). Such cards form a simply operated filing system for which various aids are provided.

ISIP (Iron and Steel Industry Profiles)

A weekly service for a year (beginning any time, covering any subject, and charged *pro rata*) in which sheets are sent to subscribers arranged according to declared fields of subject interest and containing full abstracts, book titles, and translation references. Such profiles forming a current awareness service can be mailed (by air, when appropriate) direct to subscribers or in a batch to a company. An order form sent with the weekly profiles enables orders for loans, photocopies, and translations to be handled promptly.

Prices

Details of subscription rates and further information will be sent on request by Mr M. L. Pearl, The Metals Society, 1 Carlton House Terrace, London SW1Y 5DB.

Production of an aluminium-rich magnesium silicide alloy from atomized powder

T. Sheppard and H. McShane

The production of an aluminium-rich magnesium silicide alloy by extrusion from the powder phase is described. The pressure requirements of such a process are investigated and it is shown that the operation may be described as thermally activated. The strain-rate sensitivity is shown to be less than the equivalent cast and extruded material. The mechanical properties of the as-extruded product are far superior to those of the conventional alloy and the powder material is heat-treatable.

Until the advent of modern atomizing techniques the production of components from aluminium parts was hindered to a large extent by the cost of powders. Atomization has overcome this main obstacle, although in general the dispersion-hardening effect is not so pronounced because the Al_2O_3 content is reduced compared with the original SAP-type alloys. An additional obstacle to widespread use of these light alloys is that the oxide dispersion acts as a vacancy barrier during the sintering process, prolonging that operation. A convenient process which ensures that the powder compact forms a homogeneous 100% dense product is extrusion, which can be carried out at high or low temperature with large strains. It has been shown[1,2] that such a process eliminates the sintering operation and it is suggested that energy which is termed 'redundant' in the extrusion of cast ingots is utilized to assemble the powders into solid form. Powder compacts also have an advantage over the normal ingot because less pressure is required[3] to effect extrusion. This is due to the differing rheological nature of the quasi-static deformation zone.

The atomizing process has other advantages in addition to the dispersion-hardening effect of the oxide film which almost invariably develops as an envelope surrounding each particle. The particles are usually cooled at a rate far in excess of those found in the normal continuous casting of aluminium alloys. This rapid cooling gives a fine eutectic, due to nucleation at lower temperatures, and the size and nature of precipitates can be expected to differ. In a heat-treatable alloy the oxide film and the differing nature of the precipitates may together be expected to alter the heat-treatment reaction. There appears to be no reported literature on this subject.

The Al–Mg–Si system, when aluminium-rich, is among the most widely used aluminium alloys, having architectural and structural applications. The object of the present work was to examine the rate-controlling deformation mechanism, the nature of product densification, the alloy structure, and the effect of oxide dispersions on the ageing process.

EXPERIMENTAL
Material
The air-atomized Al–Mg–Si (HE9) alloy powder, supplied by Borax Consolidated Limited, nominally contained 0·5 wt.-%Mg, 0·5 wt.-%Si, balance Al. Initially the powder particle size distribution was obtained using standard 200 mm BS sieves stacked on an Endrock mechanical shaker to sieve a standard weight of powder (175 g) for a specified time (1 h). The results are shown in Table I.

Samples of the powder were analysed by the Imperial College Analytical Services Laboratory. The chemical composition is given in Table II.

Preparation for extrusion
To facilitate handling at the press, the powder was compacted into billets using a 150 ton Tangye hydraulic press. To ensure easy removal of the billets from the die the tool surfaces were cleaned and painted with a stearic acid–chloroform lubricant before each compaction.

Table I   Size distribution of Al–Mg–Si alloy powder

Particle size, μm	Weight percent
+ 355	2·14
−355 + 180	30·77
− 180 + 106	25·73
− 106 + 90	5·39
− 90 + 75	5·20
− 75 + 63	5·65
− 63 + 53	5·15
− 53	19·72

Table II   Chemical analysis of powder (remainder Al) (wt.-%)

O	Mg	Si	Cr	Cu	Fe	Mn	Ti	Zn	Ni
0·062	0·33	0·12	0·01	0·014	0·15	0·10	0·014	0·025	0·004

THE PRODUCTION OF FIBRE REINFORCED ALUMINIUM BY A POWDER EXTRUSION TECHNIQUE

H.B. McSHANE and T. SHEPPARD
John Percy Research Group, Department of Metallurgy,
Imperial College of Science and Technology, London

SUMMARY

The paper reports results of experiments designed to produce a fibre rein-forced alloy using an aluminium matrix and a B_2O_3, SiO_2 fibre.

It is shown that during extrusion the glass powder elongates into fibres having a favourable aspect ratio. The relationships between mechanical properties and process variables are reported and include the results of 120 experimental runs. The structure, substructure and bonding are investigated in some detail. It is shown that tensile properties are improved, elongation is acceptable and impact strength only slightly deteriorates when compared with the matrix material.

INTRODUCTION

Probably the single most important factor precluding the widespread use of fibre re-inforced material is the cost of the production. The most common method of manufacture of composites involves coating of the individual fibres by the matrix material, aligning the coated fibres in a suitable direction and finally bonding by hot or cold pressing. Sheppard and Chare [1] have shown that when extruding aluminium and aluminium alloy powders the particulate nature of the cold compacted billet is re-tained well into the deformation zone; assuming solid properties only near the exit of this zone. Thus, there is much interparticle movement, cohesion and segregation of particles within this zone. Moreover, individual particles are elongated within the zone and are processed such that their aspect ratio on completion of deform-ation is related to the extrusion ratio. Thus, if a reinforcing material could be identified which was essentially viscous at extrusion temperature and considerably stronger at room temperature it should be possible to produce a composite by a ran-dom mixing process prior to extrusion; the reinforcing fibres being formed as part of the extrusion process.

It was, therefore, decided to inves-tigate a range of glasses as the reinforcing medium. The most suitable appeared to be the boron based group and from these a B_2O_3 - 10% SiO_2 was selected because:

(i) B_2O_3 has a low softening point which is much less than the temperatures obtained when extruding aluminium or alum-inium alloys. It is thus vis-cous at processing temperatures.

(ii) B_2O_3 forms a good bond with alum-inium during extrusion. An essen-tial feature which is necessary to ensure that the fibres do not 'pull-out' of the matrix on application of a load

(iii) B_2O_3 with 10% SiO_2 is a glass with good mechanical properties and hence a strong composite would be expected.

The later consideration is based quite simply on consideration of the rule of mixing:-

$$\sigma_{COMP} = (1 - x) \sigma_m + x \sigma_G$$

It should be noted, however, that a critical fibre length exists which must be exceeded if the stress on the fibres is to approach their ultimate tensile stress. Shorter fibres produce a stress concentration effect which produces com-posite failure by decohesion of the fibres with the matrix and hence the potential load bearing capabilities of the fibre are not utilized. Appendix I shows that the critical length for the system reported in this communication cannot be achieved at extrusion ratios less than 10. The main weakness of the glass selected is that its modulus is approximately equal to that of the matrix so that transfer of load within the composite cannot be expec-ted to be 100% efficient.

The experiments reported here, therefore used B_2O_3-10% SiO_2 in an aluminium rich mag-nesium silicide matrix. The matrix material was selected because of its wide-spread commercial use as a medium strength, cheap, extruded aluminium alloy for archi-tectural and other purposes.

This communication compares the pro-perties and structure of the reinforced extrude with those of an undoped product produced from the matrix material. The effect of the process parameters upon the product are reported. Thus, the inter-relation of structure and properties with

extrusion temperature, ram speed, extrusion ratio, wt-% glass, tensile test temperature and strain rate are examined

EXPERIMENTAL WORK

Materials

The glass of composition 90% B_2O_3 - SiO_2 was prepared by roller mixing carefully weighed amounts of the constituent oxides which were fused in fireclay crucibles and poured into steel moulds. The product was then crushed, ground and sieved to produce a glass powder. The size distribution of the glass was found by sieving a 200g sample for one hour in a standard sieve shaker.

The air atomized Al-Mg-Si powder was also supplied by Borax Consolidated Ltd., and the particle size distribution was obtained using standard 200mm BS sieves stacked on an Endrock mechanical shaker to sieve a standard weight of powder (175g) for a specified time (one hour). The results of the powder analysis are shown in Table I.

Table I - Particle Size Distributions

B_2O_2	SiO_2	Al-Mg-Si	
Sizeμ	wt%	Sizeμ	wt%
+250	9.42	+355	2.14
+180	20.03	+180	32.91
+125	33.33	+106	58.64
+ 90	46.71	+ 90	64.03
+ 75	52.03	+ 75	69.23
+ 53	62.86	+ 63	74.92
+ 45	69.50	+ 53	80.07
- 45	28.15	- 53	18.72

Samples of the metal matrix powder were analysed by the Imperial College Analytical Services Laboratory and the chemical composition is given in Table II.

Table II - Chemical Analysis of Powder

(Remainder Al) wt %

O	Mg	Si	Cr	Cu	Fe
0.062	0.33	0.12	0.01	0.014	0.15

Mn	Ti	Zn	Ni
0.10	0.014	0.025	0.004

Preparation of Billets

The glass and metal powders were roller mixed in pre-determined proportions for two hours. The billets were produced by compacting this powder in a 75mm diameter

boronised tool steel ram and die set. Pressures were exerted by a 1.5MN Tangye hydraulic press giving a maximum compacting pressure of $346MN/m^2$. The tool surfaces were lubricated with a mixture of chloroform and stearic acid. After preparation it was necessary to store the billets in plastic containers with silica gel in order to prevent disintegration due to adsorption of water from the atmosphere.

Extrusion

The extrusions were performed on a 5MN ENEFCO extrusion press after preheating the billets in an air circulating furnace. A disc of solid Al-Mg-Si material was placed in front of the billet as has been reported in previous work[2]. This was found to be more critical than in the extrusion of purely metallic components.

Examination of Product Properties and

Structure

Specimens were prepared from the same location in each extrusion to ensure that structure and property variation along the extrusion did not influence the results. The electron microscope foils were prepared by grinding on water-lubricated silicon carbide paper to a thickness of ~15mm followed by thinning using a standard window technique. The electropolishing was carried out in a solution of 30% Nitric Acid in methanol under a potential difference of 15V and at a temperature of $-30^\circ C$. The transmission microscopy was carried out on an AEI EM6 100kV electron microscope.

Standard Hounsfield Number 12 specimens were machined for tensile tests performed at room temperature and temperatures up to $400^\circ C$. The tensile tests were performed on an Instron Tensile Testing machine fitted with a split furnace for the high temperature tests.

Impact tests on notched specimens were carried out using a Hounsfield balanced impact machine, the mode of testing being identical to the standard Izod test but with a differing specimen geometry. The energy reading given by this machine was therefore multiplied by a factor of 2.4 in order to obtain the corresponding Izod value.

RESULTS AND DISCUSSION

Extrusion Processes

The effect of varying temperature and extrusion ratio on the pressure required for extrusion is shown in Fig. 1. Extrusion ratios up to 180:1 were investigated with temperature varying between 250° and $540^\circ C$. It is clear that the normal form of extrusion law is obeyed (i.e. p=a+b lnR) and from Fig. 1 the relationships shown in Table III can be obtained.

The ratio of a/b has traditionally been considered to be a measure of the redundant

work occurring during the extrusion process. Such work which does not contribute to a shape change has been shown to contribute to the welding and re-welding process during powder compact extrusion. It is useful to investigate this ratio since in powder extrusion the flow stress varies with strain and strain-rate and it is not easy to define an average flow stress. The value of a/b for a cast Al-Mg-Si alloy of similar chemical composition is 0.3 at

Table III   Pressure - Extrusion Ratio
             Formulae

Temp.	Law	a/b
250°C	p=179.2+111.0 lnR	1.61
350°C	p=122.0+ 96.1 lnR	1.27
450°C	p= 92.7+ 89.8 lnR	1.03
500°C	p= 61.3+ 91.3 lnR	0.67
540°C	p= 71.8+ 82.5 lnR	0.87

FIG 2 Effect of temperature on redundant work

FIG 1 Effect of temperature and extrusion ratio on extrusion pressure
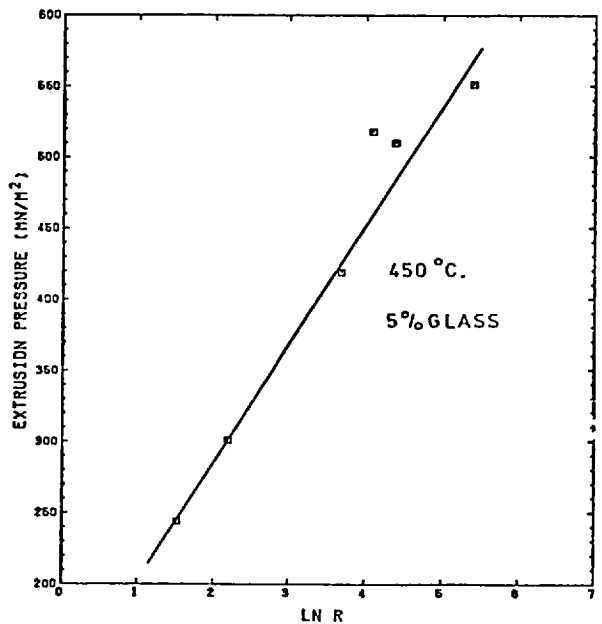
FIG 3 Effect of extrusion ratio on extrusion pressure for a composite billet,

540°C and hence it becomes clear that modes of deformation in cast and powder extrusion are not similar.

The variation of a/b with temperature is shown in Fig. 2 indicating a linear decrease in proportion of redundant work with increasing temperature. This then would support the thesis that within the redundant work term there is a component which essentially represents the energy required to ensure final cohesion of the powder mass. Clearly local welding will be easier at elevated temperatures and we would expect the powder mass to be fully compact at an earlier site in the deformation zone than at lower temperatures. This variation in a/b ratio with temperature has been observed by Ashcroft and Lawson[3] for cast commercial purity aluminium but they also observed that the ratio remained constant with temperature for an Al-Mg-Zn -Cu alloy. It would appear therefore, that the redundant work is very much a function of alloy micro-behaviour and depends upon the values of A, n and ∝ in the hyper-

bolic hot working relationship $Z=A(\sin h \propto \sigma)^n$ where A, $\propto$ and n are constant, σ is the flow stress and Z is the temperature compensated strain rate. It is known that for cast materials the values of A and σ depend upon alloy complexity and it has been shown that these values differ for cast and powder extrusion routes [4] . Fig. 3 shows that the extrusion of composite billets also produces pressure-reduction ratio relationship of the same form giving p=48.16+93.10 lnR giving an a/b ratio of 1.05 at 450°C. This would indicate that the addition of 5wt% B_2O_3-SiO_2 has very little effect on the process of extrusion. It is perhaps surprising that the lubricating effect of the viscous glass does not modify the process in some way.

vacancy concentration will result. It is further aided by a natural precipitation hardening process which occurs at room temperature over a period of weeks and is due to a fine precipitate of Mg_2Si. The room-temperature proof stress varies from 125-75 N/mm^2 over the temperature range investigated which compares with an as-extruded strength of 50-55 N/mm^2 for the normal cast alloy. The elongation varies from 20-25% which is remarkable since the cast as-extruded product is assigned a value of 12% for this property. These high elongation values are compatible with the very fine grain size observed in powder extrusion and which are a direct result of the rapid quench involved in the production of powders. Clearly, dynamic recovery processes have been the dominating deformation mechanism since recrystallisation would have modified the grain size.

The effect of varying the tensile test strain rate is shown in Fig. 5. It is clear that the strain-rate sensitivity of the material is quite different at room
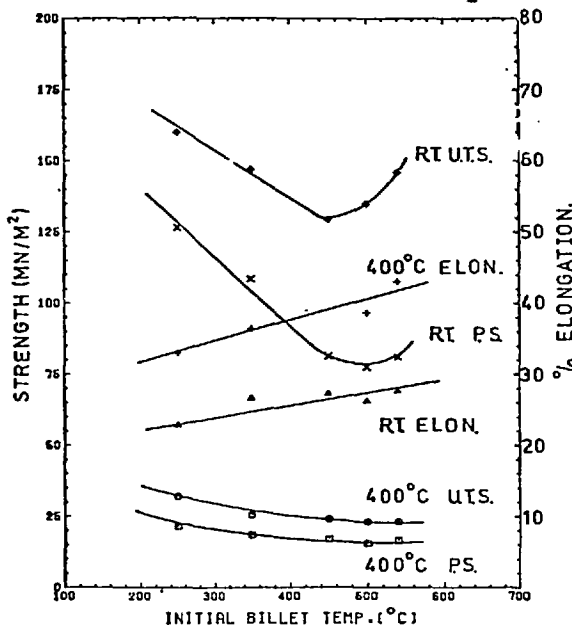

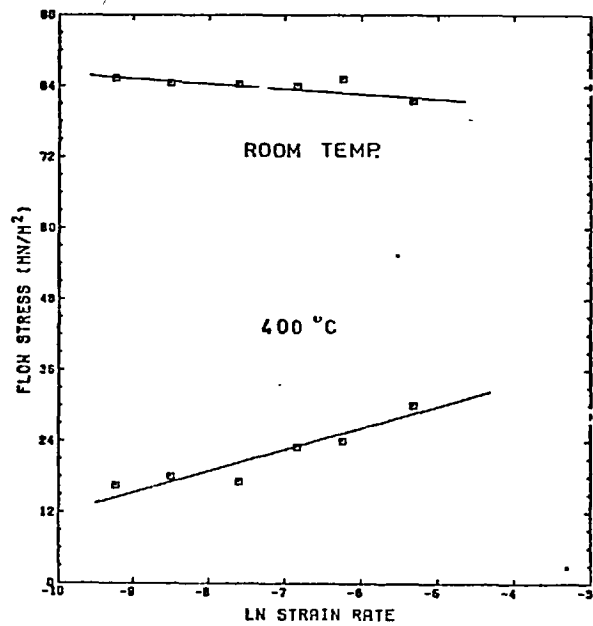FIG 4 Effect on initial billet temperature on mechanical properties

FIG 5 Effect of strain rate on mechanical strength

Mechanical Properties

(i)Matrix Material

The variation in mechanical properties with initial billet temperature is shown in Fig. 4. The room-temperature proof and ultimate stresses show the expected decrease in value with increasing billet temperature (in the range 250-480°C) which is clearly due to softening, probably by dynamic recovery. However, from 480°C to 540°C the trend is reversed; the material becomes stronger and elongations continue to improve. Thus, it is clear that at the higher extrusion temperatures a limited amount of Mg_2Si is taken into solution and on subsequent air cooling a super-satured solution with a non-equilibrium

and elevated temperature; the strain rate exponent changing from positive at 400°C to negative at room temperature. This data agrees with that presented by D'antonio et al[3] who noticed a complete change in dependence over the same temperature range and in the same strain-rate range (i.e. < 10^{-2} per sec.).

The increase in proof stress with strain rate at 400°C is readily explained by the fact that dislocation generation occurs more easily than does dislocation annihilation by dynamic recovery. The negative exponent observed at room temperature is less easily explained. Lubahm [5]

has reported, also for an Al-Mg-Si alloy, that the strain-rate sensitivity again achieves_ a minimum at room temperature and observes that it is at this temperature that strain ageing effects are most apparent. Strain ageing effects occur when a material is being plastically deformed and dislocations are pinned by solute atom clusters. The increasing concentration of stress eventually tears the dislocations away from the pinning clusters. Since the stress required to obstruct motion of dislocations is less than that required to free them, the flow is reduced. However, the solute atoms diffuse rapidly and 'repin' dislocations. Thus, the cycle is repeated. If the strain rate is increased, diffusion may not be rapid enough for 'repinning' to occur and the flow stress will be reduced. We should note however, that since serrated yielding was not observed, this explanation may be inadequate.

The effect of powder particle size on extrude mechanical properties was also investigated and it should be noted that no correlation could be found between extrusion pressure and particle size. Fig. 6 shows that decreasing particle size results in increased material properties. This can be related to the existance of a Hall-Petch type relationship in which the particle size becomes the grain size analogy and strength becomes proportional to the reciprocal of the particle dia. to some power χ (where χ is 1-2). As the particle size decreases the average number of dislocations per unit volume increases because grain boundries may be formed by dislocations. It is also possible to observe dislocations in as-atomized powders which are presumably due to the high residual stresses due to rapid cooling at the atomizing stage.

(ii) Composite Material

The weight percent fraction of glass in the billet was found to have no significant effect upon the extrusion process variables indicating that attainment of properties occurred at a late stage in the deformation zone.

The significance of glass fraction on mechanical properties is illustrated in Fig. 7. Simple fibre theory and the rule of composites would suggest that strength should vary linearly with the glass content. The ultimate stress appears to agree with such simple theory in the range 0-8 wt% glass. However, above this fraction there is a decrease in strength which occurs because of the disparity in bulk moduli between matrix and glass ($K_{matrix}=26.2 \times 10^9 \ N/m^2 \quad K_{glass}=13.8 \times 10^9 \ N/m^2$) Thus when the material emerges from the die the glass recovers elastically, significantly more than does the metal matrix and causes premature failure of the mate-
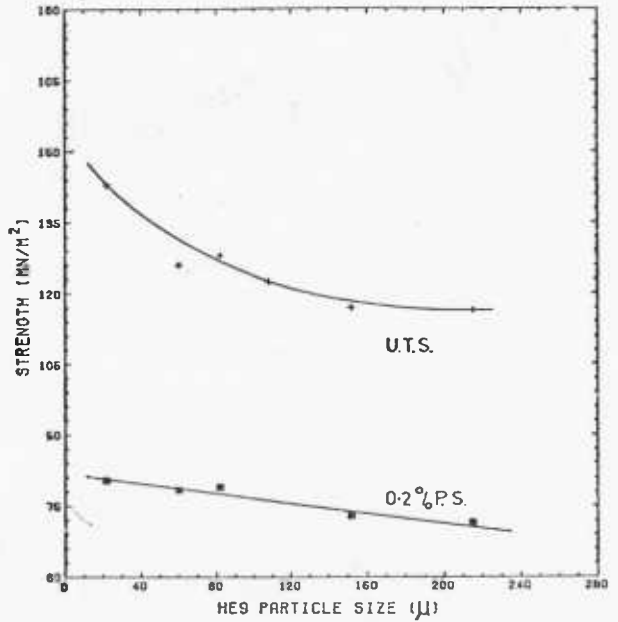

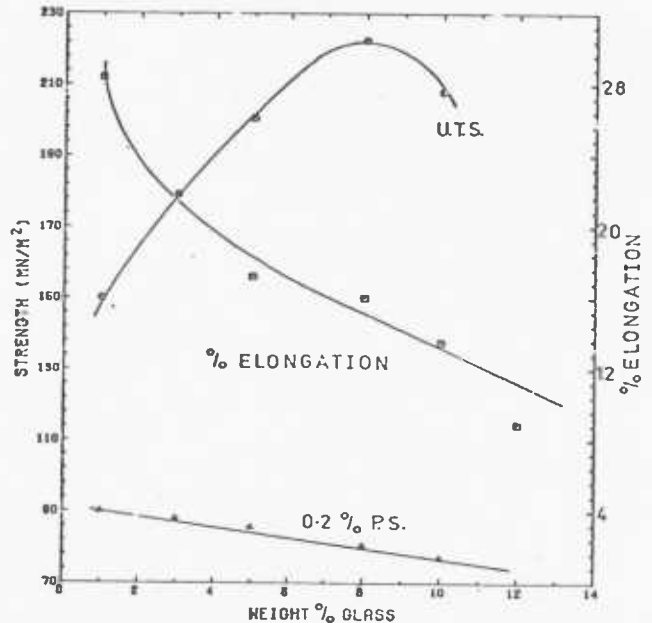FIG 6 Effect of powder particle size on mechanical properties

FIG 7 Effect of glass content on mechanical properties

rial. The strengthening would be improved if 'ideal' cylindrical fribres were formed. In fact Fig. 8 shows that formation within the die is far from ideal, the glass being squeezed as a viscous liquid into spaces between adjacent powder particles.

The effect of glass content on the proof stress is as expected, very small. Basic

(a)

(b)

FIG 8

FIG 9 Effect of extrusion temperature on
mechanical strength of composite
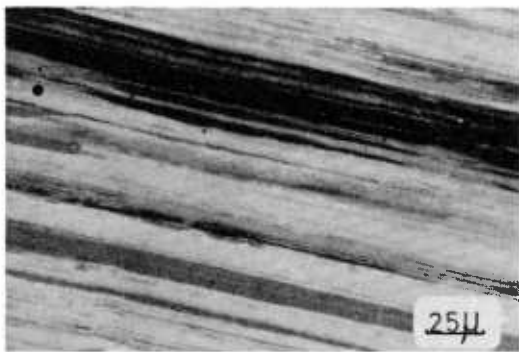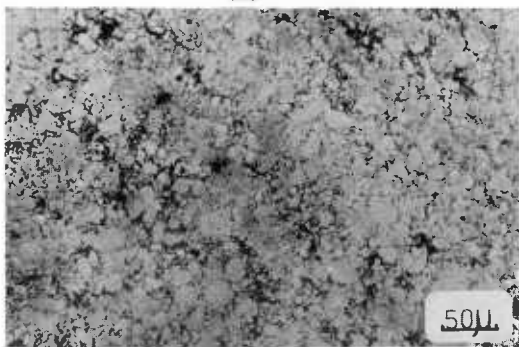
fibre theory pre-supposes that the matrix
will yield in order to fully exploit the
load transfer. Thus, we might expect a
very small decrease in proof stress with
increasing glass content.

Fig. 9 illustrates the effect of ex-
trusion temperature upon the room tempe-
rature strength of the composite. The
ultimate tensile stress shows an almost
linear increase with temperature whilst
the proof stress deteriorates very slightly
The process parameters affect ultimate
stress values in a manner completely op-
posite to the matrix material. This is
because the chemical bonding of matrix
and fibre is so much more efficient at
high temperatures. This strengthening
effect more than compensates for the soften-
ing in the initial matrix due to dynamic
recovery. The proof stress is seen to
decrease rather more rapidly with tempe-
rature than is the case for the matrix
material. This is again clearly associ-
ated with the stress concentration effect
as the load is transferred from the matrix
to the composite.

Decreasing the glass particle size
has a similar effect to decreasing the
matrix particle size except that the
major change occurs in the levels of
ultimate strength obtainable. Fig. 10
shows that the optimum glass particle
size is about 40 μ. The explanation
must be that as particle size decreases
the surface/volume ratio increases ex-
posing a greater area for chemical bond-
ing with the matrix. Under these condi-
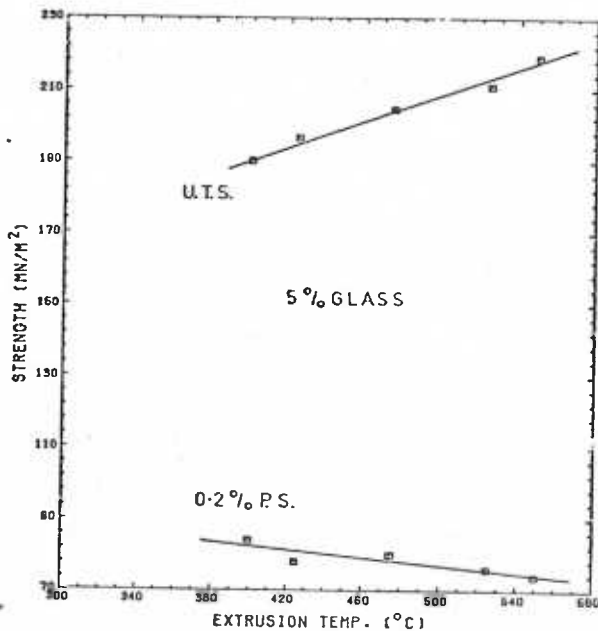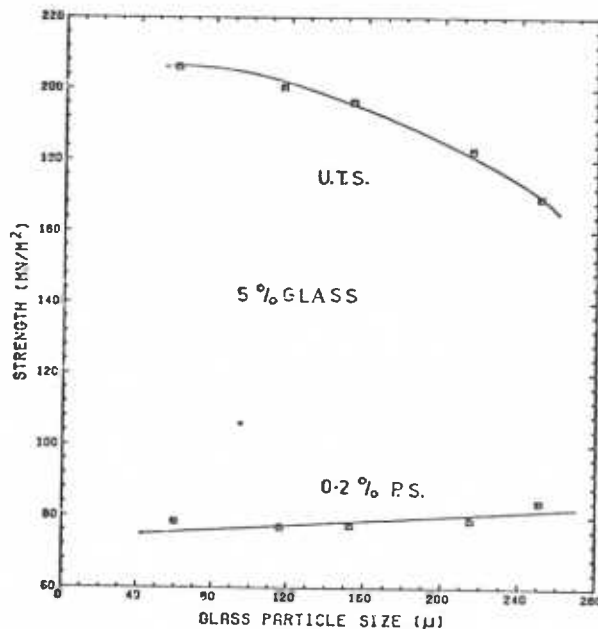tions fibres would then tend to break

FIG 10 Effect of glass particle size on
mechanical properties

rather than 'pull-out' and hence the com-
posite strength increases. There must
however, clearly be some stage at which
all fibres are breaking and hence no fur-
ther advantage would accrue from further
increases in surface area/volume ratio.

The glass particle size has little effect on the proof stress since at this stress the fibre is not bearing a substantial portion of the load.

One of the primary aims of fibre strengthening is to protect strong but brittle fibres by surrounding with a weak but ductile matrix. Thus, in theory the notch ductility of a composite should be satisfactory if only because if a notch forms in one fibre (perpendicular to the fibre) it will only propagate throughout that fibre before being blunted in the ductile matrix. Thus the notch ductility of the composite is of some interest, indicating whether the composite is behaving correctly and indeed will continue to behave correctly during service. Fig.11 shows that for glass weight fractions up
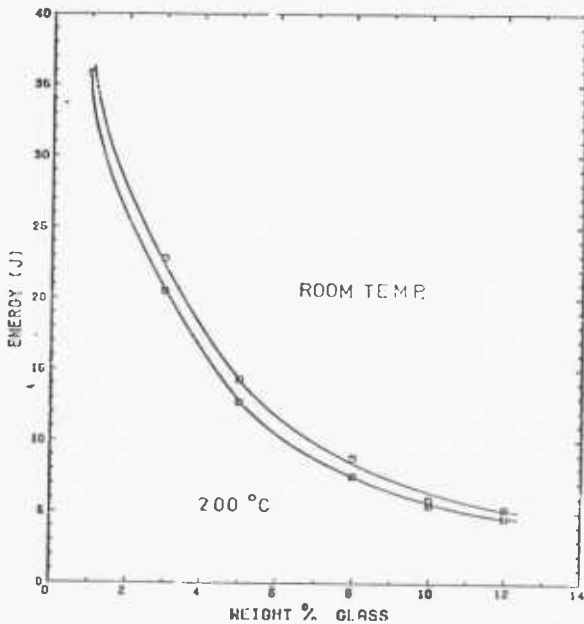

FIG 11 Effect of glass content on notch ductility

to 2% the notch ductility is 28.4 N-m compared to 42.17 N-m for the matrix material. Further additions of glass cause a rapid decrease in notch ductility which appears to be caused by the difference in elastic constants of the fibre and matrix materials. This results in premature cracking of the matrix weakening its resistance to crack propagation. Impact tests were also conducted using specimens heated to 200°C and Fig. 11 indicates that at this temperature there is only a small reduction in toughness.

Table IV shows the comparison between as-extruded composite and matrix material properties together with typical figures for an as-cast and extruded alloy.

Table IV -Optimum Properties of Materials (extruded at 450 C)

	Proof Stress N/mm^2	Ultimate Stress N/mm^2	Elong- ation %	Notch Ductility N-m
'As-cast'	55.0	101	12	43.1
Matrix	81.5	129.5	27	42.2
Composite (5% glass)	87	201	17	14.4

Extrudate Stucture

(i) Matrix Material

When examined under the optical microscope the product exhibited a fibrous cold-worked type structure as shown in Fig. 12(a) The original particles have been elongated into the extrusion direction and measurements confirmed that elongation of the particles was approximately proportional to the extrusion ratio. This cold-worked type microstructure was produced in extrusions performed above the recrystallisation temperature of the alloy and the transverse microstructure (Fig. 12(b)) confirms the equiaxial nature of the structure. It was not possible to detect any deviation from this structure over the wide range of extrusions investigated confirming that a substructure must be present and that dynamic recovery was the prevailing deformation mechanism.

The transmission electron microscope reveals a structure consisting of subgrains which are in general elongated in the extrusion direction (Fig. 13(a)) and are equiaxed in the transverse direction (Fig. 13(b)). This confirms that dynamic
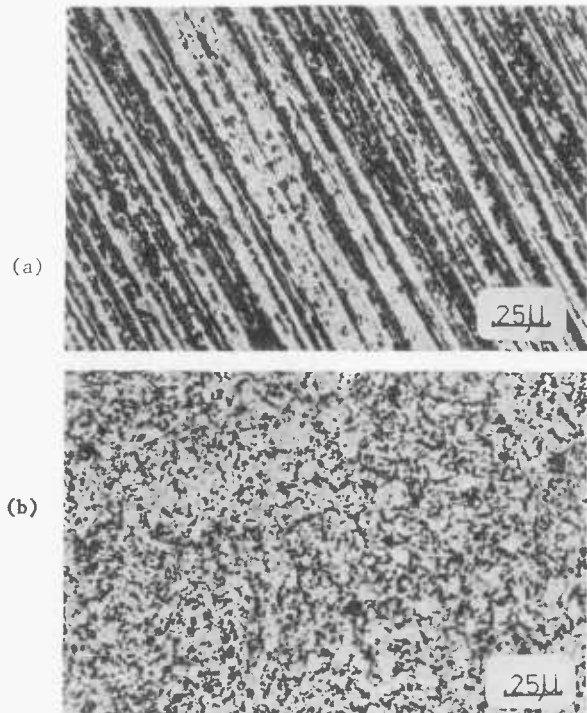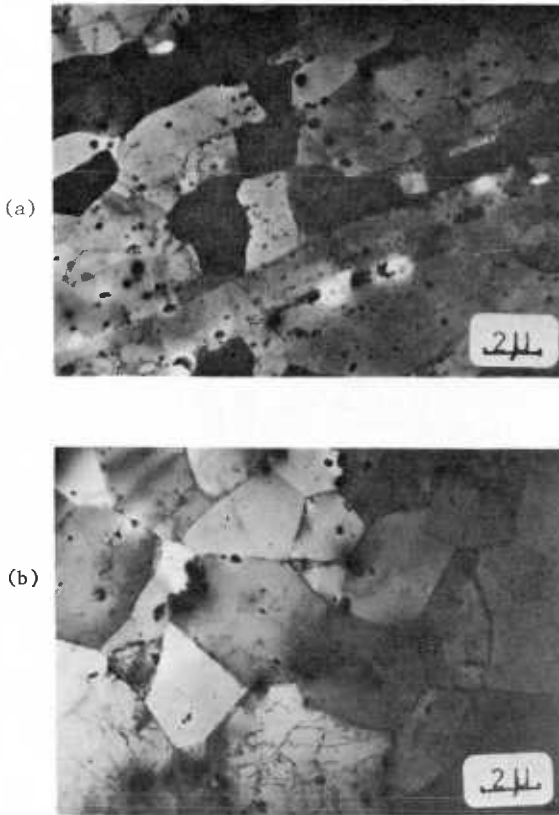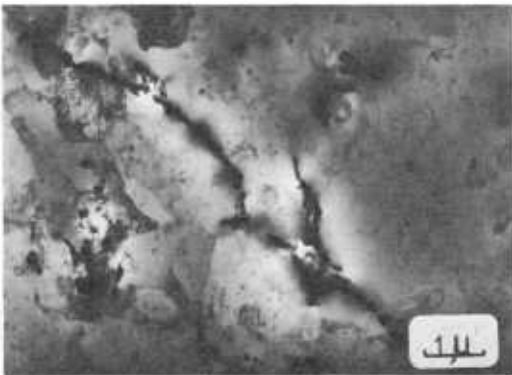

(a)

(b)

FIG 12

(a)

(b)

FIG 13

from a region in the deformation zone of a partially extruded billet. It illustrates very clearly how the oxide layer surrounding a particle is broken up and elongated during the extrusion process. This photograph was taken at a location in the middle of the deformation zone and it is evident that the particulate nature of the billet is still preserved at this stage. The oxide has already been elongated and it is also possible to discern that the hard oxide layer penetrates the original particle before assuming its final position in the extrusion direction.

Fig. 15 shows the increase in sub-grain size which occurs with increase in extrusion temperature (i.e. decrease in temperature compensated strain rate). Such a
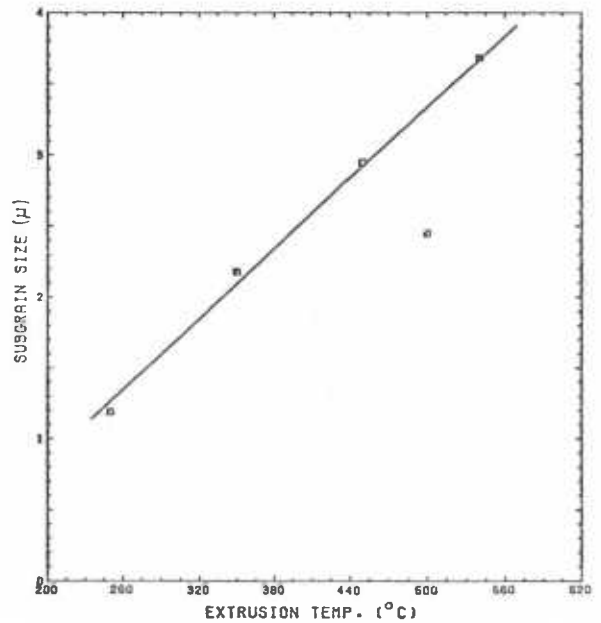

FIG 15 Effect of extrusion temperature on
         sub-grain size.

recovery has occurred. The discontinuous nature of the original oxide film is evident and original boundaries may still be detected and identified by the drawn out debris of the original oxide. The apparent presence of oxide in the centre of grains is attributed to the orientation selected during the thinning operation, such oxide being the remains of that surrounding a neighbouring grain. Fig. 14 is an electron micrograph taken from a foil prepared

relationship has been established for a number of aluminium alloys produced by the conventional method by Sheppard and Raybould [6] . At higher temperatures dislocations have a greater thermal energy and the recovery mechanisms, usually climb and cross slip, operate more readily. Hence, sub-grains are first formed and recovery occurs by tangling and untangling of subgrain boundaries such that the sub-grain size increases thus lowering the overall dislocation density. This is a direct result of the sub-grain boundaries consisting of tangles of dislocations.

FIG 14

Extrudate Structure

(ii) Composite

The optical micrographs Figs 8(a) and (b) illustrate the imperfect nature of the fibres formed by the extrusion process. The transverse section illustrates the wide variety of transverse shapes of the fibres and shows quite clearly that transverse viscous flow of glass has occurred during passage of the composite through the deformation zone. The longitudinal micrograph indicates that fibre cross-section also varies along its length but in general the aspect ratio is satisfactory. The 'cold worked' appearance of the matrix material suggests once more that dynamic recovery remains the deformation mode during composite extrusion. It is just possible to locate very small microcracks in this micrograph which of course, would have a deleterious effect on properties. Fig. 16 is a macrograph taken of an extrusion stopped during the ram stroke and clearly shows the development of structure within the deformation zone. It illustrates the
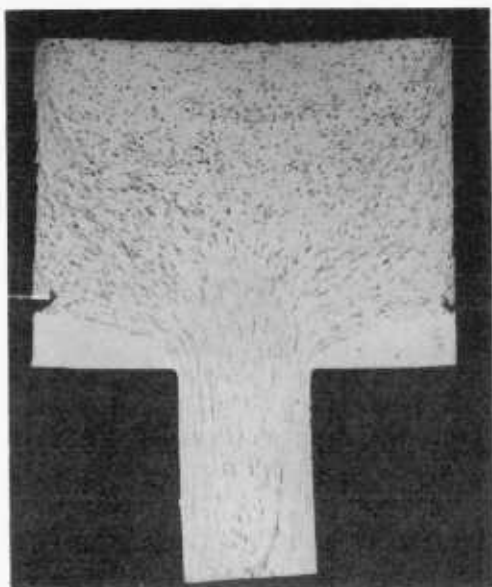

FIG 16

inhomogeneous nature of the extrusion process which causes glass particles located near the surface of the billet to be elongated to a much greater extent than those located on the central axis. Nevertheless all fibres seen to have a suitable aspect ratio although this wide variation in fibre cross-section makes analysis difficult. It would certainly be worthwhile to investigate the effect of indirect extrusion upon the formation of fibres since this is inherently a more homogeneous process.

It was not possible to investigate the composite material under the electron microscope because thinning of foils caused the glass fibres to fall out of the matrix. However, the scanning electron micrograph shown in Fig. 17 is
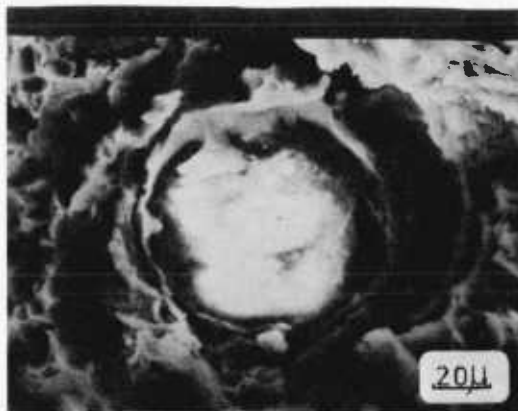

FIG 17

interesting. This shows the crater left by a fibre on the fracture surface (the fibre has disappeared by hydroysis). Microcracks can be descerned around the fibre-matrix interface and even voids between fibre and matrix. These voids are in fact too large to be due to thermal shrinkage so most probably they have occurred during the polishing operation. The shell around the crater is most distinct and consists of glass-metal interaction products which include the spinel $Mg_2Al_2O_4$ [7]

CONCLUSIONS

1) The matrix material produces an interesting and useful alloy without the addition of fibre strengthening.

2) The extrusion of randomly mixed glass and aluminium alloy particles produces a coherent composite material containing discontinuous glass fibres having a suitable aspect ratio.

3) The maximum useful wt % glass is approximately 8. The addition of a greater glass content causes mechanical properties to fall.

4) High extrusion temperatures (low temperature compensated strain rates) are desirable for optimum mechanical properties.

5) Greatly enhanced tensile properties are produced by incorporating glass fibres in the matrix.

ACKNOWLEDGEMENTS

APPENDIX

The Minimum Extrusion Ratio required for a Coherent Product

Assuming that the glass particles are spherical with radius r_1 and that after extrusion their shape is cylindrical with radius r_2 and length ℓ .

$$\text{The ratio } \frac{r_1^2}{r_2^2} = R \text{ the extrusion ratio.}$$

Continuity requirements of the glass reinforcement yields

$$\frac{4}{3} R^{\frac{3}{2}} r_2 = \ell$$

The critical fibre length $\ell_c = \frac{r_2 \sigma_f}{\tau}$

where σ_f is the stress in the fibre and τ the fibre shear strength.

Hence for fibre reinforcement to be satisfactory

$$\frac{4}{3} R^{\frac{3}{2}} \quad r/2 \;>\; \frac{r_2 \sigma_f}{\tau}$$

For this system $\sigma_f = 2412 \text{ MN/m}^2$

$\tau = 100/\sqrt{3} \text{ MN/m}^2$

Hence $R = 9.94$

REFERENCES

1. P.J.M. CHARE and T. SHEPPARD (1974)
Int. Journal Powder Met. and Powder Techn.,
10, (3), p.203.

2. T. SHEPPARD and H.McSHANE (1976),
Powder Met., 19, (3), p. 121

3. R. D'ANTONIO, R.J. MACIAG, K. MUKERJEE,
G.J. FISCHER (1968), Trans. AIME, 242,
pp.2295

4. T. SHEPPARD and P.J.M. CHARE (1975),
Powder Met., 18, p.1.

5. J.D. LUBAHN and R.P. FELGAR (1961),
"Plasticity and Creep of Metals", Wiley

6. D. RAYBOULD and T. SHEPPARD (1972),
J.I.M., 101, p.73.

7. R. THOMPSON et Al (1976), 19, (4), p.181.